

**Gravity Modeling, Seismic Stratigraphy, and Thermal Maturity Modeling
of Hydrocarbons of the Permian Foreland Basin, USA, and the Sergipe-
Alagoas Rifted-Passive Margin, Brazil**

by
Hualing Zhang

A dissertation submitted to the Department of Earth and Atmospheric Sciences, College of
Natural Sciences and Mathematics
in partial fulfillment of the requirements for the degree of

DOCTOR OF PHILOSOPHY

in Geology

Chair of Committee: Paul Mann

Committee Member: Dale E. Bird

Committee Member: Kurt Rudolph

Committee Member: John Suppe

University of Houston
August 2021

Copyright 2021, Hualing Zhang

DEDICATION

To my parents.

To rocks.

To the little curious me in this giant universe.

ACKNOWLEDGMENTS

I thank Dr. Paul Mann for his guidance and support on my doctoral dissertation and his supervision throughout my graduate career at the University of Houston. I appreciate the Conjugate Basins, Tectonics, and Hydrocarbons (CBTH) industry sponsors for funding my employment as a graduate research assistant that allowed me to undertake and complete my doctoral studies at the University of Houston. Special thanks go to Dr. Dale Bird, Kurt Rudolph, and Dr. John Suppe for their service on my dissertation committee and their willingness to provide guidance and contributions throughout this project.

I also thank Mark Nibbelink (Enervus) and James Keay (TGS) for providing me well logs from the Permian Basin. I thank Scott Paton and Alan Morgan from Bell Geospace for providing me the full tensor gravity gradient data from the Permian Basin. I thank Renata Ribeiro de Lima at Agência Nacional do Petróleo, Gás Natural e Biocombustíveis (ANP) for her assistance and Igor Aquilino (Geopost) for his assistance for access to data for my Brazil study. I thank Dr. Ana Krueger for her assistance with my data request through ANP and sharing her extensive knowledge of Brazilian basins with me. Special thanks to Drs. James Deckelman and Kyle Reuber at ION for providing me two deep-penetration seismic reflection lines from Brazil, and to J.V. Lima and Herman Lebit at PGS for providing critical 2D seismic reflection grids from Brazil. I would like to thank numerous people, including academic researchers, industry professionals, and students at CBTH, especially Sean Romito, Nawaz Bugti, Marcus Zinecker, Mei Liu, and Lei Sun, for providing numerous insights, points of view, and support during my Ph.D. studies. Finally, I would like to thank my parents and friends for their support and encouragement throughout my graduate career.

ABSTRACT

The Permian Basin in west Texas is by far the most prolific oil-producing onshore basin in the U.S., and the Sergipe-Alagoas Basin is the sixth-largest hydrocarbon producing basin in Brazil. The purpose of this dissertation is to better understand the changing tectonic setting, crustal structure, and sedimentary basin fill influenced the hydrocarbon potential of these two basins.

In **Chapter 2**, I created 2D and 3D gravity models to better define the tectonic origin of the Abilene gravity minimum (AGM) underlying the northern Permian Basin. I inferred the AGM as a Precambrian rift zone composed of lower density granitic and metasedimentary rocks. Basement structure defines the limits of deep basinal areas that may host productive, thermally mature source rock kitchens controlled in part by strike-slip faults aligned with AGM edges.

In **Chapter 3**, I created a 3D full tensor gradiometry (FTG) gravity model for the northeastern Delaware Basin. Tzz inversion results provide detailed density distribution than conventional gravity inversion. Faults are expressed as steep gradients on Tzz map. Low-density source body edges, defined from Txz and Txy calculated anomalies, correlate with low-density areas are inferred to be hypogenic karst features in the central and southwestern study area.

In **Chapter 4**, I define three domains of the rifted, continental crust in the Sergipe-Alagoas basin based on 2D seismic interpretations and 2D and 3D gravity models: 1) necked zone of continental crust; 2) hyper-extended zone of continental crust; and 3) the outer domain. The conjugate margin in northern Gabon, west Africa is wider with greater stretching

and is explained by Precambrian basement fabrics that were oriented in a near-orthogonal to continental rifting.

In **Chapter 5**, I used 2D seismic and well logs to define four megasequences bounded by regional unconformities: 1) pre-rift crystalline Precambrian basement, 2) syn-rift clastic sequence, 3) post-rift, sag sequence, and 4) passive margin sequence. Basin modeling shows mature Albian-Turonian source rocks overlain by Upper Cretaceous-Eocene reservoirs in the southwestern, indicating deepwater potentials. The northeastern area of the basin exhibits thin or absent source rocks due to magmatic activity and uplift during the Aptian.

TABLE OF CONTENTS

DEDICATION	III
ACKNOWLEDGMENTS	IV
ABSTRACT	V
TABLE OF CONTENTS.....	VII
LIST OF TABLES.....	XI
LIST OF FIGURES	XII
CHAPTER 1 : INTRODUCTION TO THIS DISSERTATION ...	1
History and development of this dissertation.....	1
Rationale, topics, and organization of this dissertation.....	9
Summary of Chapter 2	10
Summary of Chapter 3	11
Summary of Chapter 4	12
Summary of Chapter 5	13
CHAPTER 2 : INTEGRATION OF REGIONAL GRAVITY MODELING, SUBSIDENCE ANALYSIS, AND SOURCE ROCK MATURITY DATA TO UNDERSTAND THE TECTONIC AND HYDROCARBON EVOLUTION OF THE PERMIAN BASIN, WEST TEXAS.....	15
Introduction.....	15
Geologic and tectonic setting.....	15
Previous interpretations of the tectonic controls on the Permian Basin subsidence.....	16
Hydrocarbon significance	18
Objectives of this chapter.....	19
Data and methods.....	22
Well data	22
Gravity and magnetic data	23
Two-dimensional gravity model	26
Three-dimensional gravity model	27
Results from two-dimensional gravity modeling.....	28
Density variations.....	28
Model A-A'	29

Model B-B'	32
Model C-C'	34
Results from three-dimensional gravity modeling.....	36
Density variation	36
3D gravity modeling framework.....	38
Crustal structure of the Permian Basin.....	40
Basin modeling results and implications for hydrocarbon exploration	41
Basin tectonic phases from subsidence analysis	41
Stratigraphy of units deposited during the five tectonic events	45
Distribution of thermal maturity with respect to Permian Basin depocenters	46
Discussion	49
Reconciling contrasting views on the regional, tectonic controls of Permian Basin subsidence	49
Permian Basin as a broken foreland basin	51
Deformational model for the rift inferred along the AGM trend.....	53
Analysis of regional burial history pattern.....	54
Effect of basement structure on thermal maturity of source rocks	57
Conclusions.....	59
Bibliography.....	62

CHAPTER 3 : DETECTING HYPOGENIC KARST FEATURES IN THE NORTHEASTERN DELAWARE BASIN, WEST TEXAS: APPLICATIONS OF FULL TENSOR GRADIENT (FTG) GRAVITY DATA.....71

Introduction.....	71
Dataset and method.....	73
Results	79
Density inversion of gravity (Tz) anomalies.....	79
Density inversion of gravity gradient (Tzz) anomalies.....	82
Density distributions	87
Application to exploration: identifying karst features that can negatively impact drilling.....	89
Conclusions.....	92
Bibliography.....	93

**CHAPTER 4 : CONTROL OF PRECAMBRIAN OROGENIC TRENDS
ON THE WIDTH AND STRUCTURAL ZONATION OF THE
CRETACEOUS, CONJUGATE RIFTED MARGINS OF
NORTHEASTERN BRAZIL AND NORTHERN GABON.....96**

Introduction.....	96
Tectonic mechanisms for wide versus narrow rifted conjugate margins.....	96
Objectives and tectonic significance of this chapter.....	97
Tectonic, geologic, and hydrocarbon setting of Late Jurassic-Albian rifts related to the opening of the South Atlantic Ocean.....	99
Previous studies of the crustal structure of the onland and offshore Sergipe-Alagoas Basin.....	101
Hydrocarbons of the Brazilian margin.....	102
Dataset and methods used in this chapter.....	103
Results of this chapter from structural interpretations of 2D, deeply-penetrating, seismic reflection lines.....	109
Results from this chapter showing an Aptian magma-rich, syn-rift event.....	117
Seaward-dipping reflectors (SDRs).....	117
Sills and related features.....	120
Results from this chapter based on 2D and 3D gravity models.....	123
Regional tectonic features determined from gravity and magnetic anomalies.....	123
Results from this chapter based on 2D gravity modeling.....	126
Gravity model 1.....	126
Gravity model 2.....	128
Results from this chapter based on 3D gravity modeling.....	130
Discussion.....	134
Controls of orogenic basement fabric on the stretching factors observed for the northeastern Brazil and Gabon rifted-passive margins.....	134
Comparison of the crustal structure of the northeastern Brazilian rifted-passive margin to its conjugate margin in North Gabon.....	137
Implications for hydrocarbon exploration on both conjugate margins.....	139
Conclusions of chapter 4.....	139
Bibliography.....	142

CHAPTER 5 : TECTONOSTRATIGRAPHIC EVOLUTION AND THERMAL MATURITY MODELING OF THE SERGIPE-ALAGOAS RIFTED-PASSIVE MARGIN, NORTHEASTERN BRAZIL ...153

Introduction.....	153
Tectonic setting of the Northeast Brazilian rifted-passive margin.....	153
Four tectonostratigraphic phases of South America-Africa continental rifting and oceanic spreading.....	157
Hydrocarbon history and potential of the Sergipe-Alagoas basin	159
Previous stratigraphic studies of the Sergipe-Alagoas basin	161
Objectives and significance of this chapter.....	162
Dataset and methods used in this chapter	162
Seismic reflection data and well logs.....	162
Basin thermal modeling setup and key parameters.....	163
Results of sequence stratigraphic interpretation of the Sergipe-Alagoas basin	164
Four tectonostratigraphic units affecting the deepwater basin.....	164
Seven seismic facies of the Sergipe-Alagoas basin	167
Pre-rift, basement rocks (Early Neocomian).....	169
Syn-rift megasequence (Neocomian-Middle Aptian)	173
Post-rift, early sag megasequence (Middle to Late Aptian).....	176
Passive margin megasequence (Late Aptian to Recent)	178
Late Cretaceous slumps and MTDs	180
Paleocene deepwater channel complex.....	184
Eocene to Present passive margin	186
Burial history and thermal modeling of the Sergipe-Alagoas Basin.....	188
1D model thermal maturities of source rocks based on two well logs.....	188
Regional maturity trends predicted by lithospheric thermal modeling integrating (3D)	191
Discussion	196
Structural restoration illustrating main tectonic events affecting basin history.....	196
Main elements of the Sergipe-Alagoas petroleum system.....	200
Direct hydrocarbon indicators (DHI) compared with basin model predictions.....	202
Conclusions	204
Bibliography.....	206

LIST OF TABLES

Table 3.1 Mean values and standard deviations for Tzz inversions on the ground surface, top
Rustler Formation of Late Ochoan age, and Combined sedimentary layers.....83

LIST OF FIGURES

Figure 2.1 Geological setting of the Permian Basin.	16
Figure 2.2 Regional cross-sections in the Permian Basin.	21
Figure 2.3 Structural map of the top of the Precambrian basement beneath the Permian Basin basement by Ruppel et al. (2008).	23
Figure 2.4 Gravity anomalies of the Permian Basin.	25
Figure 2.5 Total magnetic field anomalies of the Permian Basin study area from the North America grid compiled by the USGS.	26
Figure 2.6 Density intervals assigned for gravity modeling with simplified stratigraphy and generalized lithology of the Permian Basin region.	29
Figure 2.7 Regional 2D gravity modeling A-A' trending north-south across the Midland Basin and collinear with a previous gravity model by Adams and Keller (1996).	31
Figure 2.8 Regional 2D gravity model B-B' trending north-south across the Delaware Basin and collinear with a previous gravity model by Adams and Keller (1996).	33
Figure 2.9 Regional 2D gravity model C-C' trending east-west across the entire northern Permian Basin.	35
Figure 2.10 Density grids used for gravity modeling.	37
Figure 2.11 Summary of structural inputs used for gravity modeling.	39
Figure 2.12 Inverted crustal structure.	40
Figure 2.13 Summary of density inversion results for the upper crust.	41
Figure 2.14 Subsidence history with five, numbered tectonic stages from the Cambrian through Neogene based on representative exploration wells.	44
Figure 2.15 Maturity modeling based on representative exploration wells.	47
Figure 2.16 Permian Basin as a broken foreland basin.	52
Figure 2.17 Regional burial history pattern.	55
Figure 2.18 Effect of basement structure on source rocks thermal maturity.	58
Figure 3.1 Geological settings of the Permian Basin and study area.	72
Figure 3.2 Geologic map of the study area and FTG survey area (grey box).	74
Figure 3.3 FTG survey.	78
Figure 3.4 Density inversion results of Tz gravity.	80
Figure 3.5 Inversion results of vertical components on the combined layer.	84
Figure 3.6 Inversion results of horizontal components on the combined layer. ...	86
Figure 3.7 Resultant density distribution from Tz and Tzz inversions.	87
Figure 3.8 Karst features identification.	89
Figure 4.1 Free-air gravity map from Sandwell et al. (2014) of the Equatorial and South Atlantic Oceans.	98
Figure 4.2 Topographic and bathymetric map of the Sergipe-Alagoas rifted-passive margin showing the locations of the dataset used in this chapter.	104
Figure 4.3 Gravity anomalies in the study region.	107
Figure 4.4 Deep-penetration, depth-converted ION Span seismic reflection line A-A' through the central Sergipe sub-basin.	111
Figure 4.5 Deep-penetration, depth-converted ION Span seismic reflection line B-B' through the southern Sergipe sub-basin.	114
Figure 4.6 Zoom of depth-converted seismic reflection image A-A' of SDRs ..	119

Figure 4.7 Zoom of depth-converted seismic image B-B' of SDRs	120
Figure 4.8 Examples of volcanic sills.	122
Figure 4.9 Filtered gravity anomalies in showing regional tectonic features.	125
Figure 4.10 Gravity model 1.	127
Figure 4.11 Gravity model 2.	129
Figure 4.12 Resulted Moho structure from 3D gravity model.....	132
Figure 4.13 Resulted crustal structure from 3D gravity model.....	133
Figure 4.14 Relationship between basement fabric orientation and the stretching factors.	136
Figure 4.15 Gravity model of the Brazilian and west African margins.	138
Figure 5.1 Free-air gravity map of the Central Atlantic showing the conjugate margins of the Sergipe-Alagoas basin and the North Gabon basin.....	154
Figure 5.2 Datasets used in this study.	155
Figure 5.3 Chronostratigraphic summary and seismic well-tie of the Sergipe–Alagoas Basin	159
Figure 5.4 Representative, north-south seismic profile along the Sergipe-sub basin showing the five megasequences.....	165
Figure 5.5 Representative seismic reflection facies 1 through 7 (SF 1-7) of the Sergipe-Alagoas Basin.....	169
Figure 5.6 Pre-rift, basement rocks.....	170
Figure 5.7 Syn-rift megasequence.....	174
Figure 5.8 Post-rift, early sag megasequence.....	177
Figure 5.9 Early Cretaceous source rocks.....	179
Figure 5.10 Late Cretaceous slumps and MTDs.....	182
Figure 5.11 Paleocene deepwater channel complex.	185
Figure 5.12 Passive margin megasequence.....	187
Figure 5.13 Burial plot and thermal history model for ANP well 1-BRSA-1104-SES.	189
Figure 5.14 1-D burial and thermal basin model based on log from ANP well 1-ALS-6-AL (6-AL).	190
Figure 5.15 Modeled vitrinite reflectivity for the Riachuelo source interval.	192
Figure 5.16 Modeled transformation ratio for the Riachuelo source interval.....	193
Figure 5.17 Modeled vitrinite reflectivity for the Cotinguiba source interval....	194
Figure 5.18 Modeled transformation ratio for the Cotinguiba source interval. ..	196
Figure 5.19 Structural restoration of seismic line A-A' (location of line shown in map of Figure 5.2).	198
Figure 5.20 Source rock and reservoir rock “sweet spots”.	202
Figure 5.21 Examples of direct hydrocarbon indicators as compiled from seismic lines in the southwestern Alagoas sub-basin	203

CHAPTER 1 : INTRODUCTION TO THIS DISSERTATION

History and development of this dissertation

I grew up in Xinjiang that is an autonomous region of the People's Republic of China located in northwestern China and close to Central Asia. Xinjiang is the largest political subdivision of China and accounts for one-sixth of China's total land area. Xinjiang is split by the Tien Shan mountain range, which divides it into two large basins: the Dzungarian to the north and the Tarim to the south. These large basins contain an estimated 20% of China's oil, gas, and coal deposits, and the oil refining and petrochemical industry now make up up about 60% of Xinjiang's economy.

I was raised in Urumqi, which has a population of 3.5 million people and is the capital and largest city of Xinjiang. Situated near the center of the Asian continent, Urumqi has the distinction of being the most remote city from any sea in the world. Urumqi has undergone rapid development since the 1990s and is now an important commercial and political center in Xinjiang. I acquired an early interest in geology as my father is a petroleum geologist, and I went on frequent family trips into the spectacular natural areas surrounding Urumqi.

Following high school graduation in Urumqi in 2011, I began my undergraduate geology major at the China University of Petroleum in Beijing (CUPB), where I was selected for a dual degree university exchange program in petroleum geology. The dual degree program began with two years of courses at CUPB (2011-2013), followed by two years where I continued in the geology major in English-speaking classes at the Department of Geosciences at the University of Tulsa (TU) in Oklahoma, where I graduated cum laude with my BS degree in geology in May 2015. During the summer of 2014, between my junior and senior years, I was an exploration

geology intern at PetroChina's Xinjiang Oilfield Company in Urumqi. My summer project focused on 3D seismic interpretation and hydrocarbon play development in the Junggar Basin of western China.

During the four-year CUPB-TU program, I ranked in the top 3% of my class in my major subjects in my two years at CUPB and completed the program at TU with a 3.91/4.0 GPA. At my graduation from TU in 2015, my academic accomplishments were recognized by the University of Tulsa by my induction into the Tulsa Engineering and Natural Sciences Honors and Awards Program and by the Tulsa Geosciences Department awarding me their A. N. Murray Award in Geosciences for Academic Excellence.

Following my graduation from the TU, I was accepted into the MS program at Jackson School of Geoscience of the University of Texas at Austin in August 2015. My MS research project was carried out at the UT Bureau of Economic Geology (BEG), which is located 15 km north of the main UT campus in Austin. At the BEG, my research was supervised by Dr. Qilong Fu, an expert in Permian Basin sedimentology and stratigraphy. My MS project focused on lithofacies description, depositional process interpretation, and reservoir quality evaluation of the deep-water fine-grained sediments in the Wolfcampian Formation in the southeast Midland Basin, West Texas. Methods used for this research include detailed core descriptions, well log correlations, petrographic examinations using standard microscopy and scanning electron microscope (SEM), and geochemical analyses that include XRF, XRD, and TOC analyses of core samples. For my study, I integrated these observations into a model for depositional cyclicity and used this model to predict the promising reservoir intervals in the deep-water Permian Basin.

I presented my final MS results as a poster entitled “Lithofacies, Diagenesis, and Reservoir Quality Evaluation of Wolfcamp Unconventional Succession in the Midland Basin, West Texas” at the AAPG Annual Convention & Exhibition in Houston in May 2017 and at the GSA Annual Meeting in Seattle in October 2017. My poster was selected to be one of 15 posters selected from over 200 student posters to be part of the AAPG Student Poster competition. During my final semester at UT in 2017, I was part of the Imperial Barrel Award (IBA) Competition, where our five-person team presented the petroleum geology of offshore Northern Carnarvon Basin, Southwest Australia, and placed third in the competition with nine other universities in the AAPG Gulf Coast section.

I met with Dr. Paul Mann during the AAPG Imperial Barrel Award Competition in 2017, where he was supervising the UH team. He encouraged me to apply to the Ph.D. program at the University of Houston, where I was accepted and joined Dr. Mann’s group, called the Conjugate Basin’s Tectonics and Hydrocarbons Consortium (CBTH) in July 2018. For the next 1.5 years, my project was an integration of gravity and stratigraphic data from the Permian Basin, West Texas, which formed Chapter 2 of this dissertation and was published in the journal *Interpretation* in 2021. For this chapter, I made use of the stratigraphic information acquired from my MS study at UT and appreciate additional inputs provided by Dr. H. Scott Hamlin and his colleagues working on the Permian Basin at the BEG.

For the Permian Basin study, I greatly appreciate the supervision of Dr. Dale Bird for the gravity analysis along with the supervision of the structural and stratigraphic aspects of the study by Dr. Mann, Dr. Suppe, Kurt Rudolf (UH and Rice adjunct professor, former Chief Geologist, ExxonMobil), and Charles Sternbach (UH adjunct professor, President, Star Creek Exploration).

I also thank Mark Nibbelink at Enervus and James Keay (TGS) for providing me with additional well logs from the Permian Basin that were used in this chapter.

During my poster presentation at the 2018 HGS Sheriff Lecture, I met Scott Paton of Bell Geospace, who kindly offered their full tensor gradiometry (FTG) gravity data in the northeastern Delaware Basin that I used in Chapter 3 of this dissertation. I greatly appreciate the efforts of Scott Paton and his colleague at Bell Geospace, Dr. Alan Morgan, for their efforts in making the high-resolution, FTG gravity data set available for my research at the University of Houston. I also greatly appreciate the supervision of Dr. Dale Bird on the FTG gravity analysis that is described in Chapter 3 of this dissertation. In June 2021, Chapter 3 was submitted in a slightly modified form for publication in the *Journal of Applied Geophysics*.

Starting in 2020, I began working on the Sergipe-Alagoas rifted-passive margin in northeastern Brazil. I thank Dr. Ana Krueger (Bluware and UH adjunct professor) for her assistance with my data request for seismic data and well logs through Agência Nacional do Petróleo, Gás Natural e Biocombustíveis (ANP) and for her suggestions on my study. I also thank Ms. Renata Ribeiro de Lima at ANP for her assistance and Mr. Igor Aquilino at Geopost for his assistance with access to Brazilian data from Geopost. Special thanks to Drs. James Deckelman and Kyle Reuber at ION for kindly providing me two, deep-penetration ION seismic reflection lines from my area and to J.V. Lima and Herman Lebit at PGS for kindly providing valuable, deep-penetrating 2D seismic grids. Finally, I thank Dr. Jeff Corrigan at Zetaware for providing the Genesis and Trinity software that was used for Chapter 5 and Mr. Josh Sellars at Seequent for arranging licenses for Oasis Montaj software used in Chapters 2-5 of this dissertation.

During the approximately three-year duration of this dissertation (September 2018 to July 2021), I have made 14 presentations at conferences on my research that were recognized, with receiving three, third-place awards in student competitions in 2020 and 2021. I also made ten presentations at the annual sponsors meeting of CBTH and during in-person and virtual office visits to CBTH sponsors. All 24 presentations of both types are summarized in chronological order below. I appreciate the financial support from Dr. Mann and the industry sponsors of the CBTH Consortium that provided the financial support for my graduate research assistantship for the past three years, along with the cost of meeting registrations and all travel costs to meetings.

Event	Title of presentation	Date/Award
2018 CBTH Year-End Sponsors Meeting, University of Houston, Texas	Basin-wide comparison of faulting, fracturing and subsidence history in the Permian Basin, West Texas (Talk)	September 21, 2018
2018 HGS-EAS Sheriff Lecture and EAS student poster session, Houston, Texas	Using regional subsidence analysis to define five, Late Precambrian to Eocene structural-tectonic phases in the Permian Basin, west Texas (Poster)	November 12, 2018
2019 Annual Meeting AAPG Student Expo, George R. Brown Conference Center, Houston, Texas	Integration of structural analysis and gravity modeling in the Permian Basin, West Texas (Poster)	September 5, 2019
2019 CBTH Year-End Sponsors Meeting, University of Houston	Integration of gravity modeling, sedimentary facies, and subsidence analysis to understand the tectonic stages of the Paleozoic to recent Permian Basin, West Texas (Talk)	September 27, 2019
2019 UH Department of Earth and Atmospheric Sciences, Student Research Day	Integration of gravity modeling, sedimentary facies, and subsidence analysis to understand the tectonic stages of the Paleozoic to recent	April 26, 2019

	Permian Basin, West Texas (Poster)	
2019 AAPG ACE Annual Meeting, San Antonio, Texas	Timing of Paleozoic-Cenozoic tectonic events in the Permian Basin, West Texas, from integrated subsidence and structural studies (Poster)	May 23, 2019
CBTH office visit to BP, Houston, Texas	Integration of subsidence analysis, structural studies, and gravity modeling to understand the tectonic stages of the Paleozoic to recent Permian Basin, West Texas (Talk)	May 29, 2019
CBTH office visit to Total, Houston, Texas	Integration of subsidence analysis, structural studies, and gravity modeling to understand the tectonic stages of the Paleozoic to recent Permian Basin, West Texas (Talk)	June 21, 2019
2019 Gulf Coast Association of Geological Societies Annual Meeting (now called GeoGulf), Houston, Texas	Integration of subsidence analysis and gravity modeling in the Permian Basin, West Texas (Poster)	October 24, 2019
2019 HGS-EAS Sheriff Lecture and EAS student poster session, Houston, Texas	Integrating gravity modeling and structural analysis to understand regional basement structure framework in the Permian Basin, West Texas (Poster)	November 11, 2019
Virtual office visit with ION-Geophysical (Houston) by CBTH	Crustal structure of the Sergipe-Alagoas rifted-passive margin, northeastern Brazil based on 3D gravity modeling (Talk)	March 31, 2020
Virtual office visit with Petrobras (Rio de Janeiro) by CBTH	Crustal structure of the Sergipe-Alagoas rifted-passive margin, northeastern Brazil based on 3D gravity modeling (Talk)	March 31, 2020
Virtual office visit with Total (Houston, Paris, and Pau, France) by CBTH	Crustal structure of the Sergipe-Alagoas rifted-passive margin, northeastern	April 9, 2020

	Brazil based on 3D gravity modeling (Talk)	
Virtual office visit with Shell (Houston) by CBTH	Crustal structure of the Sergipe-Alagoas rifted-passive margin, northeastern Brazil based on 3D gravity modeling (Talk)	April 29, 2020
Virtual office visit with Bell Geospace (Houston) by CBTH	Evaporite karst characterization in the Delaware Basin, West Texas (Talk)	July 30, 2020
2020 CBTH Year-End Sponsor's Meeting, University of Houston (online)	Crustal structure of the Sergipe-Alagoas rifted-passive margin, northeastern Brazil based on gravity modeling (Talk)	September 25, 2020
2020 AAPG ACE Annual Conference (online)	Integration of structural analysis and gravity modeling in the Permian Basin, West Texas (Poster)	September 29, 2020 This poster received the third-place award for best presentation at the 2020 AAPG Student Poster Competition (15 poster entries culled from over 200 submitted student posters)
Invited virtual talk at 2020 Seequent Users Conference (North America and UK groups)	Evaporite karst characterization in the Delaware Basin, West Texas (Talk)	October 6, 2020
2020 AAPG Virtual Student Expo	Integration of structural analysis and gravity modeling in the Permian Basin, West Texas (Poster)	October 9, 2020
2020 HGS-PESGB Virtual Africa Conference	Synthesis of crustal structure and hydrocarbon potential: North Gabon-Equatorial Guinea (West Africa) and Sergipe-Alagoas (Northeastern Brazil) conjugate margins (Poster)	October, 29, 2020
2020 HGS Sheriff Student Poster Presentations (online)	Crustal structure of the Sergipe-Alagoas rifted-passive margin, northeastern	November 9, 2020 This poster received the third-place award for best student presentation in the

	Brazil based on gravity modeling (Poster)	category of advanced MS and Ph.D. students
AAPG Virtual Latin America and Caribbean Region Research Symposium	Integration of structural analysis and 2D gravity modeling of the ultra-thin Sergipe-Alagoas rifted-passive margin, northeastern Brazil (Talk)	November 3, 2020
2020 American Geophysical Union Virtual Fall Annual Meeting	Deep crustal structure of the Sergipe-Alagoas rifted-passive margin, northeastern Brazil based on deeply-penetrating reflection data and 2D gravity modeling (Poster)	December 15, 2020
2021 UH Department of Earth and Atmospheric Sciences, Student Research Day	Integration of basin analysis and gravity modeling for the Sergipe-Alagoas rifted-passive margin, northeastern Brazil (Talk)	April 30, 2021 This oral presentation received the third-place award for best student presentation in the category of advanced Ph.D. students

Rationale, topics, and organization of this dissertation

The Permian Basin is the most prolific oil-producing onshore basin in the United States, and the Sergipe-Alagoas Basin is the sixth-largest hydrocarbon-producing basin in Brazil along the rifted-passive margin of the Brazilian South Atlantic margin. The purpose of this dissertation is to: 1) integrate potential field data and subsurface data such as well logs and regional deep seismic to gain a better understanding of the crustal structure and tectono-stratigraphic evolution in these two hydrocarbon-rich basins; 2) create basin models to understand heat flow distribution and source rock maturity; (3) guide future hydrocarbon exploration areas by constraining sediment accommodation space, major source rocks and reservoirs, and hydrocarbon play fairways and prospectivity.

This dissertation addresses these main topics in two geographic areas (Permian Basin, west Texas and Sergipe-Alagoas Basin in northeastern Brazil):

Chapter 2: integrates regional gravity modeling, subsidence analysis, and source rock maturity data to understand the tectonic and hydrocarbon evolution of the Permian Basin, West Texas.

Chapter 3: detects hypogenic karst features in the northeastern Delaware Basin, west Texas, through applications of Full Tensor Gradient (FTG) gravity data.

Chapter 4: defines the structural domains of the rifted continental crust of the Sergipe-Alagoas rifted margin of northeastern Brazil to understand the control of Precambrian orogenic trends on the width and crustal structure of these domains in northeastern Brazil and its conjugate margin in northern Gabon.

Chapter 5: maps the main sedimentary sequences of the Sergipe-Alagoas basin to understand its tectonostratigraphic evolution and to apply thermal maturity modeling to predict its most productive hydrocarbon zones.

As of the time of submission of this dissertation, Chapter 2 has been published as Zhang, H., Mann, P., Bird, D.E., and Rudolph, K., 2021. Integration of regional gravity modeling, subsidence analysis, and source rock maturity data to understand the tectonic and hydrocarbon evolution of the Permian Basin, West Texas. *Interpretation*, 9(1), 161-181.

Summary of Chapter 2

The Permian Basin of West Texas and southeast New Mexico is currently the most prolific oil-producing basin in the United States. This region experienced deformation and extreme (up to 500 m/my) subsidence, especially in the Delaware Basin during the Late Paleozoic assembly of Pangea. In this chapter, I created regional 2D and 3D gravity models that incorporate density and lithological controls from wireline logs, published seismic refractions, and regional cross-sections to investigate the larger-scale geometry of the Permian Basin, its tectonic evolution, and the distribution of the most productive source rocks in the Permian Basin. These gravity models better define the regional northeast-trending gravity low called the Abilene gravity minimum (AGM) that underlies the Permian Basin. Based on its gravity signature, I infer the AGM to be underlain by a belt of Precambrian, low-density mixture of granite and metasedimentary rocks. Structural inversion results show that the depth to the top of both the lower crust and the Moho is depressed beneath the AGM. Subsidence analysis from the wells in both basins defines five tectonic phases from Cambrian to recent with maximum subsidence

during the main deformational phase, resulting in sediment deposition up to 2.4 km thick. I propose that the geo-body under AGM may have acted as a zone of preferential weakness in a “broken foreland basin” setting that accommodated regional shortening related to the Marathon orogeny and coeval orogenies along the Sonoran margin and Nevadan margin. Basement depth in the Permian Basin defines the limits of deep basinal areas that may host the most productive and thermally mature source rock kitchens – localized in depocenters controlled in part by left-lateral strike-slip faults align with the edges of the AGM. The deeper basement of the Delaware basin has resulted in its broader zone of thermal maturity.

Summary of Chapter 3

High-resolution, high-precision airborne full tensor gradiometry (FTG) gravity data is a useful tool for interpreting hypogenic karst features and related shallow geohazards because higher-resolution FTG data can identify subtle, density changes separating karst voids and the surrounding host rocks. Structurally, the Tzz density inversion produced steep gradients, which are inferred as faults due to their large density offsets. Low-density source body edges, outlined from Txz and Txy calculated anomalies, correlate with low layer density areas that I infer as the locations of hypogenic karst features within the late Permian Guadalupian and Ochoan strata. I conclude that the central and southwestern parts of the study area are at higher risks for drilling because of more dense karst features, while the northeastern part of the study area is at lower risk because of few karst features.

Summary of Chapter 4

The Sergipe-Alagoas Basin is a Late Cretaceous to recent rifted-passive margin basin that forms a 290-km-wide zone of onshore and offshore rifts that separate 36-km-thick crust of the un-rifted São Francisco craton and associated foldbelts of Paleoproterozoic age from the 9-km-thick, Aptian oceanic crust of the South Atlantic Ocean. In Chapter 4, I define three structural domains of the rifted, continental crust that underlie the on- and offshore Sergipe-Alagoas Basin based on interpretations on deep-penetrating industry 2D seismic reflection lines and 2D and 3D gravity models in the offshore rifted zone: **Domain 1** is the 18-km thick, 26-km-wide necked zone of continental crust with sediment-filled, half-grabens; **Domain 2** is the 10-km-thick, 45-km-wide hyper-extended zone of continental crust with magmatic filled, half-grabens; and **Domain 3** is the 9-km-thick, 12-km-wide outer domain before getting into the oceanic crust. The conjugate margin of the Sergipe-Alagoas rifted margin is located 2500 km across the South Atlantic Ocean in northern Gabon in western Africa. The continental rift zone of the northern Gabon margin exhibits similar structural domains as observed in Brazil, but Gabon exhibits a wider zone of thinned, continental crust (~150 km) and a greater degree of stretching ($\beta = 4$) that is explained by relatively stronger, Precambrian basement fabrics that were oriented in a near-orthogonal direction to continental rifting. The Sergipe-Alagoas margin in northeastern Brazil is more narrow (~90 km) and exhibits a lesser degree of stretching ($\beta = 2.5$) that is explained by a relatively weaker, Precambrian basement fabric that was oriented in a sub-parallel to oblique direction to continental rifting.

Summary of Chapter 5

A grid of 200 line-kms of 2D seismic data, 51 wells, and a compilation of published literature were used in Chapter 5 to construct a Mesozoic to recent, tectonostratigraphic framework Sergipe-Alagoas rifted-passive margin of northeastern Brazil. The tectonostratigraphic history of the basin was described according to the structural surfaces and isopach maps of four megasequences bounded by regional unconformities: 1) pre-rift Precambrian crystalline basement; 2) normal-fault-bounded, clastic syn-rift sequence of Neocomian-Middle Aptian age; 3) post-rift, early sag clastic sequence of Middle to Late Aptian age; 4) mainly clastic, passive margin sequence of Late Aptian to recent age. Within the tectonostratigraphic framework, I used the grid of 2D seismic reflection data and well logs to identify and map the key elements of the productive petroleum system of the shelf, slope, and deep basin that includes: 1) **Marine shale source rock** of the Albian-Cenomanian Riachuelo and Cenomanian-Turonian Cotinguiba Formation, 2) **Known and inferred clastic reservoirs** within Upper Cretaceous to Eocene MTDs and stacked channel/deepwater channel complex associated with the turbidite system fed by voluminous sands of the Sao Francisco fluvial-deltaic system, 3) **structural traps** related to minor faults in the passive margin section and **stratigraphic traps** related to slope pinch-outs; and 4) sealing intervals formed by intercalated hemipelagic marine shale within the Upper Cretaceous to Eocene section. Using these model parameters, I conducted 1D thermal modeling of two deep wells and 3D regional thermal modeling using lithospheric thickness and heat-flow estimates constrained by the deep crustal structure of the basin described in Chapter 4. Model results indicate a 100-km-wide fairway of mature Cretaceous source rocks in the southwestern half of the basin that would have expelled hydrocarbons across the shelf, slope, and deep basin beginning in the Early Paleocene and continuing to the present day.

Examples of direct hydrocarbon indicators are shown on seismic lines from this proposed fairway. The largest exploration risk in the northeastern part of the basin is due to thin or absent source rocks related to Cenozoic seamounts and volcanic plateaus.

CHAPTER 2 : INTEGRATION OF REGIONAL GRAVITY MODELING, SUBSIDENCE ANALYSIS, AND SOURCE ROCK MATURITY DATA TO UNDERSTAND THE TECTONIC AND HYDROCARBON EVOLUTION OF THE PERMIAN BASIN, WEST TEXAS

The following chapter is based on: Zhang, H., Mann, P., Bird, D.E., and Rudolph, K., 2021.

Integration of regional gravity modeling, subsidence analysis, and source rock maturity data to understand the tectonic and hydrocarbon evolution of the Permian Basin, West Texas.

Interpretation, 9(1), 161-181.

Introduction

Geologic and tectonic setting

The Permian Basin of West Texas and southeast New Mexico is located in the distal foreland area of the Ouachita-Marathon-Sonoran fold-thrust belt (Yang and Dorobek, 1995; Poole et al., 2005; Ruppel, 2019) and was likely subjected to other, more distant, late Paleozoic orogenic effects from the southwestern and western margins of North America (Leary et al., 2017; Ewing, 2019). The Permian Basin covers an area of 220,000 km² of West Texas and southeastern New Mexico and includes three major components: in the west, the Delaware Basin (DB) contains up to 6.4 km, mainly Paleozoic strata that dip eastward; in the center is the relatively elevated area of the north–south-trending Central Basin Platform (CBP); and in the east, the Midland Basin (MB) contains up to 4.4 km of mainly Paleozoic strata (Matchus and Jones, 1984; Dutton et al., 2005; Figure 2.1).

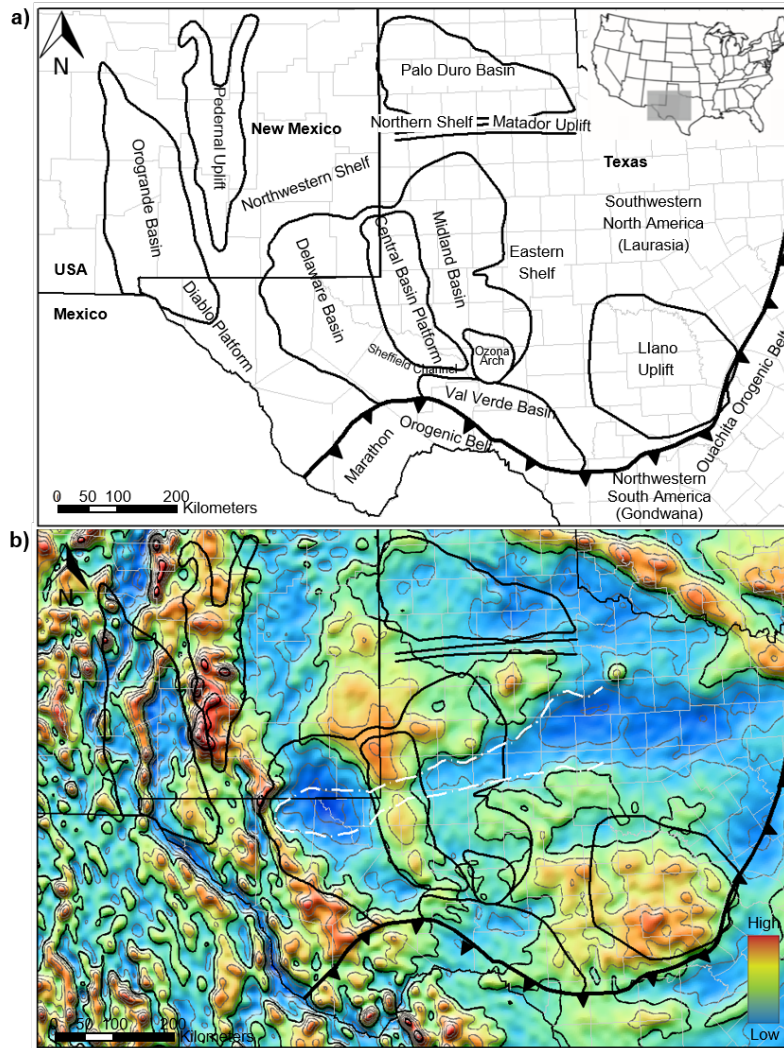


Figure 2.1 Geological setting of the Permian Basin. **a)** Geographic setting of the Permian Basin region showing major basin names. **b)** Vertical gradient of gravity anomalies of the Permian Basin region showing gravity expression of major basins and the AGM outlined by the white dashed line (modified from Garcia et al., 2014).

Previous interpretations of the tectonic controls on the Permian Basin subsidence

Previous regional geologic studies by Graham et al. (1975), Kluth and Coney (1981), Dickinson and Lawton (2003), and Poole et al. (2005) all characterized the Marathon-Ouachita orogeny as a diachronous, late Paleozoic collision that youngs from the south-central USA (late

Mississippian) to West Texas and New Mexico (Permian) and into northern Mexico (Permian) along a suture zone between Gondwana and Laurentia. Orogenic deformation was proposed to have begun in the Late Mississippian near the Black Warrior Basin in western Alabama and northern Mississippi and migrated southwestward, creating a set of foredeep basins that include the Arkoma Basin of southeastern Oklahoma and Central Arkansas and the Fort Worth Basin of northern Texas as the result of the flexure of the continental margin of North America by a north- and northwest-directed thrust sheet (Graham et al., 1975; Dickinson and Lawton, 2003). Along the southern margin of the Permian Basin, thin-skinned convergence emplaced the allochthonous Marathon fold-thrust belt, whereas thick-skinned deformation formed the Devils River Uplift during Pennsylvanian and Wolfcampian time (Ewing, 2019).

Previous interpretations by Graham et al. (1975) and Kluth and Coney (1981) proposed that the Ouachita-Marathon collisional orogeny was the main driver for thick-skinned deformation, which formed part of the Ancestral Rocky Mountain (ARM) system and invoked the ongoing collision of India with the Asian continent as a modern, structural analog. More recent interpretations of the Ouachita-Marathon belt and ARM to the north have emphasized that many of these late Paleozoic basement uplifts trend north-south and therefore reflect shortening from either the northwest-trending Sonoran margin to the southwest in Mexico or the north-south-trending Nevadan margin in the western USA (Dickinson and Lawton, 2003; Poole et al., 2005; Leary et al., 2017; Ewing, 2019).

Contractional deformation and intricate faulting controlled the formation of the two late Paleozoic sub-basins of the Permian Basin: the Midland and Delaware Basins - along with structural highs that include the Central Basin Platform, the Diablo Platform, and the Ozona Arch (Hills, 1972; Frenzel et al., 1998; Ewing, 2019) (Figure 2.1). Detrital zircon studies

indicate that sediment sources into the syn-orogenic Permian Basin included: 1) the distal Appalachian orogenic belt far to the west or east (Soreghan and Soreghan, 2013; Xie et al., 2018; Gao et al., 2019); 2) the Ouachita orogenic belt in the southeast (Soreghan and Soreghan, 2013; Xie et al., 2018); and 3) peri-Gondwanan terranes from nearby southern orogenic highland in the southwest (Xie et al., 2018; Gao et al., 2019; Liu and Stockli, 2020; Soto-Kerans et al., 2020).

Hydrocarbon significance

The Permian Basin is the most prolific oil-producing basin in the United States, with an estimated 5 billion barrels of proven conventional oil reserves (Dutton et al., 2004; 2005). The Permian Basin has generated hydrocarbons for over a century and has supplied more than 33.4 billion barrels of oil and about 118 trillion cubic feet of natural gas as of September 2018 (EIA report, 2018).

With advances in technology such as hydraulic fracturing and horizontal drilling, unconventional oil and gas reservoirs have become an important target for petroleum exploration in the Permian Basin. Unfortunately, high-quality 2D and 3D seismic coverages have not been made widely available for research studies, including Ewing (2019) and this chapter. For this reason, I rely on public access potential fields data (i.e., Daniels et al., 2002; Pavlis et al., 2012) to help to understand the regional tectonic controls on the basin, including its broader context in the late Paleozoic tectonic events that include deformation along the Ouachita-Marathon belt and within the coeval ARM orogeny.

Objectives of this chapter

This Chapter aims to better understand the structural and depositional responses of the Permian Basin region to the potentially combined effects of the Marathon-Ouachita orogeny and the ARM orogeny by integrating subsidence history basin structure and the underlying crustal structure of the Permian Basin. A prominent 650-km-long, northeast-trending negative gravity anomaly exhibits an average magnitude of 136 mGal, extends across the northern Permian Basin, and forms one of the main topics of our regional study (Figure 2.1b).

This gravity anomaly was named the Abilene gravity minimum (AGM) by Adams and Keller (1994), who inferred that it represented a highly elongated batholith of the Early Mesoproterozoic age (Adams and Keller, 1995; 1996; Keller 2019). Adams and Keller (1995, 1996) built regional 2D gravity models of the deep structure in the Permian Basin. In his most recent gravity models, Keller (2019) reinterpreted the Abilene gravity minimum as underlain by Early Mesoproterozoic granitic and metasedimentary rocks and/or sediments with lower density comparing to the rest of the upper crust. A well penetrated basement in the AGM southwest of Abilene and encountered granite with a U-Pb age of 1078 ± 23 Ma (Ewing et al., 2019).

Ewing et al. (2019) described the diverse Proterozoic basement in the Permian Basin in terms of its lithological compositions and radiometric ages. The Southern Granite-Rhyolite Province (SGR) to the north of the AGM is characterized by interbedded volcanic and sedimentary rocks and sills (1400-1320 Ma) (Ewing et al., 2019). To the southwest of the AGM, the Permian Basin basement is considered to be correlative with the exposed Llano Uplift (Mosher, 1998).

The tectonic origin of the AGM is not well understood. Adams and Keller (1996) attributed the AGM to an elongated batholith formed by Precambrian subduction processes that

were later modified by orogenic processes along the suture between the southern edge of the Laurentian continent and accreted, island arc terranes to the south. Mosher (1988) proposed that this region formed as a Precambrian back-arc basin that accompanied north-dipping subduction along the structural boundary, now known as the Llano Front.

In order to understand the origin and deformational history of the enigmatic AGM, I incorporated 296 industry wells with seismic refraction station controls to generate both 2D and 3D gravity models for understanding the crustal framework of the Permian Basin, including its relation to the AGM. Compared to previous gravity models, this chapter added the lower crust and mantle layers to provide a complete crustal structure of the region. The results of the deep structure were then compared to basin modeling results on the two most prolific Permian Basin source rocks (the Woodford and the Wolfcamp shales) to provide insights into future hydrocarbon exploration (Figure 2.2).

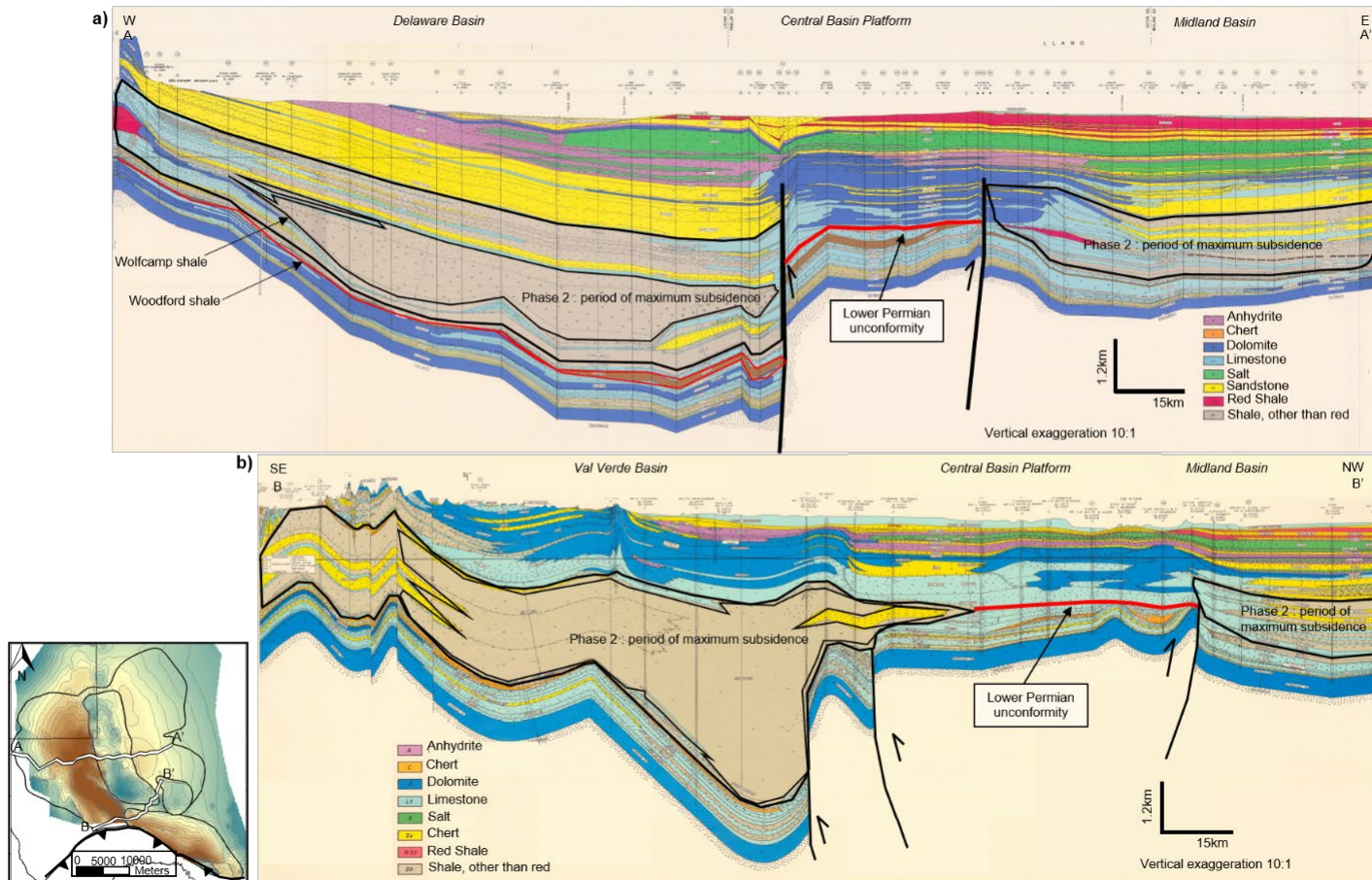


Figure 2.2 Regional cross-sections in the Permian Basin. **a)** Regional, east-west trending, 193 km long cross-section across DB, CBP, and MB showing sediment packages thickening toward the high-angle normal faults bounding the CBP (modified from Matchus and Jones, 1984). Lower Permian unconformity was observed on the CBP. **b)** Regional, southwest–northeast-trending, cross-section across the VVB, CBP, and MB showing syn-orogenic, clastic wedge thickening toward the high-angle reverse faults bounding the CBP (modified from Feldman and Chairman, 1962). The lower Permian unconformity was observed on the CBP.

Data and methods

Well data

Well logs used for 2D and 3D gravity modeling include 166 wells provided by TGS and 130 wells provided by the Enverus (Figure 2.3). Most wells are deep enough to reach the Ordovician Ellenburger Formation, which lies within 100-500m of the top of the crystalline basement. Using previous publications (i.e., Matchus and Jones, 1984) and 30 wells that contain formation tops provided by Enverus as control points, six key formation tops were correlated that include: 1) top of the Rustler Formation, 2) top of the Leonardian(Cisuralian), 3) top of the Strawn Formation, 4) top of the Barnett Formation, 5) top of the Devonian (Woodford Formation), and 6) top of the Ellenburger Formation. The top of the Leonardian is defined as the top of the Bone Spring Formation in the Delaware Basin, the top of the Spraberry Formation in the Midland Basin, and the top of the Glorieta Sandstone Member in the Central Basin Platform.

In this chapter, I conducted basin modeling of six representative wells from the Permian Basin using Petromod 1D (Figure 2.3). The basin models were used to better understand the uplift and subsidence history and its relationship to the Marathon-Ouachita orogeny and ARM orogeny (Leary et al., 2017; Ewing, 2019). Well logs and cross-sections for basin modeling were compiled from previous publications by Feldman and Chairman (1962) and Matchus and Jones (1984).

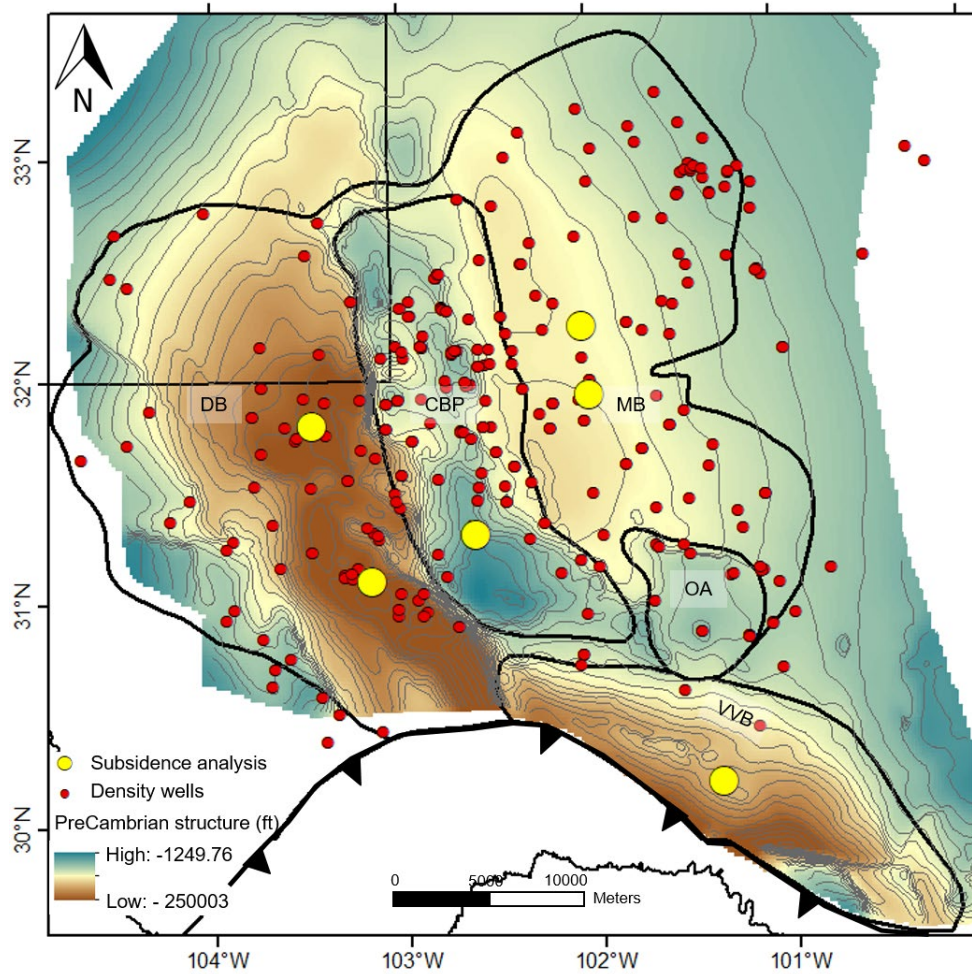


Figure 2.3 Structural map of the top of the Precambrian basement beneath the Permian Basin basement by Ruppel et al. (2008) showing the locations of well logs (the red dots) used in this chapter for well correlations and gravity modeling. The locations of the wells used for subsidence analysis are shown by the yellow dots. DB: Delaware Basin, MB: Midland Basin, CBP: Central Basin Platform, VVB: Val Verde Basin, OA: Ozona Arch.

Gravity and magnetic data

Open-file gravity and magnetic data were used for developing integrated geophysical models to infer deep structure and basin depocenters. Gravity data over the study region combines onshore Bouguer gravity anomalies of the Decade of North American Geology (DNAG) gravity grid that is spaced at 6 km and compiled by the National Oceanic and

Atmospheric Administration. The DNAG grid covers for the US, and the EGM2008 gravity model from Pavlis et al. (2012) covers Mexico (Figure 2.4a).

Residual Bouguer gravity anomalies were then derived by subtracting a 10-km-upward continuation of Bouguer anomalies from the original Bouguer gravity grid (Figure 2.4b). The derived residual gravity anomalies enhance short wavelengths at the expense of long wavelengths, thus improving the imaging of geological features with subtle gravity anomalies. Magnetic data over the study area are from magnetic anomaly maps of the North America grid that was compiled by the USGS (Daniels et al., 2002) (Figure 2.5).

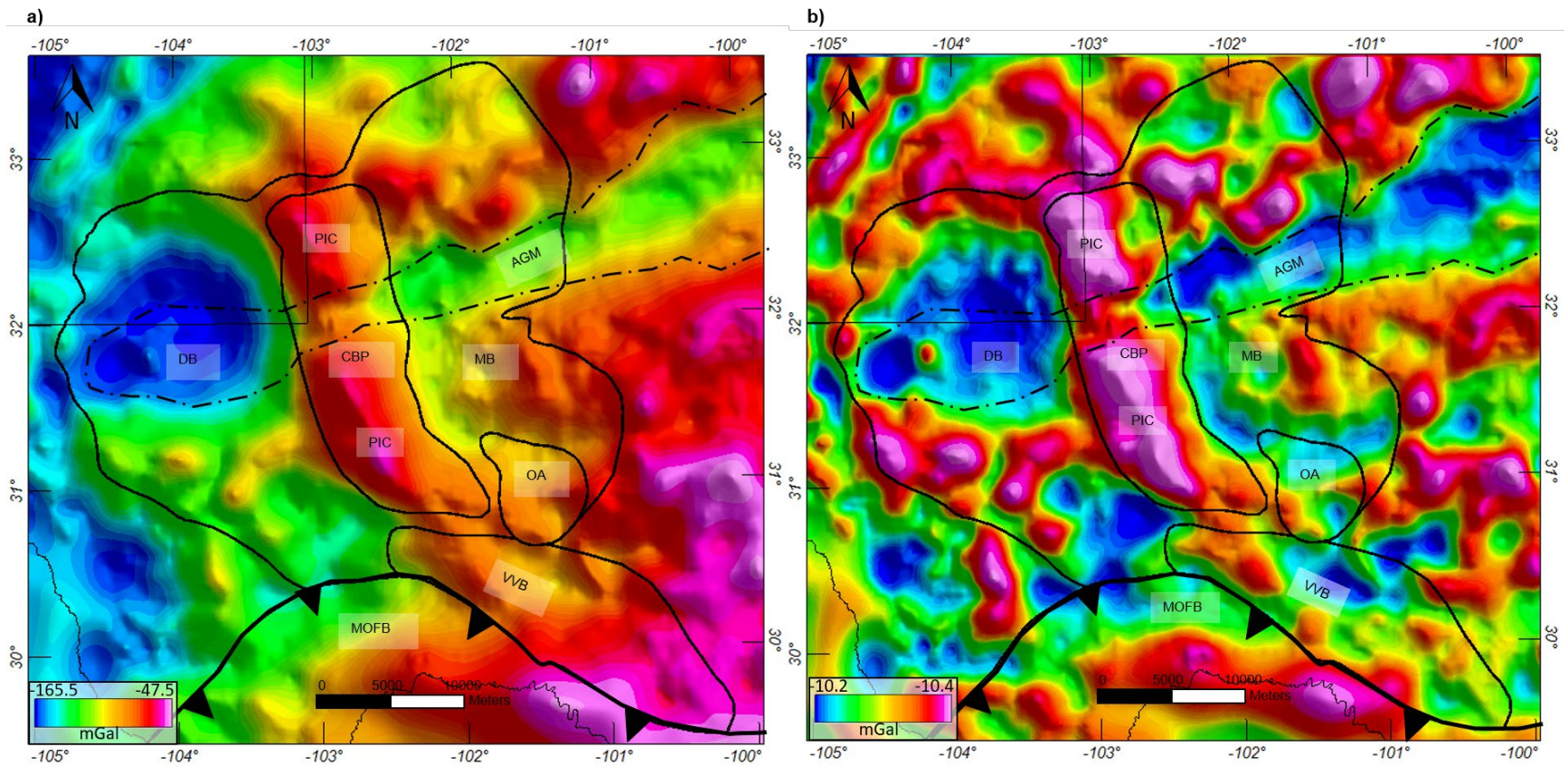


Figure 2.4 Gravity anomalies of the Permian Basin. **a)** Bouguer gravity anomalies of the Permian Basin region which combines the DNAG gravity grid in the US side and the EGM2008 gravity grid in the Mexico side, showing major basins and structural high. The Abilene gravity minimum (AGM) is an ENE-trending major gravity low in the northern Permian Basin. The Pecos Intrusive Complex shows as NNW trending gravity high in the Central Basin Platform. DB: Delaware Basin, MB: Midland Basin, CBP: Central Basin Platform, VVB: Val Verde Basin, OA: Ozona Arch, MOFB: Marathon-Ouachita orogenic fold belt, PIC: Pecos Intrusive Complex. **b)** Residual Bouguer gravity anomalies of the Permian Basin study area derived from the Bouguer gravity. The boundary of the AGM is identical on the residual Bouguer gravity anomaly map.

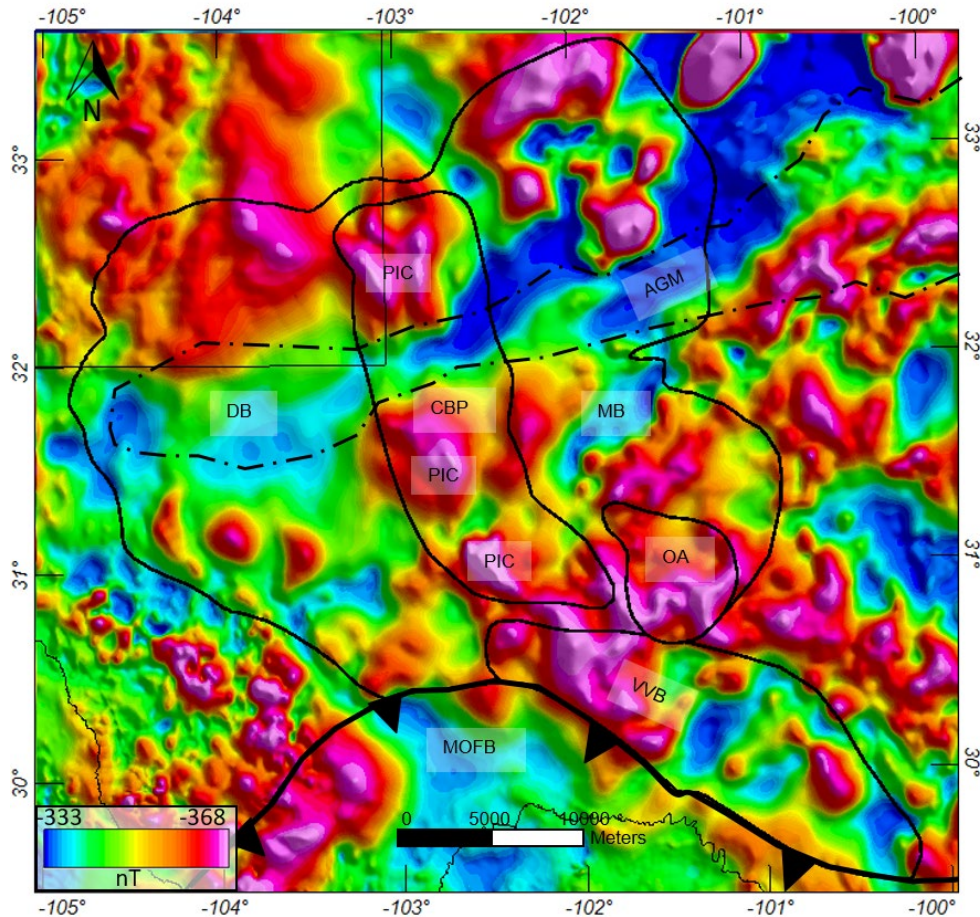


Figure 2.5 Total magnetic field anomalies of the Permian Basin study area from the North America grid compiled by the USGS. Magnetic high anomalies in the Central Basin indicate potential areas of igneous intrusions, such as the Pecos Intrusive Complex (PIC). The Abilene gravity minimum (AGM) forms a linear magnetic low across the northern Permian Basin.

Two-dimensional gravity model

All gravity modeling was performed using Geosoft's Oasis Montaj software. Three regional 2D gravity models were generated, incorporating density and structural controls of the six key formations from well log interpretation, regional cross-sections from Matchus and Jones (1984), refraction stations for regional control of basement and Moho horizon depths, and from previously published gravity models by Adams and Keller (1996).

The density inputs of the upper crust, lower crust, and upper mantle used in my model were 2.75, 2.9, 3.3 gm/cc, respectively. These density values were consistent with ranges of densities applied to crust and mantle layers in numerous studies, including 2D and 3D models (i.e., Adams and Keller, 1996; Hall, 2018). The 2D gravity models were also compared with the 3D gravity inversion results to test the consistency of the crustal structural details.

Three-dimensional gravity model

The 3D gravity model uses structural and density grids that incorporate inputs from well interpretations and previous publications. The basement grid was calculated by subtracting the Ellenburger isopach, as mapped by Ruppel et al. (2008) from the top of the Ellenburger horizon. My initial input Moho grid was derived from an isostatic calculation (Blakely, 1995).

$$dm = h(\rho_t/\Delta\rho) + ds$$

In this equation, all depths are in km, dm and ds are the Moho depth with the compensation depth (33 km) at the shoreline (the isobaric Moho depth), h is elevation, ρ_t is the average crustal density, and $\Delta\rho$ is the density contrast at the base of the crust. My initial input for the top of the lower crust grid was created by splitting the depth from the basement to Moho into half.

The density inputs of the upper crust, lower crust, and upper mantle used in my model were 2.75, 2.9, 3.3 gm/cc, respectively. Sedimentary rock densities were extracted from bulk density logs and gridded. Structural inversion of the Moho in my 3-D gravity model was performed using a method of Fourier transform technique for calculating potential field anomalies produced by uneven layers described by Parker (1973).

Results from two-dimensional gravity modeling

Density variations

Stratigraphy and lithology within the two sub-basins and the Central Basin Platform vary greatly (Figure 2), especially during the orogenic period from Late Mississippian to Mid Permian. For example, the Wolfcamp Formation in the Midland Basin contains a mixture of limestone, silt, and shale, while the Wolfcamp Formation in the Central Basin Platform is dominated by carbonate rocks (Figure 2). Therefore, by comparing the density values from bulk density logs and previous studies (Djeddi, 1979; Adams and Keller, 1996), I divided the sedimentary rocks above the basement into seven layers (Figure 2.6). Each density layer consists of one or more formations that share similar density values, and density within these similar layers was considered constant. Density values vary from 2.45 gm/cc to 2.8 gm/cc as a result of lithological variation between formations (Figure 2.6).

System	Delaware	g/cc	CBP	g/cc	Midland	g/cc	Litho.	Tectonic phases
Quaternary	Holocene Sand		Holocene Sand		Holocene Sand			5. Basin re-activation phase
Tertiary						4. Stable platform phase		
Cretaceous		2.45		2.45		2.45		
Jurassic								
Triassic								
Permian	Rustler		Rustler		Rustler			3. Post-deformational, subsidence phase
	Cherry Canyon	2.57	San Andres	2.67	San Andres	2.54		
	Bone Spring		Glorieta		Spraberry			
Penn.	Wolfcamp	2.59	Wolfcamp	2.68	Wolfcamp	2.54		2. Main deformational phase
	Strawn	2.56	Strawn	2.60	Strawn	2.58		
Mississippian	Barnett	2.56	Barnett	2.58	Barnett	2.57		1. Precollisional, Tobasa Basin and transition phase
Devonian	Woodford		Woodford		Woodford			
Silurian	Fusselman	2.71	Fusselman	2.65	Fusselman	2.67		
Ordovician	Simpson		Simpson		Simpson			
	Ellenburger	2.8	Ellenburger	2.8	Ellenburger	2.8		

Dolomite	Limestone	Anhydrite	Chert
Sandstone	Siltstone	Shale	

Figure 2.6 Density intervals assigned for gravity modeling with simplified stratigraphy and generalized lithology of the Permian Basin region. Density values were extracted from density logs from wells shown as red circles in Figure 2.3. Dashed lines indicate major unconformities. Density values change from 2.45g/cc to 2.8g/cc due to lithological variation between formations.

Model A-A'

Model A-A' is a 292-km-long, north-south regional cross-section through the Midland Basin (Figure 2.7). This model was modified from a previous gravity model by Adams and Keller (1996) by adding the lower crust and the upper mantle layers as well as additional constraints from well logs and a published seismic refraction station (Gaherty, 2004). Model A-A' crosses the AGM in the northern Midland Basin and shows that the AGM was produced by a geo-body of lower density (2.64 gm/cc) compared to the adjacent upper crust. Although the density of the AGM is similar to a granitic intrusion, the geo-body underlying the AGM produces magnetic low anomaly,

which differs from a granitic body that generally produces magnetic high anomalies (Figure 2.5). Based on my observations, modeling results, and previous interpretations by Keller (2019), I interpret the AGM as a mixture of granitic and metasedimentary rocks with a lower density relative to the upper crust.

Another elongate and sub-parallel gravity low in the southern Midland Basin produces gravity and magnetic anomalies similar to the AGM (Figures 5, 7). This gravity low is related to a distinct source similar to the metasedimentary or granitic belt underlying the AGM. Model A-A' shows the presence of an intrusive mafic body in the northern Midland basin (Figure 2.7), which was inferred from its distinctive magnetic amplitude (Adams and Keller, 1996; Keller, 2019; Figure 2.5). The model shows that the total crustal thickness of the Midland basin ranges from 33 to 35 km.

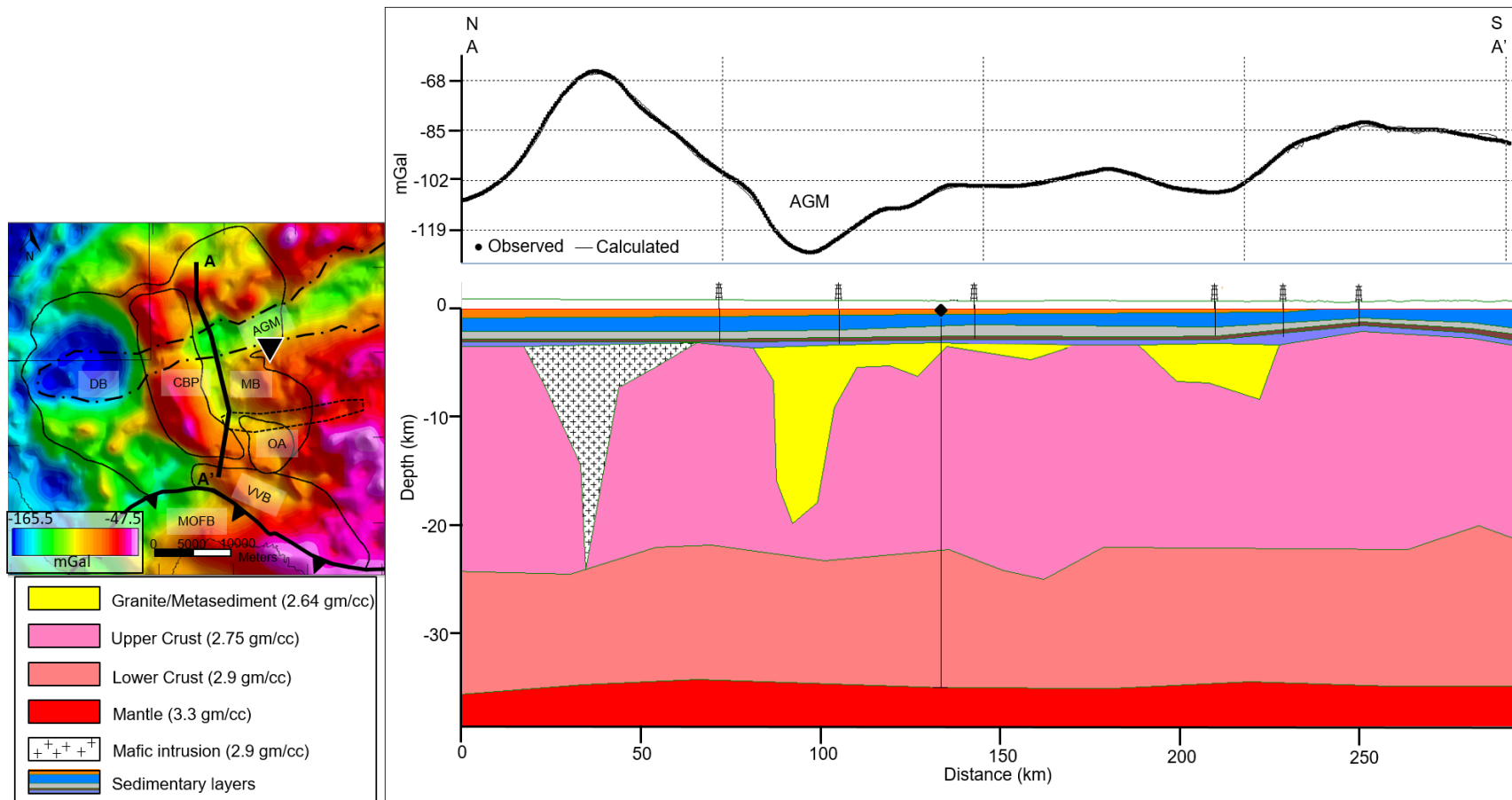


Figure 2.7 Regional 2D gravity modeling A-A' trending north-south across the Midland Basin and collinear with a previous gravity model by Adams and Keller (1996). The model location is shown in the base map to the left. The dotted line shows the location of an inferred and elongate mixture of granitic and metasedimentary rock 50 km to the south and sub-parallel to the Abilene gravity minimum. A single refraction station is shown as an inverted black triangle on the base map that was projected onto the plane of the section to constrain the model along A-A'. The calculated gravity response closely fits the observed gravity signal.

Model B-B'

Model B-B' is a 240-km-long, north-south regional cross-section through the Delaware Basin (Figure 2.8). This model is roughly coincident with the section shown by Adams and Keller (1996) (Figure 2.9). My model B-B' contains more constraints from well logs and refraction stations (Rommy et al., 1962; Jackson and Pakiser, 1966; Mitchell and Landisman, 1971; Dumas, 1981) than the previous model of Adams and Keller (1996).

I added the lower crust and the upper mantle layers to Model B-B' to better constrain the deeper crustal structure. This model crosses the AGM in the northern Delaware Basin. Like model A-A', the geo-body that produced the gravity low in this area was interpreted as a mixture of granitic and metasedimentary rocks. The modeled geo-body is much wider (127 km) than the Midland Basin (60 km), and its thickness ranges from 2.7 to 12.4 km.

P wave velocity from seismic refraction stations across the Abilene gravity minimum showed a lower value of 5.95 km/s compared to other locations (averaging 6.7 km/s). This observation further supports the inferred presence of the mixture of granite and metasedimentary rocks underlying the Abilene gravity minimum (Keller, 2019). The presence of an intrusive mafic body in the southern Delaware Basin was inferred from its distinctive magnetic amplitude (Adams and Keller, 1996; Keller, 2019) (Figure 2.5). The total crustal thickness across this area is thicker than the Midland Basin and ranges from 36.9 to 38.8 km.

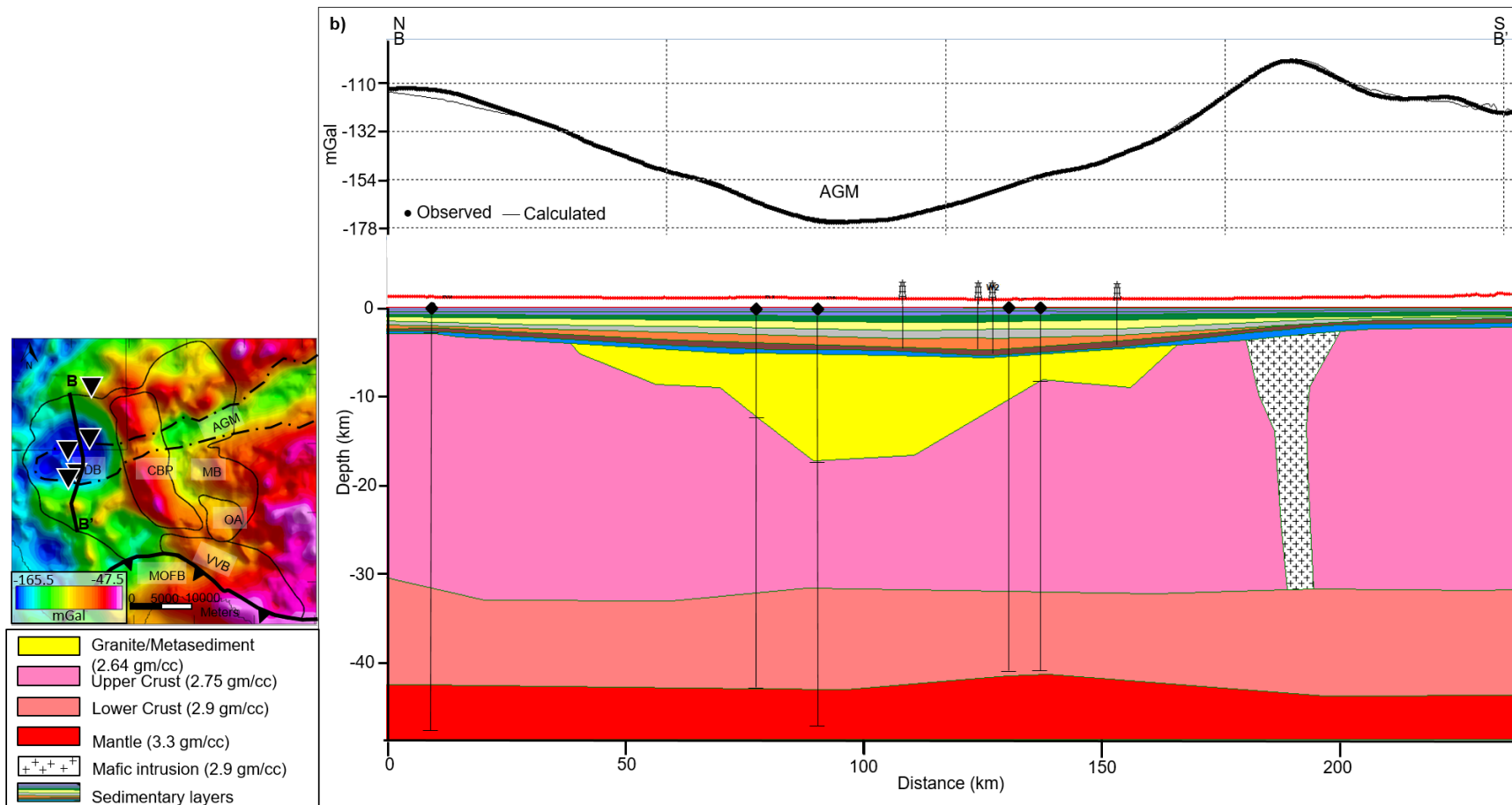


Figure 2.8 Regional 2D gravity model B-B' trending north-south across the Delaware Basin and collinear with a previous gravity model by Adams and Keller (1996). The model location is shown on the base map on the left. Five refraction stations are shown as inverted black triangles on the base map and were projected onto the plane of the section to constrain the model along B-B'. The calculated gravity response closely fits the observed gravity signal. A mafic intrusion body was added in the south based on the magnetic signal from Figure 2.5.

Model C-C'

Model C-C' was constructed along the east-west regional cross-section from Matchus and Jones (1984). Model C-C' passes from west to east through the Delaware Basin, the Central Basin Platform, and the Midland Basin (Figure 2.9). Model C-C' was also well constrained using well logs and refraction data (Dumas, 1981; Gaherty, 2004; Shen et al., 2013). Model C-C' is consistent with Model A-A' and B-B' at their intersection points.

As shown in Figure 2.8, model C-C' traverses through the AGM in the Delaware Basin and partially in the Midland Basin. The AGM in the eastern Delaware Basin was interrupted by an intrusive mafic body whose location was constrained by its distinctive magnetic signal as an isolated magnetic high. The depth to Moho and depth to the top of the lower crust is shallower in the Central Basin Platform as the likely result of less sedimentary overburden and the absence of the mixture of granitic and metasedimentary rocks in the upper crust, as shown in Figure 2.8. The total crustal thickness is the least (31.9 km) along model C-C' beneath the Central Basin Platform. Similar to the previous two models, the Moho on model C-C' is relatively deeper beneath the center of the AGM (average 42 km).

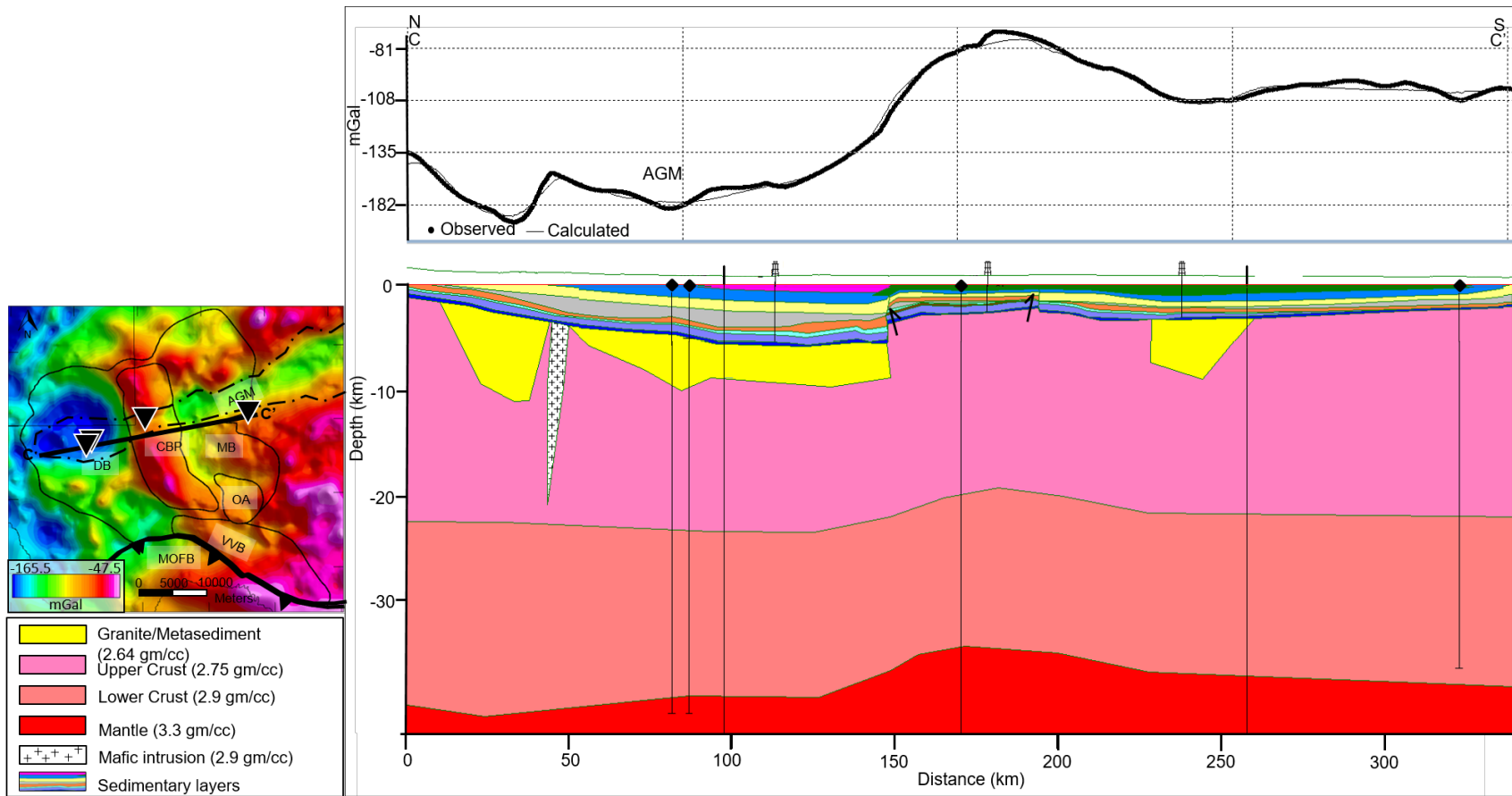


Figure 2.9 Regional 2D gravity model C-C' trending east-west across the entire northern Permian Basin. The model location is shown on the base map on the left. Four refraction stations are shown as inverted black triangles on the base map and were projected onto the plane of the section to constrain the model along C-C'. Locations of Model A-A' and B-B' were tied with model CC'. A mafic intrusion body was added in the east based on the magnetic signal from Figure 2.5. Moho depth is deeper beneath the Delaware Basin and the shallowest in the Central Basin Platform. The calculated gravity response closely fits the observed gravity signal.

Results from three-dimensional gravity modeling

Density variation

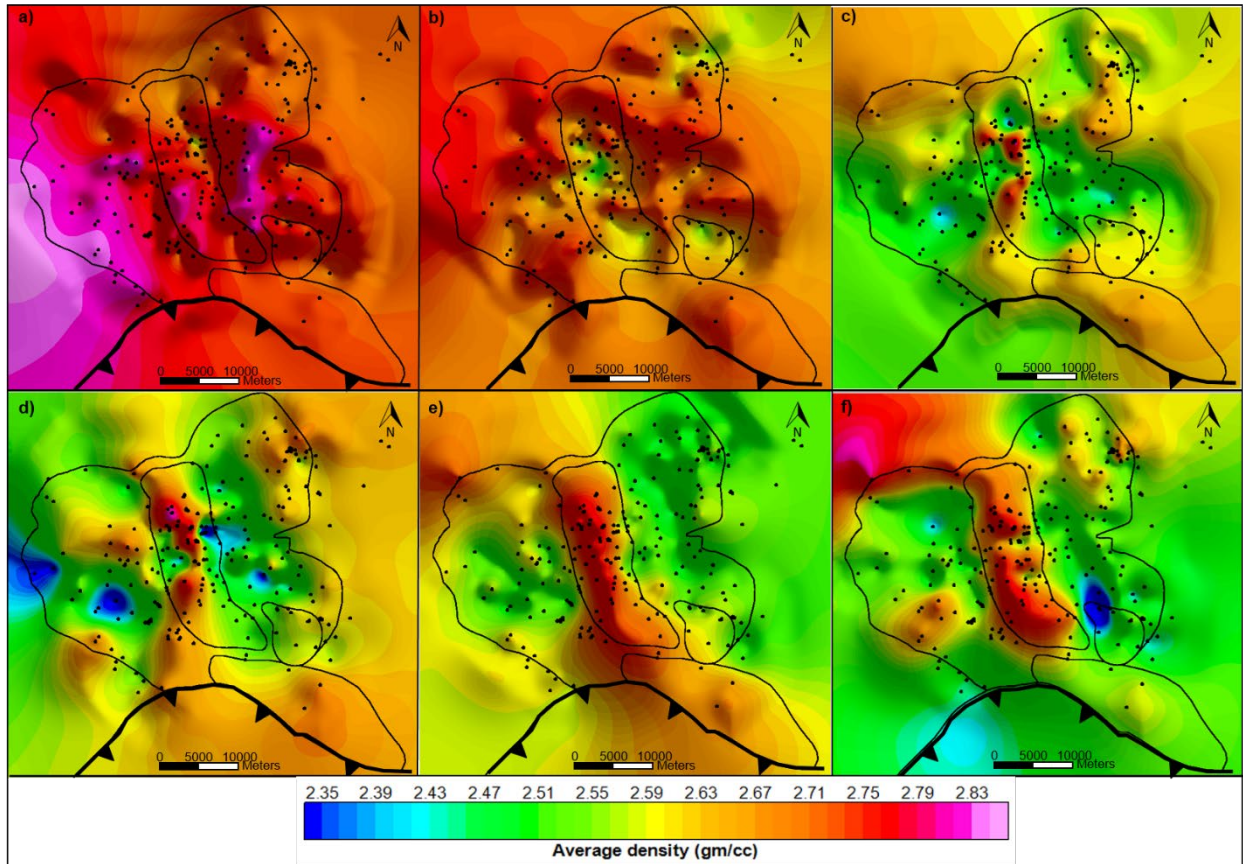
Based on the bulk density logs, the sediment density within the Permian Basin region varies both vertically between formations and laterally within the same stratigraphic intervals. Similar to 2D gravity modeling, I divided the sedimentary layers into seven density layers separated by seven horizons.

The seven density layers include: 1) surface stations (topography) – top Rustler Formation, 2) top Rustler Formation – top of the Leonardian, 3) top of the Leonardian – top of the Strawn Formation, 4) top of the Strawn Formation – top of the Barnett Formation, 5) top of the Barnett Formation – top of the Devonian (Woodford Formation), 6) top of the Barnett Formation – top of the Ellenburger Formation, and 7) top of the Ellenburger Formation – top basement. Each of these horizons was interpreted and correlated across the study region. The top of the Leonardian is defined as the top of the Bone Spring Formation in the Delaware Basin, the top of the Spraberry Formation in the Midland Basin, and the top of the Glorieta Sand Member in the Central Basin Platform.

Average density values within each layer were calculated at every well location (1614 measurements) to incorporate density variations within the Permian Basin and were then gridded (Figure 2.10). The average density between the Ellenburger Formation and the basement varies from 2.66 gm/cc to 2.85 gm/cc (Figure 2.10a). Higher density was observed in the western Delaware Basin and central Midland Basin. Areas with low-density anomalies may be due to the effect of karst weathering within the lower Ellenburger Formation (Loucks, 2008).

Density values vary greatly throughout the study region from top Devonian to top Strawn Formation because of lithological differences (Figure 2) between the two sub-basins and the platform (Figure 2.10b, 10c, 10d). The Central Basin platform is more carbonate-dominated compared to the two sub-basins, which are clastic-dominated. The Delaware Basin consists of thicker, fine-grained sediments compared to those of the Midland Basin. Density values become more uniform between the top of the Leonardian and top Rustler and show a higher value on the platform and lower values within the two sub-basins (Figure 2.10e). The average density above the Rustler Formation was set constant to 2.45 gm/cc based on Adams and Keller (1996) because the density logs used in this chapter did not cover the interval above the Rustler Formation.

Figure 2.10 Density girds used for gravity modeling. **a)** The average density between the top Ellenburger Formation and the basement. Density values range between 2.83g/cc to 2.78g/cc. **b)** The average density between top Devonian Formation and top Ellenburger. Density values vary from 2.77g/cc to 2.61g/cc. **c)** The average density between top Barnett Formation and top Devonian. Density values vary from 2.67g/cc to 2.50g/cc. Density high anomalies were observed on the CBP due to changes in bed thickness affected by the Devonian unconformity. **d)** The average density between top Strawn Formation and top Barnett. Density values vary from 2.68g/cc to 2.46g/cc. **e)** The average density between the top Lower Permian Formation and top Rustler. Density values vary from 2.71g/cc to 2.51g/cc. **f)** Top Rustler Formation to top Lower Permian. Density values vary from 2.77g/cc to 2.45g/cc. Black dots are the well control points.



3D gravity modeling framework

Formation tops bounding the density intervals were correlated using 296 well logs as the structural input for the 3D gravity model (Figure 2.11). In general, the Delaware Basin received thicker sediments, as shown by the deeper depocenters shown in Figure 2.11a-d. The top Ellenburger Formation reaches a depth of 6200 m below sea level beneath the deepest area of the central Delaware Basin (Figure 2.11a).

The Central Basin Platform is a structural high separating the Delaware and Midland Basins. During upper Demoinesian (upper Strawn) through lower Wolfcamp time, the Central Basin Platform underwent up to 1000 m of uplift and erosion to create a hiatus known as the

lower Permian unconformity (Matchus and Jones, 1984; Figure 2.10d). The Lower Permian (Wolfcampian and Leonardian) section is relatively uniform in thickness in both the Delaware and Midland Basins (Figure 2.11e) and was partially filled by the top of the Rustler Formation (Figure 2.11f).

The 3-D gravity model includes ten layers, including the same seven sedimentary layers described above, the upper crust, the lower crust, and the upper mantle.

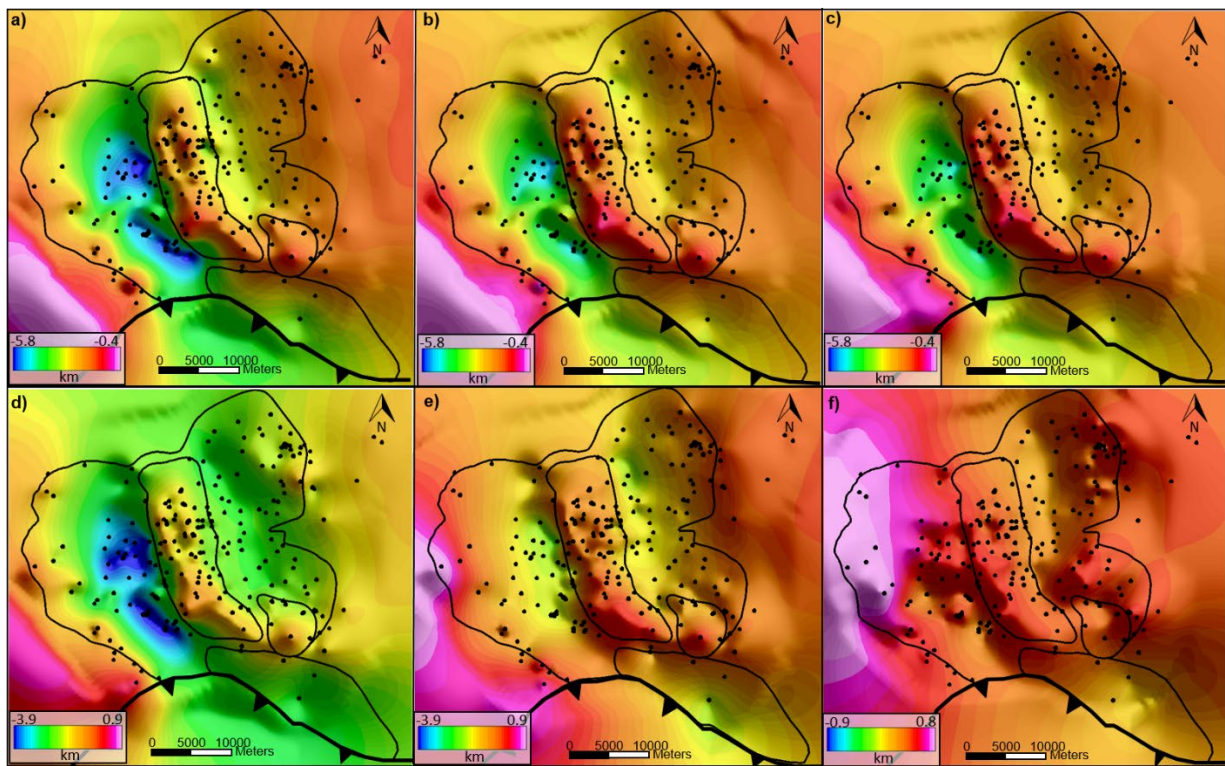


Figure 2.11 Summary of structural inputs used for gravity modeling. **a)** Top Ellenburger Formation, which reaches 6200 m below sea level beneath the central Delaware Basin. **b)** Top Devonian Formation. **c)** Top Barnett Formation. **d)** Top Strawn Formation. **e)** Top Lower Permian Formation that was partially eroded across the southern Central Basin Platform during early Permian. **f)** Top Rustler Formation. Black dots are the well control points.

Crustal structure of the Permian Basin

Using gravity data, I completed a 3D structural inversion of both the Moho and the lower crust of the Permian Basin. The calculations were iterated until the best fit crustal model was derived. The inverted Moho revealed a deep root underlying the Abilene gravity minimum that varies in depth from 5 km beneath the Delaware Basin to 3 km beneath the CBP and the Midland Basin (Figure 2.12a). Similarly, the top of the lower crust is deepest beneath the Abilene gravity minimum, especially in the northern Delaware Basin (Figure 2.12b).

I also carried out a density inversion of the upper crust of the Permian Basin. The results suggest that lower density zones exist beneath the Abilene gravity minimum that is also observed on my 2D gravity models (Figure 2.13a). Isolated higher density values correlate with the locations of igneous intrusions mapped by Adams and Keller (1996) (Figure 2.13a, b).

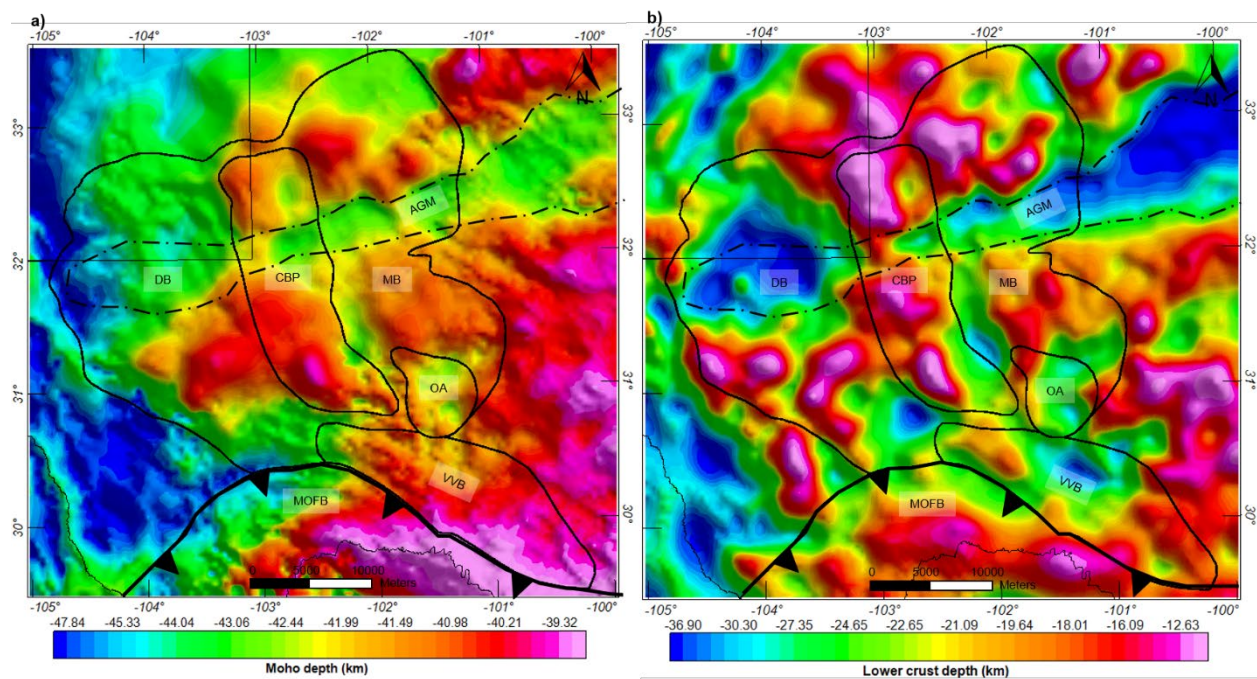


Figure 2.12 Inverted crustal structure. **a)** Inverted Moho structure derived from 3D gravity inversion shows a deeper Moho (42.2–45.3km) beneath the location of Abilene gravity minimum compared to the adjacent areas (38.7–41.8km). **b)** Inverted lower crust structure from 3D gravity

inversion shows a deeper lower crust (21.9–36.9km) beneath the location of Abilene gravity minimum than in the adjacent areas (10.9–21.4km).

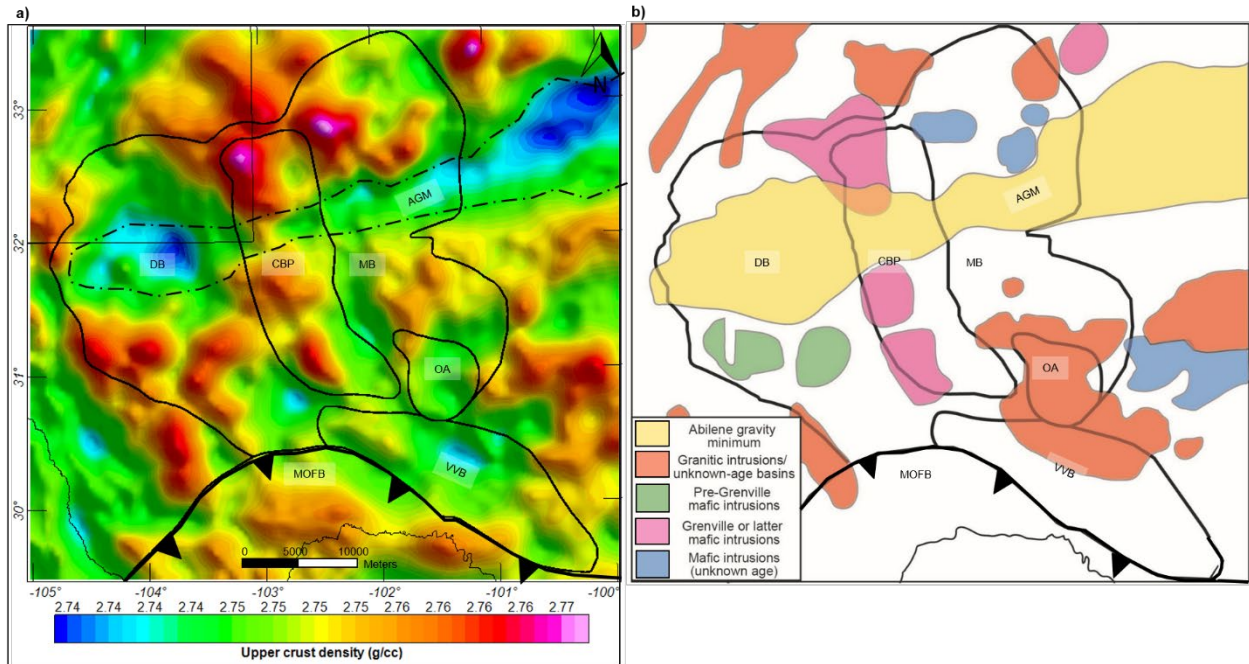


Figure 2.13 Summary of density inversion results for the upper crust. **a)** Density value distribution shows a linear density low in the upper crust at the location of the Abilene gravity minimum, which closely matches the 2D gravity results. **b)** Basement geology of the Permian Basin study area (modified from Adams and Keller, 1996) showing major basement features labeled in Figure 2.1. Locations of igneous intrusion in b correlate with density highs in a.

Basin modeling results and implications for hydrocarbon exploration

Basin tectonic phases from subsidence analysis

Subsidence analysis using Petromod 1D was carried out for this chapter that included sediment decompaction and paleowater depth estimates based on the depositional height of carbonate platform margins, as shown in previous regional cross-sections (Feldman and Chairman, 1962; Matchus and Jones, 1984).

Subsidence plots from the wells were divided into five tectonic phases in general agreement with previous subsidence studies (Horak, 1985; Ewing and Christensen, 2016; Ewing, 2019; Ruppel, 2019):

1) **Pre-deformational, Tobosa Basin and transition phase** extended from the Ordovician to Early Pennsylvanian with deposition of shallow-marine carbonate facies to deeper marine mudstone facies;

2) **Main deformational and subsidence phase** extended from the Early Pennsylvanian to the end of Permian with deposition of mixed, siliciclastic-carbonate deep-marine facies in the basins and shallow-water carbonates facies on the platforms; sediment packages up to 2.4 km thick within the basin. Latest Permian (Ochoan) deposits are dominated by evaporites, including over one km of anhydrite and halite in the Delaware Basin;

3) **Post-deformational, low subsidence phase** occurred during the Triassic with deposition of a thin interval of non-marine redbeds;

4) **Stable platform phase** extended from the Jurassic to Eocene with significant deposition occurring only during the Cretaceous and represented by shallow marine carbonates and subsidiary clastic rocks. Some minor Laramide deformation effects occurred from the Late Cretaceous to Middle Eocene;

5) **Basin exhumation/tilting phase** occurred from the Late Eocene to the present and was related to Trans-Pecos volcanism, followed by Neogene Basin and Range extension to the west. This event tilted the western area of the Delaware Basin, Diablo Platform, and Northwest Shelf to the east, with accompanying erosion of much of the Ochoan and some Guadalupian strata in this area.

Three representative subsidence plots from the Midland Basin, the Delaware Basin, and the Central Basin Platform were annotated with the above five tectonic phases, as shown in Figure 2.14. The subsidence rate was relatively slow (average rate of 13 m/my) in the pre-deformational phase, Tobosa Basin, and transition phase.

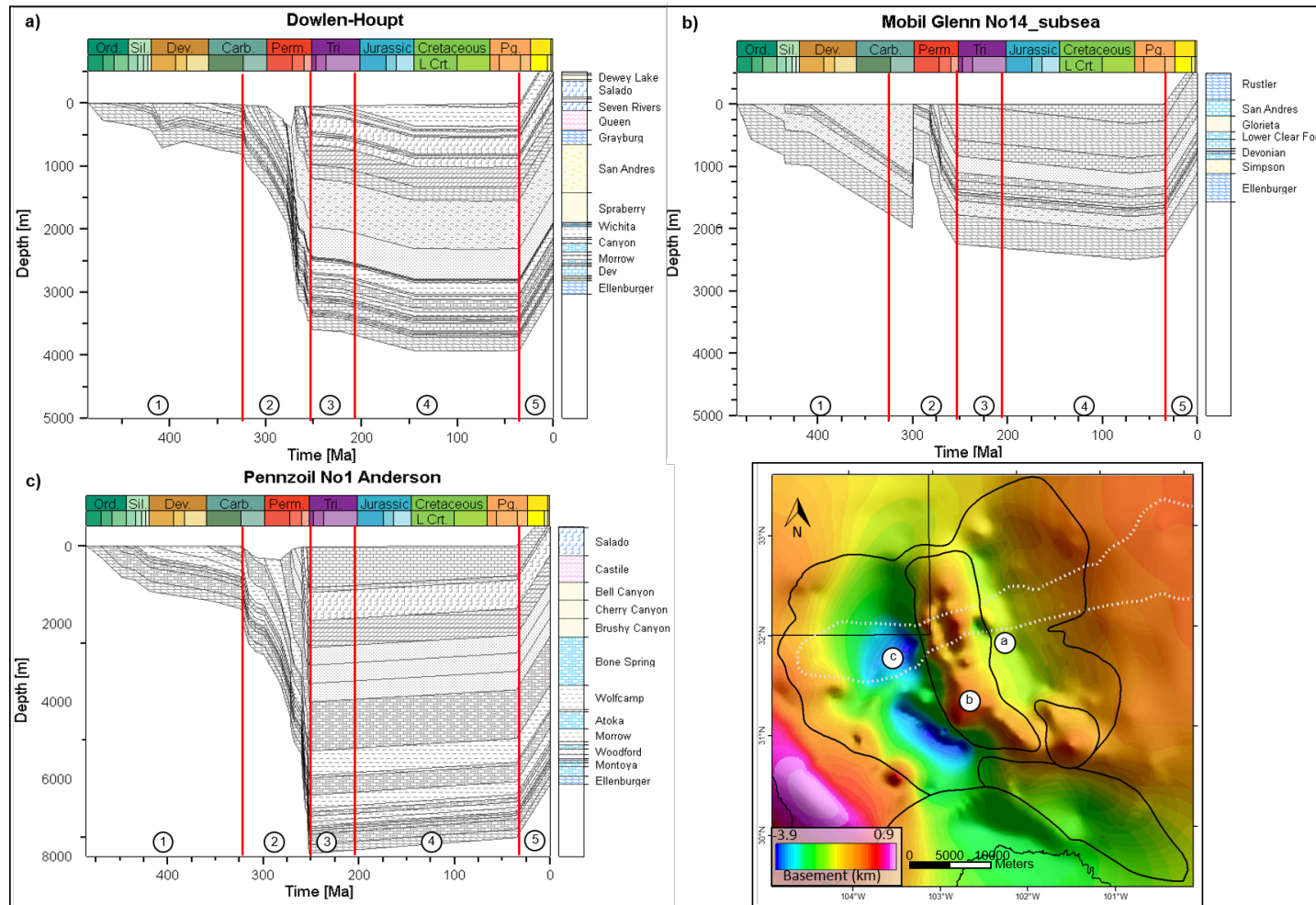


Figure 2.14 Subsidence history with five, numbered tectonic stages from the Cambrian through Neogene based on representative exploration wells for **a)** Midland Basin – Dowlen-Haupt No. 1 well, central Midland county; **b)** Central Basin Platform – Mobil Glenn No. 14 well, southern Crane county, and **c)** the Delaware Basin – Pennzoil No. 1 Anderson well, central Loving county. Five tectonic phases include: 1) Pre-deformational, Tobasa Basin and transition phase; 2) Main deformational phase; 3) Post-deformational, subsidence phase; 4) Stable platform phase, and 5) Basin reactivation phase.

Subsidence history curves show a marked increase in subsidence rate occurred during the early Pennsylvanian as the region entered its main deformational phase and period of maximum subsidence. Subsidence reached its maximum rate (500 m/my in the Delaware Basin) during the Middle Permian. During the post-deformational phase in the Triassic, the Permian Basin region underwent minor subsidence at a rate of 0-2 m/my.

Subsidence decreased abruptly during the Triassic and remained stable during the stable platform phase. After the post-Paleozoic stabilization of the region, subsidence was only punctuated by uplift during the late Cretaceous-Eocene Laramide Orogeny and later during the Miocene to recent basin and range extensional event.

Stratigraphy of units deposited during the five tectonic events

Lithological components vary laterally between the Central Basin Platform and the flanking Delaware and Midland Basins during the main deformational phase from Early Pennsylvanian to Late Permian (Galley, 1958; Adams, 1965; Ruppel, 2019) (Figure 2).

The Central Basin Platform is a late Paleozoic carbonate platform dominated by limestone and dolomite. The main sediment packages of the Delaware Basin are composed of fine-grained mudstone with interbedded sandstone (around 20%). In comparison, the sediment packages in the Midland Basin consist of more limestone (around 15%) and sandstone (around 30%) with minor shale (Matchus and Jones, 1984). These sediment packages are bounded by high-angle thrust faults active during periods of maximum thrusting occurring in the Pennsylvanian and especially during Wolfcamp time (Figure 2.2). Up to 1000 m of erosion or non-deposition was observed on the Central Basin Platform due to uplift along the bounding thrust faults while the adjacent Delaware and Midland basins were undergoing rapid subsidence

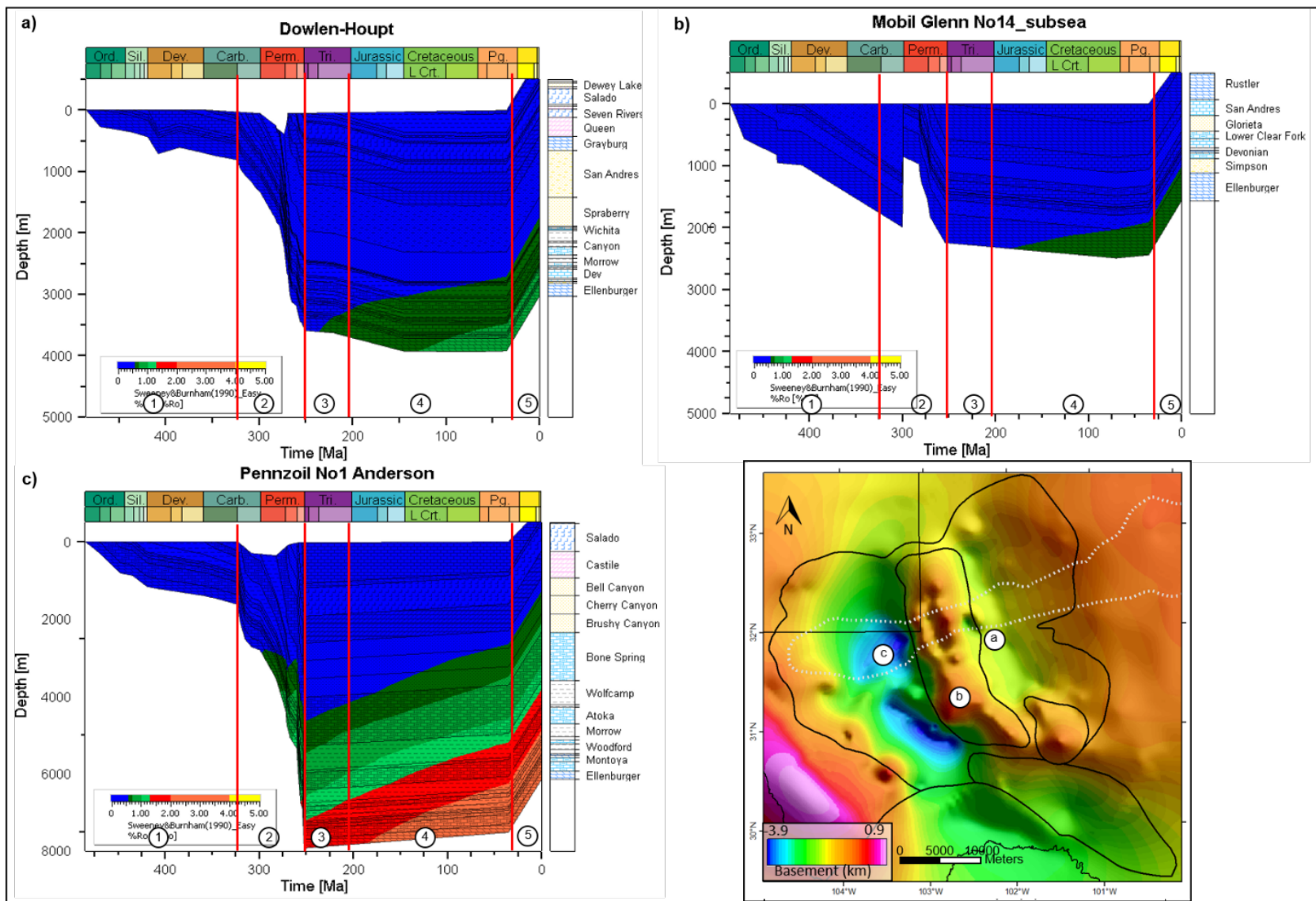
(Figure 2.2). Tectonic activity in this region decreased greatly following the late Permian (Guadalupian) and ceased by the end of the Permian (Ewing, 2019).

Distribution of thermal maturity with respect to Permian Basin depocenters

Thermal maturity was modeled at the same locations as the wells that were used for subsidence analysis (Figure 2.15). The maturity profile was calibrated with corrected bottom-hole temperature data from Southern Methodist University (SMU) geothermal laboratory database and vitrinite reflectance data from the USGS database (USGS, 2012). It should be noted that alternate measures of maturity by Manos and Perez (2018) using Raman spectroscopy yielded different results for the Permian Basin than the maturity results that I present here. My basin modeling assumed constant heat flow over geological time, and heat flow information was based on the regional geothermal map of North America (Blackwell and Richards, 2004). Two major hydrocarbon source rocks focused in this chapter are the Wolfcamp shale and the Woodford shale. In general, the Delaware Basin is more thermally mature than the Midland Basin. The Central Basin platform lies within the immature zone due to less burial and a large amount of uplift and erosion during the early Permian (Figure 2). In the Delaware Basin, the maturity profile indicates that the top and base of the Woodford shale lies in the overmature zone with thermal maturity higher than 2%Ro (Figure 2.15a). The Wolfcamp shale is partially in the oil window and partially in the gas window (Figure 2.15a). In contrast, in the southern Central Basin Platform, the Wolfcamp shale is in the immature zone, while the Woodford shale was eroded below during the Lower Permian Unconformity (Figure 2.15b). In the Midland Basin,

most of the Wolfcamp shale and the Woodford shale are currently in the oil window, with Ro values ranging from 0.5-1.5% (Figure 2.15c).

Figure 2.15 Maturity modeling based on representative exploration wells for **a)** Midland Basin – Dowlen-Haupt No. 1 well, central Midland county; **b)** Central Basin Platform – Mobil Glenn No. 14 well, southern Crane county, and **c)** the Delaware Basin – Pennzoil No. 1 Anderson well, central Loving county. Major hydrocarbon source rocks in the Midland Basin have entered the oil window. In the Delaware Basin, major source rocks are partially in the oil window, while deeper source rocks, such as the Woodford shale, have entered the gas window. Major source rocks are mostly immature in the shallowly-buried and partially eroded Central Basin Platform.



Discussion

Reconciling contrasting views on the regional, tectonic controls of Permian Basin subsidence

Earlier interpretations of the Ouachita-Marathon-Sonoran orogenic belt by Graham et al. (1975), Kluth and Coney (1981), and Dickinson and Lawton (2003) emphasized its diachronous, east-to-west progression during the Pennsylvanian and Permian and its tectonic control on a near-field, elongate, suture-parallel foreland basin adjacent to a thin-skinned, northward-vergent fold-thrust belt (Hickman et al., 2009). Kluth and Coney (1981) proposed the modern India collision with central Asia as an analog for the far-field deformation effects of the Ancestral Rocky Mountains triggered by the Ouachita-Marathon-Sonoran orogenic belt.

A later generation of geoscientists that includes Marshak et al. (2000) and Craddock et al. (2017) recognized many far-field structural effects in the North American craton. These late Paleozoic structures were attributed to a single or slightly-varying, north-south, Ouachita-Marathon-Sonora stress field that reactivated and inverted intra-cratonic features of the Ancestral Rocky Mountains and areas as distant as the upper Midwest that included Precambrian rifts and older, orogenic belts. Marshak et al. (2000) proposed that strike-slip faulting was a common mode of reactivation of these older structures, including Precambrian faults, rifts, and suture zones.

In a more recent revision of these earlier ideas of far-field, late Paleozoic deformational effects, Leary et al. (2017) and Ewing (2019) have pointed out that the orientation of north-south basement uplifts that comprise the widespread Ancestral Rocky Mountains (ARM) orogenic event is oriented at right angles to the compression direction of the Ouachita-Marathon-Sonoran orogeny and are better explained by a uniform, northeast-directed compression related to

orogenic shortening events along the Pacific margin of North America. Therefore, the northwest- or north-directed shortening related to the Ouachita-Marathon-Sonora event was a less significant “soft orogeny” in comparison to the “harder” northeast-directed Pacific orogenies (van Staal and Zagorevski, 2020).

One concept that can help reconcile these differing views of the structural controls of the late Paleozoic Permian Basin is the concept of a contiguous versus broken foreland basin, as illustrated in active foreland basins along the Andean margin of South America (Strecker et al., 2012). *Contiguous foreland basins* are those formed adjacent to a fold-and-thrust belt and result from accommodation space created by the flexural response of the crust to the topographic load of the fold-and-thrust belt, such as the Arkoma Basin and the Fort Worth Basin. This leads to the familiar suite of contiguous foreland basin depozones: the wedge-top, foredeep, forebulge, and backbulge (DeCelles and Gilles, 1996). Contiguous foreland basins in the northern Andes form in a retro-arc position adjacent to areas of steeper subduction and extensional type arcs (Strecker et al., 2012).

In contrast, *broken foreland basins* are formed in areas of flat subduction and compressional type arcs where retro-arc convergence is accommodated along reactivated, high-angle structures in the basement. Uplift along these reactivated basement structures is disparate in space and time and creates ranges and basins that are limited in their along-strike length and occur far inboard and remote from the main topographic and deformation front of the orogen. These broken foreland basins tend to be isolated and restricted from one another and quite different in appearance from the more familiar and much larger, contiguous foreland basins (Strecker et al., 2012).

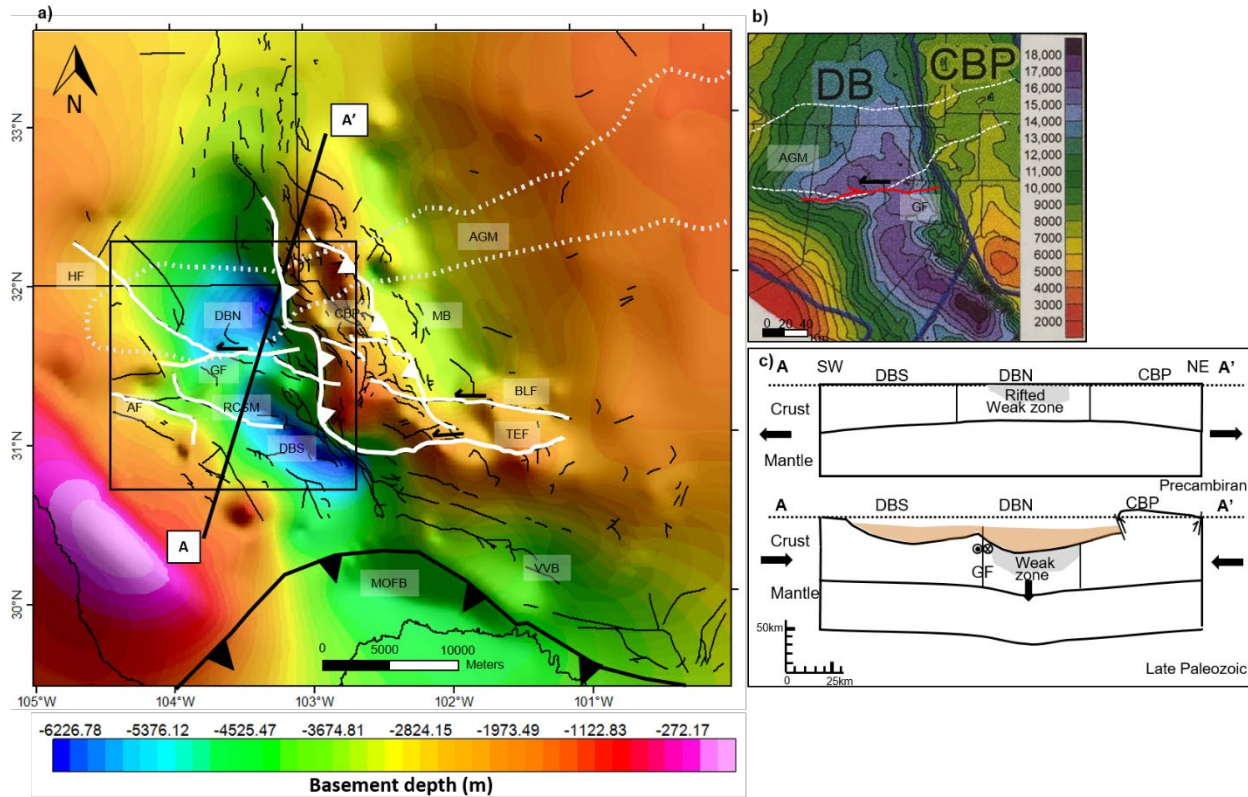
Permian Basin as a broken foreland basin

While the Permian Basin lies less than 100 to 400 km north of the Marathon, thin-skinned, fold and thrust belt (Hickman et al., 2009), its main depocenter is oriented at right angles to the Marathon thrust front orientation. Galley (1958, 1970) proposed that this unusual orientation is related to the reactivation of a Precambrian rift formed at ~1100 Ma and later reactivated during the Marathon orogeny and the formation of the Ancestral Rocky Mountains. These north-south rift trends are not easily mapped on potential field data as the Permian Basin is crosscut by the ENE-trending AGM that I have described in this paper (Figure 2.4). I also noted rapid gravity changes along the boundaries between the AGM, the CBP, and the flanking two sub-basins.

Along with Adams and Keller (1995, 1996) and Keller (2019), I have focused on the reactivation of the regional crustal feature marked by the AGM. Major basement-involved structures have been repeatedly activated during subsequent plate collisions and rifting events (e.g., Kluth and Coney, 1981; Marshal et al., 2000; Thomas, 2006; Craddock et al., 2017; Snee and Zoback, 2018). As shown in Figure 2.16a, several regional-scale faults are known to exist in the Permian Basin region (Walper, 1977; Shumaker, 1992; Yang and Dorobek, 1995; Ewing, 2019). One prominent feature is the east–west-striking left-lateral strike-slip Grisham fault along the southern margin of the AGM and was active during the period of maximum Permian subsidence, as shown on the Permian thickness map (Shumaker, 1992; Ewing, 2019; Ruppel, 2019) (Figure 2.16b). This ENE-trending basement ridge defined on its northern edge by the Grisham fault is roughly parallel to the northernmost salient of the Marathon fold and thrust belt 100 km to the south. For a strike-slip fault, this is an unexpected orientation for reactivation invoking north-south shortening associated with the Marathon orogeny. Leary et al. (2017) and

Ewing (2019) have proposed that the Grisham fault reflects a northeast-southwest shortening that could be the composite response to the Marathon, Sonoran, and Nevadan belts. In addition to the Grisham fault, two other strike-slip fault zones (Big Lake, Todo-Elkhorn) mapped by Ewing (2019) are shown in Figure 2.16a. Moreover, the Central Basin Platform itself shows three left-lateral deflections in its overall north-south trend (Figure 2.16a). The central and northern Central Basin Platform was bound by the northwest-southeast trending Monahans and the Hobbs transverse zone, respectively, as discussed by Ewing (2019).

Figure 2.16 Permian Basin as a broken foreland basin. **a)** Comparison of Paleozoic faults distribution (thin black lines) with mapped by Ruppel et al. (2008) and Ewing (2019) and the Abilene gravity minimum (white dotted line). Major NW-SE trending faults are marked as white lines. Major thrust faults are the boundary of Central Basin Platform is marked by the thick, white line. The black box shows the location of b). DBN: North Delaware Basin. DBS: South Delaware Basin. BLF: Big Lake fault, TEF: Todd-Elkhorn fault, GH: Grisham Fault, HF: Huapache fault, AF: Apache fault, RCSM: Rojo Caballos-San Martine fault zone. **b)** Thickness of Permian rocks (as measured from the base Permian to the surface) in the Delaware Basin. Grisham left-lateral strike-slip fault is shown by the red line (modified from Ruppel, 2019). The Abilene gravity minimum is shown by the white dashed polygon. **c)** Conceptual model for convergence of the crustal structure with a pre-existing, rifted zone of weakness (modified from Gemmer et al., 2002). The model shows the crust and mantle response to east-west compression during phase 2 main deformational phase from Early Pennsylvanian to Late Permian. The rifted zone of weakness (Abilene gravity minimum) acts as a load that presses down the region adjacent to the weak zone due to the lateral strength in the crust and mantle. The location of the modeled line is labeled in a), GF: Grisham fault.



Deformational model for the rift inferred along the AGM trend

I propose that the underlying crustal structure of the AGM also plays an important role in generating the large amount of subsidence observed during the Marathon and ARM orogenic events. I propose that the elongate mixture of granitic and metasedimentary rocks with a lower density as interpreted from gravity modeling (Figure 2.7, 8, 9, 13a) - acted as a zone of weakness that collapsed and focused extreme syn-orogenic subsidence (Phase 2, Figure 2.14). Syn-orogenic deformation included left-lateral shearing along the Grisham fault that coincides with the ENE-trending southern edge of the AGM (Figure 2.16a). It should be noted that this local east-west-trending basement low adjacent to the Grisham fault is a second-order effect, with the primary Delaware basin depocenter remaining in a north-south orientation.

As a result of Permian shortening, the crust and upper mantle of the AGM, which I inferred as a Precambrian rift feature - similar to those described by Marshak et al. (2000) or as proposed by Mosher (2017) - were depressed along the rift-controlled, preexisting zone of weakness, as illustrated in Figure 2.16c. An analog of the response of the lithosphere under compression along a preexisting weakness zone has been described from the eastern North Sea by Gemmer et al. (2002) (Figure 2.7). The results from my gravity structural inversion further confirmed that both the depth to the lower crust and Moho are deeper below the AGM (Figure 2.13).

Analysis of regional burial history pattern

I compiled subsidence analysis representative wells of seven sedimentary basins along the Marathon-Ouachita orogenic belt and part of the ARM system that include from east to west: 1) the Arkoma Basin, 2) the Anadarko Basin, 3) the Palo Duro Basin, 4) the Val Verde Basin, 5) the Midland Basin, 6) the Delaware Basin and 7) the Orogrande Basin to analyze the subsidence pattern on a regional scale (Figure 2.17a, d). I measured the distance between each geohistory site and from the western edge of the Black Warrior Basin, where the continental collision is thought to have begun (e.g., Graham et al., 1975; Dickinson and Lawton, 2003).

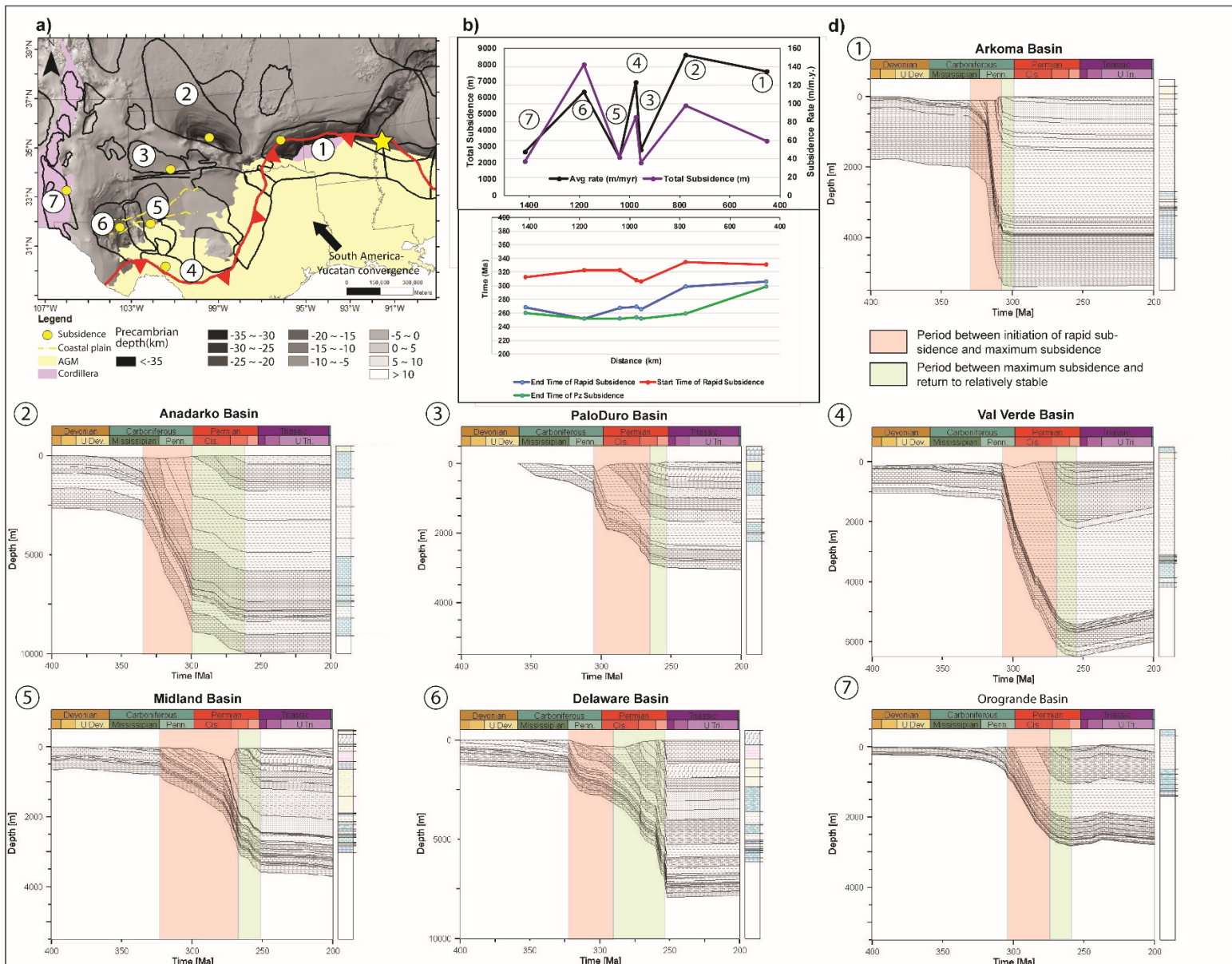
In Figure 2.17b, I plotted the measured distance versus the average subsidence rate during the period of maximum subsidence during the Pennsylvanian-Permian orogenic period and total subsidence for the seven basins. The basins with the higher average subsidence rates from east to west are the Arkoma Basin (135 m/my), the Anadarko Basin (152 m/my), the Val Verde Basin (123 m/my), and the Delaware Basin (113 m/my). With the exception of the Anadarko Basin, these higher rate basins are within 150 km of the Ouachita-Marathon

deformation front. The more distant basins except for the Delaware Basin (the Palo Duro Basin – 480 km and the Orogrande Basin – 440 km) show lesser average subsidence rates (49 m/my and 47 m/my, respectively) and total sedimentation (Fig. 17b). The Delaware Basin shows the highest total subsidence of 8000 m as it continued to subside at a high subsidence rate up to the end of the Permian.

In Figure 2.17c, I plotted the measured distance versus the start and times for the most rapid period of the presumed climax of orogenic activity – along with the end time for all orogenic activity - for the seven basins. These plots show a slight younging trend from east to west over the 1000 km distance with an average rate of 0.04 cm/yr. This rate is considerably less than the rate of 0.6 mm/yr that I calculated using the data provided by Leary et al. (2017).

My younging rate is similar to the rate of 0.02 mm/yr that I calculated using data provided by Ewing (2019). My data indicate that the South America-Yucatan collision occurred almost synchronously along the Ouachita-Marathon thrust front, and for that reason, higher sedimentation occurred in the more proximal basins as a consequence of an elevated highland generated along this zone (Gao et al., 2019; Liu and Stockli, 2020; Soto-Kerans et al., 2020).

Figure 2.17 Regional burial history pattern. **a)** Location of the representative wells of seven sedimentary basins along the Marathon-Ouachita orogenic belt and part of the ARM system, including 1) the Arkoma Basin, 2) the Anadarko Basin, 3) the Palo Duro Basin, 4) the Val Verde Basin, 5) the Midland Basin, 6) the Delaware Basin and 7) the Orogrande Basin. Basemap was modified from Marshak et al. (2017). **b)** Plot showing maximum subsidence rate for the seven basins compared to their estimated distance from the easternmost location where continental collision is thought to have begun (labeled as a start). **c)** Plot showing the time of most rapid subsidence initiation and the time of maximum subsidence rate for the seven basins versus estimated distance away from the location where continental collision began (labeled in start). **d)** Subsidence analysis for the seven basins marked with the period from the initiation of rapid subsidence to reaching their maximum subsidence rate followed by the end of rapid subsidence and with an eventual return to basin stability.



Effect of basement structure on thermal maturity of source rocks

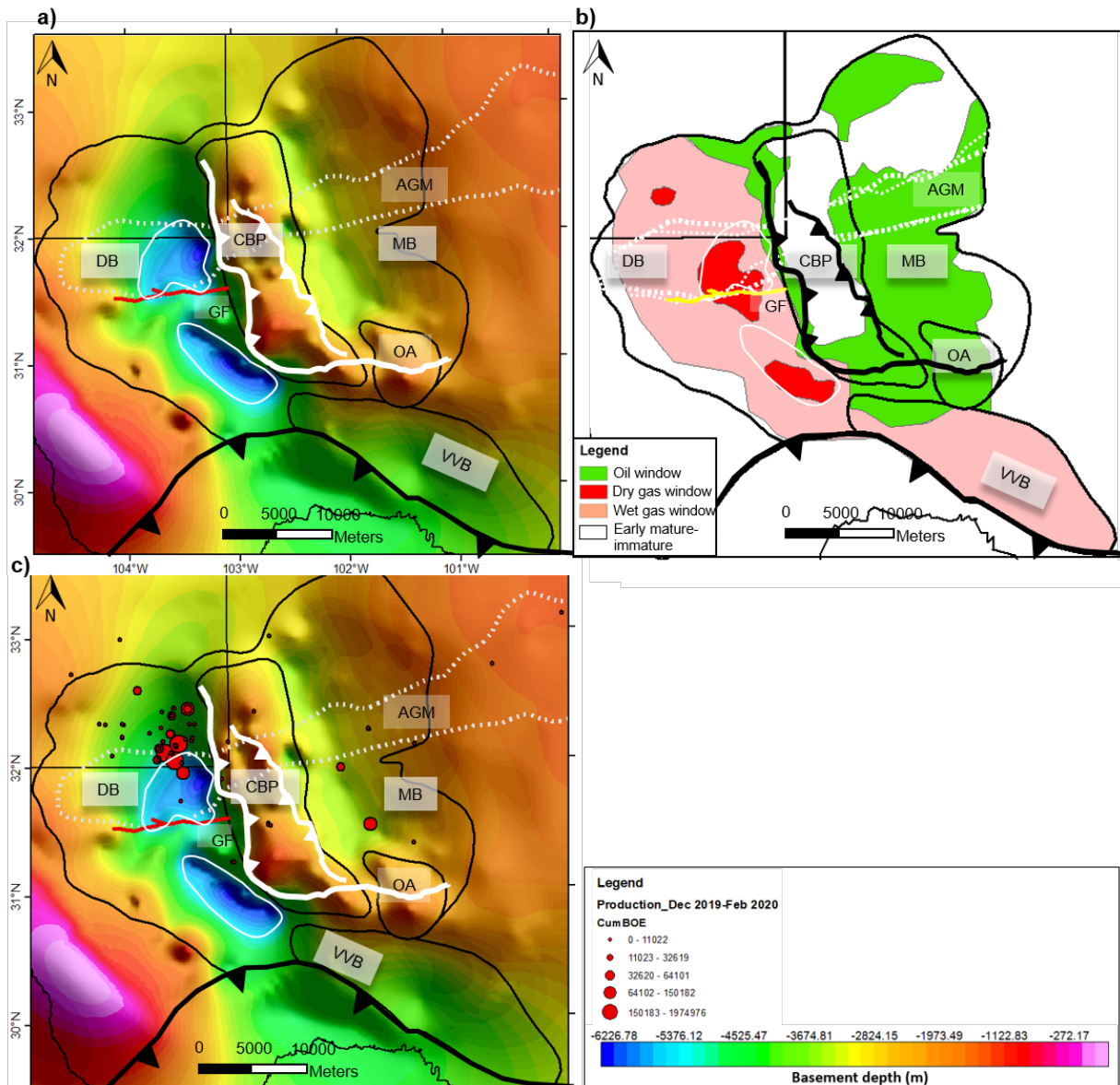
The top to basement depth shown in Figure 2.18a was constrained by gravity modeling, well logs, and previous subsurface mapping summarized by Ruppel (2008). Two depocenters were observed in the northwest and southeast Delaware Basin (Figure 2.18a). The depocenter in the northern Delaware Basin is called the Malaga sub-basin by Ewing (2019). The depocenter in the northern Delaware Basin overlies the ENE trend of the Abilene gravity minimum and is bounded in the south by the Grisham fault (Figure 2.18a).

Basement depth was then compared with thermal maturity and production trend in this region. I combined my maturity modeling results with previous maturity studies in the Permian Basin to generate a maturity map of top Devonian (modified from Echegu, 2013 and Jarvie et al., 2017). The maturity map shows that the dry gas window, which has the highest thermal maturity, correlates with the thicker depocenters in the Delaware Basin (Figure 2.18b). The location of maturity associated with the deeper depocenters also correlates with the most recent production trends in the Permian Basin unconventional plays (Figure 2.18c). Thermal maturity is also related to the presence of granitic/mafic intrusion bodies, which will produce higher heat flow. The study by Manos and Perez (2018) using Raman spectroscopy of carbonaceous material shows that the highest maturity gradient lies in an area of higher heat flow in the southwestern Delaware Basin in western Pecos County, which they attribute to the area of Cenozoic intrusions. The location of the highest maturity gradient also correlates with the presence of two major bodies of Pre-Grenville mafic intrusions (Adams and Keller, 1996; Manos and Perez, 2018), as shown in Figure 2.13a.

Production information from Enverus shows that from December 2019 to February 2020, new wells started to produce in a concentrated area in the northwestern Delaware Basin that

correlates with these areas of more mature basement depocenters (Figure 2.18c). The Delaware Basin has been the site of recent large increases in unconventional hydrocarbon production, especially from the Wolfcamp and Bone Spring formations. While reservoir characteristics are the primary driver, I speculate that thicker sediments and higher thermal maturity may have contributed to this sweet spot of recent oil production.

Figure 2.18 Effect of basement structure on source rocks thermal maturity. **a)** Depth to basement map constrained by gravity model, well logs, and the previous study by Ruppel (2008). Two depocenters were observed in the Delaware Basin (in white polygon). **b)** Top Devonian maturity map modified from Echeagu (2013) and Jarvie et al. (2017) showing the distribution of the oil window, wet gas window, dry gas window, and areas that are early mature to immature. Zones of basement depocenters from (a) are shown as white polygons. **c)** Basement structure with production wells for a three-month period (Dec 2019-Feb 2020) based on data provided by Enverus. New wells that start production with a promising BOE concentrated in the northern Delaware Basin. Zones of basement depocenters from (a) are shown as white polygons.



Conclusions

I developed three regional 2D gravity model that incorporates the following data sources:

- 1) density and lithological controls from industry well logs drilled to the Ordovician Ellenburger Formation;
- 2) published seismic refraction data; and
- 3) published, regional cross-sections in the Permian Basin. Because sediment densities and basinal stratigraphy vary between the three

components of the Permian Basin – the Midland Basin, the Delaware Basin, and the Central Basin Platform - I divided the sedimentary section above the crystalline basement into seven layers for the 2D model. The result of this gravity modeling improved the boundaries of a 34-108-km-wide, 650-km-long east-west-trending Abilene gravity minimum (AGM) over the northern Permian Basin, which I infer is underlain by a belt of Early Mesoproterozoic, granitic and metasedimentary rocks with a lower density compared to the surrounding areas of the upper crust.

I also generated a 3D model incorporating structural and density controls from well logs. Structural inversion results show that depth to both the top lower crust and Moho is deeper below the AGM, especially beneath the deep depocenter of the northern Delaware Basin. Density inversion results further confirm that upper crust density is lower beneath the AGM.

Subsidence analysis based on deep wells in the Permian Basin allows division of the stratigraphic section into five tectonic phases:

- 1) Pre-deformational, Tobasa Basin and transition phase from the Ordovician to Early Pennsylvanian;
- 2) Main deformational and subsidence phase from the Early Pennsylvanian to Late Permian;
- 3) Post-deformational, low subsidence phase from Late Permian to Late Triassic;
- 4) Stable platform phase from the Jurassic to Eocene.
- 5) Basin exhumation/tilting phase from Late Eocene to present

The maximum subsidence (up to 421m/my) happened during the main deformational phase with sediment packages up to 2.4 km thick.

I propose that the belt of granitic and metasedimentary rocks inferred from gravity modeling acted as a zone of preferential weakness in a “broken foreland basin” setting that accommodated regional shortening related to the Marathon orogeny to the south and to coeval orogenies along the Sonoran margin to the southwest and Nevadan margin to the west. Basement depth in the Permian Basin defines the limits of deep basinal areas that may host the most productive and thermally mature source rock kitchens. These deep and localized depocenters are controlled in part by Permian strike-slip faults align with the edges of the AGM. High maturity zones for hydrocarbons overlie deeper basement depocenters and are delineated by my basement maps. The deeper (4.2-6.2km) basement of the Delaware basin has resulted in its broader zone of oil and gas maturity than observed above the shallower (1.6-3.6 km) basement of the Midland Basin.

Bibliography

- Adams, J.E., 1965. Stratigraphic-tectonic development of Delaware Basin. AAPG Bulletin, 49 (11), 2140-2148.
- Adams, D.C. and Keller, G.R., 1994. Possible extension of the Midcontinent Rift in west Texas and eastern New Mexico. Canadian Journal of Earth Sciences, 31(4), 709-720.
- Adams, D.C. and Miller, K.C., 1995. Evidence for late Middle Proterozoic extension in the Precambrian basement beneath the Permian Basin. Tectonics, 14(6), 1263-1272.
- Adams, D.C. and Keller, G.R., 1996. Precambrian basement geology of the Permian Basin region of West Texas and eastern New Mexico: A geophysical perspective. AAPG Bulletin, 80(3), 410-431.
- Blackwell, D.D. and Richards, M., 2004. Geothermal Map of North America dataset. American Association of Petroleum Geologists, Tulsa, Oklahoma.
- <https://www.smu.edu/Dedman/Academics/Departments/Earth-Sciences/Research/GeothermalLab/DataMaps/GeothermalMapofNorthAmerica>, accessed Dec 10, 2019.
- Craddock, J., Malone, D., Porter, R., Compton, J., Luczaj, J., Konstantinu, A., Day, J., and Johnston, S., 2017. Paleozoic reactivation structures in the Appalachian-Ouachita-Marathon foreland: Far-field deformation across Pangea. Earth-Science Reviews, 169, 1-34.
- Daniels, V.B., Patricia, C.A., Mark, H.R., Victoria, P.C., Ronald, R.S., Phillips, S.J., Ravat, J.D., 2002. Digital data grids for the magnetic anomaly map of North America.
- <https://mrdata.usgs.gov/magnetic/>, accessed Jan 5, 2019.

- Escalona, A. and Yang, W., 2013. Subsidence controls on foreland basin development of northwestern offshore Cuba, southeastern Gulf of Mexico. *AAPG Bulletin*, 97(1), 1-25.
- Dickinson, W.R., and Lawton, T.F., 2003. Sequential intercontinental suturing as the ultimate control for Pennsylvanian Ancestral Rocky Mountains deformation. *Geology*, 31, 609–612.
- Dutton, S.P., Kim, E.M., Broadhead, R.F., Breton, C.L., Raatz, W.D., Ruppel, S.C. and Kerans, C., 2004. Play analysis and digital portfolio of major oil reservoirs in the Permian Basin: Application and transfer of advanced geological and engineering technologies for incremental production opportunities, 1-428. <https://www.osti.gov/servlets/purl/828411>, accessed Jan 15, 2019.
- Dutton, S.P, Kim, E.M., Broadhead, R.F., Raatz, W.D., Breton, C.L., Ruppel, S.C, and Kerans, C., 2005. Play analysis and leading-edge oil-reservoir development methods in the Permian Basin: Increased recovery through advanced technologies. *AAPG Bulletin*, 89(5), 553–576.
- Dumas, D.B., 1982, Seismicity of west Texas. Unpublished Ph.D. dissertation, the University of Texas at Dallas, 1-94.
- Echegu, S., 2013. Geological and Geochemical Investigation of the Petroleum Systems of the Permian Basin of West Texas and Southeast New Mexico. Unpublished Ph.D. dissertation, University of Houston, 1-195.
- Ewing, T.E., 1993. Erosional margins and patterns of subsidence in the late Paleozoic west Texas basin and adjoining basins of West Texas and New Mexico: Carlsbad Region, New Mexico and West Texas. *New Mexico Geological Society 44th Annual Field Conference*, 155-166.

- Ewing, T.E., 2016. Texas through time: Lone Star geology, landscapes, and resources. Bureau of Economic Geology Udden Series No.6., 431p.
- Ewing, T.E., 2019. Tectonics of the West Texas (Permian Basin) — Origins, structural geology, subsidence, and later modification *In* Ruppel, S. C., ed., 2019, *Anatomy of the Paleozoic basin: the Permian Basin, USA (vol.1, ch. 3)*. The University of Texas at Austin, Bureau of Economic Geology Report of Investigations 285. AAPG Memoir, 118, 63-96.
- Ewing, T.E., Barnes, M.A., and Denison, R.E., 2019. Proterozoic Foundations of the Permian Basin, West Texas and Southeastern New Mexico — a review. *In* Ruppel, S. C., ed., 2019, *Anatomy of the Paleozoic basin: the Permian Basin, USA (vol.1, ch. 3)*. The University of Texas at Austin, Bureau of Economic Geology Report of Investigations 285. AAPG Memoir, 118, 63-96.
- Feldman, M.L. and Chairman, JR., 1962. Southwest-northeast cross section, Marathon region to Midland Basin, 1:252,500. West Texas Geological Society Publication, 62-47.
- Frenzel, H.N., Bloomer, R.R., Cline, R.B., Cys, J.M., Galley, J.E., Gibson, W.R., Hills, J.M., King, W.E., Seager, W.R., Kottlowski, F.E. and Thompson III, S., 1988. The Permian Basin region: Sedimentary cover—North American craton: US, Boulder, Colorado. Geological Society of America, the Geology of North America, 2, 261-306.
- Gaherty, J.B., 2004. A surface wave analysis of seismic anisotropy beneath eastern North America. *Geophysical Journal International*, 158(3), 1053-1066.
- Galley, J.E., 1958. Oil and geology in the Permian Basin of Texas and New Mexico: North America: Habit of oil—a symposium. American Association of Petroleum Geologists, Special Publication, A215, 395-446.

- Galley, J.E., 1970. Some principles of tectonics in the Permian Basin. *In* W.J. Stewart, ed., *Basins of the Southwest*, West Texas Geological Society Publication, 1, 5-20.
- Gao, Z., Perez, N. D., Miller, B., and Pope, M. C., 2019. Competing sediment sources during Paleozoic closure of the Marathon-Ouachita remnant ocean basin. *Geological Society of America Bulletin*, 132 (1/2), 3-16.
- Garcia, E.S., Sandwell, DT and Smith, W.H., 2014. Retracking CryoSat-2, Envisat and Jason-1 radar altimetry waveforms for improved gravity field recovery. *Geophysical Journal International*, 196 (3), 1402-1422.
- Gemmer, L., Nielsen, S.B., Huuse, M. and Lykke-Andersen, H., 2002. Post-mid-Cretaceous eastern North Sea evolution inferred from 3D thermo-mechanical modeling. *Tectonophysics*, 350 (4), 315-342.
- Graham, S.A., Dickinson, W.R., and Ingersoll, R.V., 1975, Himalayan-Bengal model for flysch dispersal in the Appalachian-Ouachita system. *Geological Society of America Bulletin*, 86, 273–286.
- Hall, S. A., Bird, D. E., McLean, D. J., Towle, P. J., Grant, J. V., and Danque, H. A., 2018. New constraints on the age of the opening of the South Atlantic basin. *Marine and Petroleum Geology*, 95, 50-66.
- Hickman, R., Varga, R., and Altany, R., 2009. Structural style of the Marathon thrust belt, West Texas. *Journal of Structural Geology*, 31, 900-909.
- Hills, J.M., 1972. Late Paleozoic sedimentation in west Texas Permian Basin. *AAPG Bulletin*, 56 (12), 2303-2322.
- Horak, R.L., 1985. Tectonic and hydrocarbon maturation history in the Permian Basin. *Oil & Gas Journal*, 83 (21), 124-129.

- Jackson, W.H. and Pakiser, L.C., 1965. Seismic study of crustal structure in the southern Rocky Mountains. US Geological Survey, 525, 85-92.
- Jarvie, D.M., Prose, D.A., Jarvie, B.M., Drozd, R.J., and Maende, A., 2017. Conventional and Unconventional Petroleum Systems of the Delaware Basin, USA. AAPG Annual Convention and Exhibition.
- <http://www.searchanddiscovery.com/abstracts/html/2017/90291ace/abstracts/2612939.html>, accessed Feb 1, 2020.
- Keller, G. R., 2019. Constraints on structural and tectonic interpretations of the Permian Basin based on gravity and magnetic data. In Ruppel, S. C., ed., 2019, *Anatomy of the Paleozoic basin: the Permian Basin, USA (vol.1, ch. 2)*. The University of Texas at Austin, Bureau of Economic Geology Report of Investigations 285. AAPG Memoir, 118, 31-42.
- Liu, L. and Stockli, D.F., 2020. U-Pb ages of detrital zircons in lower Permian sandstone and siltstone of the Permian Basin, west Texas, USA: Evidence of dominant Gondwanan and peri-Gondwanan sediment input to Laurentia. GSA Bulletin, 132(1-2), 245-262.
- Loucks, R.G., 2008. Review of the lower Ordovician Ellenburger group of the Permian Basin, West Texas.
- http://www.beg.utexas.edu/resprog/permianbasin/PBGSP_members/writ_synth/Ellenburger Draft_022206.pdf, accessed on May 15th, 2020.
- Macedo, J. and Marshak, S., 1999. Controls on the geometry of fold-thrust belt salient. Geological Society of America Bulletin, 111(12), 1808-1822.
- Matchus, E.J., and Jones, T.S., 1984. East-west cross section through Permian Basin of West Texas, 1:250,000. West Texas Geological Society Publication, no. 84-79.

- Manos, T.A. and Perez, N., 2018. Thermal Maturity Modeling of Organic-Rich Mudrocks in the Delaware Basin Using Raman Spectroscopy of Carbonaceous Material. AAPG ACE 2018.
- Marshak, S., 2004. Salients, recesses, arcs, Oroclines, and syntaxes— A review of ideas concerning the formation of map-view curves in fold-thrust belts. *In* K. R. McClay, ed., Thrust tectonics and hydrocarbon systems. AAPG Memoir, 82, 131-156.
- Marshak, S., Domrois, S., Abert, C., Larson, T., Pavlis, G., Hamburger, M., Yang, X., Hersh, G., and Chen, C., 2017. The basement revealed: Tectonic insight from a digital elevation model of the Great Unconformity, USA cratonic platform. *Geology*, 5, 391-394.
- Marshak, S., Karlstrom, K. and Timmons, J.M., 2000. Inversion of Proterozoic extensional faults: An explanation for the pattern of Laramide and Ancestral Rockies intracratonic deformation, United States. *Geology*, 28(8), 735-738.
- Mitchell, B.J. and Landisman, M., 1971. Geophysical measurements in the southern Great Plains. *In* Heacock, G. J., ed., *The structure and physical properties of the Earth's crust*, 14, 77-93.
- Pavlis, N.K., Holmes, S.A., Kenyon, S.C. and Factor, J.K., 2012. The development and evaluation of the Earth Gravitational Model 2008 (EGM2008). *Journal of Geophysical Research: Solid Earth*, 117(4), 1-38.
- Pawlewicz, M., C. E., Barker, S. McDonald, 2005. Vitrinite reflectance data for the Permian Basin, West Texas and Southeast New Mexico. USGS Open-File Report, 2005-1171, accessed Sept 1, 2019.
- Poole, F., Perry, W., Madrid, R., and Amaya-Martinez, R., 2005. Tectonic synthesis of the Ouachita-Marathon-Sonora orogenic margin of southern Laurentia: Stratigraphic and

- structural implications for timing of deformational events and plate-tectonic model: in Anderson, T., Nourse, J., McKee, J. and Steiner, M., eds., The Mojave-Sonora megashear hypothesis: Development, assessment and alternatives. GSA Special Paper, 393, 5453-596.
- Ruppel, S.C, 2008. Permian Basin synthesis project: data and models for recovering existing and undiscovered oil resources from the largest oil-bearing basin in the US GIS dataset, <http://www.beg.utexas.edu/research/areas/permian-basin-synthesis>, accessed Oct 19, 2018.
- Ruppel, S. C., ed., 2019. Anatomy of the Paleozoic basin: the Permian Basin, USA (vol.1). The University of Texas at Austin, Bureau of Economic Geology Report of Investigations 285. AAPG Memoir, 118, 412 p.
- Soto-Kerans, G.M., Stockli, D.F., Janson, X., Lawton, T.F. and Covault, J.A., 2020. Orogen proximal sedimentation in the Permian foreland basin. *Geosphere*, 16(2), 567-593.
- Romney, C., Brooks, B.G., Mansfield, R.H., Carder, D.S., Jordan, J.N. and Gordon, D.W., 1962. Travel times and amplitudes of principal body phases recorded from Gnome. *Bulletin of the Seismological Society of America*, 52(5), 1057-1074.
- Ross, C.A. and Ross, J.R., 1987. Late Paleozoic sea levels and depositional sequences. In Ross, C.A. and Haman D., eds., *Timing and Depositional History of Eustatic Sequences: Constraints on Seismic Stratigraphy*. Cushman Foundation for Foraminiferal Research Special Publication, Washington, D. C., 24, 137-149.
- Shen, W., Ritzwoller, M.H. and Schulte-Pelkum, V., 2013. A 3-D model of the crust and uppermost mantle beneath the Central and Western US by joint inversion of receiver functions and surface wave dispersion. *Journal of Geophysical Research: Solid Earth*, 118 (1), 262-276.

- Shumaker, R.C., 1992. Paleozoic structure of the Central Basin uplift and adjacent Delaware basin, west Texas. *AAPG Bulletin*, 76(11), 1804-1824.
- Snee, J.E.L. and Zoback, M.D., 2018. State of stress in the Permian Basin, Texas and New Mexico: Implications for induced seismicity. *The Leading Edge*, 37(2), 127-134.
- Stewart, S.W. and Pakiser, L.C., 1962. Crustal structure in eastern New Mexico interpreted from the GNOME explosion. *Bulletin of the Seismological Society of America*, 52 (5), 1017-1030.
- Soreghan, G.S., and Soreghan, M.J., 2013. Tracing Clastic Delivery To the Permian Delaware Basin, USA: Implications For Paleogeography and Circulation In Westernmost Equatorial Pangea Tracing Clastic Dispersal to the Westernmost Pangean Suture. *Journal of Sedimentary Research*, 83 (9), 786–802
- U.S. Energy Information Administration report, October 2018. Permian Basin Wolfcamp Shale Play Geology review,
https://www.eia.gov/maps/pdf/PermianBasin_Wolfcamp_EIARreport_Oct2018.pdf,
accessed February 2019.
- Van Staal, C., and Zagorevski, A., 2020. Accretion, soft and hard collision: Similarities, differences, and an application from the Newfoundland Appalachian orogeny. *Geoscience Canada*, 47, 103-118.
- Walper, J. L., 1977. Paleozoic tectonics of the southern margin of North America. *Gulf Coast Association of Geological Societies*, 27, 230–241.
- Xie, X., Anthony, J.M. and Busbey, A.B., 2019. Provenance of Permian Delaware Mountain Group, central and southern Delaware Basin, and implications of sediment dispersal

pathway near the southwestern terminus of Pangea. *International Geology Review*, 61(3), 361-380.

Yang, K.M. and Dorobek, S.L., 1995. The Permian Basin of west Texas and New Mexico: flexural modeling and evidence for lithospheric heterogeneity across the Marathon Foreland. *SEPM Special Publication*, 52, 37-50.

CHAPTER 3 : DETECTING HYPOGENIC KARST FEATURES IN THE NORTHEASTERN DELAWARE BASIN, WEST TEXAS: APPLICATIONS OF FULL TENSOR GRADIENT (FTG) GRAVITY DATA

Introduction

The Permian Basin of West Texas and southeast New Mexico is located in the foreland area of the Ouachita-Marathon fold-thrust belt, and it is divided into three major structural components: the Delaware and Midland Basins are separated by the Central Basin Platform on the west and east, respectively (Figure 3.1a, b). Extensive karst development in carbonate and evaporate strata occur in shallow sediments of the Delaware Basin and are mainly associated with late Permian Guadalupian and Ochoan strata (Stafford, 2017; Figure 3.1c). Recent studies of hypogenic karst features have focused on outcrops (Ochoan Castile and Rustler formations) within the western and central Delaware Basin (e.g., Scholle et al., 2004; Stafford, 2013; Stafford, 2017; Majzoub et al., 2017; Stafford et al., 2018).

In the Castile formation, a range of hypogene speleogenesis commonly occurs from ~100 m deep isolated rise structures to maze caves and intrastratal brecciation (Stafford, 2017; Figure 3.1d). Hypogene karst in shallow Salado and Rustler formations are largely associated with cross-formational breccia pipes and intra-stratal brecciation (Stafford, 2017; Figure 3.1d). However, in the eastern portion of the Delaware Basin, much of the soluble rock is buried beneath northeast dipping strata of Guadalupian and Ochoan age (Figure 3.1d), so the potentially karsted Salado and Rustler Formations remain less studied.

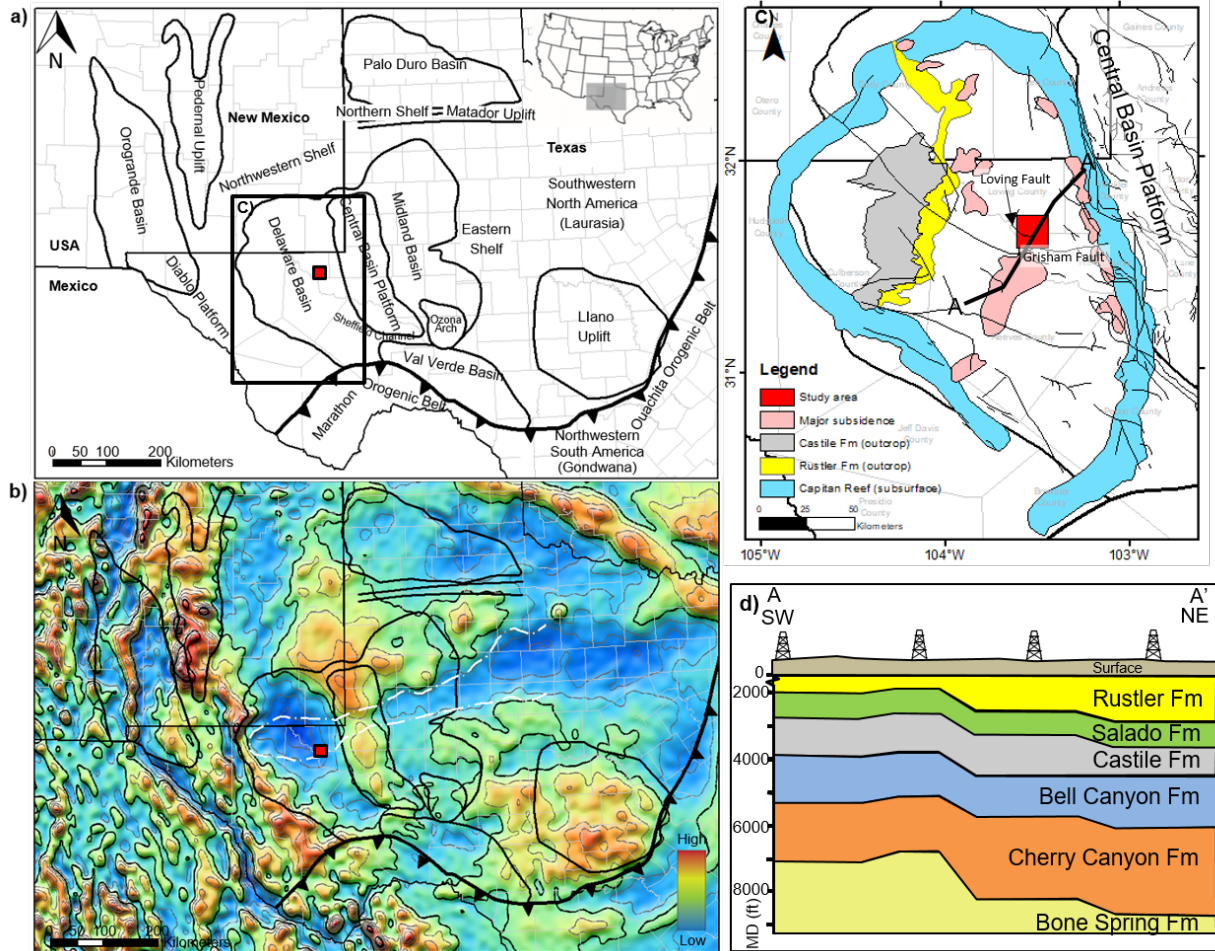


Figure 3.1 Geological settings of the Permian Basin and study area. **a)** Physiographic setting of the Permian Basin with major basin names and the study area outlined by the red box (modified from Zhang et al., 2021). **b)** Regional Bouguer gravity anomalies over the Permian Basin show major basins and regional structures, such as the Central Basin Platform (modified from Garcia et al., 2014). **c)** Geological map of the Delaware Basin with the locations of selected major units related to hypogenic karst features. Paleozoic fault distribution (thin black lines) was mapped by Ruppel et al. (2008) and Ewing (2019), including the Grisham Fault and the Loving Fault. **d)** Cross-section (flattened on the top Rustler layer) through the study area based on well correlations depicting stratigraphic units in the northeastern Delaware Basin with a northeast dip.

Hypogenic karst features are often linked to geohazards during drilling operations in the highly productive Permian Basin (Dutton et al., 2004, 2005). For example, Morgan et al. (2018) reported that a drilling operator in Culbertson County, western Delaware Basin, experienced

significant drilling fluid loss in several wells after penetrating open voids in the initial 500 feet of drilling. As a result, the drillers were forced to abandon the boreholes.

High-resolution, high-precision FTG data is an exploration tool used to detect and map source bodies as defined by their subtle density contrasts - especially those within close proximity to the measurement platform. The short wavelength resolution of FTG enables the identification of small density sources required for detailed hydrocarbon and mineral exploration. Successful applications include salt dome detection in Louisiana, USA (Murphy and Mumaw, 2004); low-density sedimentary deposits mapped in the Judd Basin, offshore NW Europe (Murphy and Mumaw, 2004); and the detection of intrusion-hosted sulfide mineralization in Newfoundland, Canada (Mataragio et al., 2009). Interpreting FTG data for the purpose of karst detection is similar to these above examples because karst voids are often less dense than their host rocks.

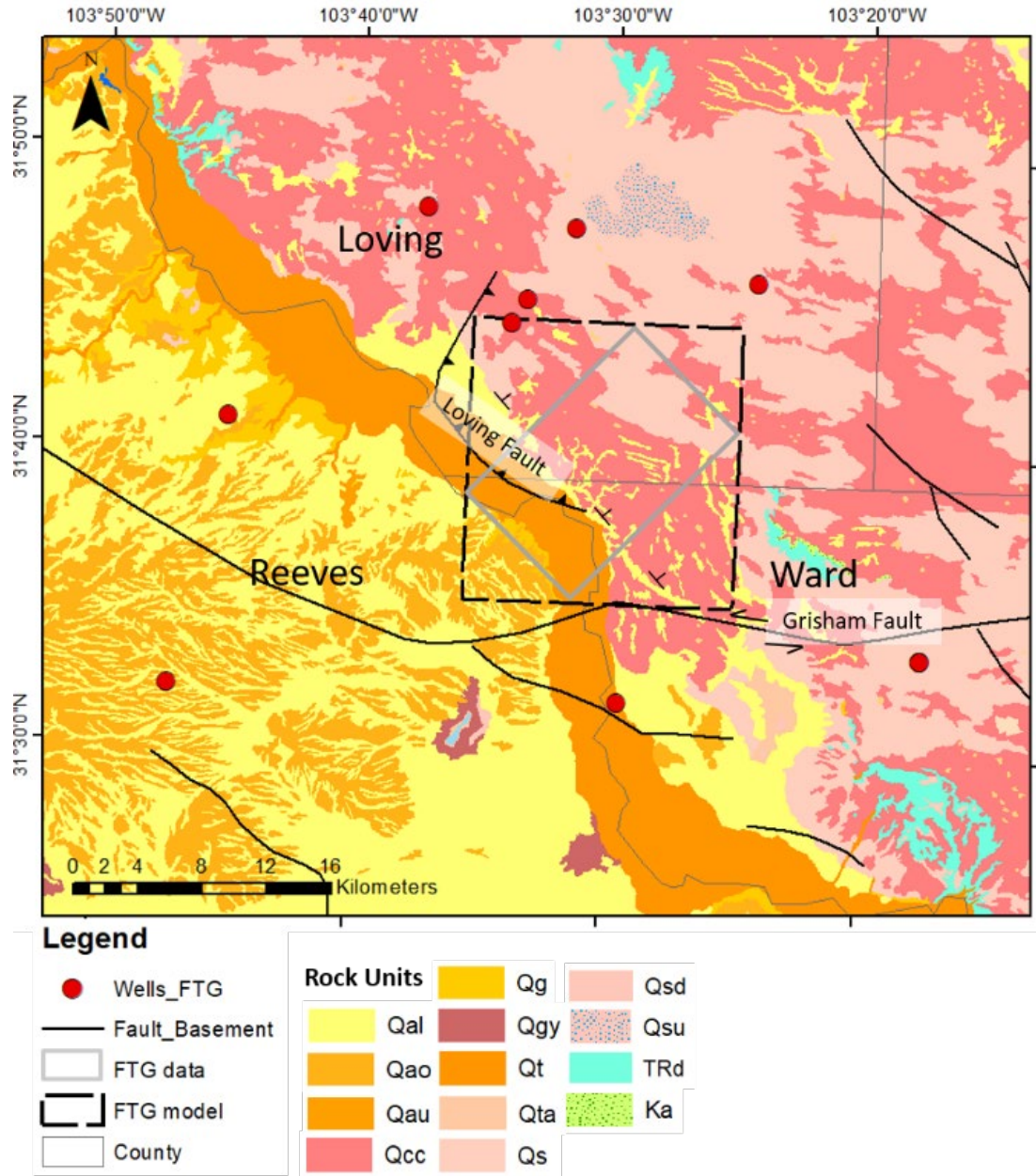
My study applied high-resolution FTG gravity data to infer dissolution karsting related caverns, systems of caverns, and zones with high porosity in the Dewey Lake, Ruslter, Salado and Castile Formation of the late Permian Ochoan age in the northeastern Delaware Basin (Figure 3.1a). The results presented in this chapter demonstrate how FTG data can be applied to de-risk karst-related geohazards.

Dataset and method

The 144 km² airborne, terrain-corrected FTG gravity survey was flown by Bell Geospace, over Loving, Ward, and Reeves Counties, with survey lines spaced every 50 meters (Figure 3.2). The Loving fault, a northwest-striking normal fault (Ruppel et al., 2008), diagonally crosses the

survey area and is truncated at its southern end by the east-striking Grisham, left-lateral strike-slip fault to the south (Ruppel et al., 2008; Figure 3.2). The Loving Fault was originally mapped by Ruppel et al. (2008) using well logs as a reverse fault. Nine well logs provided by Enverus were projected into the survey area for stratigraphic, lithological, and density control (Figure 3.2).

Figure 3.2 Geologic map of the study area and FTG survey area (grey box). The 3D model area is outlined by the black dashed line. Well locations for logs used in the study are shown as red dots. Faults are represented by black lines, including the Grisham and Loving Faults.



Gravity gradients are measures of the spatial rate of change of gravitational acceleration.

Gravitational acceleration \vec{g} is the gradient of gravitational potential, Φ , as shown below

(Martinez et al., 2013),

$$\vec{g} = \nabla\Phi = \left(\frac{\partial\Phi}{\partial x}, \frac{\partial\Phi}{\partial y}, \frac{\partial\Phi}{\partial z}\right) = (g_x, g_y, g_z). \quad (1)$$

The gradient of the acceleration, \vec{g} , is the gravity gradient tensor field, T (Telford et al., 1990), is defined as,

$$T = \nabla \vec{g} = \nabla \nabla \Phi = \begin{bmatrix} \frac{\partial^2 \Phi}{\partial x^2} & \frac{\partial^2 \Phi}{\partial x \partial y} & \frac{\partial^2 \Phi}{\partial x \partial z} \\ \frac{\partial^2 \Phi}{\partial y \partial x} & \frac{\partial^2 \Phi}{\partial y^2} & \frac{\partial^2 \Phi}{\partial y \partial z} \\ \frac{\partial^2 \Phi}{\partial z \partial x} & \frac{\partial^2 \Phi}{\partial z \partial y} & \frac{\partial^2 \Phi}{\partial z^2} \end{bmatrix} = \begin{bmatrix} T_{xx} & T_{xy} & T_{xz} \\ T_{yx} & T_{yy} & T_{yz} \\ T_{zx} & T_{zy} & T_{zz} \end{bmatrix}. \quad (2)$$

The Earth's gravity field is a smooth vector field that is conservative, harmonic, irrotational, and solenoidal.

The gravity field satisfies Laplace's equation in source-free regions, and its gradient tensor is symmetric and traceless (Blakely, 1995): i.e., $T_{xy} = T_{yx}$, $T_{xz} = T_{zx}$, and $T_{yz} = T_{zy}$ (symmetry), and the Laplacian, $T_{xx} + T_{yy} + T_{zz} = 0$ (zero trace). Reconciling gravity (Tz) and gravity gradient (Tzz) amplitude units reveal an enormous difference in resolution.

Consider gradient units (Eotvos, or Eo) in terms of gravity units (mGal/m): $100 \text{ Eo} = 1/100 \text{ mGal/m}$. This means that gradient anomalies modeled in this chapter are far smaller than gravity surveys can resolve.

Five independent tensor components together with the vertical tensor component and gravity (Tz) are displayed in Figure 3.3a. The FTG survey, due to its size and line spacing, captured wavelengths between 90 m and 16 km and is therefore far more detailed than the regional open-file gravity data (Martinez et al., 2013).

Each tensor component represents directional changes in the magnitude of the tensor field, and they can therefore be associated with different geology attributes. For example, source edges, or lateral changes in density such as faults, produce T_{xz} and T_{yz} anomaly maxima/minima directly over these density contrasts but lie directly beneath the gradients of T_{xx} and T_{yy} components. T_{zz} anomalies overlie the mass centers of density sources.

Gravity gradient data were processed to follow the North-East-Down (NED) standard. Figure 3.3b shows modeled FTG anomalies over a low-density prism to simulate a karst feature. Note that T_{xz} anomalies are produced by density contrasts that trend roughly north-south, and T_{yz} anomalies are produced by density contrasts that trend roughly east-west. The focused survey size and ultra-short acquisition line spacing provided us an excellent opportunity to examine the area for subtle density variations in the near-surface sedimentary section.

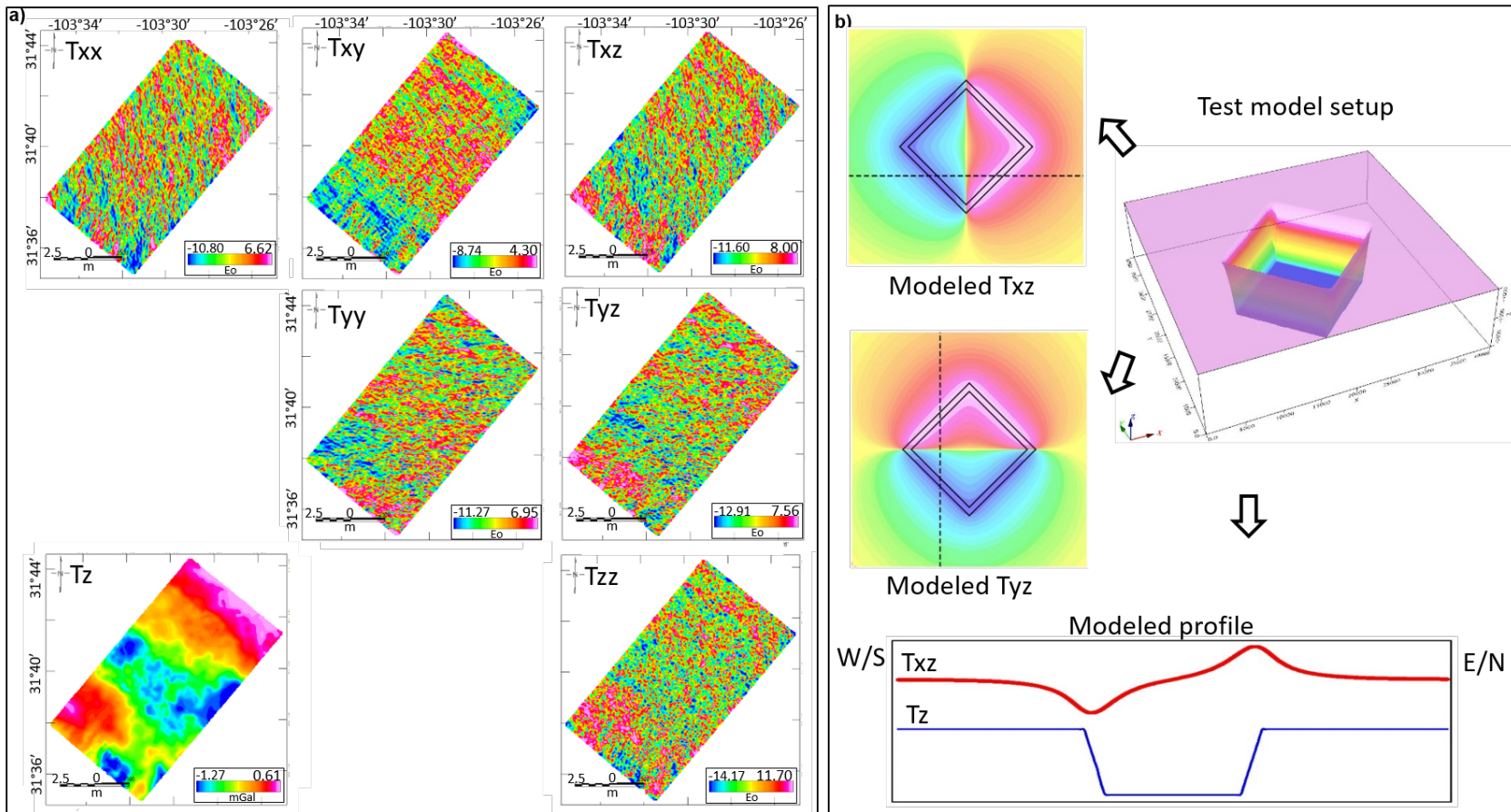


Figure 3.3 FTG survey. **a)** FTG survey data. **b)** Modeled FTG Txz and Tyz component anomalies over a low-density prism. Note that these anomalies overlie structures that trend roughly north-south and east-west, respectively. The component calculation direction follows the NED standard with Txz calculated from west to east and Tyz calculated from south to north.

A 3D gravity model was created, using Seequent's *Oasis Montaj* software, which employs forward and inverse frequency-domain algorithms (Cordell and Henderson, 1968; Parker, 1972; Bott, 1973; Li and Chouteau, 1998). The model included ten layers: seven sedimentary, two crystalline crust, and an upper mantle. The model used structural and density grids extracted from a recent basin-scale model (Zhang et al., 2021).

A structural inversion of the Moho horizon was first conducted to improve the long-wavelength crustal geometry in the study area. Density inversions were then conducted, using both Tz and Tzz fields, on two sedimentary layers individually (topography-top Rustler Formation and top Rustler Formation-top Leonardian), then these layers combined (topography-top Leonardian). Below I refer to these layers as Surface, Rustler, and Combined, respectively.

Results

Density inversion of gravity (Tz) anomalies

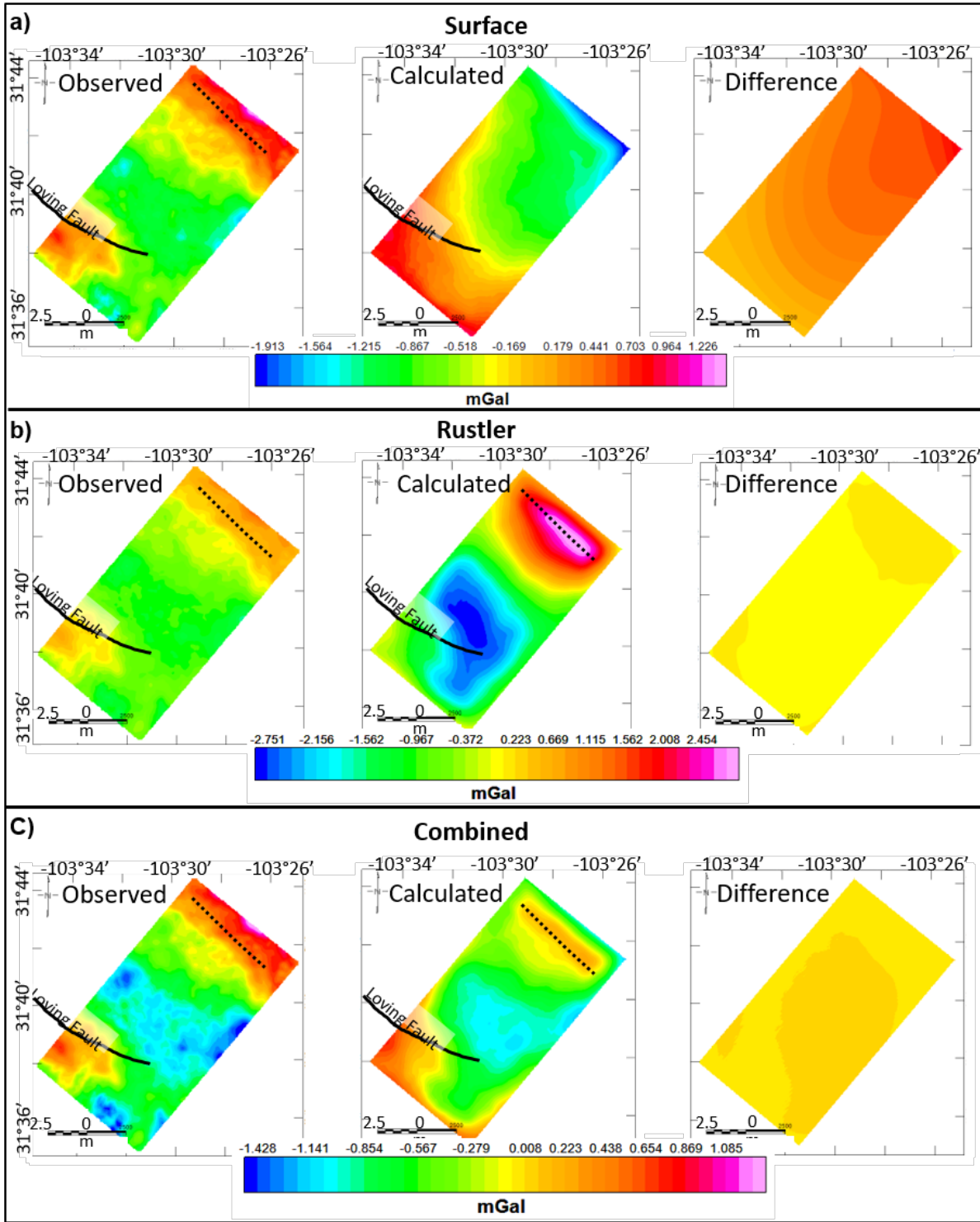
Figure 3.4 summarizes Tz gravity density inversion results of the Surface, Rustler, and Combined sedimentary layers. The Tz gravity inversion provided a good result, although the difference range between the observed and calculated gravity was small (-0.30 to 0.61mGal). The density control of this uppermost layer is less than deeper layers because there are fewer density measurements from this shallower interval.

Density control for the Rustler layer was better as was the fit between the calculated and observed gravity anomaly with a difference of -0.06 to 0.21mGal (Figure 3.4b). The gravity maximum over the southwestern part of the study area was interpreted to be related to the previously unmapped Loving Fault (Figure 3.2; Figure 3.4b). Another unmapped regional fault

system may produce the high-amplitude gravity anomaly along the northeast boundary of the study area (Figure 3.4b).

The best results were achieved with the gravity density inversion between topography and the top Leonardian formation with a resulting, small difference range of -0.09 to 0.01 mGal (Figure 3.4c). The fit between the calculated and observed gravity was further improved and revealed more details about the central and northeastern parts of the study area, including a subtle expression of the the Loving Fault (Figure 3.4c).

Figure 3.4 Density inversion results of Tz gravity. **a)** Density inversion results of Tz gravity on the surface layer showing the observed, calculated gravity, and anomaly differences. **b)** Density inversion results of Tz gravity on the top Rustler Formation layer. **c)** Density inversion results of Tz gravity on the combined layer. The dotted line shows the possible location of an unmapped and unnamed fault.



Density inversion of gravity gradient (Tzz) anomalies

Layer densities derived from the gravity (Tz) inverse models were set as the initial densities for the gradient (Tzz) inverse models and the same workflow was then employed with the density inversions conducted individually on the upper two layers followed by a density inversion on the combined layers.

Tzz inversion results were successful with negligible differences between the calculated and observed Tzz of less than 10 Eo (or 0.001 mGal/m). Similar to the Tz density inversion, the combined layer inversion produced the best results with the the mean values and standard deviations for all FTG inversions summarized on Table 3.1. These results show small differences between the observed and calculated FTG (highlighted in green). I used Tzz inverted densities to calculate the remaining tensor components that I compared with the measured data (Table 3.1).

Table 3.1 Mean values and standard deviations for all Tzz inversions on the ground surface, top Rustler Formation of Late Ochoan age, and Combined sedimentary layers (ground surface to top Leonardian). The color codes of red, blue, and green correspond to bad, average, and good results with as defined by a 1 Eo difference (bad), 1- 0.5 Eo (average), and less than 0.5 Eo (good).

		Observed		Calculated		Difference	
Inverted layer	Component	Mean (Eo)	Std (Eo)	Mean (Eo)	Std (Eo)	Mean (Eo)	Std (Eo)
Surface	Tzz	1.631	8.124	-1.261	2.076	0.488	0.786
	Txz	-0.286	5.825	-2.923	1.388	1.477	0.362
	Tyz	-1.798	5.737	-1.600	1.658	1.073	0.290
	Txx	-0.413	5.150	0.552	1.035	-0.308	0.562
	Tyy	-1.218	5.077	0.709	1.482	-0.180	0.400
	Txy	-1.898	3.318	-0.825	0.634	0.224	0.217
Rustler	Tzz	1.631	8.124	-2.450	10.833	1.291	0.671
	Txz	-0.286	5.825	-1.342	6.638	1.536	0.574
	Tyz	-1.798	5.737	0.024	6.439	0.509	0.317
	Txx	-0.413	5.150	1.339	6.315	-0.950	0.555
	Tyy	-1.218	5.077	1.110	6.264	-0.341	0.394
	Txy	-1.898	3.318	-1.070	2.358	0.403	0.411
Combined	Tzz	1.631	8.124	-1.748	4.767	0.936	0.726
	Txz	-0.286	5.825	-1.830	2.933	0.661	0.398
	Tyz	-1.798	5.737	-0.702	3.167	0.734	1.151
	Txx	-0.413	5.150	0.934	2.611	-0.623	0.517
	Tyy	-1.218	5.077	0.814	3.006	-0.313	0.374
	Txy	-1.898	3.318	-0.955	1.221	0.267	0.251

Figure 3.5 shows the inversion results of tensor components with vertical elements (Tzz, Txz, Tyz). The calculated Tzz results produce relatively high-amplitude positive anomalies over the southwestern and northeastern study areas with differences ranging from -1.21 to 3.53 Eo. The Txz component enhances north-trending anomalies with a difference range of -7.96 to 2.72 Eo. Calculated Tyz enhances east-trending anomalies with difference ranges from -0.76 to 1.51 Eo.

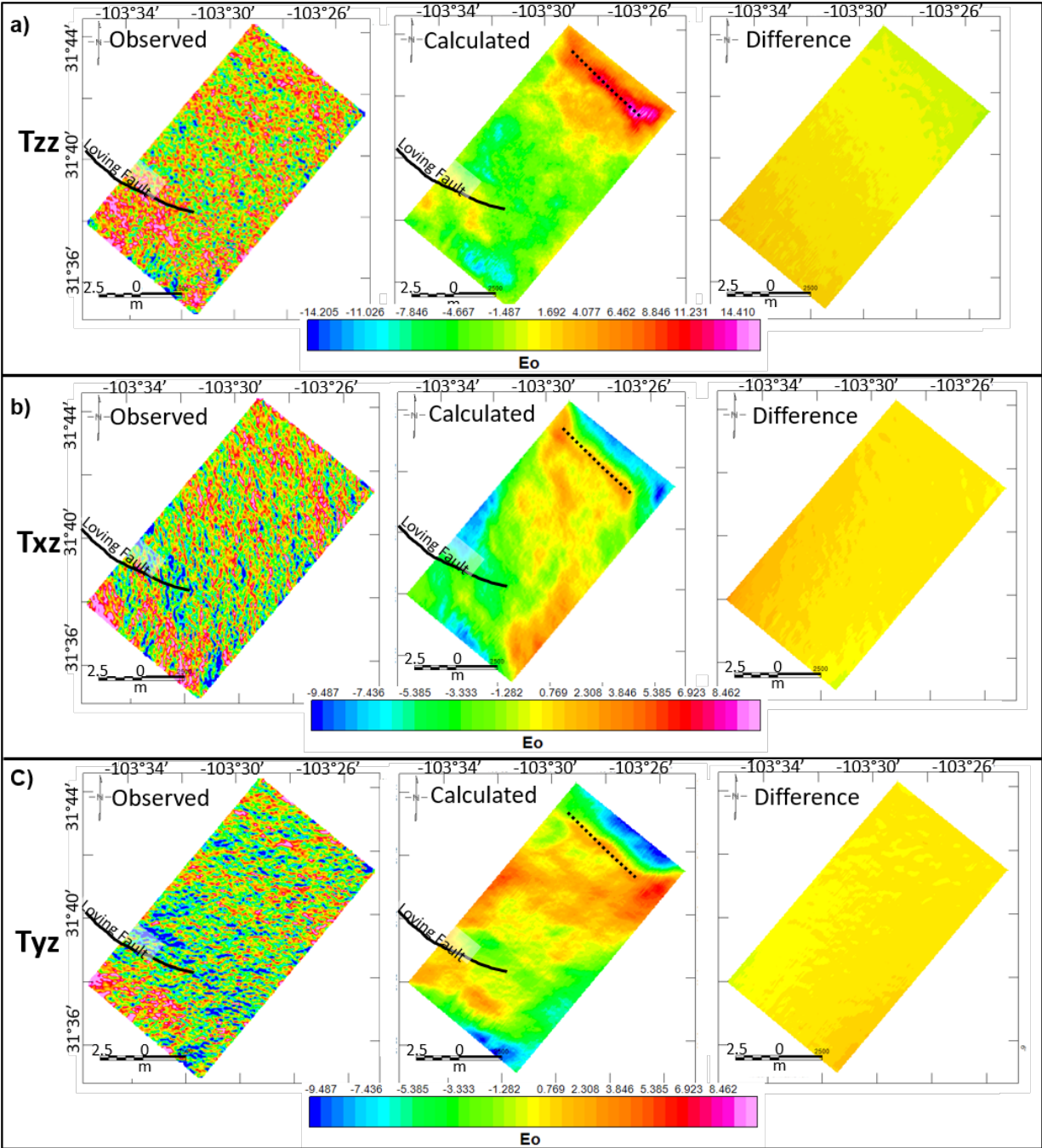


Figure 3.5 Inversion results of vertical components on the combined layer. **a)** Inversion results of Tzz on the combined layer. **b)** Inversion results of Txz on the combined layer. **c)** Inversion results of Tyz on the combined layer. The black line indicates the trace of the Loving Fault. The dotted line shows the possible location of an unmapped and unnamed fault.

Comparisons of calculated and observed tensors with horizontal elements (T_{xx} , T_{yy} , T_{xy}) are shown in Figure 3.6. Calculated T_{xx} gravity reveals subtle north-oriented anomalies superimposed on a broader north-trending anomaly over the center of the study area with a difference from the observed T_{xx} ranging from -2.16 to 0.36 Eo.

Similarly, calculated T_{yy} shows subtle east-trending anomalies superimposed on a broader east-trending anomaly over the southern two-thirds of the study area. This difference ranges from -1.49 to 1.08 Eo. Calculated T_{xy} shows a low-amplitude positive anomaly over the center of the study area that shows a difference that ranges from -0.61 to 1.23 Eo.

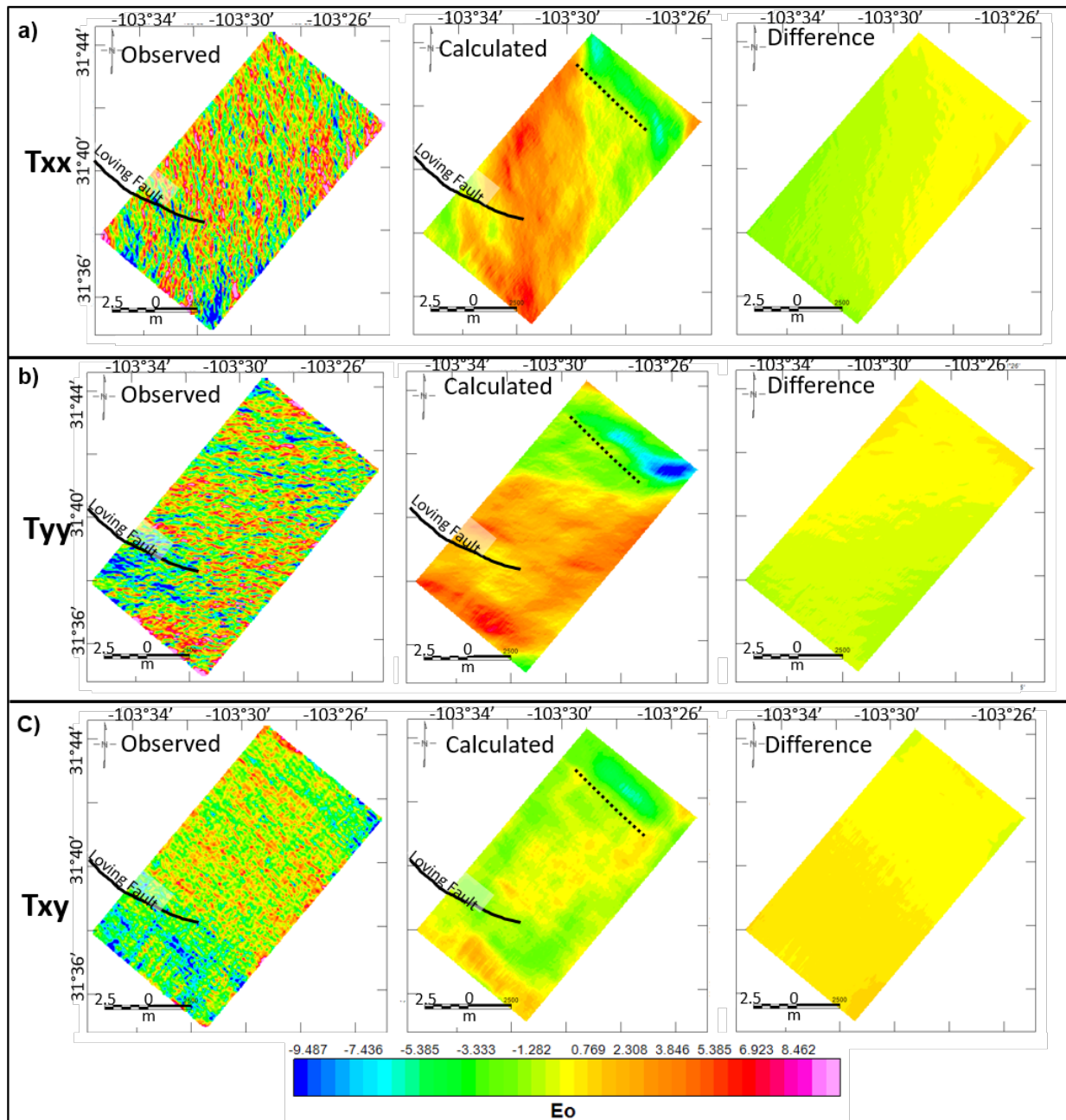


Figure 3.6 Inversion results of horizontal components on the combined layer. **a)** Inversion results of T_{xx} on the combined layer. **b)** Inversion results of T_{yy} on the combined layer. **c)** Inversion results of T_{xy} on the combined layer. The black line indicates the trace of the Loving Fault. The inferred, unnamed fault is shown as a dotted line along the northeastern edge of the study area and is not expressed on the horizontal element components.

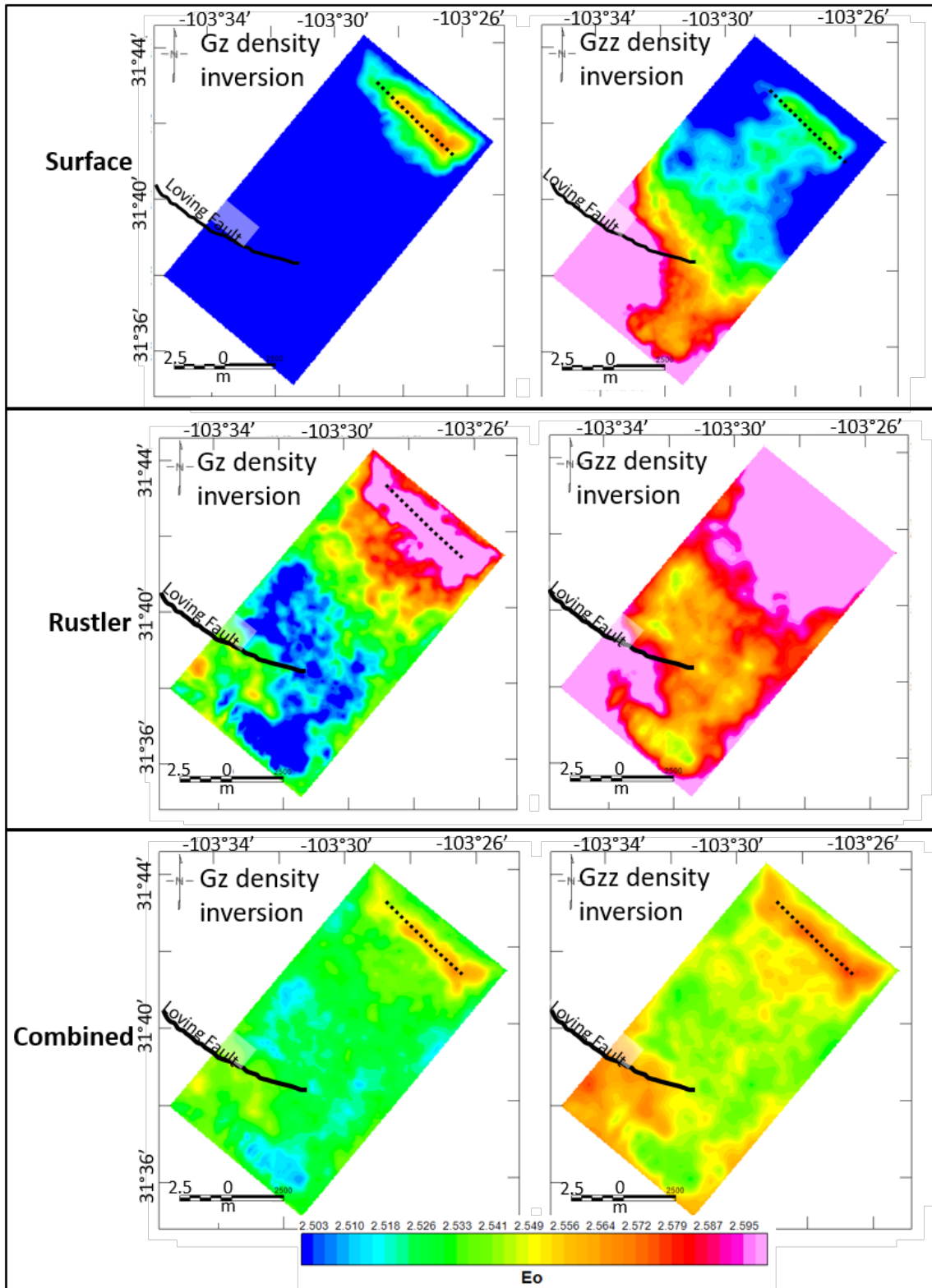
Density distributions

The density distribution generated by the Tz inversion ranges from 2.38 to 2.66 g/cc (Figure 3.7). The Tzz density inversions produce a similar density range of 2.42 to 2.74 g/cc (Figure 3.7).

Unsurprisingly, Tzz inverted densities display more detailed density variations than Tz. For example, all Tzz inversions of the topographic surface, the top Rustler Formation, and the combined layers produce higher densities that correlate with the Loving Fault, while only the Tz inversion of the combined layers is able to reveal a slight trend along the fault (Figure 3.2; Figure 3.7).

Density is more variable in the uppermost layer because it is more likely to be affected by data noise. Inversions on the Top Rustler and combined layer inversions produce the best Tzz results, with detailed density variations in the central and southern parts of the study area, where sharp density gradients are inferred as faults that offset density layers or possible karst boundaries (Figure 3.7). The northwest-striking density high along the northeastern edge of the area might represent an unmapped regional fault or another karst boundary (Figure 3.7).

Figure 3.7 Resultant density distribution from Tz and Tzz inversions : Surface, Rustler, and Combined sedimentary layers. The NW-SW trending Loving Fault is the black line. The dotted line shows the possible location of an unmapped fault.



Application to exploration: identifying karst features that can negatively impact drilling

I used Tzz inversion results of the combined layer as a guide to map possible locations of hypogenic karst features. Calculated Txz anomalies from the Tzz inversion reveal source edges oriented at high angles to the east-trending, computation direction (Figure 3.3b).

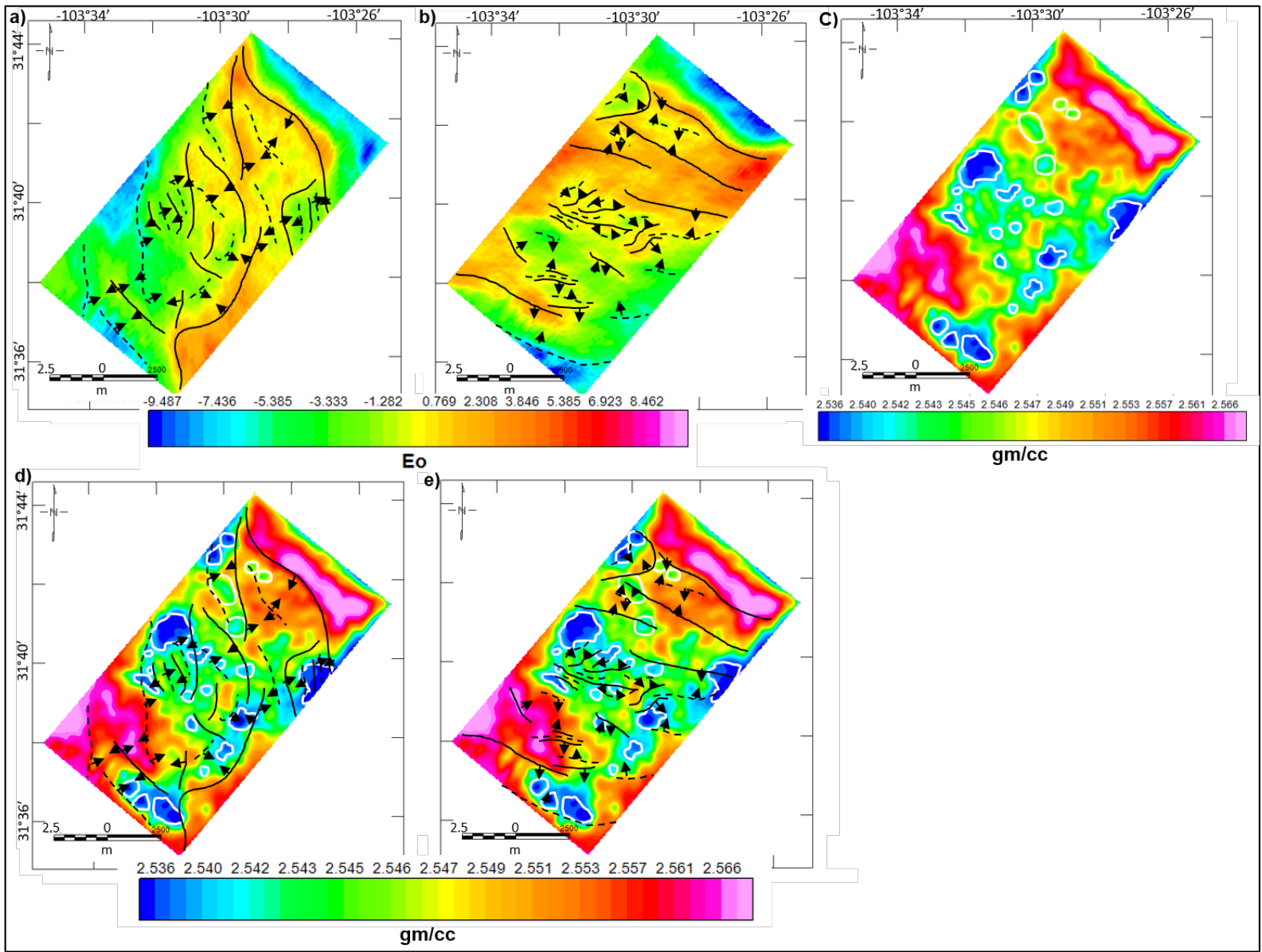
Following calculated anomalies from my model in Figure 3.3b, I drew black lines through positive anomalies related to the eastern edges of low-density source bodies. I also drew dashed black lines through negative anomalies related to western edges of low-density source bodies (Figure 3.3b, Figure 3.8a).

Similarly, calculated Tyz anomalies reveal source edges oriented at high angles to the south-to-north computation direction. So, as above, I drew black lines through positive anomalies related to northern edges of low-density source bodies and dashed black lines through negative anomalies related to southern edges of low-density source bodies (Figure 3.3b, Figure 3.8b).

I then combined these directional results with the Tzz density inversion to predict the locations of the most concentrated hypogenic karst locations (Figure 3.8c). The locations of low-density anomalies correlate well with the mapped source edges from the resulted Txz and Tyz (Figure 3.8d, e). These may be considered higher drilling risk locations because of the more dense concentration of karst features. Density inversion results from the northeastern study region show a slower density of karst features and therefore may be considered as lower-risk drilling targets.

Figure 3.8 Karst features identification. **a)** Calculated Txz anomalies from the Tzz density inversion on the combined layer. Black lines trace positive anomalies and suggest a low-density source body edge in the eastern area, while dashed black lines trace negative anomalies and a low-density source body edge in the west. Arrows point towards low-density source bodies. **b)**

Calculated T_{yz} from T_{zz} inversion on the combined layer. Black lines trace positive anomalies and suggest a northern low-density source body edge, while dashed black lines trace negative anomalies and suggest a southern low-density source body edge. **c)** Inverted densities from T_{zz} density inversion on the combined layer. Lower densities are outlined in white, correlating with the edges mapped in a) and b). **d)** Inverted densities with low-density outlines and mapped source edges from a). **d)** Inverted densities with low-density outlines and mapped source edges from b).



Conclusions

I present innovative interpretation techniques for working with FTG gravity data. Terrain-corrected FTG data is useful for detailed source body interpretation by capturing subtle density variations. The focused survey size and ultra-short acquisition line spacings provided me an excellent opportunity to examine the area for subtle density variations in the near-surface sedimentary section.

Three-dimensional Tzz density inversion results provide a more detailed density distribution than Tz density inversion results. Structurally, the Tzz density inversion produced steep gradients which I have interpreted as faults because of the large density offsets. I infer that low-density source body edges indicate possible locations of hypogenic karst features that are outlined from Txz and Txy calculated anomalies and correlated with low-layer density areas. I conclude that the central and southwestern parts of the study area are at higher risks for drilling due to a more dense concentration of karst features while the northeastern part of the study area is at lower risk because of a lower density of karst features.

Bibliography

- Blakely, R. J., 1995. Potential theory in gravity and magnetic applications. Cambridge University Press.
- Bott, M.H.P., 2012. Inverse methods in the interpretation of magnetic and gravity anomalies. *Methods in computational physics*, 13, 133-162.
- Cordell, L. and Henderson, R.G., 1968. Iterative three-dimensional solution of gravity anomaly data using a digital computer. *Geophysics*, 33(4), 596-601.
- Dutton, S.P., Kim, E.M., Broadhead, R.F., Breton, C.L., Raatz, W.D., Ruppel, S.C. and Kerans, C., 2004. Play analysis and digital portfolio of major oil reservoirs in the Permian Basin: Application and transfer of advanced geological and engineering technologies for incremental production opportunities, 1-428. <https://www.osti.gov/servlets/purl/828411>, accessed Jan 15, 2019.
- Dutton, S.P, Kim, E.M., Broadhead, R.F., Raatz, W.D., Breton, C.L., Ruppel, S.C, and Kerans, C., 2005. Play analysis and leading-edge oil-reservoir development methods in the Permian Basin: Increased recovery through advanced technologies. *AAPG Bulletin*, 89(5), 553–576.
- Ewing, T.E., Barnes, M.A., and Denison, R.E., 2019. Proterozoic Foundations of the Permian Basin, West Texas and Southeastern New Mexico — a review. *In* Ruppel, S. C., ed., 2019, *Anatomy of the Paleozoic basin: the Permian Basin, USA (vol.1, ch. 3)*. The University of Texas at Austin, Bureau of Economic Geology Report of Investigations 285. AAPG Memoir, 118, 63-96.

- Garcia, E. S., Sandwell, D. T., and Smith, W. H., 2014. Retracking CryoSat-2, Envisat and Jason-1 radar altimetry waveforms for improved gravity field recovery. *Geophysical Journal International*, 196, 1402–1422.
- Li, X. and Chouteau, M., 1998. Three-dimensional gravity modeling in all space. *Surveys in Geophysics*, 19(4), 339-368.
- Majzoub, A.F., Stafford, K.W., Brown, W.A. and Ehrhart, J.T., 2017. Characterization and delineation of gypsum karst geohazards using 2D electrical resistivity tomography in Culberson County, Texas, USA. *Journal of Environmental and Engineering Geophysics*, 22(4), 411-420.
- Martinez, C., Li, Y., Krahenbuhl, R. and Braga, M.A., 2013. 3D inversion of airborne gravity gradiometry data in mineral exploration: A case study in the Quadrilátero Ferrífero, Brazil. *Geophysics*, 78(1), 1-11.
- Mataragio, J. and Kieley, J., 2009. Application of full tensor gradient invariants in detection of intrusion-hosted sulfide mineralization: Implications for deposition mechanisms. *First Break*, 27(7), 1-4.
- Morgan, R.A., Jorgensen, G., Payton, S., and Stafford, K.W., 2018. Detection and Avoidance of karst related shallow geohazards using ultra high resolution full tensor gravity gradiometry in the Delaware Basin, Texas. AAPG ACE abstract.
- Murphy, C.A. and Mumaw, G.R., 2004. 3D Full Tensor Gradiometry: a high resolution gravity measuring instrument resolving ambiguous geological interpretations. *ASEG Extended Abstracts*, 1, 1-4.
- Parker, R.L., 1973. The rapid calculation of potential anomalies. *Geophysical Journal International*, 31(4), 447-455.

- Ruppel, S.C, R. Loucks, C. Kerans, R. H. Jones, H. S. Nance, C. L. Breton, S. Hamlin, J. Gale, J. Kane, A. McDonnell, E. Guevara, F. Wang, R. Reed, W. Wright, H. Rowe, N. Guven, R. Day-Stirrat, D. Jarvie, H. Zeng, and Q. Fu, 2008. Permian Basin synthesis project: data and models for recovering existing and undiscovered oil resources from the largest oil-bearing basin in the US GIS dataset, <http://www.beg.utexas.edu/research/areas/permian-basin-synthesis>, accessed Oct 19, 2018.
- Scholle, P.A., Goldstein, R.H. and Ulmer-Scholle, D.S., 2004. Classic upper Paleozoic reefs and bioherms of west Texas and New Mexico. New Mexico Institute of Mining and Technology, Socorro, NM, 1-178.
- Stafford, K.W., 2017. Hypogene evaporite karst of the greater Delaware Basin. In LaMoreaux, J. W., ed., *Hypogene Karst Regions and Caves of the World (ch. 3)*, Springer, 531-542.
- Stafford, K.W., Ehrhart, J.T., Majzoub, A.F., Shields, J.M. and Brown, W.A., 2018. Unconfined hypogene evaporite karst: West Texas and southeastern New Mexico, USA. *International Journal of Speleology*, 47(3), 1-13.
- Telford, W. M., L. P. Geldart, and R. Sheriff, 1990. Applied geophysics. Cambridge University Press.
- Zhang, H., Mann, P., Bird, D.E., and Rudolph, K., 2021. Integration of regional gravity modeling, subsidence analysis, and source rock maturity data to understand the tectonic and hydrocarbon evolution of the Permian Basin, West Texas. *Interpretation*, 9(1), 161-181.

CHAPTER 4 : CONTROL OF PRECAMBRIAN OROGENIC TRENDS ON THE WIDTH AND STRUCTURAL ZONATION OF THE CRETACEOUS, CONJUGATE RIFTED MARGINS OF NORTHEASTERN BRAZIL AND NORTHERN GABON

Introduction

Tectonic mechanisms for wide versus narrow rifted conjugate margins

Davison (1997) first described wide and narrow rifted margins from the conjugate margins of the South Atlantic Ocean as two contrasting end-members of rifted passive margins. “Wide margins” of the South Atlantic - which can be up to 600 km wide - represent extension and smooth necking of the lithosphere from an original thickness of 30-35 km to a thinned continental crust down in the range of 10-15 km. In contrast, “narrow margins” are less than 100 km in width, exhibit much steeper and abruptly thinned continental crust, and are commonly found in two tectonic settings: fracture zone intersections with continental margins and orthogonally-rifted zones. Wide margins tend to exhibit broad, gently dipping continental shelves with deeply buried rifts with source rocks mature at depths of 2-3 km, whereas narrow margins tend to have rifts exposed onland with source rocks mature at shallow depths (1-2 km) and post-rift histories of uplift and inversion.

Davison (1997) proposed five possible tectonic and lithospheric mechanisms to explain the tectonic origin and distribution of wide vs. narrow margins: 1) **opening direction relative to the trend of the margin**: transform and fracture zone margins juxtapose oceanic and continental crust in an abrupt manner with minimal extension of the continental crust and generally result in steep and narrow margins; transtensional margins as those of the Equatorial Atlantic in northern Brazil also form narrow margins; 2) **strain rate**: Bassi et al. (1993) used numerical modeling to

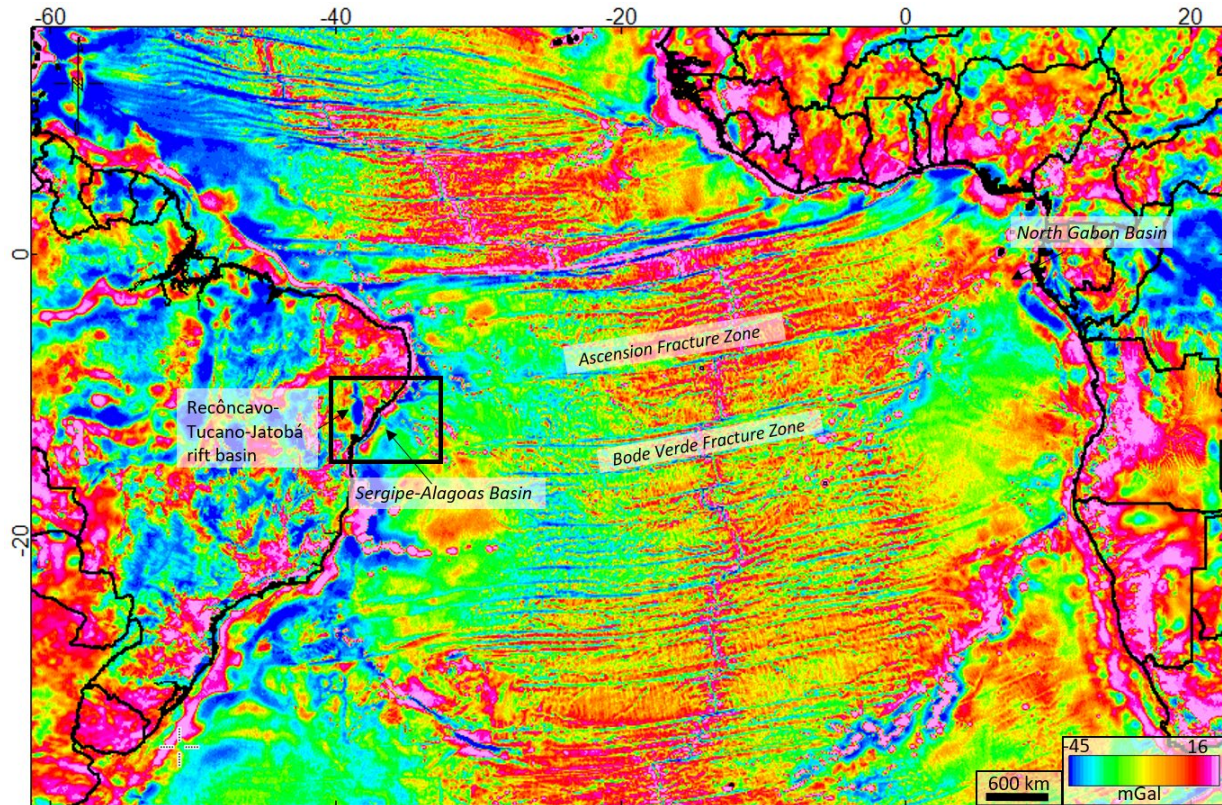
propose that fast strain rates favor narrow rift zones while slower strain rates lead to strain hardening with an outward widening of the rifted area to produce a wider rift zones; 3) **lithospheric temperature:** Buck (1991) proposed that initially hot crust will flow more easily to produce wider rifts; 4) **pre-existing crustal weaknesses:** Dunbar and Sawyer (1989a,b) proposed rifts that form parallel to pre-existing crustal fabric are narrow as that crust breaks more readily, while crustal fabrics that are perpendicular to the rifting direction produce wider rifts as that crust is stronger and requires more strain to rupture; more recent studies that have supported this view using a variety of observations and modeling include Jammes et al. (2010) and Reuber and Mann, (2019); and 5) **crustal thickness:** Buck (1991) and Buck et al. (1999) noted that greater crustal thicknesses (>50 km) in areas of higher than normal heat flow favored the formation of narrow margins whereas crustal thicknesses <50 km show no apparent thickness control of width of margins.

Objectives and tectonic significance of this chapter

In this chapter, I examined the crustal and tectonic controls on the relatively narrow (90 km) Sergipe-Alagoas margin in northeastern Brazil in comparison to its relatively wider conjugate margin (150 km) in northern Gabon (Figure 4.1). In this chapter, my main focus is to make new interpretations using deeply-penetrating industry 2D seismic lines acquired by ION and PGS in 2009 and integrated with 2D and 3D gravity models to define three domains of the rifted, continental crust that underlie the on- and offshore Sergipe-Alagoas basin. I compare my results with previous results by Mohriak et al. (1995, 1998, 2008) and Blaich et al. (2008), who used vintage and less penetrative seismic reflection data acquired in the period from 1984 to 1989 and recorded to depths of 10 seconds TWT.

To examine the five hypotheses of Davison (1997) for the origin of a narrow margins including my study area of the Sergipe-Alagoas margin, I incorporated the most recent geologic mapping of the Precambrian crustal fabrics of the onland area that includes the failed, Recôncavo-Tucano-Jatobá rift located 125 km west of the rifted Atlantic margin of Brazil (Gómez et al., 2019; Figure 4.1). I also integrated all of the seismic refraction results from the Sergipe-Alagoas area, including the onshore area and its failed rift, in my gravity modeling (Knize et al., 1984; Mohriak et al., 1995; Ferreira et al., 1998; Lopes et al., 2010; Pinheiro et al., 2018). These newer refraction data post-date the refraction data used for earlier studies by Mohriak et al. (1995, 1998, 2008) and Blaich et al. (2008) for the Sergipe-Alagoas margin and allow improvement in mapping the continent-ocean boundary and the geometry of the necked zone between the continent-ocean boundary (COB) and the full-thickness crust of the South American craton.

Figure 4.1 Free-air gravity map from Sandwell et al. (2014) of the Equatorial and South Atlantic Oceans showing the conjugate, rifted-passive margins of the Sergipe-Alagoas Basin in northeastern Brazil and the North Gabon Basin in west-central Africa. The major fracture zones that are shared by the conjugate margins include the Ascension Fracture Zone and the Bo de Verde Fracture Zone. These continuous fracture zones track the paths of oceanic opening following the continental rifting of the two margins. The box in northeastern Brazil indicates my study area of the Sergipe-Alagoas rifted-passive margin that forms the focus of this chapter.



Tectonic, geologic, and hydrocarbon setting of Late Jurassic-Albian rifts related to the opening of the South Atlantic Ocean

Tectonic evolution of South Atlantic opening. The South Atlantic rift system developed during the Mesozoic breakup of the late Palaeozoic Gondwana supercontinent with rifting started in the far South Atlantic and propagated northwards during the early Cretaceous (Aslanian et al., 2009). Full-fit, pre-Cretaceous late reconstructions have been improved due to the improved mapping of precise points in Paleozoic and Precambrian orogenic belts on both the South American and African conjugate margins (e.g., Beglinger et al., 2012; Matos et al., 2021; Moulin et al., 2021).

Most workers agree that the timing of initial South Atlantic rifting began in the Late Jurassic-Early Cretaceous in the far south Atlantic and reached the Equatorial Atlantic by Late Albian. Lithospheric stretching and highly-oblique rifting in the Equatorial Atlantic of northeastern Brazil culminated in the onset of seafloor spreading, which occurred around during Late Aptian to Early Albian times (118-112 Ma) and produced long, transform faults in the Equatorial rift zone (Chang et al., 1992; Moulin et al., 2005, 2010; Mohriak et al., 2008; Torsvik et al., 2009). The constant magnetic polarity period from Early Aptian to Campanian times (110-100 Ma) prevented recognizable seafloor spreading magnetic anomalies. As a result, the reconstruction of plate motion during the early drift stage and the precise COB location has remained poorly resolved on the basis of magnetic data (e.g., Chang et al., 1992; Karner and Driscoll, 1999). For this reason, studies of crustal structure as the one described in this chapter can be useful for more precise mapping of the COB.

Most previous workers recognized the importance of rift-related, Neocomian-Albian (135-104 Ma) magmatism in the formation of the rifted margin. In the south from southern Brazil to Argentina, volcanic margins are characterized by 4-20-km-thick, syn- to post-rifting volcanic flows of Albian to age (112-104 Ma) known as “seaward-dipping reflectors” (e.g., Reuber et al., 2016; Zinecker, 2020; Matos et al., 2021), whereas from central Brazil to the Equatorial Atlantic, syn-rift magmatism is less common and related to hotspot activities during the passive margin phase that ranges in age from Albian to recent (100-0 Ma).

Wide versus narrow margins resulting from the Cretaceous rifting period. The south-to-north opening of the South Atlantic created two differently-oriented, rifted-passive margins along the Brazilian margin: the more east-west oriented, Equatorial rifts of the Equatorial Atlantic in northern Brazil and the more north- to northeast-oriented East Brazil rift

system (EBRIS) (Matos, 2000; Figure 4.1). The North Brazilian Equatorial margin evolved in response to a broad transform separating South America and Africa and resulted in complex, shear-dominated basins that include the Barreirinhas, Ceara, and Potiguar basins that generally form steep and narrow margins (Davison, 1997).

In contrast, most of the East Brazilian margin - that includes from south to north the Pelotas, Santos, Campos, Espírito Santo, Mucuri, Cumuruxatiba, Jequitinhonha, Camamu-Almada, Jacuípe, and Sergipe-Alagoas rifted-passive margin basins - evolved into a passive margin as a consequence of orthogonal crustal extension (Chang et al., 1992) and therefore tends to form wide margins.

The study area of this chapter focused on the onshore Recôncavo-Tucano-Jatobá (RTJ), and the offshore Jacuípe and Alagoas-Sergipe basins, which are located in the northeastern part of the EBRIS between the Ascension Fracture Zone to the north and the Bo de Verde Fracture Zone to the south (Figure 4.1). The oblique opening of the South Atlantic Ocean separated the Sergipe–Alagoas Basin from its conjugate margin, the North Gabon Basin of west Africa (Figure 4.1).

Previous studies of the crustal structure of the onland and offshore Sergipe-Alagoas Basin

The onshore RTJ and the offshore Jacuípe and Alagoas-Sergipe basins are located in the northeastern part of the EBRIS between the Ascension Fracture Zone to the north and the Bo de Verde Fracture Zone to the south (Figure 4.1). An earlier study of the deep structure of the Sergipe-Alagoas basin by Mohriak et al. (1995) interpreted its crustal structure based on deep-penetration seismic reflection transects across the northern area of the Sergipe-Alagoas Basin and the southern area of the Sergipe sub-basin. These authors also used their interpretation of the

seismic reflection transects to constrain a regional 2D gravity model across the southern Sergipe sub-basin. In a later study, Mohriak et al. (1998) refined the 2D gravity model of the Sergipe-Alagoas basin at the same locations described in Mohriak et al. (1995) that was based on a more detailed interpretation of the same two seismic lines that they had previously interpreted in this 1995 paper.

Blaich et al. (2008) extended the 2D gravity model of the southern Sergipe sub-basin further offshore using the same seismic profile previously used by Mohriak et al. (1998) and proposed a very rapid crustal thinning and possible mantle underplating at the Sergipe Basin. But since the seismic line they used was vintage and did not extend further enough offshore, the presence of mantle exhumation remained speculative.

A more recent study by Caixeta et al. (2014) generated a regional 2D gravity model for the northern Sergipe-Alagoas Basin. Their gravity model, along with age dating of Albian-Cenomanian volcanics interbedded with marine rift sediments in this region, supported a hyper-extended margin that coincides with the transition zone of continental crust as described by Péron-Pinvidic et al. (2015) from other Atlantic rifted margins. In this chapter, I provide a more complete crustal structural framework and a high-resolution crustal thickness model for the Sergipe-Alagoas Basin.

Hydrocarbons of the Brazilian margin

The Sergipe–Alagoas Basin, is the sixth largest, hydrocarbon-producing basin of the eastern Brazilian rifted margin (Azambuja Filho, 1998). The northeastern Brazilian margin and its conjugate West African margin have been the intense focus of extensive hydrocarbon exploration since the early 2000s. Fundamental to understanding the hydrocarbon resources of

the Sergip-Alagoas Basin is understanding its crustal-scale evolution, its heat flow history, the architecture of onshore and offshore basins, and the precise location of its COB, especially in the framework of other studies of the Atlantic rifted margins (Davison and Underhill, 2021; Péron-Pinvidic et al., 2015).

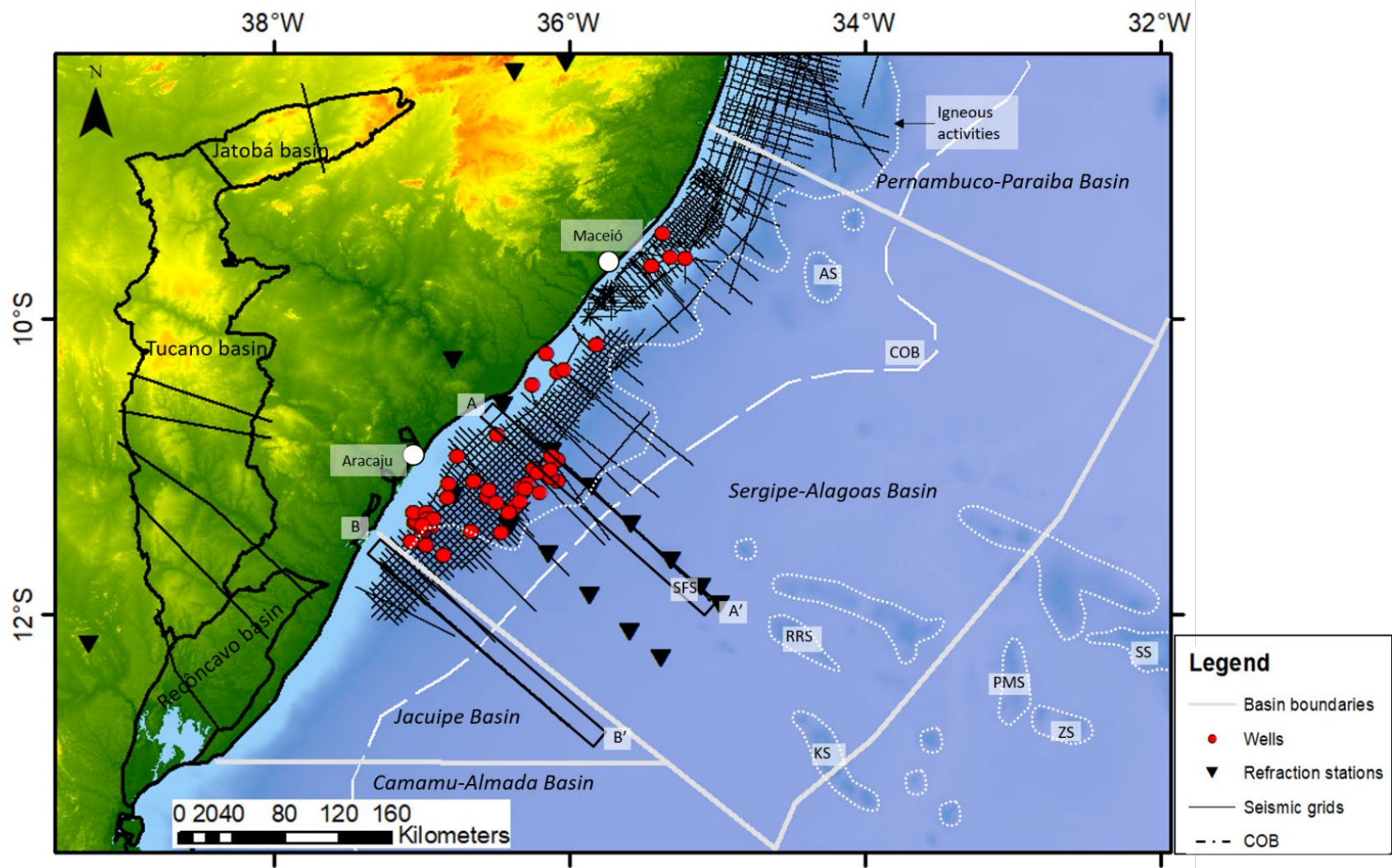
Dataset and methods used in this chapter

Seismic reflection, seismic refraction, and well data. Both open file and proprietary data are used for making interpretations in this chapter. Proprietary sources include seismic reflection and well data kindly provided by ION and PGS in Houston and ANP in Brazil under agreements with Dr. Mann, myself, and the CBTH project at the University of Houston that provided the guidelines for using these data in this dissertation and for related publications.

Seismic reflection data include: 1) two, 2D, deeply-penetrating, 188-200-km-long, depth-converted seismic reflection lines from ION that were acquired in 2009 and recorded to a depth of 40 km; 2) 2D seismic reflection survey in two-way time with 14,223 line-kms of 2D seismic profiles extracted from the Brazil 2D Megasurvey provided by PGS, acquired in 2009. and recorded to a depth of 12s TWT, and 3) 2D seismic reflection survey in two-way time provided by ANP, acquired in 1980-2006, and recorded to a depth of 8s TWT (Figure 4.2).

Well data include 51 ANP well logs with lithologies, gamma, resistivity, neutron density, and checkshots. Open-source data include published regional seismic cross-sections (Milani and Davison, 1988; Blaich, 2008; Gordon et al., 2017). This chapter also makes use of a compilation of seismic refraction stations (Knize et al., 1984; Mohriak et al., 1995; Ferreira et al., 1998; Lopes et al., 2010; Pinheiro et al., 2018).

Figure 4.2 Topographic and bathymetric map of the Sergipe-Alagoas rifted-passive margin showing the locations of the dataset used in this chapter that in the offshore area includes two deep-penetration ION Span lines marked A-A' and B-B', grids of 393 line kms of 2D seismic reflection data, well logs (red dots), and refraction stations from previous workers (inverted black triangles). In the onland area, data used include 2D seismic lines and refraction stations. In the offshore area, tectonic features include offshore basin boundaries (straight, white lines), Cretaceous seamounts volcanic plateaus (outlined by white dots with abbreviations for their names provided), and the continent-ocean boundary (COB – outlined by the dashed white line). **Abbreviations for Cretaceous (117-94 Ma) seamounts on oceanic crust:** **AS** = Alagoas seamount; **KS** = Klenova Seamount; **PMS** = Paulo Moreira Seamount; **RRS** = Romano Russo Seamount; **SAS** = São Francisco Seamount; **SS** = Stocks Seamount; **ZS** = Zembruscki Seamount.



Gravity and magnetic data used in this chapter. The gravity data used in this chapter are a grid of five-arc-minute, satellite-derived marine free-air gravity anomalies kindly provided for public access by Scripps Institution of Oceanography (Sandwell et al., 2014). This marine grid was merged with a grid of five-arc-minute, geoid-derived, land, free-air gravity anomalies (Pavlis et al., 2012; EGM2008; Figure 4.3a).

The magnetic data used in this chapter is the EMAG2 (version 3) magnetic anomaly grid from the National Oceanic and Atmospheric Administration (NOAA) with a spatial resolution of 2 arc minutes (Meyer et al., 2017; Figure 4.3b).

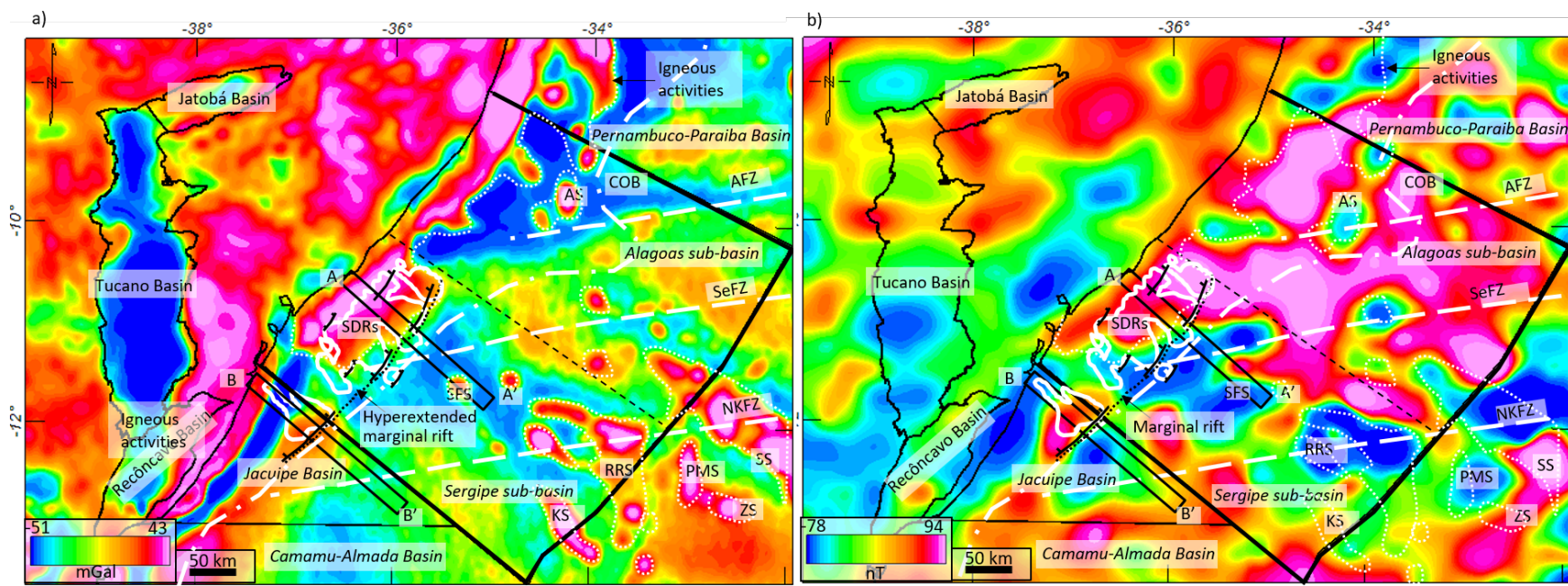


Figure 4.3 Gravity anomalies in the study region. **a)** Free-air gravity anomalies showing major tectonic features of the study area from Sandwell et al., 2014); **fracture zones** in the oceanic crust are white, dashed lines and include: AFZ = Ascension Fracture Zone; SeFZ = Sergipe Fracture Zone; NKFZ = N’Komi Fracture Zone; **continent-ocean boundary (COB)** separating thinned continental crust from the oceanic crust is white, dashed-dotted line; **seaward-dipping reflectors (SDRs)** are outlined in solid white lines; **large, normal faults bounding half-grabens** in thinned, continental crust are shown as black lines; seamounts and magmatic plateaus on the oceanic crust are highlighted with white dots with their names identified in the caption of Figure 4.2. **b)** Total magnetic anomalies showing major tectonic features of the study area from (Pavlis et al., 2012; EGM2008) using the same symbols and abbreviations as on the gravity map in a).

2D and 3D gravity modeling done in this chapter. Both 2D and 3D gravity modeling were conducted using the Geosoft OASIS Montaj modeling software purchased by Dr. Mann as an educational license for the CBTH group. The 2D gravity models were based on interpretations of two, deeply-penetrating seismic reflection lines that were part of the larger, ION Greater BrasilSPAN 2D seismic survey acquired in 2009. These two lines were provided to me by ION in an agreement between CBTH and ION. The initial 3D gravity model consisted of five layers separated by four horizons that included: 1) stations, 2) topography, 3) top upper crust, and 4) isostatic Moho.

The stations horizon is equivalent to the topography for land areas and is equivalent to sea level for the marine parts of the study area. The topographic horizon was created by merging the Gtopo30 land grid (Gesch and Greenlee, 1999) with the offshore area of the Terrain-Base grid (Row and Dunbar, 1995). This horizon was merged with the seafloor bathymetry as I interpreted it to from the merged seismic reflection grids.

The top upper crust horizon was created by subtracting the sediment thickness grid from the topographic grid. The sediment thickness grid merged data from the Total Sediment Thickness of the World's Oceans and Marginal Seas (Whittaker et al., 2013; Divins, 2003) with data from a Global Sediment Thickness (Laske and Masters, 1997). The resulting grid was then merged with top of basement interpretations from seismic offshore and published, offshore cross-sections (Milani and Davison, 1988; Blaich, 2008; Gordon et al., 2017) to improve the resolution of the gravity model. The initial Moho grid was derived from an isostatic calculation (Blakely, 1995).

$$dm = h (\rho_t/\Delta\rho) + ds$$

In this equation, all depths are in km; d_m and d_s are the Moho depth with the compensation depth (33 km) at the shoreline; h is elevation; ρ_t is the average crustal density; and $\Delta\rho$ is the density contrast at the base of the crust.

The density of water, crystalline crust, and upper mantle used in the model were 1.03, 2.85, and 3.3 g/cc, respectively. Sedimentary rock densities were gridded as a function of the thickness of the entire section by integrating each grid node over an exponential decay function that simulates clastic compaction of sedimentary rocks (Cordell, 1973; Chakravarthi et al. 2013). Moho structural inversion in the 3D gravity model was performed using a method described by Parker (1973), which established a Fourier transform technique for calculating potential field anomalies produced by uneven layers. The convergence limit of the inversion was set to 3 mGal, and after five iterations, the algorithm converged, which is an excellent test result.

Results of this chapter from structural interpretations of 2D, deeply-penetrating, seismic reflection lines

Interpretation of ION deep-penetration seismic transect A-A'. Seismic profile A-A' is a 198-km-long, northwest-trending ION deep penetration, depth-converted, seismic reflection line that was recorded to a depth of 40 km across the central Sergipe sub-basin (Figure 4.2). Syn-rift sedimentary rocks of inferred Neocomian age and seaward dipping reflectors (SDRs) of the same inferred age fill the pre-rift grabens on the northwestern side of the profile. Sedimentary packages of Aptian to Recent age within this region are up to 9 km thick (Figure 4.4).

Profile A-A' traverses the São Francisco seamount that has been radiometrically dated by Wessel (2001) as Aptian (114 Ma) with sedimentary layers of Albian to Recent age (110-0 Ma)

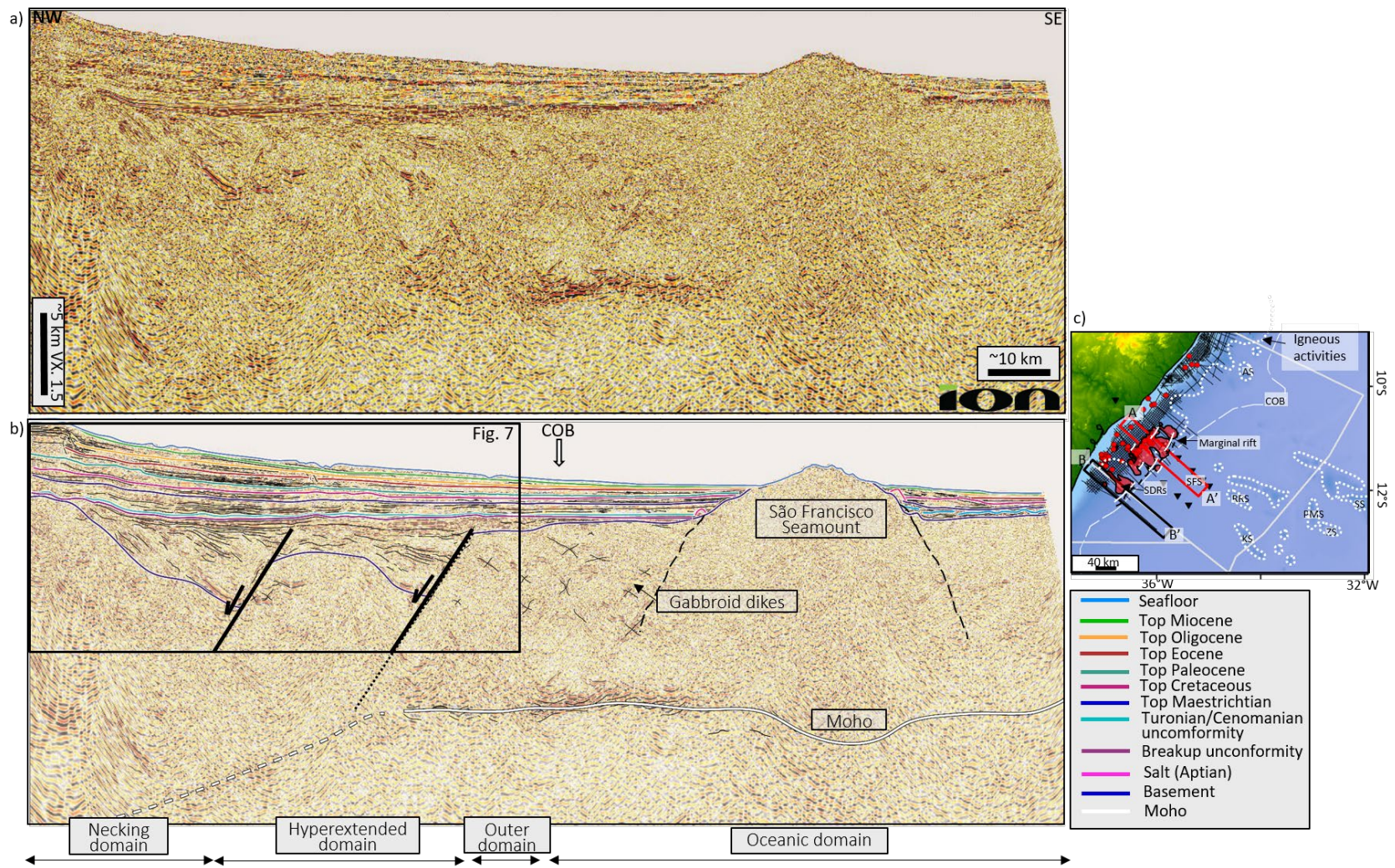
onlapping the western edge of the seamount (Figure 4.4). A Moho reflector at a depth of 22 km is interpreted along with two, small Aptian salt bodies that are observed along the eastern and western sides of the seamount.

Based on the geometry of the top basement and Moho reflectors, the nature of the crust, and its relation to the overlying sedimentary rocks, I define four rift domains and associated domain boundaries based on the terminology proposed by Péron-Pinvidic et al. (2015) for rifted, continental crust in other areas of the circum-Atlantic Ocean:

- 1) The **necking domain** is the region where the top of the basement and Moho reflector begin to converge, and the continental crust thins to 11-19 km in thickness (Figure 4.4b). The Moho reflector is not well expressed within the necking domain that is characterized by a marked basinward increase in total accommodation space (Sutra and Manatschal 2012) as shown by the syn-rift graben bounded by landward (NE)-dipping and planar normal fault (Figure 4.4b).
- 2) The **hyperextended domain** shows a rapid crustal thinning of the continental crust to a 6-10 km thickness range. Weak Moho reflectors are observed in the hyperextended domain and become sub-parallel to the top of the basement reflector near the margin of the hyperextended domain (Figure 4.4b).
- 3) The **outer domain** is a 9-km-wide transition zone adjacent to the oceanic domain (Figure 4b). High-amplitude reflectors exhibit variable dip directions that vary from landward-dipping to near-horizontal and to seaward-dipping in the outer domain. These high-amplitude reflectors are interpreted as the intra-gabbroic dikes based on similar reflectors known from areas of drilled, rifted margins (Ranero et al., 1997; Bécel et al., 2015; Norcliffe et al., 2018).

4) The **oceanic domain** is characterized by parallel-sided, top basement and Moho reflections and the presence of gabbroid dikes marked by large X-shapes based on their similarity to better-studied examples imaged in oceanic crust worldwide (Ranero et al., 1997; Reston et al., 1999; Bécel et al., 2015; Norcliffe et al., 2018; Figure 4.4b). The Moho reflector is prominent at a depth of 17 km beneath the oceanic domain except in the area of the seamounts. The average crustal thickness of the oceanic domain is 9-11 km which is slightly thicker than the standard oceanic crust of 6-8 km and is considered an intermediate thickness oceanic crust by Péron-Pinvidic et al. (2015). I attribute the slightly thicker oceanic crust to the nearby seamount, which may have produced an underplating effect in the surrounding region of oceanic crust.

Figure 4.4 Deep-penetration, depth-converted ION Span seismic reflection line A-A' through the central Sergipe sub-basin. **a)** Uninterpreted seismic reflection line A-A' recorded to a depth of 2.6km. **b)** Seismic line A-A' with the interpretation of crustal domains defined in other areas by Péron-Pinvidic et al. (2015) with age picks of overlying sedimentary horizons based on mapping of the seismic grid shown in Figure 4.2 and described in detail Chapter 5. **c)** Basemap showing the location of ION line A-A' depicted as the red rectangle and the COB is shown dashed white line. The area of hyperextended continental crust with marginal rifts in the Sergipe subbasin is shown by the white lines with tick marks on the downthrown side of the normal faults. SDRs are shown as the light red polygon and are confined in the marginal rift zone. Seamounts and magmatic plateaus on the oceanic crust are highlighted with white dots with their names identified in the caption of Figure 4.2.



Interpretation of ION deep-penetration seismic transect B-B'. Seismic profile B-B' is a 184-km-long, northwest-trending ION, depth-converted, deep-penetration seismic reflection line that spans the southwestern edge of the Sergipe sub-basin and the northeastern edge of the Jacuipe basin (Figure 4.2). The Moho reflector on line B-B' is generally more prominent than the Moho observed on seismic profile B-B' (Figure 4.5). Sediment packages observed on Line B-B' are up to 4.5 km thick, and a 68-km-wide. A 6-km-thick section of SDRs fills the half-graben rift on the northwestern side of the profile.

As done for seismic profile B-B', I use the terminology of Péron-Pinvidic et al. (2015) to define four rift domains and their boundaries based on the geometry of the top basement and Moho and the nature of the crust and its relation to the overlying sediments:

- 1) The **necking domain** forms a more narrow zone than observed on seismic profile B-B' and is marked by the convergence of the top of the basement and the Moho reflector (Figure 4.5). In the necking domain, the crustal thickness ranges 11-21 km. The Moho reflector is not prominent within the necking domain, and the necking domain includes a syn-rift half-graben that is bounded by a listric normal fault dipping to the northwest and indicating accommodation space in the basinward direction.
- 2) The **hyperextended domain** shows a more rapid crustal thinning than observed on seismic profile B-B'. The continental crust has been extremely thinned to a thickness range of 10-2.5 km. A strong Moho reflector is observed in the hyperextended domain and is sub-parallel to the top of the basement reflector. The SDRs are onlapping onto the normal fault (Figure 4.5).
- 3) The **outer domain** forms an 11.5-km-wide transition zone west of the COB marked by the presence of X-shaped, high-amplitude reflectors, which are interpreted as intra-

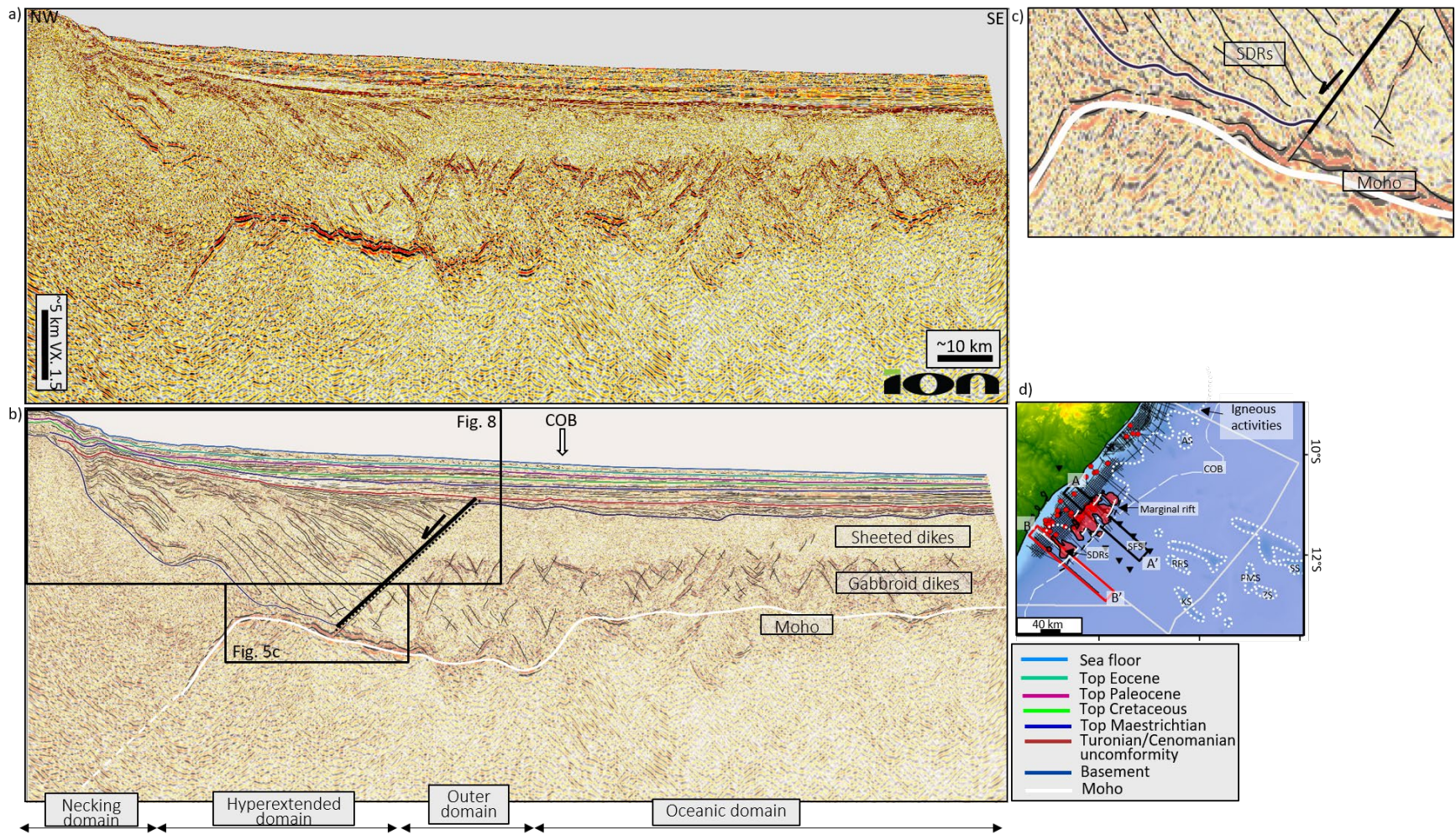
gabbroic dikes based on their similarity to better-studied examples imaged and drilled in oceanic crust in other areas (Ranero et al., 1997; Reston et al., 1999; Bécel et al., 2015; Norcliffe et al., 2018).

- 4) The **oceanic domain** is characterized by parallel-sided, top basement and Moho reflections and the presence of gabbroid dikes. The Moho reflector is prominent beneath the oceanic domain except for the area of numerous intra-gabbroic dikes in the central part of the oceanic domain. The crustal thickness of the oceanic domain ranges from 8.6 to 5.6 km, which is in the normal depth range for oceanic crust (Péron-Pinvidic et al., 2015).

There is a clear division of the upper and lower oceanic crust with the upper oceanic crust characterized by a zone of seismic transparency that I interpret as sheeted dikes and the uppermost gabbros as seen in other areas such as the Orange Basin (Norcliffe et al., 2018). The lower crust contains high-amplitude reflectors with highly variable dip directions that change from landward-dipping to near-horizontal to seaward-dipping. These variably-dipping reflectors are interpreted as intra-gabbroic dikes (Ranero et al., 1997; Bécel et al., 2015; Norcliffe et al., 2018). Their seismic character is consistent with examples of high- magma-supply described from oceanic crust in other areas (Ranero et al., 1997; Reston et al., 1999; Bécel et al., 2015; Norcliffe et al., 2018). In these examples from other areas, oceanic crust typically conforms to the Penrose standardized model for oceanic crust composed of basalts, dolerite dykes, and lower crustal gabbros (Vine and Moores, 1972; Norcliffe et al., 2018).

Figure 4.5 Deep-penetration, depth-converted ION Span seismic reflection line B-B' through the southern Sergipe sub-basin. **a)** Uninterpreted seismic reflection line B-B'. **b)** Seismic line B-B' with the interpretation of crustal domains with age picks of overlying sedimentary horizons

based on seismic grid mapping shown in Figure 4.2 and described in detail Chapter 5. **c)** Zoomed-in view of the SDRs onlapping onto the normal fault. **d)** Basemap showing the location of ION line B-B' depicted as the red rectangle and the COB is shown dashed, white line. The area of hyperextended continental crust with marginal rifts in the Sergipe subbasin is shown by the white lines with tick marks on the downthrown side of the normal faults. SDRs are shown as the light red polygon and are confined in the marginal rift zone. Seamounts and magmatic plateaus on the oceanic crust are highlighted with white dots with their names identified in the caption of Figure 4.2.



Results from this chapter showing an Aptian magma-rich, syn-rift event

Seaward-dipping reflectors (SDRs)

SDRs comprise high-extrusion rate lava flows that form at a subaerial spreading center during the early stages of continental rifting and have generally been attributed to subaerial volcanism associated with Large Igneous Province (LIP) formation prior to the creation of oceanic crust (Mutter et al. 1982; Planke and Eldholm 1994; Morgan and Watts, 2018). This LIP-related has been confirmed by the Ocean Drilling Program (ODP), which has shown that SDRs comprise numerous lava flows intercalated with volcanoclastic sediments (e.g., Leg 104 described by Scientific Party 1987; and Leg 152 described by Teagle and Alt 1999). SDRs have been described based on seismic reflection data from offshore Norway, Argentina, Uruguay, Greenland, the Rockall Plateau (UK), Antarctica, Southwest Africa, Northwest Australia, the East Coast USA, and India (e.g., Hinz 1981; Paton et al., 2017; Norcliffe et al., 2018; Reuber et al., 2019).

Despite all of these previous studies, the tectonic origin of SDRs remains debatable. Planke et al. (2000), Geoffroy (2005), Pindell et al. (2014), and Paton et al. (2017) proposed widely accepted models of SDR formation: as plate divergence continues, the once-elevated and subhorizontal volcanic flows progressive rotated downward toward the nascent spreading ridge, which is driven downwards as continental lithosphere is replaced by more dense oceanic lithosphere beneath the newly-formed spreading ridge.

SDRs are characterized by convex-up geometry dipping seaward with an average dip angle of 14 degrees along the South Atlantic rifted margins (Morgan and Watts, 2018). SDRs diverge downdip into a zone of chaotic seismic imaging (Mutter et al. 1982; Norcliffe et al.,

2018; Reuber et al., 2019). In addition to their characteristic, convex-up geometry, SDRs have a distinctive seismic character expressed as strong amplitude variations along with individual and well stratified volcanic and sedimentary units (Norcliffe et al., 2018). Also, seismic refraction data have revealed that SDRs are often associated with high P-wave velocity lower crustal bodies, which have been interpreted as either magmatic underplating or sill-like crustal intrusions (White et al., 2008). SDRs are locally present in the study area but most concentrated in the southeastern Sergipe sub-basin (Figure 4.4, 4.5).

Figure 4.6 is the zoomed-in view of seismic profile A-A' showing the syn-rift half-grabens filled by an inferred mix of volcanic and sedimentary units that comprise the SDRs. The more landward half-graben is filled with 3.5-km of syn-rift sedimentary rocks that are characterized by a distinctive clinof orm shape consisting of topset, foreset, and bottomset (Pellegrini et al., 2020). The seaward, half-graben is filled with a 1.2-km-wide SDRs package with an average dip angle of 13 degrees.

Figure 4.7 is the zoomed-in view of seismic profile B-B' showing a better example of the syn-rift grabens filled by a wider, 3-km-thick SDRs package. The individual SDR reflectors have a convex-up shape with dip angles ranging from 8–25 degrees. This interpretation is supported by recent studies suggesting that kilometers of normal fault offset are needed to provide the accommodation space for the extremely thick accumulations of volcanic flows comprising the SDR sequences and to achieve the asymmetrical SDR geometries (e.g., Quirk et al., 2014; Buck, 2017; McDermott et al., 2018). McDermott et al. (2018) shows several examples of SDRs occupying half-grabens using ~22,000 km of high-quality, depth-migrated, seismic data in offshore South America that are very similar to the examples shown here (Fig. 4.7).

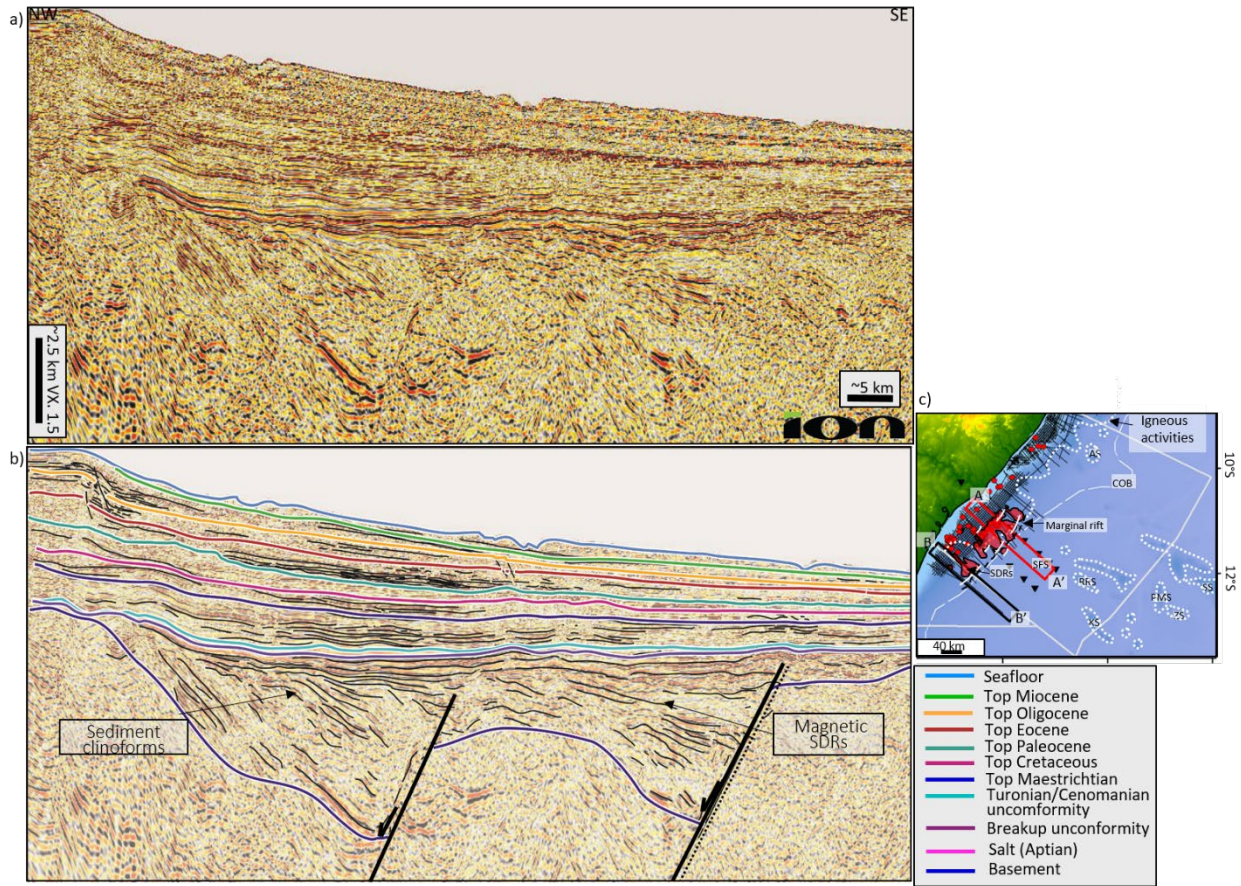


Figure 4.6 Zoom of depth-converted seismic reflection image A-A' of SDRs from ION seismic line in Figure 4.4 showing sediment- and volcanic-filled half-graben in the hyperextended, marginal rift zone. **a)** Uninterpreted seismic reflection line A-A'. **b)** Interpreted reflector geometries showing inferred sedimentary and less magnetic fill to the northwest and inferred magmatic SDRs with a strong positive magnetic anomaly as seen on the map in Figure 4.3b to the southeast. **c)** Basemap showing the location of ION line B-B' depicted as the red rectangle and the COB is shown dashed, white line. SDRs are shown as the light red polygon and are confined in the marginal rift zone. Seamounts and magmatic plateaus on the oceanic crust are highlighted with white dots with their names identified in the caption of Figure 4.2.

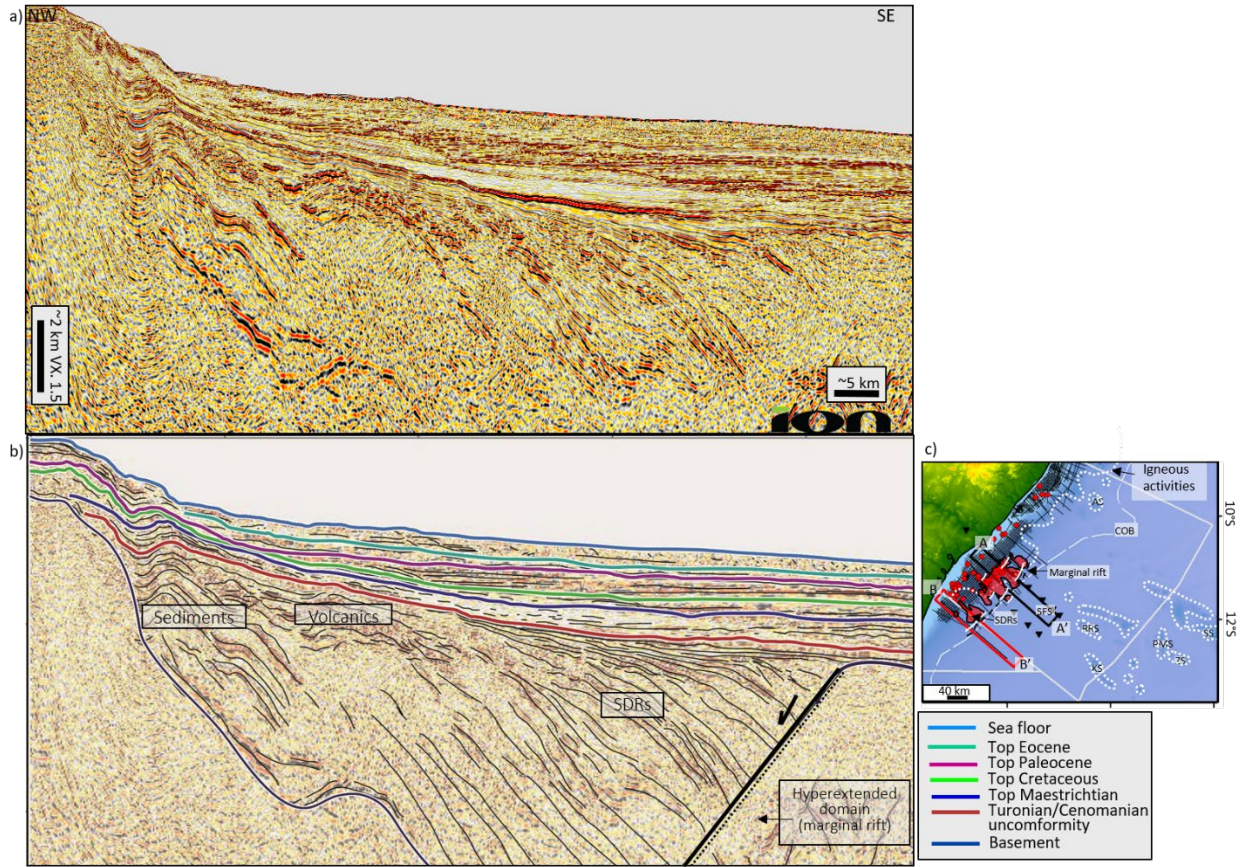


Figure 4.7 Zoom of depth-converted seismic image B-B' of SDRs from ION seismic line showing sediment- and volcanic-filled half-graben in the hyperextended, marginal rift zone. **a)** Uninterpreted seismic reflection line B-B'. **b)** Interpreted reflector geometries showing inferred sedimentary and less magnetic fill to the northwest and inferred magmatic SDRs with a strong positive magnetic anomaly as seen on the map in Figure 4.3b to the southeast. **c)** Basemap showing the location of ION line B-B' depicted as the red rectangle and the COB is shown dashed, white line. SDRs are shown as the light red polygon and are confined in the marginal rift zone. Seamounts and magmatic plateaus on the oceanic crust are highlighted with white dots with their names identified in the caption of Figure 4.2.

Sills and related features

Sills are commonly observed from seismic reflection data on volcanic margins, such as the Vøring Basin on the mid-Norwegian margin (Jamtveit et al., 2004) and the Ceduna sub-basin in southern Australia (Magee et al., 2013). In Brazil, sills are commonly observed in the central

Sergipe sub-basin and southern Alagoas sub-basin and are characterized by their strata-concordant, saucer-shaped, or laccolithic morphology high-amplitude reflections (Schofield and Totterdell, 2008; Jackson, 2012; Geng et al., 2020; Figure 4.8).

Sills commonly show eye-like structures, interpreted as ancient hydrothermal eruption centers similar to mud volcanoes, and may reach several kilometers in diameter (Planke et al., 2003; Jamtveit et al., 2004). The vent complexes are associated with a positive perturbation of the topographic relief at the top Cretaceous palaeosurface, creating a forced fold at the top (Figure 4.8c; Geng et al., 2020).

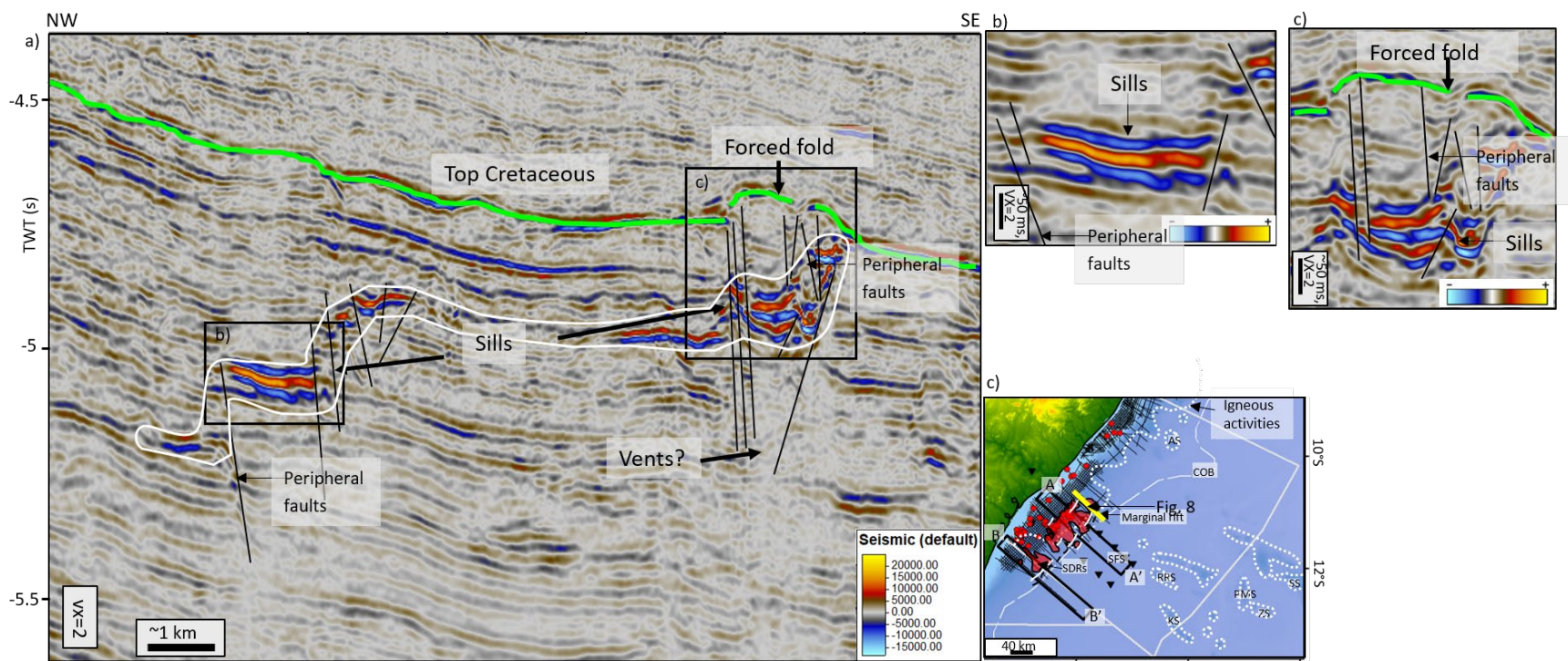


Figure 4.8 Examples of volcanic sills. **a)** Examples of volcanic sills intruded in the depth range of 4500-5500 ms (4.7-5.8 km) in sedimentary rocks of late Cretaceous age (Calumbi Formation) in the central Sergipe sub-basin (dip line location is shown by the yellow line on the location map in 8c). As commonly observed for sills described in other areas, a forced fold is formed above the sill as it displaces the overlying rock; peripheral faults form at the fold boundaries. Semi-continuous, high-amplitude zone highlighted in white shows the zone of sills and dikes may be interconnected over a lateral distance of 15 km. Volcanic feeders may also be present beneath the larger sill to the southeast (white polygon). **b)** Zoom of sills to the northwest and their peripheral faults. **c)** Zoom of sills to the southeast with a forced fold and peripheral faults. **d)** Basemap showing the location of the seismic line in A as the yellow line. The areas of hyperextended continental crust with marginal rifts in the Sergipe subbasin are shown by the white lines with tick marks on the downthrown side of the normal faults. SDRs are shown as the light red polygon and are confined in the marginal rift zone. Seamounts and magmatic plateaus on the oceanic crust are highlighted with white dots with their names identified in the caption of Figure 4.2.

Results from this chapter based on 2D and 3D gravity models

Regional tectonic features determined from gravity and magnetic anomalies

Gridded gravity and magnetic data are used in this chapter to identify buried faults and geologic contacts. On the gravity map, the Brazilian continental shelf is generally characterized by a low gravity anomaly (Figure 4.3a). In the seaward direction, the free-air gravity rises rapidly, and the shelf edge is marked by the transition from a gravity low along the shelf to the gravity high within the South Atlantic oceanic basin. Oceanic fracture zones trend southwest-northeast and are expressed as low anomalies both on the gravity anomaly map (Figure 4.2a) and on the magnetic map (Figure 4.2b).

Another prominent feature observed on the gravity map of the Brazilian margin are seamounts characterized by a sub-circular, high-amplitude anomaly (Figure 4.3a). Seamounts are observed as low anomalies on the magnetic map and commonly form linear southeast to northwest trends (Figure 4.2b). The onshore rift basins are expressed as gravity lows (Figure 4.2a).

The magnitude of free-air gravity anomalies is heavily dependent upon the topography, and for this reason, free-air gravity anomalies are not well suited for making detailed regional interpretations. As a result, I use filtered gravity data to provide a basis for my more detailed mapping of crustal structures.

The residual Bouguer gravity map in Figure 4.9a minimizes the effects of deep-Earth structures and enhances shallower structures, such as faults and igneous intrusions, and volcanoes. Oceanic fracture zones are more evident using the residual Bouguer gravity filter to highlight their low anomalies (Figure 4.9a). These oceanic fracture zones can be traced to the

edge of the continental shelf and even in areas deeply buried by sediments. Regional highs mark the onshore Sergipe rifts on the residual Bouguer anomaly, but the continental margin is associated with gravity lows onshore and on the continental shelf. The outlines of seamounts are more clear on the residual Bouguer map (Figure 4.9a) than on the free-air gravity map (Figure 4.3a).

The total horizontal gradient (THG) map enhancement displays the rate of change between points of a gridded gravity dataset (Blakey, 1995). Figure 4.9b is a map of THG of the Bouguer gravity that highlights the rate of change of the observed Bouguer gravity from point to point and measured in mGal/m. As a result, THG acts as an edge detector for identifying geobodies across the study area.

Volcanic seamounts and rifts are easily identified since they both represent a rapid transition from one dominant lithology to another. Volcanic features are characterized by “doughnuts” – or circular anomalies with high rates of change on the exterior and a small “hole” with a low rate of change in the center (Figure 4.9b). The prominent high-amplitude anomalies observed parallel and close to the continental margin are “edge-effect” anomalies that characterize the shelf break (Figure 4.9b). The onshore RTJ rift system is marked by high anomalies on the THG map (Figure 4.9b).

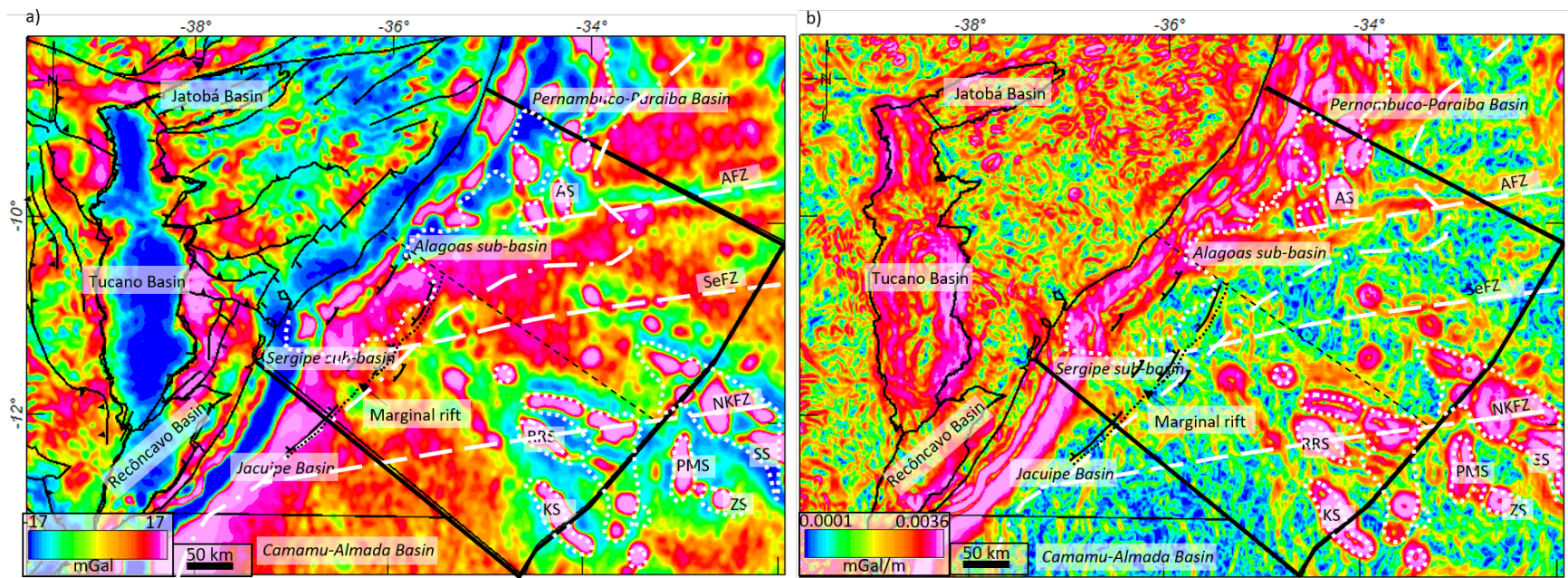


Figure 4.9 Filtered gravity anomalies in showing regional tectonic features. **a)** Computed residual (8 km upward continued) Bouguer anomaly gravity data over Sergipe-Alagoas rifted-passive margin. The three fracture zones in the oceanic crust are shown by dashed, white lines. Outer marginal rift filled in part by magmatic SDRs forms a gravity high, while inner marginal rift thought to be less filled by SDRs forms a prominent gravity low in the southwestern part of the study area. Circular gravity highs outlined with white dots are Cretaceous-Paleogene seamounts. **b)** Total horizontal gradient (THG) of the Bouguer gravity anomaly with cooler colors representing a low rate of change and a more homogeneous source from point to point. Volcanic seamounts and the continent-ocean transition are observed on the THG map because both types of features represent a rapid transition from one dominant lithology to another. SDRs form prominent highs parallel to the margin along the Sergipe sub-basin, seamounts, and volcanic plateaus cluster in the Alagoas sub-basin. Seamounts and magmatic plateaus on the oceanic crust are highlighted with white dots with their names identified in the caption of Figure 4.2.

Results from this chapter based on 2D gravity modeling

Two 2D forward models of gravity were constructed and analyzed in this chapter to constrain the depth, thickness, and type of crust under the Sergipe-Alagoas Basin and the onshore RTJ basins. Both gravity models incorporated constraints from seismic reflection lines, seismic refraction stations, well logs, and published cross-sections.

Gravity model 1. Model 1 is 490-km-long and oriented west-southeast from the western edge of the onland Tucano rift basin to the central Sergipe sub-basin (Figure 4.10). The previous seismic interpretation on seismic profile A-A' is adapted for this model along with previous interpretations by Blaich et al. (2008) for the onland, failed Tucano Basin. The model is also constrained by well logs and seismic refraction stations that are shown in Figure 4.2.

Observed free-air gravity values range from 63 mGal at the shelf break to -113 mGal over the central Tucano Basin. The resulting geometry matches the previously shown seismic interpretation of a 60 km wide, 4.9 km thick package of SDRs and syn-rift sediments (Figure 4.10). Continental crust is thinnest at the base of the SDR package - where the continental crust is 7 km thick (Figure 4.10). The Moho surface correspondingly has a step-up geometry at the continent-ocean transition and is deeper (21 km) beneath the Aptian seamount (Figure 4.10).

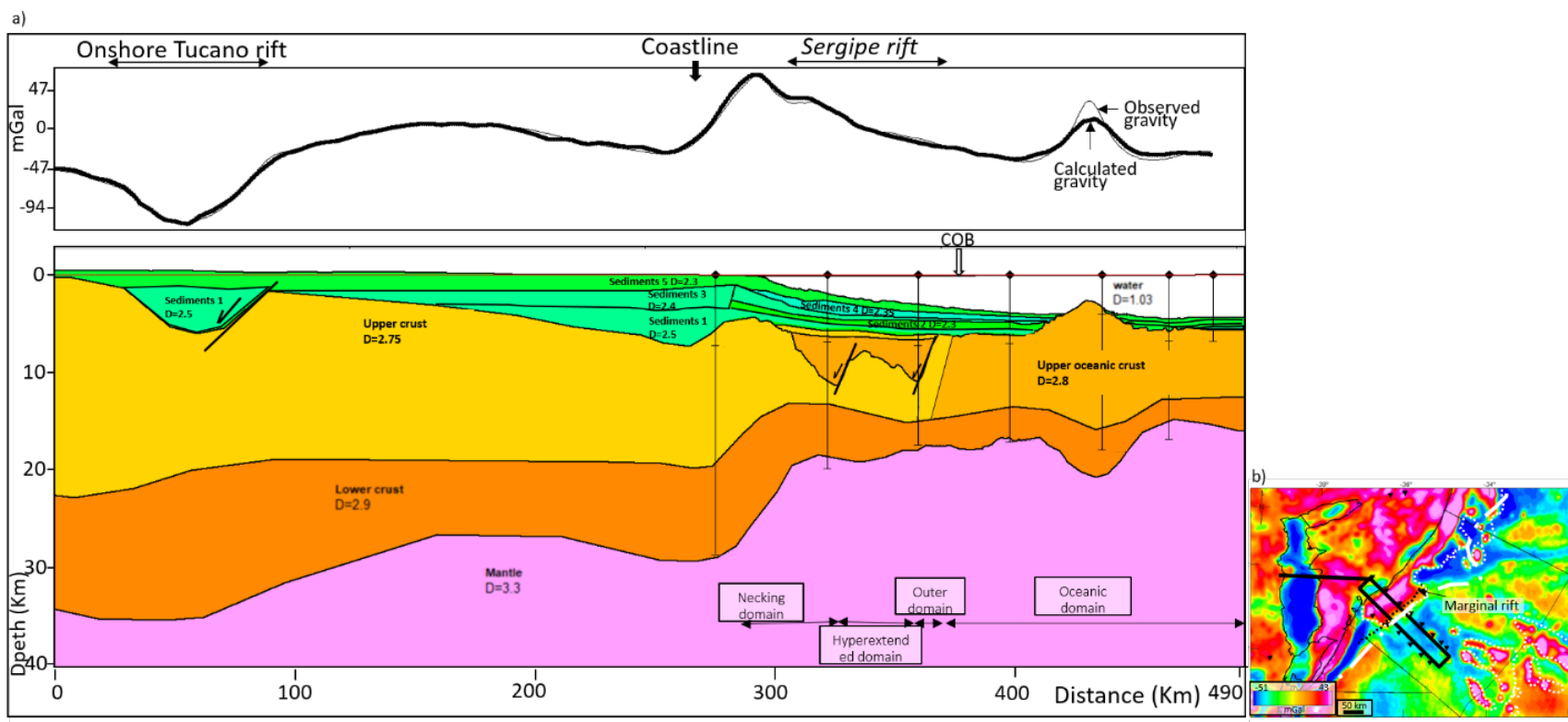


Figure 4.10 Gravity model 1. **a)** Forward-modeled 2D gravity profile through onshore, Aptian Tucano half-graben, a coastal mountain range, and the offshore, central Sergipe rifted-passive margin. **b)** Map of free-air gravity anomalies of the study area from Sandwell et al. (2014). The black line shows the location of the onshore gravity model crossing the Tucano continental rift in a), and the black rectangle shows the location of its offshore continuation in the Sergipe rifted-passive margin. Seamounts and magmatic plateaus on the oceanic crust are highlighted with white dots. White lines show large normal faults bounding the marginal rifts in the hyperextended zone.

Gravity model 2. Model 2 is 368-km-long and oriented west to southeast from the northwestern edge of the Recôncavo rift basin to the southern Sergipe sub-basin (Figure 4.11). Well logs and seismic refraction stations constrain the model along with the previous seismic interpretation on seismic profile B-B' shown in Figure 4.5 and the structural interpretations by Milani and Davison (1988) for the Recôncavo Basin.

Observed free-air gravity values range from 27 mGal at the shelf break to -135 mGal over the central Recôncavo Basin. The modeled crustal geometry matches my seismic interpretation of a 66 km wide, 5 km thick package of SDRs and syn-rift sediments, as shown in Figure 4.11. The continental crust is thinnest at the base of the SDR package - where it is 3.4 km thick (Figure 4.11).

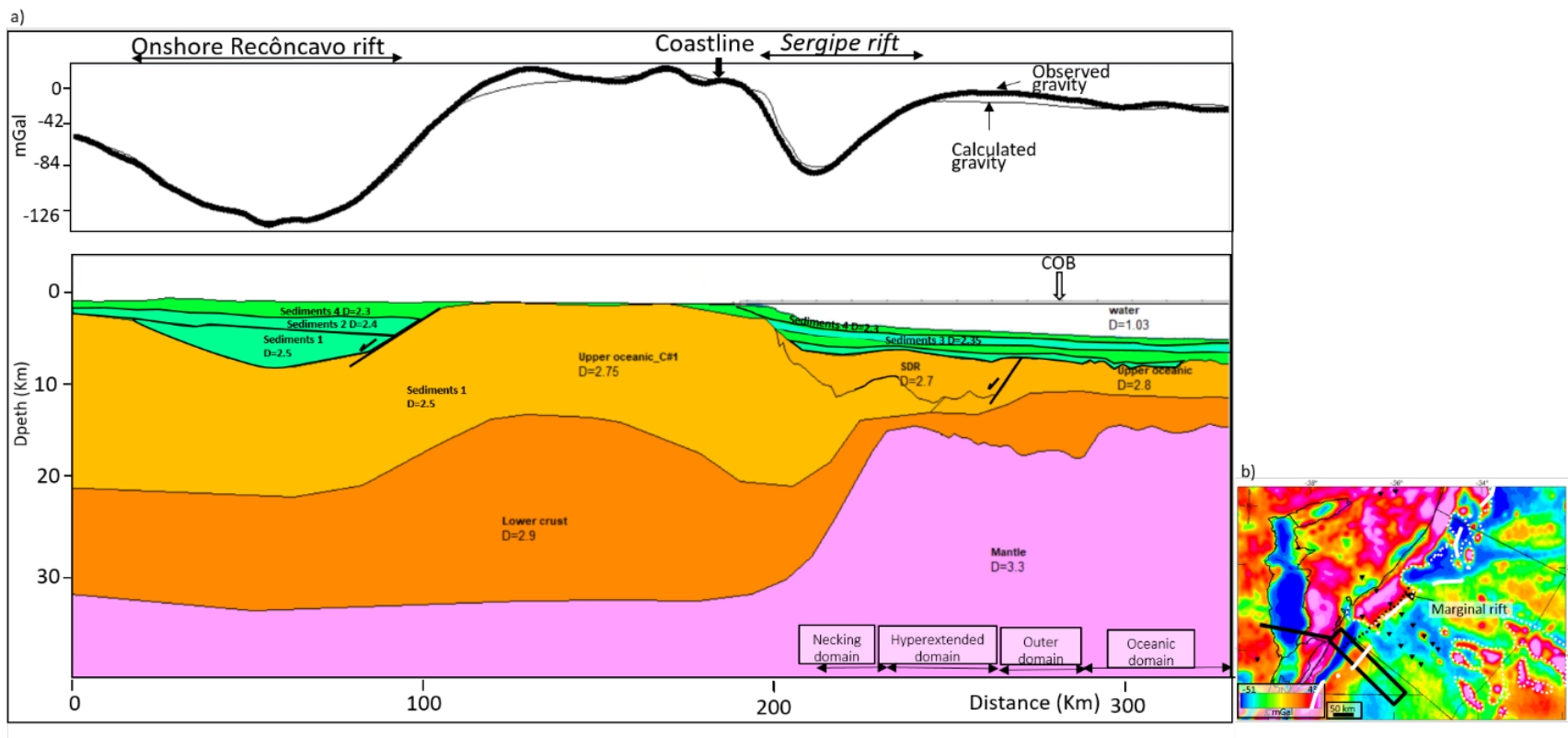


Figure 4.11 Gravity model 2. **a)** Forward-modeled 2D gravity profile through the onshore, Late Jurassic-Early Cretaceous Recôncavo rift basin, a coastal mountain range, and the offshore, southern Sergipe rifted-passive margin. **b)** Map of free-air gravity anomalies of the study area from Sandwell et al. (2014). The black line shows the location of the onshore gravity model crossing the Recôncavo continental rift in a), and the black rectangle shows the location of its offshore continuation across the southern Sergipe rifted-passive margin. Seamounds and magmatic plateaus on the oceanic crust are highlighted with white dots. White lines show large normal faults bounding the marginal rifts in the hyperextended zone.

Results from this chapter based on 3D gravity modeling

The 3D model inversions are separated into unconstrained and constrained results. Before each inversion run, 3D forward calculations were used to apply level shifts to the calculated gravity fields in order to minimize the average difference with the observed gravity field. The initial unconstrained inversion was performed on the isostatic Moho, and this horizon was adjusted such that its elevation depth ranged from -16 to -41 km (Figure 4.12a). The deepest Moho (-40 km) occurs within the onshore RTJ rift. In regions of the continental crust, the elevation depth ranges from -28 to -33 km. In regions of oceanic crust, the elevation depth ranges from -20 to -16 km.

After the initial unconstrained Moho was determined, the refraction data and seismic interpreted Moho were merged with the resulting unconstrained Moho to finalize the model in the constrained inversion. After the constrained inversion, the Moho ranges from -12 to -45 km in elevation depth (Figure 4.12b).

The largest differences between the unconstrained and constrained inversion results are in the region of the southwestern edge of the Sergipe sub-basin, where the Moho was adjusted upward. In regions of continental crust, the elevation depth ranges from -22 to -29 km and in regions of oceanic crust, the elevation ranges from -12 to -19 km. Seamounts with deeper roots in the mantle were noted as being the shallowest features in the modeled area and reach elevation depths around 12 km.

The basement map in Figure 4.9a shows that basement elevation depth ranges from 0 to -11 km, with the deepest basement elevation in the central Tucano rift. The basement depth is deeper in the Sergipe sub-basin and its SDR section. Synthetic and planar normal faults are strike

northeast and southwest with subsidiary east and northwest-striking faults dominating the basement structure in the offshore region (Figure 4.13A).

Crustal thickness was calculated by calculating the difference between the elevation depths of the top of the basement (Figure 4.13a) and the constrained Moho (Figure 4.13b). The crustal thickness ranged from 0 to over 40 km. The COB is mapped and represents the thinning of the crust from about 14 km to 7 km (Figure 4.13b). The COB shows that the Sergipe sub-basin has a wider zone (90 km) of rifted continental crust compared to the thinner zone (75 km) of the Alagoas sub-basin. The deeper basement and wider continental margin in the Sergipe sub-basin match the current hydrocarbon exploration lease blocks shown in Figure 4.2.

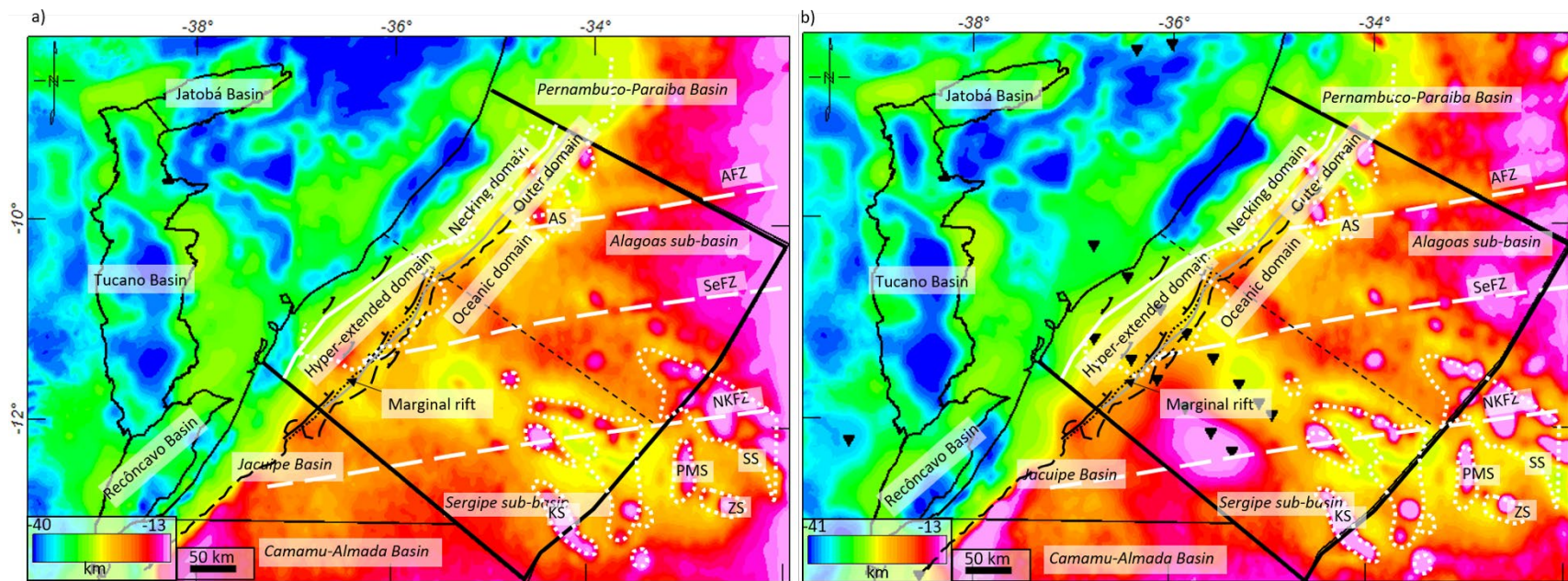


Figure 4.12 Resulted Moho structure from 3D gravity model. **a)** Moho calculated from an unconstrained inversion using the unconstrained model setup with units of elevation ranging from -16 to -41 km. **b)** Moho calculated from constrained inversion using the constrained model setup with units in elevation ranging from -12 to -45 km. Locations of refraction stations are shown as inverted triangles. Black lines show large normal faults forming the marginal rifts in the hyperextended, necking domain with the continental outer domain shown as a gray line adjacent to the continent-ocean boundary (COB) and the Aptian-Albian oceanic crust with three prominent fracture zones occurring in the seaward location.

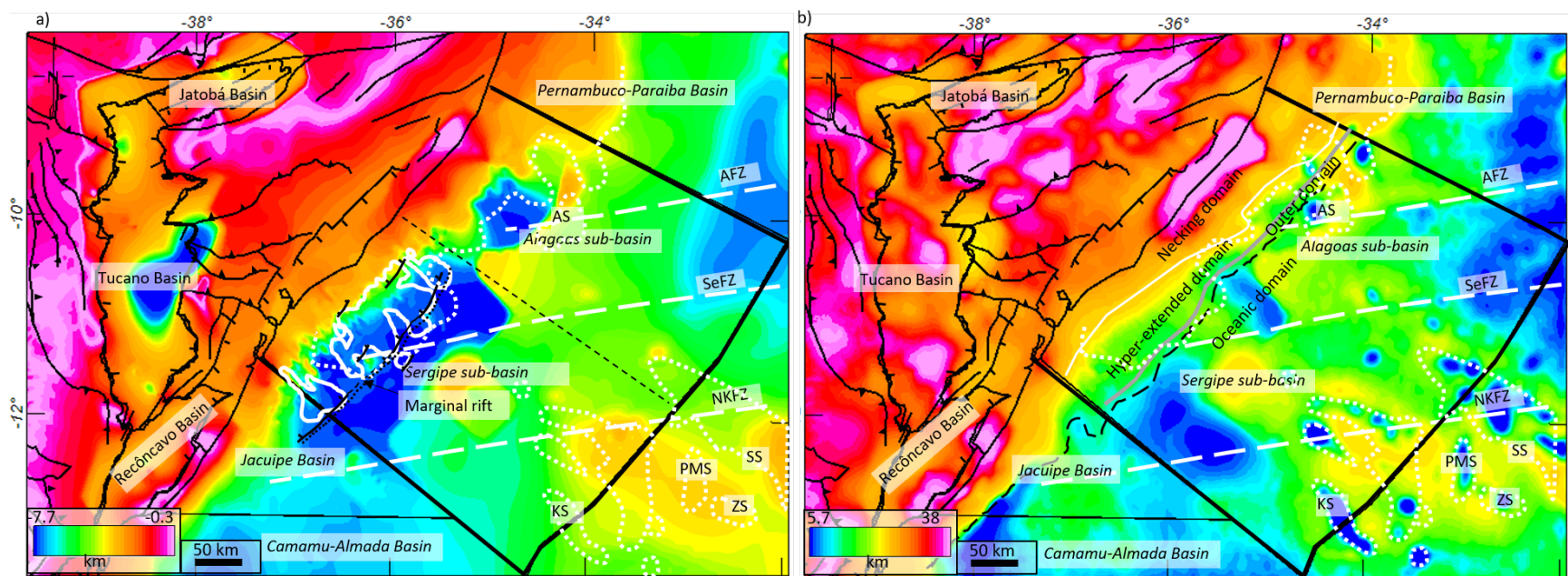


Figure 4.13 Resulted crustal structure from 3D gravity model. **a)** Basement structure map compiled from seismic reflection lines, refraction stations, published seismic cross-sections and global grids. White polygons outline the SDRs present in the marginal rifts of the hyperextended, necked zone of basement depth ranging from -6.6 to -7 km. Seamounts and magmatic plateaus on the oceanic crust are highlighted with white dots. **b)** Inverted crustal thickness map generated from 3D gravity model showing the areas of marginal rifts in the hyperextended, necking domain with the continental, outer domain shown as a gray line adjacent to the continent-ocean boundary (COB). The thickness range of the continental crust in the necking domain is from 25 to 36 km. Oceanic crust ranges in thickness from 7 to 9 km. Abbreviations for seamounts are provided in the caption of Figure 4.2.

Discussion

Controls of orogenic basement fabric on the stretching factors observed for the northeastern Brazil and Gabon rifted-passive margins

The structural framework of the rifted zone in the Sergipe-Alagoas Basin is controlled by Aptian normal fault systems striking northeast with subsidiary east- and northwest-striking faults that previous workers interpreted as transfer faults that connect the near-orthogonal normal fault segments (Milani and Davison, 1988; Chagas et al., 1993; Mohriak et al., 1998;) (Figs. 4.4, 4.5).

The conjugate North Gabon rifted margin in west Africa consists of a set of 130–150 long, asymmetrically-tilted half-grabens (called the Interior Basin) and shorter, *en echelon*, half-grabens (called the N’Komi Basin) that are separated by orthogonal transfer faults (Mounguengui and Guiraud, 2009) (Figure 4.14c).

I attribute the more narrow Brazilian rifted margin (90 km) to the near-parallelism of the Aptian rifts to the orientation of the pre-existing Precambrian to Paleozoic basement fabric (Figure 4.14b). To better understand this relationship of basement fabric to the width of the rift zone, I calculated basement stretching factors using the deep crustal information compiled in this chapter for the Sergipe-Alagoas rifted margin and from previous workers for the Gabon margin (Williams, 2008; Fernandez et al., 2020). The measurement of the total rifted zone included the necking domain, the hyperextended domain, and the outer domains based on the ION lines for the Sergipe-Alagoas Basin and the previous study by Gordon et al. (2017) for the Jacuipe Basin in the southern South Atlantic region.

As previously discussed by Reuber and Mann (2019) for the rifted margins of southern Brazil, Uruguay, Argentina, and their west African conjugates, a clear correlation emerged between narrow rifted margins, low stretching factors, and rift parallel basement trends - as did a

clear relationship between wide rifted margins, high stretching factors and rift-orthogonal or rift-oblique basement trends (Figure 4.14a).

The explanation for this correlation is the tendency for the rift-oblique and rift-orthogonal basement trends to be stronger and actively resist extension (Dunbar and Sawyer, 1989a, b). The theoretical basis for the crustal stretching over a wider zone and higher stretch factors in the case of basement fabrics prior to oceanic spreading was originally described by Dunbar and Sawyer (1989a, b). In contrast, rift-parallel basement fabrics allow rifts to form more easily and result in more narrow rifts with lower stretch factors.

Major Precambrian lineaments in the Sergipe-Alagoas basins, as shown in Figure 4.14b are sub-parallel to the northeast-trending rifts, exhibit lower stretch factors, and are relatively narrow. The basement fabrics become even more parallel to the rifts to the southwest in the Jacuipe Basin, where the rifts exhibit both lower stretching factors and narrow widths (Figure 4.14a). In contrast, the north Gabon margin exhibits Precambrian orogenic grains that are rift-orthogonal, result in a wider rift zone, exhibit higher stretch factors than the more oblique fabrics in the South Gabon Basin, which shows a narrower rift zone and lower stretch factors (Figure 4.14c).

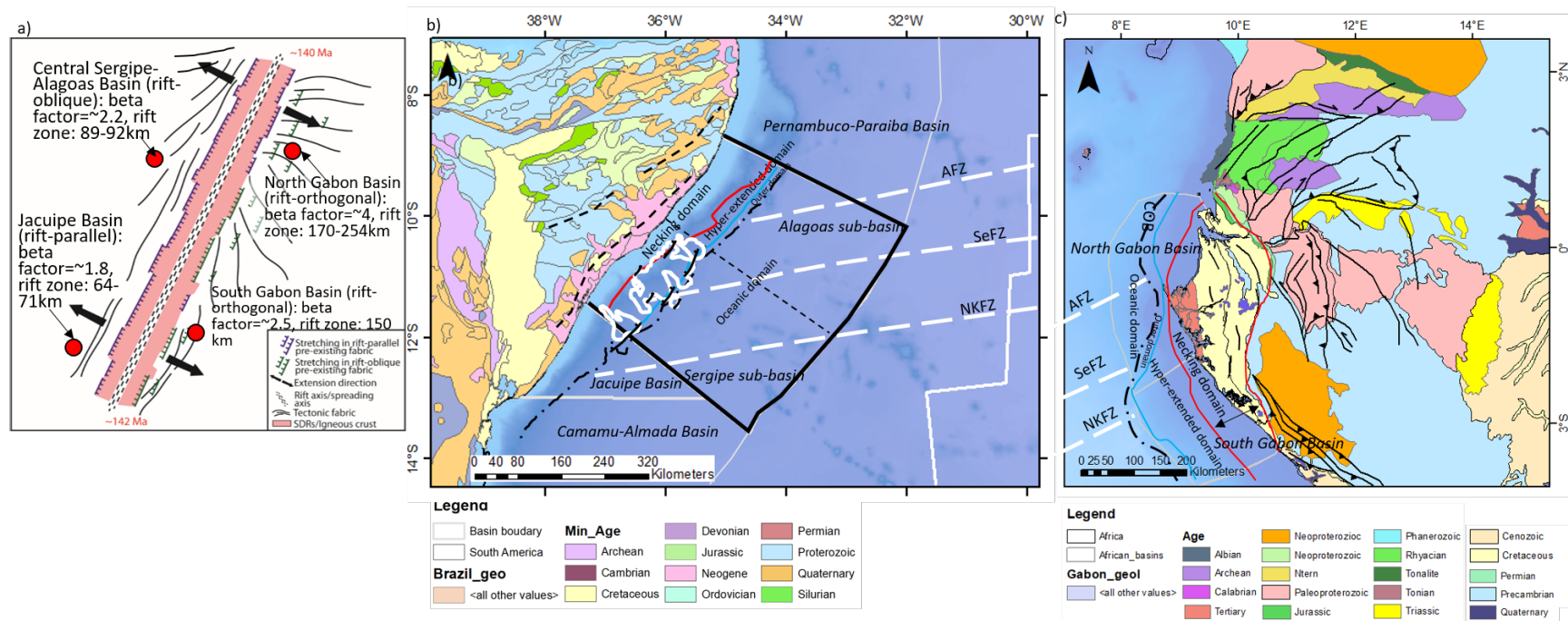


Figure 4.14 Relationship between basement fabric orientation and the stretching factors. a) Summary of the orientations of the underlying basement grain of northern Brazil and Gabon pre-rift conjugate margins with the measured widths in kms of the combined necking domain, the hyperextended domain, and the outer domains for the two conjugate margins based on the work presented in this chapter and Gordon et al. (2017) for northern Brazil and the previous study by Williams (2008) and Fernandez (2020) for the Gabon margin. Lines of section for the crustal profiles in Figure 4.15 for Brazil and Gabon are shown in yellow polygons. b) Relationship between basement fabric and stretching factors based on the geologic map from Gómez et al.(2019) of the Sergipe-Alagoas margin, which has a more narrow rift zone (89-94 km) and parallelism of the rift opening direction in the Reconcavo basin in the south slightly oblique angles in the Central Sergipe basin (20-30 degrees). I propose that the relative ease of rifting continental crust parallel to its fabric in the Reconcavo has led to a relatively narrow zone of rifting (64-71 km) lower beta factor in that area (1.8) compared to the slightly higher beta factor in the area of more oblique basement fabrics in the central Sergipe area (2.5). c) More rift-orthogonal or rift-oblique (45-120 degrees) basement trends based on geologic maps from Mounguengui and Guiraud (2009), Bankole et al.(2018), and Akame et al.(2020) in West African have led to a wider zone of rifting (150-170 km) than observed on the Brazilian margin. **Fracture zones** in the oceanic crust are white, dashed lines and include AFZ = Ascension Fracture Zone; SeFZ = Sergipe Fracture Zone; NKFZ = N’Komi Fracture Zone.

Comparison of the crustal structure of the northeastern Brazilian rifted-passive margin to its conjugate margin in North Gabon

I compared my interpretation of the Brazilian crustal structure based on seismic interpretations and gravity modeling with its conjugate margin in Equatorial Guinea and Gabon (Figure 4.15). The results allow me to compare/contrast four critical elements between the margins: 1) The West African rifted margin is wider (254 km) than the rifted margin of northeastern Brazil (89 km); 2) The continental crust in Gabon thins from 20–25 km to 6–8 km near the COB. The continental crust in Brazil thins from 14–25 km to 7–10 km near the COB. 3) A mixture of seaward-dipping reflectors (SDRs) and sediments on the Brazilian margin fills the pre-rift grabens that separate the 15-km-thick continental crust from the 8-km-thick oceanic crust (Figure 4.15b). On the African conjugate margin, SDRs fill an 11-km-deep, rifted graben that separates the 8-km-thick intruded continental crust from the 6-km-thick oceanic crust (Figure 4.15c); 4) Early Cretaceous to Eocene hotspot-related seamounts are distinct features on both conjugate margins (Figure 4.1). Hotspot-related seamounts are more common within the offshore northeastern Brazilian basins, where the oceanic crust is 40% thicker than the oceanic crust to the south that is less affected by hotspots (Figure 4.15b).

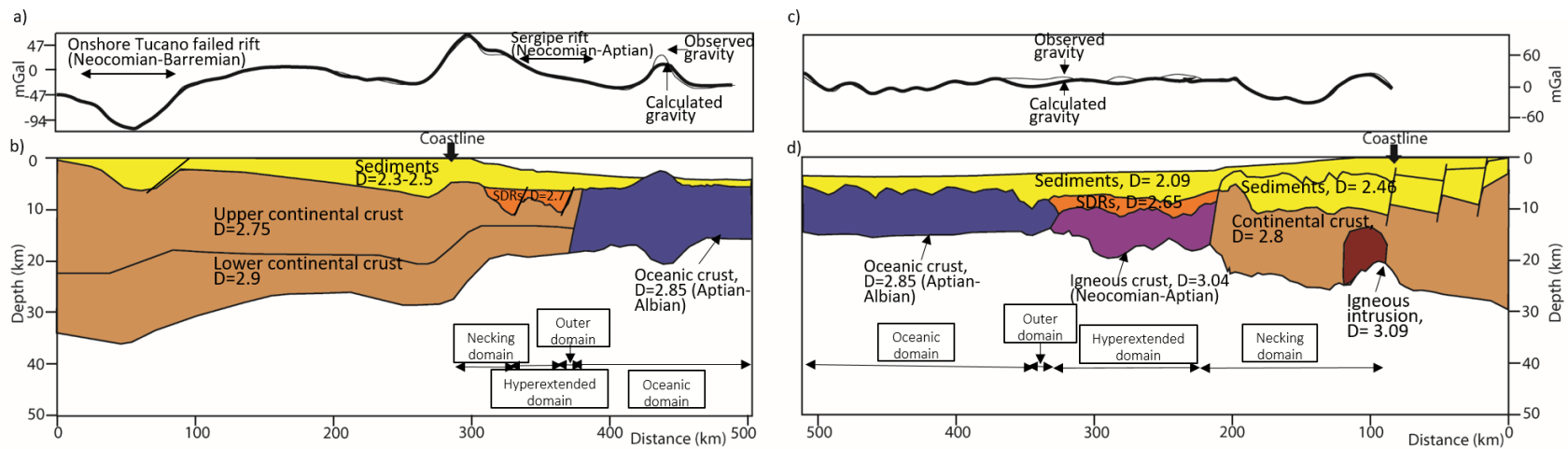


Figure 4.15 Gravity model of the Brazilian and west African margins. **a)** Gravity model of the Tocano-Central Sergipe transect using data from Sandwell et al. (2014), with the thin line being the observed gravity and the thicker line being the modeled gravity. **b)** Inferred crustal structure of the modeled gravity line in B with crustal zonation using the terminology of Peron-Pivindic et al. (2015); **c)** Gravity model of the northern Gabon transect generated by Williams (2008) with the thin line being the observed gravity and the thicker line being the modeled gravity. **d)** Inferred crustal structure of the modeled gravity by Williams (2008) with crustal zonation using the terminology of Peron-Pivindic et al. (2015).

Implications for hydrocarbon exploration on both conjugate margins

On Gabon rifted margin, hydrocarbon exploration has been successful for oil in the passive margin, post-salt section based on a Neocomian-Barremian source rock and clastic reservoirs of Aptian age, although much of the pre-rift section remains untested for hydrocarbons (Brownfield, 2016). On the northeastern Brazilian margin, hydrocarbon exploration has been moving into the deepwater region based on an Albian-Turonian source rock and paired, clastic reservoirs of the late Cretaceous age. However, much of the passive margin and pre-rift section remains untested. In Chapter 5, I propose an exploration fairway into the deepwater Sergipe-Alagoas basin based on my mapping of the thickest areas of the Albian-Turonian source rock.

Conclusions of chapter 4

Chapter 4 integrates seismic interpretation, potential field data interpretation, 2D and 3D gravity modeling to better understand the crustal structure framework in the Sergipe-Alagoas Basin and the onshore RTJ basin region. Interpretations on deep-penetrating 2D seismic lines from ION and 2D gravity models were able to define four crustal domains:

- 1) The **necking domain** is identified as the proximal continental crust defined in areas where the top of the basement and Moho reflector converge. The Moho reflector in this domain is not well expressed. The necking domain exhibits a syn-rift half-graben bounded by a northwest-dipping normal fault showing the presence of basinward accommodation space that filled with magmatic SDR volcanic flows and interbedded, sedimentary rocks.

- 2) The **hyperextended domain** is characterized by rapid crustal thinning with a vertical stretch factor of 2.5, which has thinned the continental crust to less than 10 km. A strong Moho reflector is observed and becomes sub-parallel to the top basement reflectors.
- 3) The **outer domain** is a narrow transition zone before reaching the COB. High-amplitude reflectors interpreted as the intra-gabbroic dikes.
- 4) The **oceanic domain** is characterized by parallel-sided top basement and Moho reflections. The Moho reflector is prominent in the oceanic domain except in areas of concentrated intra-gabbroic dikes and seamounts. There is a clear division of a seismically-transparent upper and lower oceanic crust with intra-gabbroic dikes in the southwestern part of the study area.

The presence of intra-gabbroic dikes, SDRs, volcanic sills indicates a magma-rich margin but not to the extent of the SDR-rich volcanic margins of the southern South Atlantic conjugate margins where SDR belts can be up to 200 km wide (Reuber et al., 2019).

The Moho surface as constrained from 3D structural inversion ranges in depth from -12 to -45 km and depth. Using this surface, a COB location is proposed that shows the continental margin narrowing to the northeastern part of the study area.

My results constrain comparisons between the rifted zone of the Brazilian margin with its conjugate in north Gabon. I propose that the wider (150 km) north Gabon rifted margin was produced by an asymmetrical South Atlantic breakup mechanism that was related to the orientation of basement fabric lineaments. These basement fabrics were sub-parallel to the rift direction in Brazil and therefore weaker and resulted in a more narrow rift zone (90 km). In Gabon, these basement fabrics were orthogonal to the rift direction and therefore stronger and resulted in a wider narrow rift zone.

SDRs are locally present on both margins and fill syn-rift half-grabens within the necked zone that separates continental crust from oceanic crust. This rift zone has been modified by Early Cretaceous to Eocene hotspot-related seamounts that form distinctive seamounts and volcanic margins on both conjugate margins. These magmatic features are more common within the offshore northeastern Brazilian basins, where the modified oceanic crust is 40% thicker than the oceanic crust to the south that is less affected by hotspot activity.

Bibliography

- Akame, J.M., Owona, S., Hublet, G. and Debaille, V., 2020. Archean tectonics in the sangmelima granite-greenstone terrains, Ntem Complex (NW Congo craton), southern Cameroon. *Journal of African Earth Sciences*, 168, 1-15.
- Alexander, M. and Aimadeddine, K., 2009, Regional structural framework of Gabon derived from public source gravity data. AAPG International Conference and Exhibition, Cape Town, South Africa, 6 p.
- Azambuja Filho, N.C. de, Cruz, F.E. da, Arienti, L.M and Hook, S., 1998. Guidebook to the rift-drift Sergipe-Alagoas Basin. In Azambuja Filho, N.C., ed., Virtual field guide of Sergipe-Alagoas basin - CD, Brazil. Rio-98 AAPG/ABGP International Conference and Exhibition, Rio de Janeiro, 1-69.
- Bankole, O.M., El Albani, A., Meunier, A., Pambo, F., Paquette, J.L., and Bekker, A., 2018. Earth's oldest preserved K-bentonites in the ca. 2.1 Ga Francevillian Basin, Gabon. *American journal of science*, 318(4), 409-434.
- Bassi, G., Keen, C.E. and Potter, P., 1993. Contrasting styles of rifting: Models and examples from the eastern Canadian margin. *Tectonics*, 12(3), 639-655.
- Bécel, A., Shillington, D.J., Nedimović, M.R., Webb, S.C., Kuehn, H., 2015. Origin of dipping structures in fast-spreading oceanic lower crust offshore Alaska imaged by multichannel seismic data. *Earth and Planetary Science Letters*, 424, 26–37.
- Beglinger, S.E., Doust, H. and Cloetingh, S., 2012. Relating petroleum system and play development to basin evolution: West African South Atlantic basins. *Marine and Petroleum Geology*, 30(1), 1-25.

- Blaich, O.A., 2008. Northeastern Brazilian margin: Regional tectonic evolution based on integrated analysis of seismic reflection and potential field data and modeling. Unpublished M.S. thesis, University of Oslo, 105 p.
- Blaich, O.A., Tsikalas, F. and Faleide, J.I., 2008. Northeastern Brazilian margin: Regional tectonic evolution based on integrated analysis of seismic reflection and potential field data and modeling. *Tectonophysics*, 458(1-4), 51-67.
- Blakely, R.J., 1995. *Potential Theory in Gravity and Magnetic Exploration*. Cambridge University Press, 441 p.
- Brownfield, M.E., 2016. Assessment of undiscovered oil and gas resources of the West-Central Coastal Province, west Africa. In Brownfield, M.E., compiler, *Geologic assessment of undiscovered hydrocarbon resources of Sub-Saharan Africa*: U.S. Geological Survey Digital Data Series 69–GG, chap. 7, 41 p.
- Buck, W.R. 1991. Modes of continental lithospheric extension. *Journal of Geophysical Research* 96(20), 161–178.
- Buck, W.R., Lavier, L.L. and Poliakov, A.N., 1999. How to make a rift wide. *Philosophical Transactions of the Royal Society of London. Series A: Mathematical, Physical and Engineering Sciences*, 357(1753), 671-693.
- Buck, W.R., 2017. The role of magmatic loads and rift jumps in generating seaward dipping reflectors on volcanic rifted margins. *Earth and Planetary Science Letters*, 466, 62-69.
- Caixeta, J.M., Ferreira, T.S., Machado Jr, D.L., Teixeira, J.L. and Romeiro, M.A., 2014. Albian rift systems in the northeastern Brazilian margin: An example of rifting in hyper-extended continental crust. *AAPG Search and Discovery*, 7, 1-13.

- Chagas, L.S., Chiossi, D.S.N., Cerqueira, R.M., Hamsi Jr, G.P., Marques, G. and Lisboa, G., 1993. Evolução tectono-sedimentar do rift da Bacia de Sergipe-Alagoas e novas perspectivas exploratórias. Petrobrás/Denest unpublished internal report, 1 p.
- Chakravarthi, V., Ramamma, B. and Reddy, T.V., 2013. Gravity anomaly modeling of sedimentary basins by means of multiple structures and exponential density contrast-depth variations: A space domain approach. *Journal of the Geological Society of India*, 82(5), 561-569.
- Chang, H.K., Kowsmann, R.O., Figureueiredo, A.M.F., Bender, A.A., 1992. Tectonics and stratigraphy of the East Brazil Rift System: An overview. *Tectonophysics* 213, 97–138.
- Cordell, L., 1973. Gravity analysis using an exponential density-depth function; San Jacinto Graben, California. *Geophysics*, 38(4), 684-690.
- Davison, I.A.N., 1997. Wide and narrow margins of the Brazilian South Atlantic. *Journal of the Geological Society*, 154(3), 471-476.
- Davison, I., Underhill, J. R, 2012. Tectonics and sedimentation in extensional rifts: Implications for petroleum systems. In D. Gao, ed., *Tectonics and sedimentation: implications for petroleum systems*. AAPG memoir, 100, 15-42.
- Divins, D. L., 2003. Total sediment thickness of the world's oceans and marginal seas. NOAA National Geophysical Data Center, Boulder, CO.
- Dunbar, J.A. and Sawyer, D.S., 1989a. How pre-existing weaknesses control the style of continental breakup. *Journal of Geophysical Research: Solid Earth*, 94(B6), 7278-7292.
- Dunbar, J.A. and Sawyer, D.S., 1989b. Patterns of continental extension along the conjugate margins of the central and North Atlantic Oceans and Labrador Sea. *Tectonics*, 8(5), 1059-1077.

- Ferreira, J.M., Oliveira, T., Takeya, M.K. and Assumpção, M., 1998. Superposition of local and regional stresses in northeast Brazil: evidence from focal mechanisms around the Potiguar marginal basin. *Geophysical Journal International*, 134(2), 341-355.
- Fernandez, O., Olaiz, A., Cascone, L., Hernandez, P., Pereira, A.D.F., Tritlla, J., Ingles, M., Aida, B., Pinto, I., Rocca, R. and Sanders, C., 2020. Geophysical evidence for breakup volcanism in the Angola and Gabon passive margins. *Marine and Petroleum Geology*, 116, 1-30.
- Geoffroy, L., 2005, Volcanic passive margins. *Geoscience*, 337, 1395–1408.
- Geng, M., Song, H., Guan, Y., Chen, J., Zhang, R., Zhang, B., and Zhang, X., 2020. Sill-related seafloor domes in the Zhongjiannan Basin, western South China Sea. *Marine and Petroleum Geology*, 122,1-17.
- Gómez, J., Schobbenhaus, C. and Montes, N., 2019. Geological Map of South America. Scale, 1:5000000.
- Gordon, A., Destro, N. and Heilbron, M., 2017. The Recôncavo-Tucano-Jatobá rift and associated Atlantic continental margin basins. São Francisco Craton, Eastern Brazil. Springer, 171-185.
- Gesch, D.B., Verdin, K.L. and Greenlee, S.K., 1999. New land surface digital elevation model covers the Earth. *EOS, Transactions American Geophysical Union*, 80(6), 69-70.
- Hinz, K., 1981. A hypothesis on terrestrial catastrophies Wedges of very thick oceanward dipping layers beneath passive continental margins; their origin and paleoenvironmental significance. *Stuttgart Schweizerbart*, H(22), 3-28.
- Jackson, C.A.L., 2012. Seismic reflection imaging and controls on the preservation of ancient sill-fed magmatic vents. *Journal of the Geological Society*, 169(5), 503-506.

- Jammes, S., Lavier, L. and Manatschal, G., 2010. Extreme crustal thinning in the Bay of Biscay and the Western Pyrenees: From observations to modeling. *Geochemistry, Geophysics, Geosystems*, 11(10), 1-26.
- Jamtveit, B., Svensen, H., Podladchikov, Y.Y. and Planke, S., 2004. Hydrothermal vent complexes associated with sill intrusions in sedimentary basins. *In* Breitzkreuz, C. and Petford, N., eds., *Physical Geology of High-Level Magmatic Systems*. London Geological Society Special Publication, 234, 233–241.
- Karner, G.D. and Driscoll, N.W., 1999. Tectonic and stratigraphic development of the West African and eastern Brazilian Margins: Insights from quantitative basin modelling. *In* Cameron, N. R., Bate, R. H. and Clure, V. S., eds., *The Oil and Gas Habitats of the South Atlantic*. London Geological Society Special Publication, 153(1), 11-40.
- Knize, S., Berrocal, J., and Oliveira, DM de, 1984. Modelo preliminar de velocidades sísmicas da crosta através de explosões locais registradas pela rede sismográfica de sobradinho – BA. *Brazilian Journal of Geophysics*, 2, 95-104.
- Laske, G. and Masters, G., 1997. A global digital map of sediment thickness, *EOS Trans. AGU*, 78, 1-483.
- Lentini, M.R., Fraser, S.I., Sumner, H.S. and Davies, R.J., 2010. Geodynamics of the central South Atlantic conjugate margins: Implications for hydrocarbon potential. *Petroleum Geoscience*, 16(3), 217-229.
- Lister, G. S., Etheridge, M. A., Symonds, P. A. 1986. Detachment faulting and the evolution of passive continental margins. *Geology*, 14, 246–250.
- Lopes, A.E., Assumpção, M., Do Nascimento, A.F., Ferreira, J.M., Menezes, E.A. and Barbosa, J.R., 2010. Intraplate earthquake swarm in Belo Jardim, NE Brazil: Reactivation of a

- major Neoproterozoic shear zone (Pernambuco Lineament). *Geophysical Journal International*, 180(3), 1303-1312.
- Meyer, B., R. Saltus, and A. Chulliat, 2017. EMAG2: Earth magnetic anomaly grid (2-arc-minute resolution) version 3. National Center for Environmental Information.
- Magee, C., Hunt-Stewart, E. and Jackson, C.A.L., 2013. Volcano growth mechanisms and the role of sub-volcanic intrusions: Insights from 2D seismic reflection data. *Earth and Planetary Science Letters*, Elsevier, 373, 41–53.
- Matos, R.M.D. De, 2000. Tectonic evolution of the Equatorial South Atlantic. *In* Mohriak, W. and Taiwani, M., eds., *Atlantic rifts and continental margins*. American Geophysical Union, 115, 331-354.
- Matos, R.M.D. De, Krueger, A., Norton, I. and Casey, K., 2021. The fundamental role of the Borborema and Benin – Nigeria provinces of NE Brazil and NW Africa during the development of the South Atlantic Cretaceous Rift system. *Marine and Petroleum Geology*, 127, 104872-104902.
- Milani, E.J. and Davison, I., 1988. Basement control and transfer tectonics in the Recôncavo - Tucano - Jatobá roft, Northeast Brazil. *Tectonophysics*, 154, 1-25.
- Mohriak, W.U., Rabelo, J.L., De Matos, R.D. and De Barros, M.C., 1995. Deep seismic reflection profiling of sedimentary basins offshore Brazil: Geological objectives and preliminary results in the Sergipe Basin. *Journal of Geodynamics*, 20(4), 515-539.
- Mohriak, W.U., Bassetto, M. and Vieira, I.S., 1998. Crustal architecture and tectonic evolution of the Sergipe-Alagoas and Jacuipé basins, offshore northeastern Brazil. *Tectonophysics*, 288(4), 199-220.

- Mohriak, W. U., M. Nemčok, and G. Enciso, 2008. South Atlantic divergent margin evolution: Rift-border uplift and salt tectonics in basins of SE Brazil. *In* R. J. Pankhurst et al., eds., *West Gondwana: Pre-Cenozoic Correlations across the South Atlantic Region*. London Geological Society Special Publication, 294, 365–398.
- Morgan, R.L. and Watts, A.B., 2018. Seismic and gravity constraints on flexural models for the origin of seaward dipping reflectors. *Geophysical Journal International*, 214, 2073–2083.
- Moulin, M., Aslanian, D., Olivet, J. L., Contrucci, I., Matias, L., Géli, L., Klingelhoefer, F., Nouzé, H., Réhault, J. P., and Unternehr, P., 2005. Geological constraints on the evolution of the Angolan margin based on reflection and refraction seismic data (ZaiAngo project). *Geophysical Journal International*, 162, 793–810.
- Moulin, M., Aslanian, D., and Unternehr, P., 2010. A new starting point for the South and Equatorial Atlantic Ocean. *Earth-Science Reviews*, 98, 1–37.
- Mounguengui, M.M. and Guiraud, M., 2009. Neocomian to early Aptian syn-rift evolution of the normal to oblique-rifted North Gabon Margin (Interior and N'Komi Basins). *Marine and Petroleum Geology*, 26(6), 1000-1017.
- Mutter, J.C., Talwani, M. & Stoffa, P.L., 1982. Origin of seaward-dipping reflectors in oceanic crust off the Norwegian margin by “subaerial seafloor spreading”. *Geology*, 10, 353–357.
- Norcliffe, J.R., Paton, D.A., Mortimer, E.J., McCaig, A.M., Nicholls, H., Rodriguez, K., Hodgson, N., Van Der Spuy, D., 2018. Laterally confined volcanic successions (LCVS); recording rift-jumps during the formation of magma-rich margins. *Earth and Planetary Science Letters*, 504, 53–63.
- Parker, R.L., 1973. The rapid calculation of potential anomalies. *Geophysical Journal International*, 31(4), 447-455.

- Paton, D.A., Pindell, J., McDermott, K., Bellingham, P. and Horn, B., 2017. Evolution of seaward-dipping reflectors at the onset of oceanic crust formation at volcanic passive margins: Insights from the South Atlantic. *Geology*, 45(5), 439-442.
- Pavlis, N. K., Holmes, S. A., Kenyon, S. C., Factor, J. K., 2012. The development and evaluation of the Earth Gravitational Model 2008 (EGM2008). *Journal of Geophysical Research: Solid Earth*, 117(B04406), 1-38.
- Pellegrini, C., Patruno, S., Helland-Hansen, W., Steel, R.J. and Trincardi, F., 2020. Clinofolds and clinothems: Fundamental elements of basin infill. *Basin Research*, 32(2), 187–205.
- Péron-Pinvidic, G., Manatschal, G., Masini, E., Sutra, E., Flament, J.M., Hauptert, I. and Unternehr, P., 2015. Unraveling the along-strike variability of the Angola–Gabon rifted margin: A mapping approach. In Sabato Ceraldi, T., Hodgkinson, R. A. and Backe, G., eds., *Petroleum Geoscience of the West Africa Margin*. Geological Society of London Special Publications, 438(1), 49-76.
- Pindell, J. L., R. Graham, and B. W. Horn, 2014. Role of magmatic evacuation in the production of SDR complexes at magma-rich passive margins. *Proceedings of the GCSSEPM Bob F. Perkins Research Conference*, 1–16.
- Pinheiro, J.M., Schnurle, P., Evain, M., Afilhado, A., Gallais, F., Klingelhoefer, F., Loureiro, A., Fuck, R., Soares, J., Cupertino, J.A. and Viana, A., 2018. Lithospheric structuration onshore-offshore of the Sergipe-Alagoas passive margin, NE Brazil, based on wide-angle seismic data. *Journal of South American Earth Sciences*, 88, 649-672.
- Planke, S. and Eldholm, O., 1994. Seismic response and construction of seaward dipping wedges of flood basalts: Vøring volcanic margin. *Journal of Geophysical Research: Solid Earth*, 99(B5), 9263-9278.

- Planke, S., P. A. Symonds, E. Alvestad, and J. Skogseid, 2000. Seismic volcanostratigraphy of large-volume basaltic extrusive complexes on rifted margins. *Journal of Geophysical Research: Solid Earth*, 105, 19335–19351.
- Planke, S., Svensen, H., Hovland, M., Banks, D.A. and Jamtveit, B., 2003. Mud and fluid migration in active mud volcanoes in Azerbaijan. *Geo-Marine Letters*, 23(3-4), 258-268.
- Quirk, D. G., Shakerley, A., and Howe, M. J., 2014. A mechanism for construction of volcanic rifted margins during continental breakup. *Geology*, 42(12), 1079-1082.
- Rabinowitz, P.D., LaBrecque, J.L., 1979. The Mesozoic South Atlantic Ocean and evolution of its continental margins. *Journal of Geophysical Research*, 84, 5973–6002.
- Ranero, C.R., Reston, T.J., Belykh, I., Gribidenko, H., 1997. Reflective oceanic crust formed at a fast-spreading center in the Pacific. *Geology*, 25, 499–502.
- Reston, T.J., Ranero, C.R. and Belykh, I., 1999. The structure of Cretaceous oceanic crust of the NW Pacific: Constraints on processes at fast spreading centers. *Journal of Geophysical Research: Solid Earth*, 104(B1), 629-644.
- Reuber, K. and Mann, P., 2019. Control of Precambrian-to-Paleozoic orogenic trends on along-strike variations in Early Cretaceous continental rifts of the South Atlantic Ocean. *Interpretation*, 7(4), 45-69.
- Reuber, K., Mann, P. and Pindell, J., 2019. Hotspot origin for asymmetrical conjugate volcanic margins of the austral South Atlantic Ocean as imaged on deeply penetrating seismic reflection lines. *Interpretation*, 7(4), 71-97.
- Reuber, K.R., Pindell, J. and Horn, B.W., 2016. Demerara Rise, offshore Suriname: Magma-rich segment of the Central Atlantic Ocean, and conjugate to the Bahamas hot spot. *Interpretation*, 4(2), 141-155.

- Row, L.W., Hastings, D.A., and Dunbar, P.K., 1995. TerrainBase Worldwide Digital Terrain Data Documentation Manual, CD-ROM Release 1.0. National Geophysical Data Center, Boulder, Colorado.
- Sandwell, D. T., Müller, R. D., Smith, W. H. F., Garcia, E., Francis, R., 2014. New global marine gravity model from CryoSat-2 and Jason-1 reveals buried tectonic structure. *Science*, 346(6205), 65-67.
- Schofield, A., Totterdell, J., 2008. Distribution, timing and origin of magmatism in the Bight and Eucla Basins. Petroleum and Marine Division, Geoscience Australia, 24, 1–19.
- Scientific Party, 1987. Site 642: Norwegian Sea. *In* Eldholm, O., Thiede, J., Taylor, E., et al., Proc. ODP, Init. Repts., 104: College Station, TX (Ocean Drilling Program), 53–453.
- Sutra, E. and Manatschal, G., 2012. How does the continental crust thin in a hyperextended rifted margin? Insights from the Iberia margin. *Geology*, 40(2), 139-142.
- Teagle, D.A.H. and Alt, J.C., 1999. Data Report: alteration and vein log of holes 917A and 918D southeast Greenland margin. *In* Larsen, H.C., Duncan, R.A., Allan, J.F., Brooks, K., Proc. ODP, Sci. Results (College Station, TX (Ocean Drilling Program), 163, 149–153.
- Torsvik, T.H., Rouse, S., Labails, C. and Smethurst, M.A., 2009. A new scheme for the opening of the South Atlantic Ocean and the dissection of an Aptian salt basin. *Geophysical Journal International*, 177(3), 1315-1333.
- Vine, F.J. and Moores, E.M., 1972. A model for the gross structure, petrology, and magnetic properties of oceanic crust. *Studies in Earth and Space Sciences: A Memoir in Honor of Harry Hammond Hess*, 195-205.
- Wessel, P., 2001. Global distribution of seamounts inferred from gridded Geosat/ERS-1 altimetry. *Journal of Geophysical Research: Solid Earth*, 106(B9), 19431-19441.

- Whittaker, J. M., Goncharov, A., Williams, S. E., Müller, R. D., Leitchenkov, G., 2013. Global sediment thickness dataset updated for the Australian-Antarctic Southern Ocean. *Geochemistry, Geophysics, Geosystems*, 14, 3297-3305.
- White, R.S. et al., 2008. Lower-crustal intrusion on the North Atlantic continental margin. *Nature*, 452, 460–464.
- Zinecker, M.P., 2020. Structural and stratigraphic evolution of three Mesozoic, rifted-passive margins: Guinea Plateau, Demerara Rise, and southeastern Gulf of Mexico. Unpublished doctoral dissertation, University of Houston, 1-309.

CHAPTER 5 : TECTONOSTRATIGRAPHIC EVOLUTION AND THERMAL MATURITY MODELING OF THE SERGIPE-ALAGOAS RIFTED-PASSIVE MARGIN, NORTHEASTERN BRAZIL

Introduction

Tectonic setting of the Northeast Brazilian rifted-passive margin

The Northeastern Brazilian Rifted Margin (NBRM) of Aptian age extends over a distance of 4800 km along the South Atlantic margin of Brazil and includes from south to north these hydrocarbon-producing, rifted segments of the margin: Jequitinhonha, Almada, Camamu, Sergipe-Alagoas, and Pernambuco-Paraíba segments (Ojeda, 1982; Ferreira et al., 2013; Figure 5.1). The Sergipe-Alagoas segment of the rifted-passive margin located in the center NBRM and forms a 90-km-wide rifted zone that underlies the coastal plain, shelf, and slope of the Sergipe and Alagoas states of northeastern Brazil. The onshore area of the basin exposes basement and sedimentary rocks that recorded all the tectonic phases of the basin's history. The onshore Sergipe-Alagoas Basin covers a coastal plain area of 13,000 km² while the total offshore area of the shelf, slope, and deep basin covers an area of 60,500 km² and reaches a maximum 4 km water depth in the area of Cretaceous oceanic crust (Azambuja Filho et al., 1998; Blaich, 2008 (Figure 5.2).

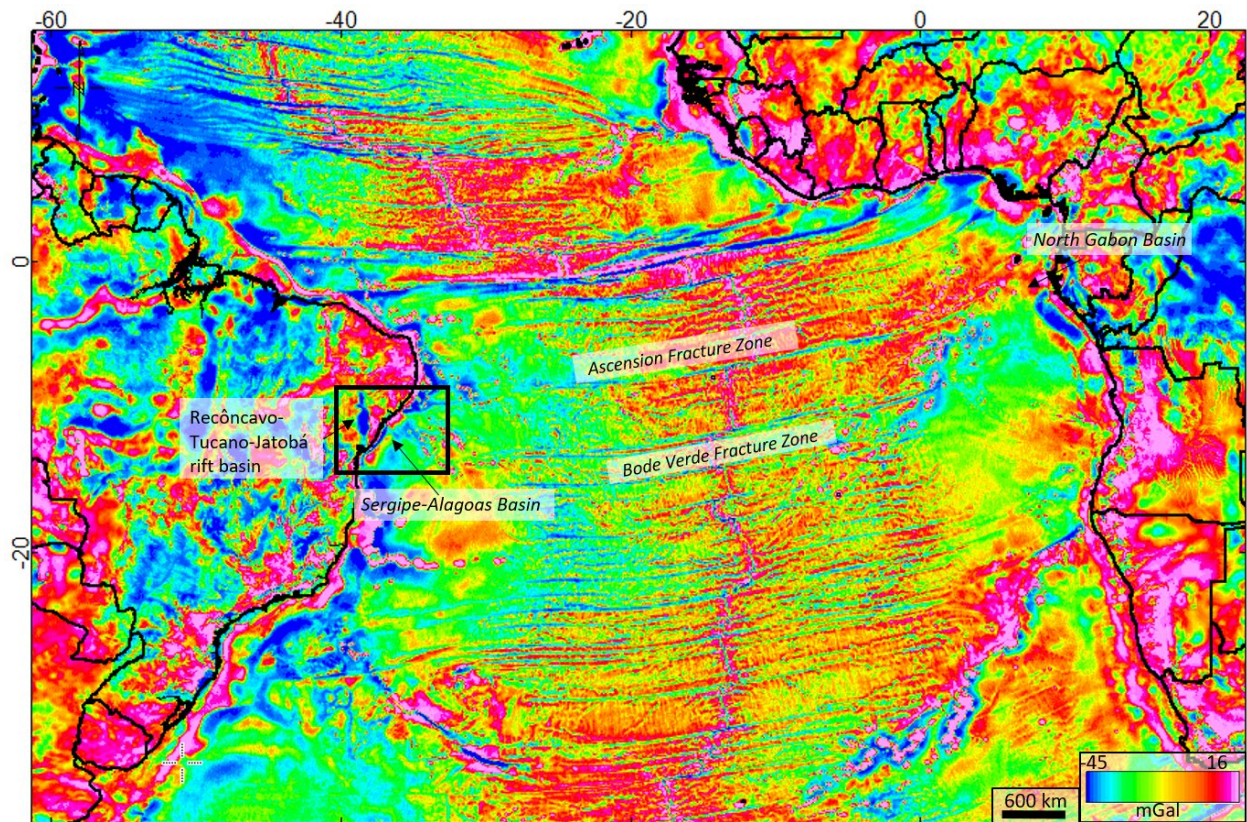


Figure 5.1 Free-air gravity map of the Central Atlantic showing the conjugate margins of the Sergipe-Alagoas basin and the North Gabon basin. The major fracture zones connecting the two conjugate rifted margins in Brazil and Gabon are the Ascension and Bo de Verde Fracture Zones. These linear fracture zones can be used to restore the widely separated, conjugate margins to their original pre-rift locations prior to the rifting and oceanic spreading along the Mid-Atlantic spreading ridge. Rectangle outlines the study area of the Sergipe-Alagoas rifted-passive margin in northeastern Brazil.

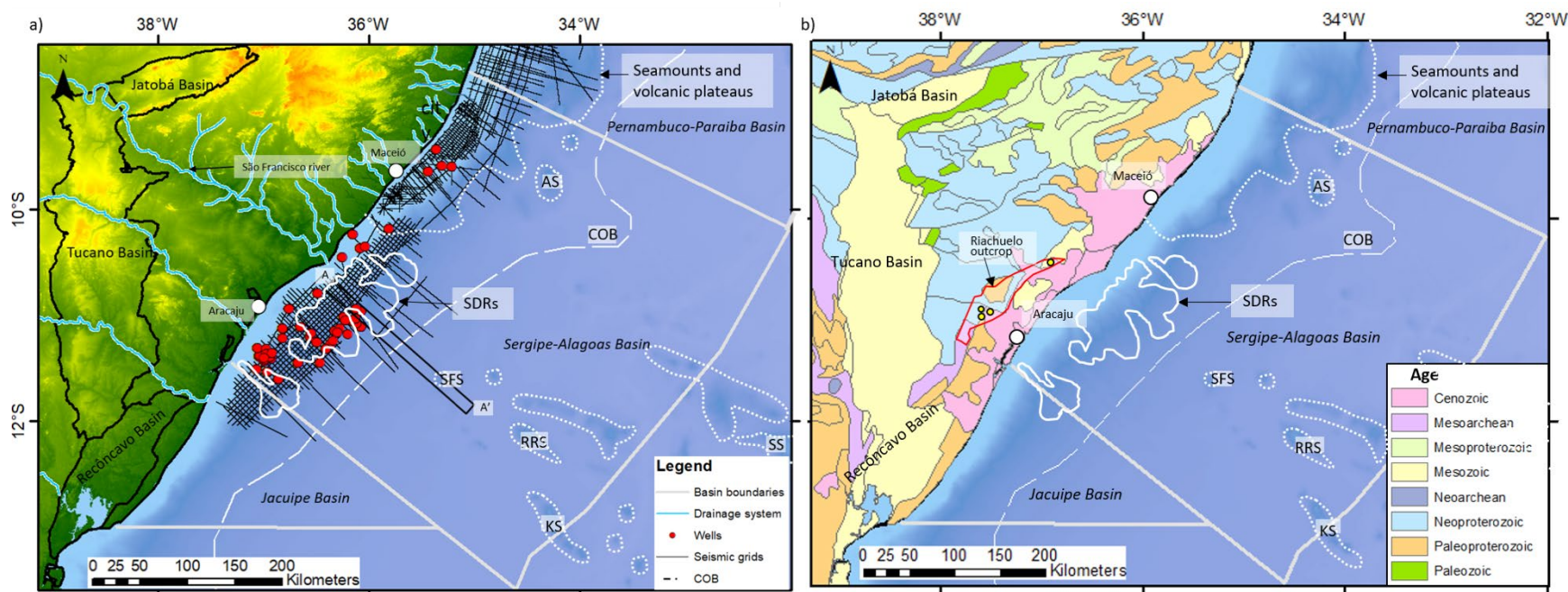


Figure 5.2 Datasets used in this study. **a)** Map of the Sergipe-Alagoas rifted-passive margin showing the locations of the various datasets used in this chapter. Major river systems of northeastern Brazil that transport clastic sediments into the offshore of the Sergipe-Alagoas Basin are shown in blue. **b)** Geological map of the onshore Sergipe-Alagoas Basin and the Recôncavo-Tucano-Jatobá (RTJ) rifted basins from (Gómez et al., 2019). Outcrop locations of the Albian-Coniacian source rocks of the Riachuelo Formation outcrop described by Fauth et al. (2021) are shown by the red polygon with individual, studied outcrop locations shown with the yellow circles. Offshore seamounts and volcanic plateaus of Late Cretaceous-Cenozoic age are highlighted by the white dotted polygons. **Abbreviations:** AS: Alagoas Seamount; KS: Klenova Seamount; PMS: Paulo Moreira Seamount; RRS: Romano Russo Seamount; SFS: São Francisco Seamount; SS: Stocks Seamount; ZS: Zemruscki Seamount.

The most important event in the evolution of the NBRM was the Late Jurassic–Early Cretaceous breakup of Pangea with the Aptian separation of South America and Africa along with a south-to-north propagating, continental rift system that eventually led to oceanic spreading (Chang et al., 1992; Neto et al., 2007; Reuber and Mann, 2019; Matos et al., 2021). In this region, the oceanic crust formed in the Early Cretaceous and de-activated the Jatobá continental rift system that extended north of the Florianópolis fracture zone and volcanic lineament (Asmus 1984) to the southern part of my study area in the Alagoas sub-basin.

Previous workers agree that the timing of NBRM rifting occurred from Neocomian to Mid-Late-Aptian (Bueno, 2004; Ponte and Asmus, 2004; Blaich, 2008; Cruz, 2008; Caixeta et al., 2014; Matos et al., 2021). In my study area the end of the syn-rift phase occurs in the Late Aptian based on the observed break-up unconformity and overlying Late Aptian sag basin that overlies the syn-rift normal faults and half grabens. Volcanism accompanied the syn-rift phase but continued into the sag and passive margin phases of the late Cretaceous through Cenozoic (Matos, 2021). According to Mounguengui and Guiraud (2009), the end of rifting on the Gabon conjugate margin ended about 10 million years earlier during the Early Aptian. This discrepancy has not been discussed by previous authors and I cannot offer any explanation for the differences in ages.

Pre-rift and early Aptian syn-rift sedimentary units were deposited, and now outcrop in the onland areas of the Recôncavo, Tucano, Jatobá, and Sergipe-Alagoas rifted margins while the offshore area of the Sergipe-Alagoas containing a sedimentary record of all three phases of the basin evolution: pre-, syn-, and post-rift. This means that subsidence of the Recôncavo, Tucano, and Jatobá and the onshore part of the Sergipe-Alagoas rift was completed by Early Aptian time.

In contrast, the offshore Sergipe-Alagoas Basin has continued to subside and accumulate sediments up to the present day (Chang et al., 1992).

Four tectonostratigraphic phases of South America-Africa continental rifting and oceanic spreading

The four main tectonostratigraphic phases are recorded by the following megasequences that have been studied in both the onland and offshore areas of the Sergipe-Alagoas basin by previous workers (Figure 5.3): 1) **the pre-rift phase** (Late Jurassic/Early Cretaceous); 2) **the rift phase** (Neocomian/Middle Aptian); 3) **the post-rift, early sag phase** (Middle-Late Aptian); and 4) **the passive margin phase** (Late Cretaceous to Recent) (Figure 5.3). These four megasequences are bounded by major regional unconformities that separate the seismic megasequences and their distinctive seismic facies that record the changing depositional environments (Feijó, 1994). Vasconcelos et al. (2019) proposed a period of basin reactivation, uplift, and fault inversion during the Neogene (Figure 5.3).

The pre-rift megasequence outcrops in onland areas of the coastal plain with a maximum sedimentary thickness of 100-300 m and includes strata that range in age from Paleozoic (mainly Carboniferous–Permian) to Mesozoic (mainly Late Jurassic–Early Cretaceous) (Milani and Davison, 1988). A Jurassic unconformity sub-divides this sequence into two units (Mohriak et al., 2000) (Figure 5.3).

Strata of the Lower Cretaceous rift megasequence were deposited in fluvial-lacustrine environments that range in age from Neocomian to Barremian. Tectonic uplift of this sequence created a regional unconformity (the so-called “breakup unconformity” that marks the end of the rift stage along the Brazilian margin (Lana, 1990; Figure 5.3).

The post-rift, early sag phase megasequence of the Middle-Late Aptian age corresponds to a proto-oceanic stage in the South Atlantic basins with localized and minor incursions of salt deposits in the basin (Figure 5.3). Salt tectonics was mainly restricted to the platform area with negligible deposition in the deeper water parts of the basin (Cainelli, 1992; Feijó, 1994).

The passive margin megasequence of the Late Cretaceous through the Cenozoic age was divided into transgressive and regressive phases that are separated by the eustatic sea-level fall during the Early Cenozoic, as documented by biostratigraphic studies (Mello, 2016; Silva et al., 2020; Fauth et al., 2021).

Previous studies of the tectonostratigraphic phases of the NRBM include Leyden et al. (1976), Guimaraes (1988), Mohriak et al. (1995), and Cainelli and Mohriak (1999), who all based their structural interpretation of the offshore Sergipe-Alagoas Basin on the same vintage seismic lines acquired in the period from 1984 to 1989.

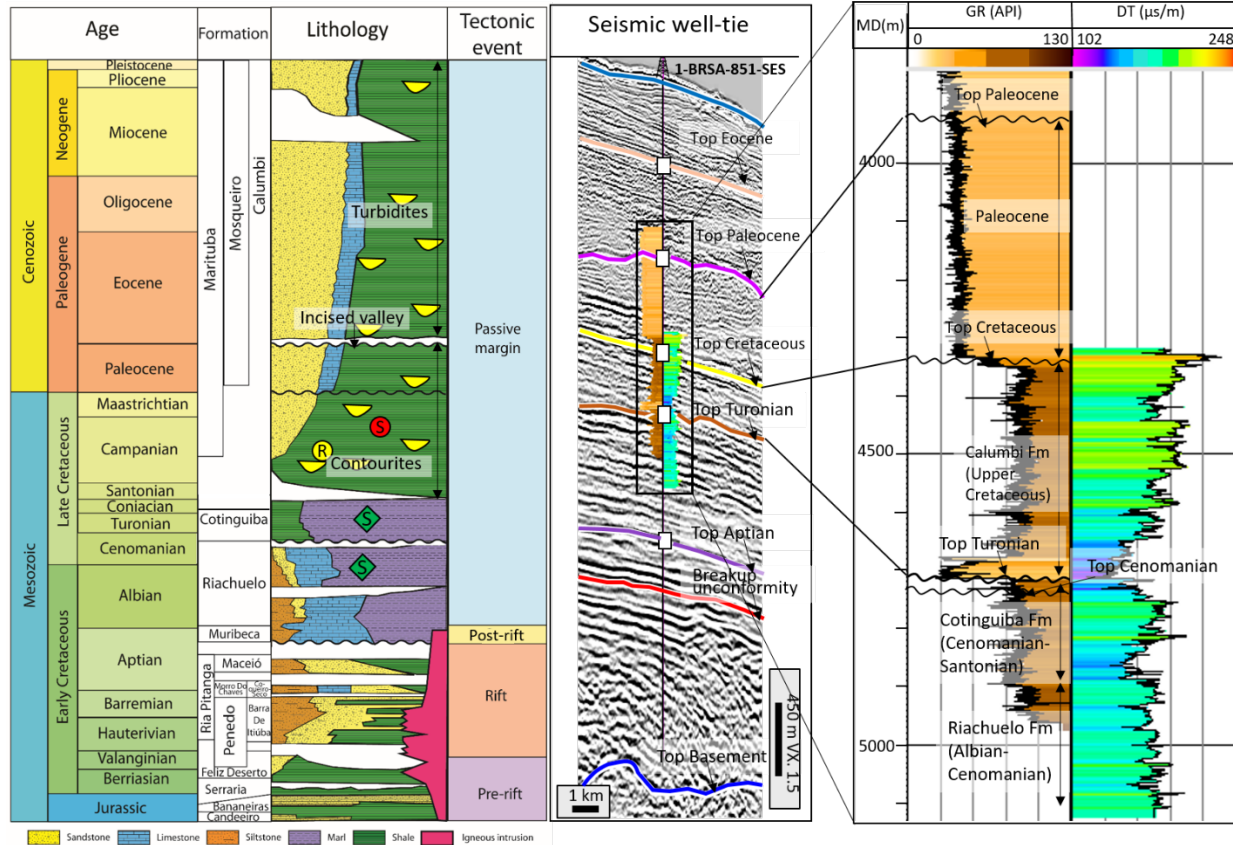


Figure 5.3 Chronostratigraphic summary and seismic well-tie of the Sergipe–Alagoas Basin showing the stratigraphy of the four main tectonic phases of the basin evolution correlated with a log of ANP well (give well number), formation names, lithologies, depositional environments, and petroleum system elements. The Palaeozoic succession is not part of the Sergipe-Alagoas Basin and instead occurred during the previous tectonic cycle – the collisional formation of Gondwana supercontinent. The enlarged well section showing the detailed Gamma-ray and sonic log curves are to the right from ANP well 1-BRSA-851-SES. The abrupt increase in the Gamma-ray log at a depth of 4340 m is related to the placement of casing during the well completion.

Hydrocarbon history and potential of the Sergipe-Alagoas basin

Exploratory activity in the Sergipe–Alagoas Basin resulted in the discovery of its largest one billion-barrel oil field in onshore Brazil (Carmópolis) at shallow drilling depth in shallow water Aptian, syn-rift clastic rocks during the late 1960s (Meister and Aurich, 1972).

The first exploratory borehole ever drilled in offshore Brazil in 1987 was also located in the Sergipe Basin. In 2012, five discoveries were made in the ultra-deepwater zone that confirmed the exploration potential of the Sergipe coastal area. In 2019, Petrobrás made the most significant gas discovery in the Sergipe-Alagoas Basin since 2006 in deep-marine turbidites of the Upper Cretaceous Calumbi Formation, making it one of the most promising frontiers in ultra-deepwater. Macellari (2017) reports light oil, natural gas, and condensate discoveries in the deep and ultra-deepwater Sergipe-Alagoas Basin.

In the onland area of the Sergipe-Alagoas Basin, the best-studied and most prolific petroleum system is based on the Aptian Muribeca Formation, which forms the clastic reservoir for the giant, onshore Carmópolis oil field (Koning, 2013). Geochemical studies of these oils reveal a lacustrine freshwater and marine hypersaline environment for their syn-rift Cretaceous source rock (Mello et al., 1991; Schiefelbein et al., 2020). Souza et al. (1995) made extensive petrographic studies of the lithic sandstone and conglomerate of the Carmópolis Member of the Muribeca Formation (Figure 5.3).

Recent exploration in the offshore basin has focused on younger reservoirs of Cenozoic and Upper Cretaceous turbidites (Beglinger et al., 2012b) (Figure 5.3). These younger reservoirs have yielded a number of major oil discoveries in the southern Sergipe Basin, including the Guaricema Field on the shelf and a series of deeper water discoveries (e.g., SES-92 and SEAL-100 by Petrobras) (Mullin et al., 2004). The offshore discoveries are charged by source rocks of Albian-Cenomanian marl and shale of the Riachuelo Formation (correlative to the Regência Formation shallow-marine shale of the Espírito Santo basin) and the Cenomanian-Turonian marine marl and mudstone of the Cotinguiba Formation (correlative to the Itajai-Acu deep-marine shale in the Santos basin) (Beglinger et al., 2012b) (Figure 5.3).

Previous stratigraphic studies of the Sergipe-Alagoas basin

The southern part of the NBRM is well studied due to recent pre-salt petroleum discoveries in the Campos, Santos, and Espírito Santo basins (e.g., Mello et al., 1994; Beglinger et al., 2012a; Contreras et al., 2012). However, the relationships between the tectonic and burial subsidence history and hydrocarbon source rock maturation history in the central and northern parts of the NBRM remain less well studied.

Unlike most of the Brazilian marginal basins, the onshore Sergipe-Alagoas basin is the only Brazilian rift zone within the NBRM that has outcrops of rocks that record the tectonic history that occurred during the Lower Cretaceous syn-rift period and during the late Cretaceous-Cenozoic passive margin period (Azambuja Filho, 1998). The uplift and exposure of these onland outcrops occurred during a late Cenozoic- Quaternary inversion event (Szatmari and Milani, 1999; Vasconcelos et al., 2019) and have allowed detailed outcrop studies of the basinal history (e.g., Feijó, 1994; Castro et al., 2019; Rigueti et al., 2020; Fauth et al., 2021). Outcrop studies in the Sergipe-Alagoas Basin have focused on outcrops of the main source rock for the on- and offshore basin, the Albian-Cenomanian Riachuelo Formation (Ponte et al., 1977; Evans, 1978; Mohriak et al., 2000; Mullin et al., 2004; Garcia and Rocha, 2012; Garcia et al., 2015; Corbett, 2015; Schrank et al., 2017; Rigueti et al., 2020; Szatmari et al., 2021) (Figure 2b).

Reviews of the deep-marine source rock and potential for hydrocarbon accumulations in the basins along the Brazilian South Atlantic margin have been carried out and include the offshore Sergipe-Alagoas Basin (Katz and Mello, 2000; Beglinger et al., 2012b). Previous tectonostratigraphic studies of the Sergipe-Alagoas Basin have focused mainly on the onshore outcrops (e.g., Araújo et al., 2012; Kifumbi et al., 2017; Castro et al., 2019; Dantas and Holz,

2020). Cruz (2008) made detailed tectono-stratigraphic studies of the offshore Sergipe sub-basin but focused only on the post-rift, early sag sequence.

Objectives and significance of this chapter

Despite the extensive hydrocarbon exploration within the on- and offshore Sergipe-Alagoas rifted-passive margin, the thermal maturity level and locations of source rock kitchen areas in the deepwater and ultra-deepwater region of the basin remain poorly defined. For this reason, the objectives of this chapter include 1) to understand the relationship between the four seismic megasequences and their controlling tectonic events; 2) to use basin modeling to reconstruct the thermal history of the basin and to predict the distribution of areas within the basin where the the main Albian-Turonian source rock interval mature for oil and gas; and 3) to use the above model results to define the hydrocarbon fairway in the deepwater frontier area of the Sergipe-Alagoas basin which remains underexplored.

Dataset and methods used in this chapter

Seismic reflection data and well logs

The dataset used in this chapter includes 200 line-km of seismic reflection data kindly provided by ION, PGS, and ANP that covers an area of approximately 173,000 km² of the offshore Sergipe-Alagoas margin (Figure 5.2). Seismic reflection data include two deeply-penetrating, depth-converted seismic reflection lines from ION, 2D seismic lines extracted from the Brazil 2D Megasurvey provided by PGS, and various grids of 2D seismic reflection survey provided by ANP (Figure 5.2a).

The seismic reflection dataset spans the shelf, slope, and basinal areas that range in water depths between -500 m to -3,800 m (Figure 5.2). Well data include 51 ANP well logs with lithologic logs, gamma, resistivity, neutron density, and checkshots that are concentrated within the shelf to the shallow-water area. Only a few of these wells have penetrated deep enough to reach the Aptian syn-rift strata and there are few wells available from ANP for the deepwater area (Figure 5.2).

Subsurface stratigraphic and biostratigraphic data was taken from well logs and published papers (e.g., Azambuja Filho et al., 1998; Petersohn et al., 2015). Figure 5.3 summarizes the seismic to well tie for the Upper Aptian to Upper Eocene stratigraphic section with formation tops derived from ANP well reports. Well log data is converted from time to depth using the checkshot and velocity function from ANP well 1-BRSA-851-SES.

Basin thermal modeling setup and key parameters

The 1D Genesis modeling package developed by Zetaware, Inc was kindly provided to CBTH by Zetaware and used to model two wells from the offshore Sergipe-Alagoas Basin. An initial 1D modeling for the thermal history used a range of parameters that included the nature and thickness of continental crust and lithosphere, lithologies and thermal properties of the sedimentary section, and the source rock types. The 1D model stratigraphy and lithology information were based on the ANP well reports and the horizons interpreted from the grid of 2D seismic reflection data (Figure 5.2).

The Genesis modeling default values were used for the compaction parameters of the formation lithologies shown on Figure 5.3 and used in the modeling. A normal hydrostatic pressure was assumed for the 1D models and a fixed temperature of 1330°C was assumed at the

base of the lithosphere (Turcotte and Schubert 2002). The total lithospheric thicknesses were extracted from the 3D gravity modeling results described in this chapter.

Crustal heat-flow variations are relevant for the modeled offshore study area because continental crust has a higher conductivity and a higher radiogenic heat production than oceanic crust (Turcotte and Schubert 2002). Paleowater depth estimations were made from biostratigraphic analyses compiled from ANP reports and related publications (Mello, 2016; Silva et al., 2020; Fauth et al., 2021).

1D models created in Genesis were imported into the 3D Trinity modeling package, where formation tops were tied with regionally mapped structural isopachs. Temperature scalar maps were used to calculate the temperature at a surface through time and to ensure that the 3D Trinity model was consistent with the 1D Genesis model. The average geothermal gradient taken for the basin was 34°C/km as compiled by Hamza et al. (2018). ‘High-’ and “low-case” geothermal scenarios were applied across the entire study area. The model’s temperature curves were fitted to the upper and lower ranges of formation temperature data with an upper limit of 40°C/km and a lower limit of 30°C/km.

Results of sequence stratigraphic interpretation of the Sergipe-Alagoas basin

Four tectonostratigraphic units affecting the deepwater basin

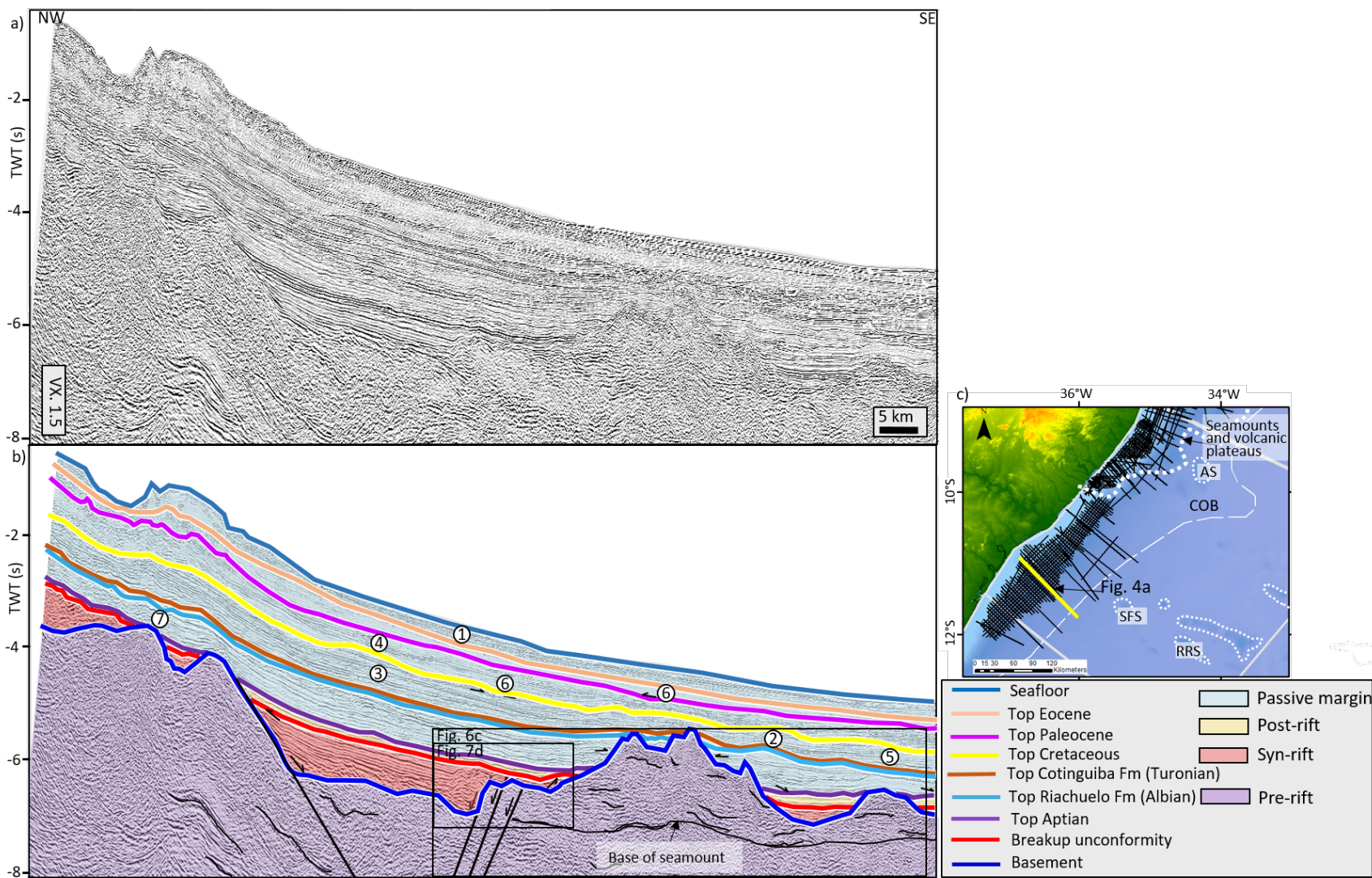
Previous workers have defined four regionally extensive tectonostratigraphic megasequences in the Sergipe-Alagoas Basin and this same megasequence terminology was used for this chapter (Feijó, 1994; Ojeda, 1982; Neto et al., 2007) (Figure 5.3). These four

megasequences are bounded by major unconformity surfaces, which are visible on most of the seismic reflection lines that were interpreted in this chapter (Figure 5.2).

Figure 5.4 shows a representative northwest-trending seismic dip line in the Sergipe sub-basin that illustrates the structural surfaces and megasequences that were mapped in this chapter. Four unconformity-bounded tectonostratigraphic megasequences were mapped across the deepwater Sergipe-Alagoas Basin using the regional 2D reflection seismic reflection data and tied to the ANP wells provided for the study.

These megasequences include 1) **the pre-rift crystalline Precambrian basement and Early Neocomian clastic megasequence** (purple shading) bounded by normal faults; 2) **the syn-rift sequence of Neocomian-Middle Aptian age** (red shading) filled by either clastic sedimentary rocks with clinoforms or layered magmatic rocks characterized by convex-upward seaward dipping reflectors (SDRs); 3) **a thin, post-rift, early sag megasequence of Middle to Late Aptian age** (yellow shading); and 4) **the passive margin of Late Aptian to present age** (blue shading) that includes deepwater channels, MTDs, turbidites, and deepwater channel complex. Each megasequence is discussed in more detail below.

Figure 5.4 Representative, north-south seismic profile along the Sergipe-sub basin showing the five megasequences and their major bounding surfaces as mapped in this chapter. **a)** Uninterpreted seismic line. **b)** Interpreted seismic line. The pre-rift megasequence is shaded in purple and bounded by normal faults and volcanic seamounts. The syn-rift megasequence is shaded in light red and onlaps onto the late Cretaceous-Cenozoic seamounts. The post-rift megasequence is the thin sedimentary unit that is shaded in yellow and the passive margin megasequence is shaded in blue. The numbers refer to seismic facies 1-7 that are observed on these areas of the line. **c)** Basemap showing the location of the seismic line in a and b in yellow. Seamounts and volcanic plateaus are highlighted in the white dotted polygon. Abbreviations: AS: Alagoas Seamount; RRS: Romano Russo Seamount; SFS: São Francisco Seamount.



Seven seismic facies of the Sergipe-Alagoas basin

Seven key seismic facies (SF1-7) are defined in Figure 5.5 using the 2D seismic grid along with well logs. The seven seismic facies provide inferred constraints on the deepwater, depositional environments where there is limited or distant well control. The observed seismic facies areas shown as numbers on the representative seismic line in Figure 5.4.

SF1 is composed of layer parallel, conformable, low to medium amplitude, semi-continuous to continuous reflectors. The interpretation of SF1 is distal hemipelagic packages of distal, turbidite-deposited sheet sands. SF1 is commonly observed in the deepwater region, where units range in age from Aptian to Miocene.

SF2 is a series of convex, discontinuous high- to medium-amplitude reflectors commonly observed in the Paleocene and Miocene strata near the top of the slope. SF2 is interpreted as a confined channel complex with onlapping channel fills.

SF3 exhibits sub-parallel bounding reflectors that are internally chaotic with discontinuous reflectors of Upper Cretaceous to Eocene age. SF3 is observed in the shelf, slope, and abyssal plain environments and is interpreted as mass transport deposits associated with catastrophic slope and shelf edge collapse.

SF4 contains compressively deformed, duplex structures with contorted reflectors and irregular, mounded tops observed on the slope and toe-of-slope region within Upper Cretaceous strata. SF4 is interpreted as submarine slumps associated with mass transport deposits.

SF 5 is a series of high-amplitude packages of reflections bounded by low-amplitude wedge-shaped packages of reflections. SF5 is observed within Upper Cretaceous and Paleocene strata and is interpreted as stacked deepwater channel-levee complexes with channel fills. This

facies overlies known Late Cretaceous source rocks and constitutes an important reservoir target in the deepwater area.

SF6 forms a high-amplitude V-shape concave reflector overlain by a series of low-to-medium amplitude reflectors observed in the slope region underlain by Upper Cretaceous strata. SF 6 is interpreted as deepwater channel complex cuts with onlapping channel fills.

SF7 is composed of medium-amplitude, continuous-to-discontinuous, downlapping reflection terminations. SF7 is observed on the shelf edge within the Miocene and Pliocene section and is interpreted as a package of oblique clinoforms deposited across the front of a prograding shelf margin delta.

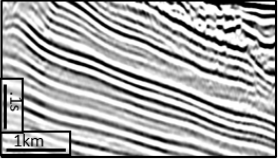
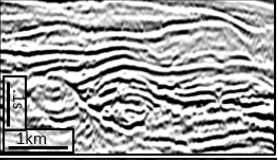
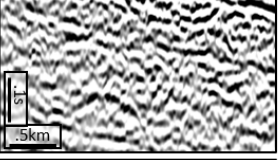
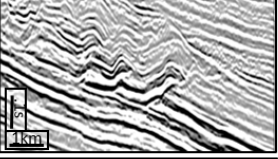
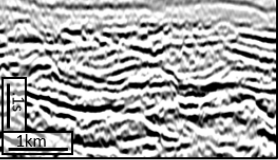
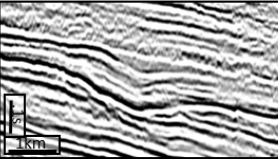
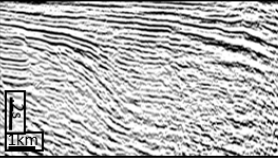
Seismic Facies	Characteristics	Interpretation
① 	Layer parallel, conformable, low to medium amplitude, semi-continuous to continuous reflectors	Distal hemipelagic sediments/ packages of distal turbidite deposited sheet sands
② 	Series of convex, discontinuous high to medium amplitude reflectors	Confined channel complex
③ 	Chaotic package of low to medium amplitude reflections bounded by conformable sequences of parallel reflections	Long-run out mass transport deposits associated with catastrophic slope collapse
④ 	Compressively deformed, duplex structure, contorted reflectors with irregular, mounded top	Submarine mass transport deposits: slumps
⑤ 	Series of high amplitude packages of reflections, bounded by low amplitude wedge shaped packages of reflections	Stacked deepwater channel-levee complexes and channel fill
⑥ 	High amplitude v-shape concave reflector overlaid by series of low to medium amplitude reflectors	Deepwater channel complex cut and the onlapping channel fill
⑦ 	Medium amplitude, continuous to discontinuous, downlapping reflection terminations	Oblique clinoform, prograding shelf margin delta front

Figure 5.5 Representative seismic reflection facies 1 through 7 (SF 1-7) of the Sergipe-Alagoas Basin with their geologic interpretations that I documented in this chapter using lines from the 2D seismic grid and well logs. See text for discussion.

Pre-rift, basement rocks (Early Neocomian)

For this chapter, all pre-rift and sedimentary rocks are considered part of the basement.

This basement megasequence is shown by the purple shading on the seismic profiles shown in this chapter (Figure 5.5).

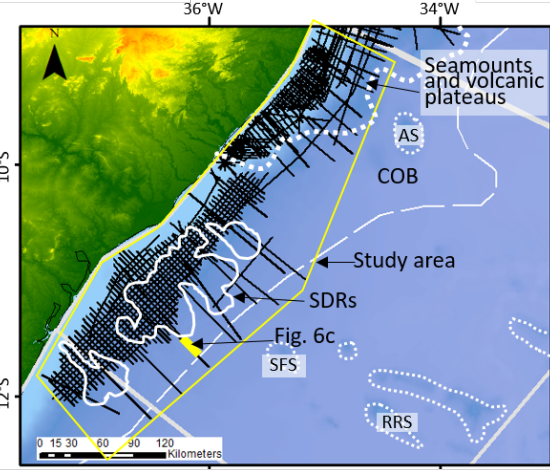
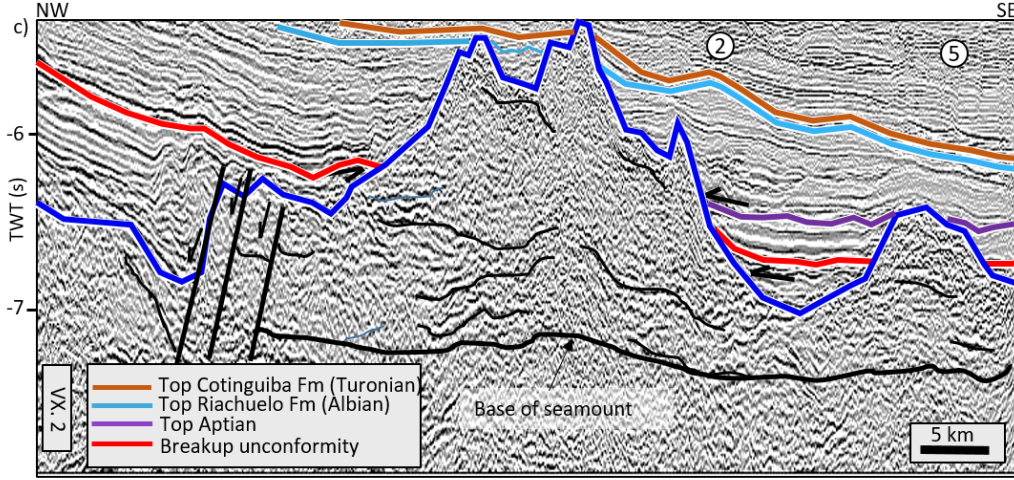
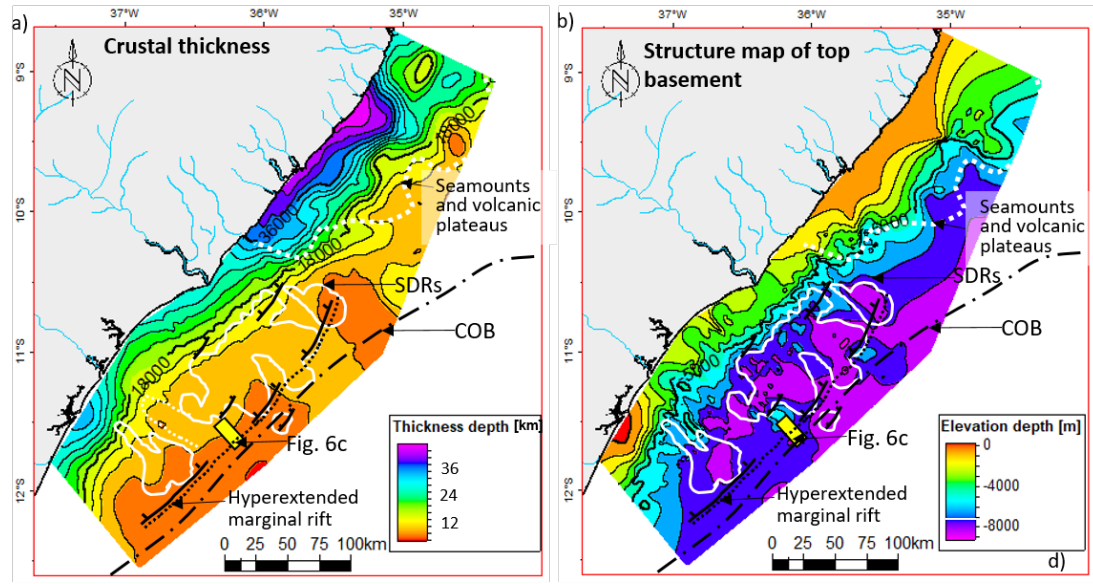
The depth to the top basement in the offshore Sergipe-Alagoas Basin ranges from -49 m in the shelf area to -8934 m in the deepwater area (Figure 5.6a) with a crustal thickness ranging from 4.8 to 2.8 km as described in greater detail in this chapter (Figure 5.6b). The circular high anomalies on the basement structural map correspond to late Cretaceous-Cenozoic seamounts as described in this chapter.

The top of the basement is locally marked by a high-amplitude, high-frequency reflector that is underlain by chaotic and discontinuous, intra-basement reflectors as observed on the seismic lines shown in Figures 5.4 and 5.6. The top basement reflector is disrupted by seamounts on the area of oceanic crust. The seamounts form mounded features with high-amplitude reflection conforming to their mounded shapes (Figure 5.7c). Calderas mark their peaks in some cases.

Normal faults are locally present along the edges of the seamounts and create possible pathways for parasitic seamount eruptions (Figure 5.6c). The base of the seamount is characterized by a semi-continuous, medium-amplitude, wavy reflector (Figure 5.6c). Syn-rift and post-rift sediments onlap the edges of the seamounts. The Albian-Cenomanian Riachuelo and Cenomanian-Coniacian Cotinguiba source rocks were uplifted and likely either eroded or buried by the volcanic flows that emanated from the seamount (Figure 5.6c).

Figure 5.6 Pre-rift, basement rocks. **a)** Regional structure map of the top basement surface based on mapping of the 2D seismic grid. Late Cretaceous-Cenozoic seamounts and volcanic plateaus are indicated by the white, dashed lines and SDRs filling half-grabens are shown by white polygons. Major normal faults are shown as black lines. **b)** Crustal thickness map made from 3D gravity inversion as described in this chapter. Late Cretaceous-Cenozoic seamounts and volcanic plateaus are indicated by the white, dashed lines and SDRs filling half-grabens are shown by white polygons. Hyperextended marginal rift in the Sergipe-subbasin is indicated by the dashed, black line and major normal faults are shown in black lines. **c)** Representative northwest-trending, strike seismic reflection line showing the top basement surface deformed by an Aptian half-graben. The numbers are seismic facies 2, and 5 as observed on this seismic line and

summarized on Figure 5.3. **d)** Basemap showing the location of the line in C as a yellow polygon. Late Cretaceous-Cenozoic seamounts and volcanic plateaus are indicated by the white, dashed lines and SDRs filling half-grabens are shown by white polygons. **Abbreviations:** **AS:** Alagoas Seamount; **RRS:** Romano Russo Seamount; **SFS:** São Francisco Seamount.



Syn-rift megasequence (Neocomian-Middle Aptian)

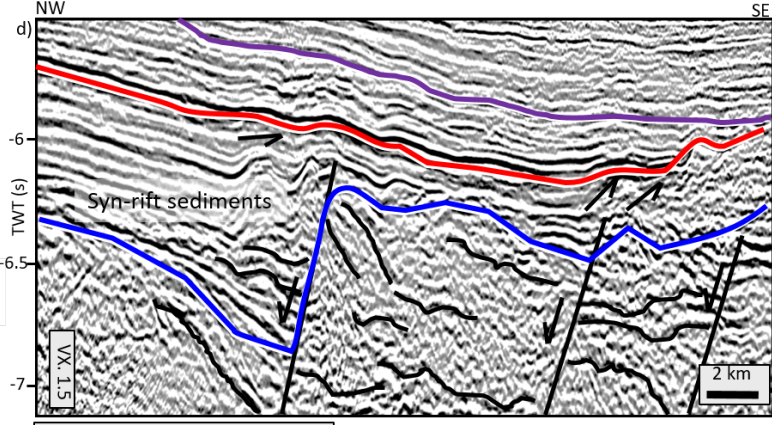
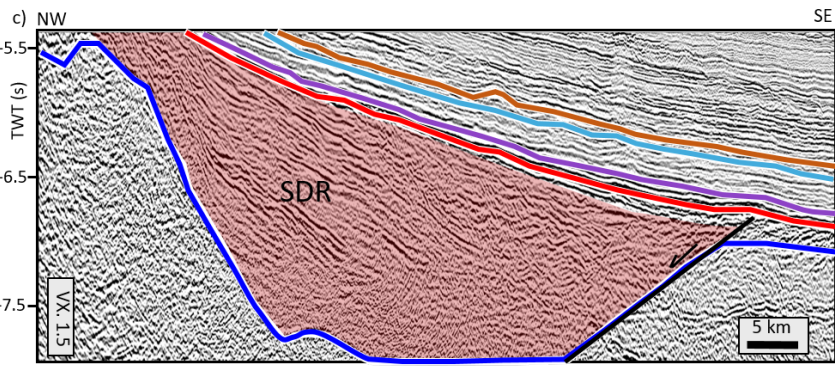
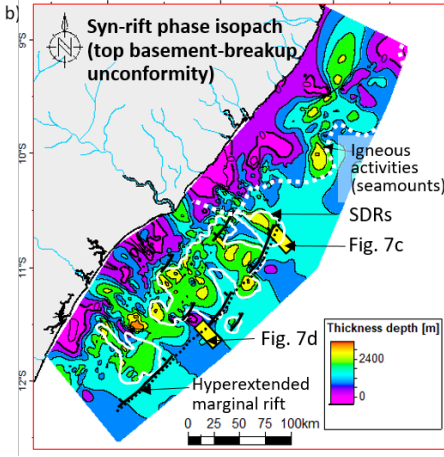
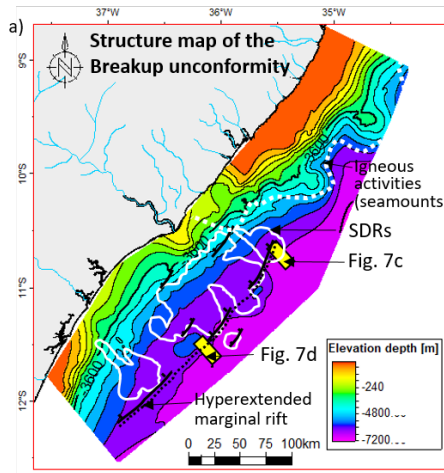
The rifting in the Sergipe-Alagoas basin started in the Early Neocomian and was recorded by a clastic, syn-rift megasequence. These siliciclastic–carbonate rocks of Neocomian-Middle Aptian age are shown by the light red shading on the seismic profiles shown in Figure 3.4. Seamounts of Late Cretaceous-Cenozoic age penetrate the sedimentary layers (Figure 5.7a). The syn-rift megasequence pinches out over the volcanic seamounts (Figure 5.7c). The Alagoas sub-basin to the northeast has a shallower shelf and steeper slope compared to the Sergipe sub-basin to the southwest, as shown on the structure map in Figure 5.7a.

The main clastic depocenter located in the southwestern study area was filled by 3.2 km of clastic sedimentary rocks - or magmatic SDRs (Figure 5.7b). The SDRs are characterized by their convex-up shape with an average dip angle of 10°. The locations of SDRs concentrated in the Sergipe sub-basin to the southwest are highlighted in white polygons in Figure 5.7b and are bounded by normal faults. This megasequence overlies the top of the basement is truncated by the overlying breakup unconformity (Figure 5.7c, d). Lower Cretaceous siliciclastic-carbonate sedimentary rocks were deposited within these fault-bounded rift basins.

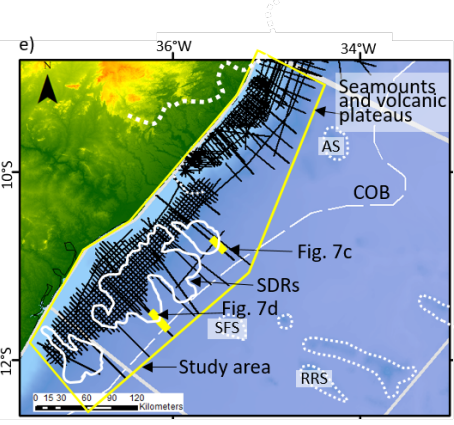
Coarser-grained siliciclastic deposits, characterized as high-to-medium-amplitude, continuous reflectors, are associated with major bounding normal faults. These coarser-grained deposits are typical for this mega-sequence and are represented by the Rio Pitanga Formation and the Penedo Formation (Mohriak et al., 2000; Figure 5.7d).

Syn-rift sedimentary rocks are truncated by the breakup unconformity, also called the “Neo-Alagoas unconformity” (Figure 5.7d). This unconformity marks the end of the syn-rift phase (e.g., Souza-Lima and Hamsi, 2003; Cruz, 2008). The breakup unconformity reflector is characterized by a high-amplitude peak and is correlatable across the entire offshore study area.

Figure 5.7 Syn-rift megasequence. **a)** Regional structure map of the Aptian breakup unconformity surface based on the mapping of the 2D seismic grid. Late Cretaceous-Cenozoic seamounts and volcanic plateaus are indicated by the white, dashed lines and SDRs filling half-grabens are shown by white polygons. Major normal faults are shown as black lines. Hyperextended marginal rift in the Sergipe-subbasin is labeled in the black dashed line. SDRs locations are shown as white polygons. Major faults are shown in black lines. **b)** Syn-rift megasequence, filled with sediments or SDRs (location in white polygon), isopach map. Igneous activities related to seamounts are highlighted in the white dotted polygon. Hyperextended marginal rift in the Sergipe-subbasin is labeled in the black dashed line. SDRs locations are shown as white polygons. Major faults are shown in black lines. **c)** Representative seismic profile showing the SDRs (red polygon) filling the rifted half-graben. **d)** Representative seismic profile (location of the line is shown in yellow) showing the syn-rift sediments filling the rifted half-graben. The syn-rift megasequence is truncated at the top by the breakup unconformity. **e)** Basemap showing the location of the line in yellow polygons. Seamounts and volcanic plateaus are highlighted in the white dotted polygon. SDRs locations are shown as white polygons. **Abbreviations:** **AS:** Alagoas Seamount; **RRS:** Romano Russo Seamount; **SFS:** São Francisco Seamount.



- Top Cotinguiba Fm (Turonian)
- Top Riachuelo Fm (Albian)
- Top Aptian
- Breakup unconformity



Post-rift, early sag megasequence (Middle to Late Aptian)

The post-rift, early sag phase marks the end of normal faulting of the syn-rift phase and the first, Aptian marine incursion into the post-rift sag basin (Blaich, 2008). The end of normal faulting accompanied a considerable slowing of basin subsidence during this quiescent period. As shown in Figure 5.8a, this unconformity surface dips gently to the southeast and was uplifted by Cenozoic volcanic seamounts in the northern part of the offshore basin. The 200-m-thick early sag megasequence is defined as the sedimentary package bounded below by the breakup unconformity and above by the top Aptian unconformity (Figure 5.8b). The sequence is shaded yellow on seismic profiles shown in this chapter (Figure 5.5, 5.8c).

The post-rift megasequence is characterized on seismic lines by a series of parallel to sub-parallel, medium-to-low amplitude reflectors inferred to be carbonate-dominated strata. Along most of eastern Brazil, the syn-rift megasequence is truncated by the sedimentary units of the post-rift megasequence - except in the northwestern study region that underwent extensive, Cenozoic magmatic uplift and intrusion (Figure 5.8b, c).

Passive margin megasequence (Late Aptian to Recent)

Early Cretaceous source rocks. The post-rift megasequence is defined as a 40-km-thick thick, clastic sedimentary package bounded below by top Aptian strata and above by the modern seafloor, which is shaded blue on seismic profiles shown in this chapter (Figure 5.6). The first two units in this megasequence are the two, major source rocks in this region: the Albian-Cenomanian Riachuelo Formation and the Cenomanian-Coniacian Cotinguiba Formation.

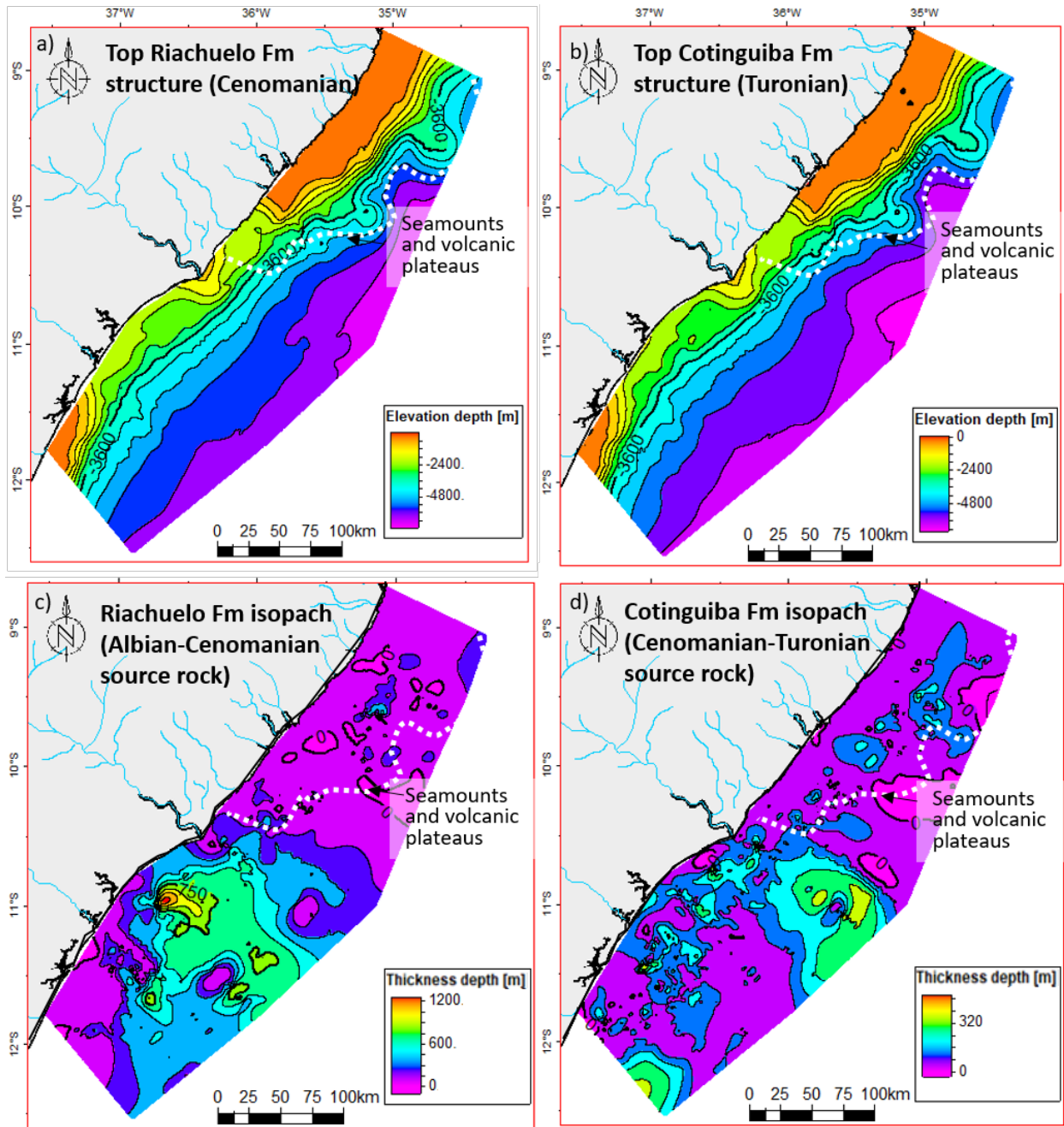
Geochemical and micropaleontological studies of these two formations have identified organic-rich sedimentary rocks deposited under marine dysoxic-anoxic conditions that can be related to the two major worldwide Cretaceous oceanic anoxic event (OAE1a and OAE2) (e.g., Koutsoukos et al., 1991a, b). In general, the two source rocks are conformable with the underlying top Aptian strata and dip to the southeast (Figure 5.9a, b). The two source rock units are characterized on seismic as low to medium reflectors with variable continuity and are inferred to be a mixture of marl and shale (Neto, 2007) (Figure 5, 5.8c).

Isopach maps were generated from the top Riachuelo formation and top Cotinguiba formation structure map to show source rock distribution and to locate major depocenters and pods of potentially mature source rocks. The Albian-Cenomanian Riachuelo source rock is mainly present in the Sergipe sub-basin to the southwest and the southwestern Alagoas Basin. The Riachuelo source rock thickness ranges from approximately 0 – 800 m along the slope.

The source rock gradually thins to 100 m towards the northeast and is only present in a small region in the central Alagoas sub-basin (Figure 5.9c). There is also a shift in the depositional axis to the younger Cenomanian-Coniacian Cotinguiba source rock sequence that is thicker in the deepwater area in the central study area (350 m) and thins onto the margin to the

northwest (50 m) (Figure 5.9d). The Cotinguiba source rock is thinner (200 m) (Figure 5.9d) than the Albian-Cenomanian Riachuelo source and is more widely distributed throughout the slope and deepwater Sergipe sub-basin (Figure 5.9d).

Figure 5.9 Early Cretaceous source rocks. **a)** Regional structure map of the top Riachuelo surface. **c)** Isopach thickness map of the Albian-Cenomanian Riachuelo source rock. **b)** Regional structure map of the Cenomanian-Coniacian Cotinguiba surface. **d)** Isopach thickness map of the Cotinguiba source rock. Seamounts and volcanic plateaus are highlighted in the white dotted polygon.



Late Cretaceous slumps and MTDs

The next unit above the two source rocks is Upper Cretaceous (Coniacian-Maestrichtian) strata dipping to the southeast (Figure 5.10a). The Upper Cretaceous isopach map illustrates the

transport path of deepwater sediments from the Sao Francisco river mouth to a deep-sea submarine fan that occupies the southern Sergipe sub-basin and southern Alagoas sub-basin (Figure 5.10b). 6-km-thick clastic depocenters in the form of shelf-edge deltas are located near the mouth of the Sao Francisco river system in the central study area (Figure 5.10b).

The Late Cretaceous period was characterized by rising sea level, coupled with continuous subsidence, which eventually led to deeper oceanic conditions across the basin (Trindade, 1992; Blaiçh 2008). Shelf carbonates are characterized by chaotic, discontinuous, medium-to-low amplitude reflectors on the narrow shelf (Figure 5.10c). Progradational and proximal coarse siliciclastic facies are characterized by high-amplitude prograding reflectors interbedded with transgressive shales and are characterized by low-amplitude, chaotic reflectors were deposited on the slope and toe of the slope (Figure 5.3). These rocks are overlain by deepwater turbidites deposits characterized by layer parallel, conformable, low-to-medium amplitude, semi-continuous to continuous reflectors (Figure 5.10c).

Slumps and mass transport deposits (MTDs) are commonly observed in the Upper Cretaceous unit that is spread across the slope and into the deep marine region (seismic facies 4). Slumps were observed on the slope, characterized by duplex structure, internal rafted or detached blocks, contorted reflectors with an irregular, mounded top, and low- and high-amplitude reflections that display evidence for compressive deformation at the base of the slope (Cainelli, 1992; Martinez et al., 2005; Figure 5.10c, d).

As shown in Figure 5.10c, Late Cretaceous to Eocene MTDs were distributed along the toe of the slope and deepwater basin with a thickness up to 255 m. Evidence of fault reactivation was observed within the syn-rift megasequence to the northwest, where it is bounded by the breakup unconformity (Figure 5.10c). MTDs are characterized by their lobate shapes, low

amplitude, chaotic reflectors, lateral pinch-out geometries, and irregular upper bedding contacts (seismic facies 3) (Figure 5.10c, e).

MTDs are characterized internally by semi-continuous to discontinuous, low-amplitude, semi-transparent, and wavy seismic reflections, as shown in Figure 5.10e (Seismic facies 3). Onlapping strata were observed both above and below the MTDs (Figure 5.10e). The Upper Cretaceous hybrid turbidite-MTD system is considered one of the major reservoirs within the study area and has been documented in previous studies (e.g., Cainelli, 1992). MTDs are also present in the northern Campos Basin, Espírito Santo Basin, southeastern Brazil and are considered to act as potential hydrocarbon reservoirs (e.g., Viana, 2001; Kamal'deen and Alves, 2014).

Figure 5.10 Late Cretaceous slumps and MTDs. **a)** Regional structure map of the top Cretaceous surface based on mapping of the 2D seismic grid. **b)** Isopach map of top Turonian to top Cretaceous. Yellow line indicates location of the dip seismic reflection line shown in c. **c)** Representative northeast-trending regional dip profile showing the distribution of MTDs and slumps shown by tan polygons. Inverted, rift-related normal faults are observed on the northwestern end of the line. The numbers are seismic facies 3-7 as summarized on Figure . **d)** Zoomed-in view of the slump feature on the slope area showing its compressively deformed reflectors. **e)** Zoomed-in view of the MTD with internal semi-transparent chaotic reflectors and lateral pinch-out geometry to the northwest. **f)** Basemap showing the location of the line in yellow. The seismic coverage area in the yellow polygon.

Paleocene deepwater channel complex

The next unit of the passive margin megasequence is a Paleocene channel complex that dips gently to the southeast (Figure 5.11a). Figure 5.11b shows the total thickness of the passive margin transgression megasequence, which includes two northwest-oriented depocenters along the central Sergipe sub-basin and central Alagoas sub-basin with a thickness up to 2 km in the central Sergipe sub-basin. The passive margin transgression sequence thickens from northeast to southwest before quickly thinning over the volcanic seamounts and onto the abyssal plains (Figure 5.11b).

The most prominent feature of this section is the Paleocene deepwater channel complex, indicating eustatic sea-level fall during the earliest Cenozoic as documented from previous studies (Mello, 2016; Silva et al., 2020; Fauth et al., 2021). Figure 5.11c shows the deepwater channel complex observed in the Alagoas sub-basin that is 1.5 km wide and 260 m deep. Sedimentary strata were observed onlapping the base of the deepwater channel complex (Figure 5.11d). The deepwater channel complex cut was filled by Eocene clastic sedimentary rocks (Seismic facies 6) (Figure 5.11d).

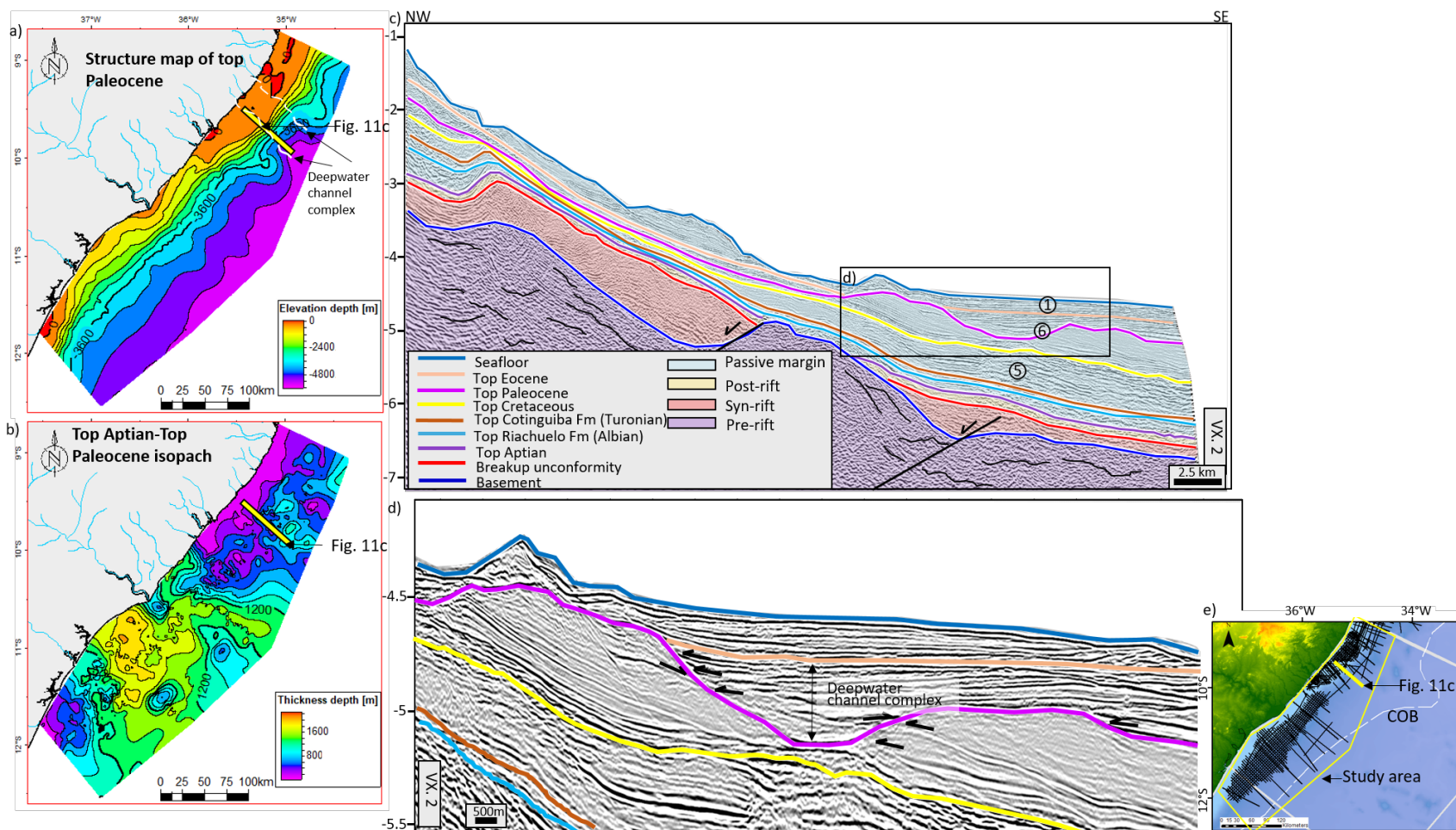


Figure 5.11 Paleocene deepwater channel complex. **a)** Regional structure map of the top Paleocene surface based on the seismic mapping. The deepwater channel complex mapped from the seismic grid are shown as white lines. **b)** Isopach map from top Aptian to top Upper Paleocene. **c)** Representative northwest-trending, regional dip seismic profile showing Eocene deepwater channel complex incised into older units. The numbers are deepwater seismic facies 1, 5, and 6 summarized on Figure 5. **d)** Zoomed-in view of the Eocene deepwater channel complex with channel fill onlapping the base of the deepwater channel complex. **e)** Basemap showing the location of the line in yellow with the area of seismic coverage area shown by the yellow polygon.

Eocene to Present passive margin

The next unit of the passive margin megasequence is the Eocene to present-day sedimentary rocks, which are more evenly distributed from northeast-to-southwest except in the northwestern Alagos sub-basin, which has been impacted by surface channel erosion and volcanic plateaus and seamounts (Figure 5.12).

Sediment thickness over 1 km characterizes the deep basin of the Alagoas sub-basin (Figure 5.12b). Submarine channels are commonly observed throughout the study area and locally the channel incises the Eocene strata as shown in Figure 5.12c.

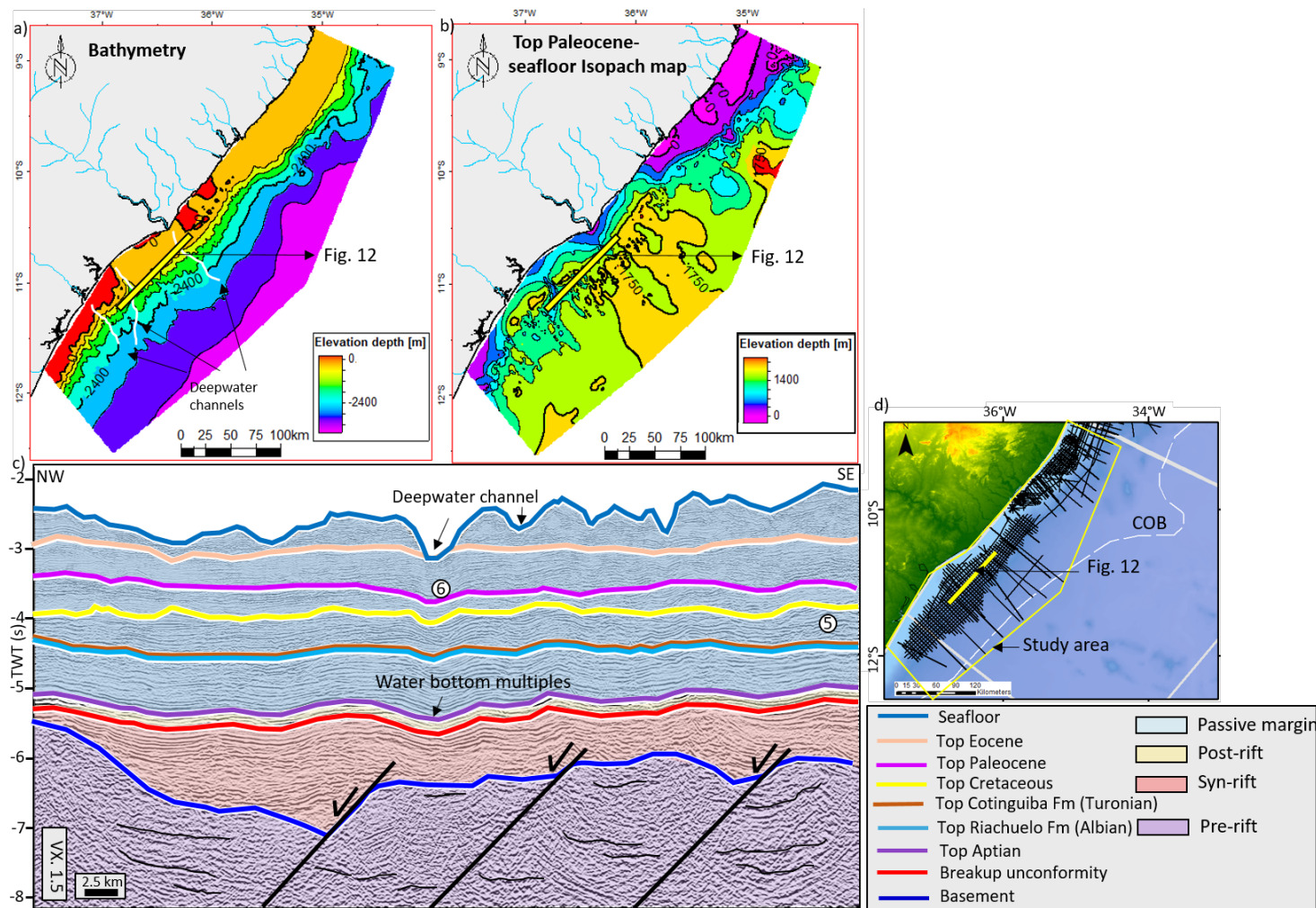


Figure 5.12 Passive margin megasequence. **a)** Regional structure map of the seafloor based on the seismic mapping. **b)** Isopach map of interval from the base of the Upper Paleocene to seafloor. The deepwater channels mapped in seismic are shown by the white lines. **c)** Representative, northeast-trending regional strike line showing the submarine channels eroding the underlying sedimentary units. The numbers indicate seismic facies 5 and 6 as observed on this seismic line. **d)** Basemap showing the location of the line in yellow. The area of seismic data coverage is shown by the yellow polygon.

Burial history and thermal modeling of the Sergipe-Alagoas Basin

1D model thermal maturities of source rocks based on two well logs

Two 1D basin models were generated based on two ANP logs from well 1-BRSA-1104-SES and well 1-ALS-6-AL) (Figure 5.14). Structural and lithological inputs used for the 1D model were extracted from well reports and seismic interpretations from the grid of 2D seismic data. Appropriate crustal thicknesses and heat-flow values based on the information presented in this chapter were used to model the burial, and thermal histories.

Figure 5.14 illustrates the burial history of the 1-BRSA-1104-SES well from ANP. The 1-BRSA-1104-SES well located in the northwestern Sergipe sub-basin was selected because it corresponds to one of the thicker Cretaceous depocenters as seen on the isopach map in Figure 5. Rapid deposition in this part of the study area occurred from Late Jurassic to Early Paleocene and deposited more than 4 km sediments (Figure 5.13a).

The Late Jurassic and Early Cretaceous intervals are predicted to currently occupy the gas window (Figure 5.13a). The Albian-Cenomanian Riachuelo Formation source rock entered the oil window in the Early Paleocene, while the Cenomanian-Coniacian Cotinguiba source rock reached the oil window in the Middle Eocene (Figure 5.13a). Both source intervals are not yet fully depleted of hydrocarbons based on their modeled transformation ratios (Figure 5.13b). The Riachuelo source rock began its transformation in the Early Paleocene and is 90% transformed in the present-day. The Cenomanian-Coniacian Cotinguiba source rock began its transformation in the Middle Eocene and is 80% transformed in the present-day. These models are calibrated using temperature data from the ANP well reports (Figure 5.13c).

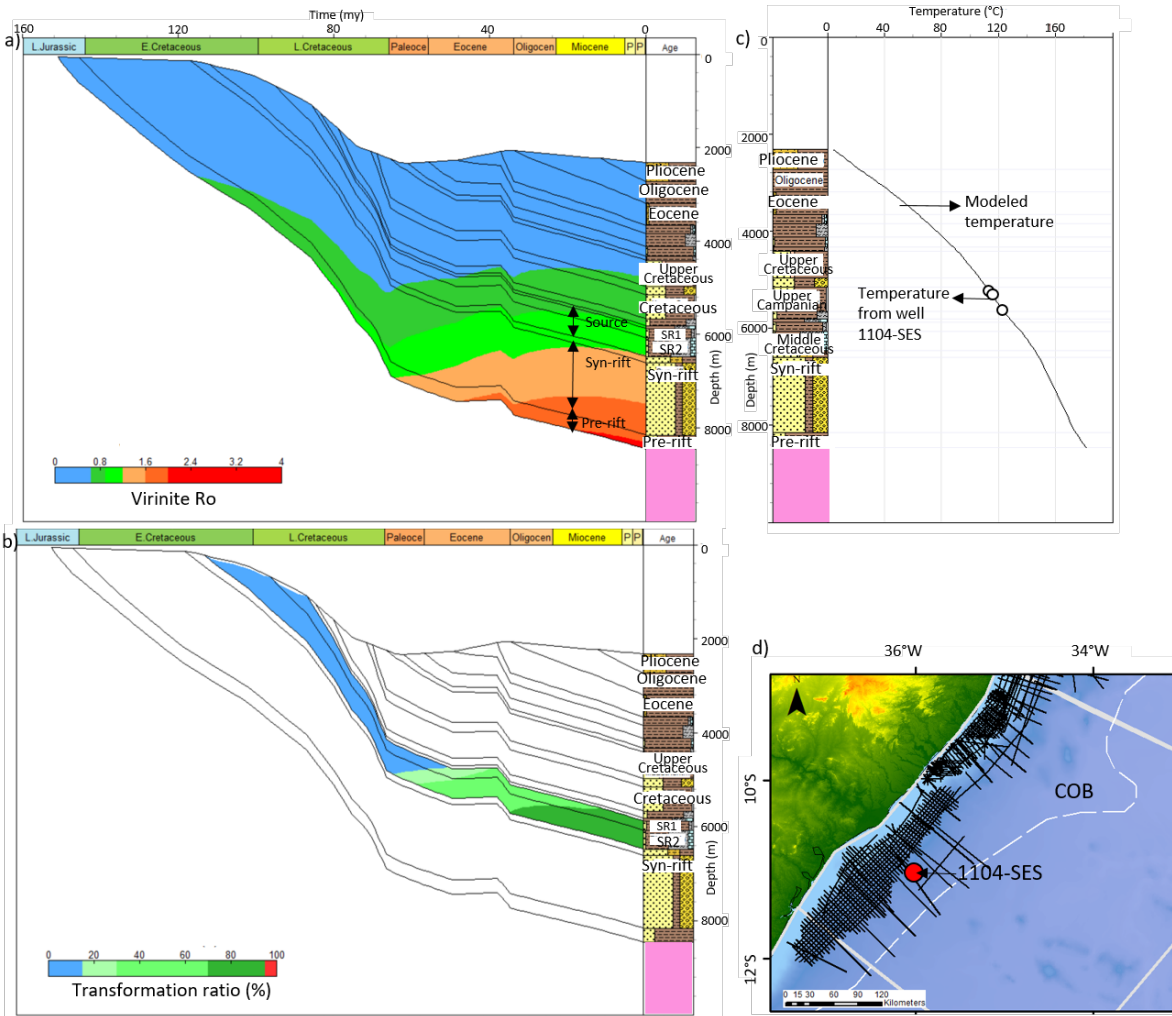


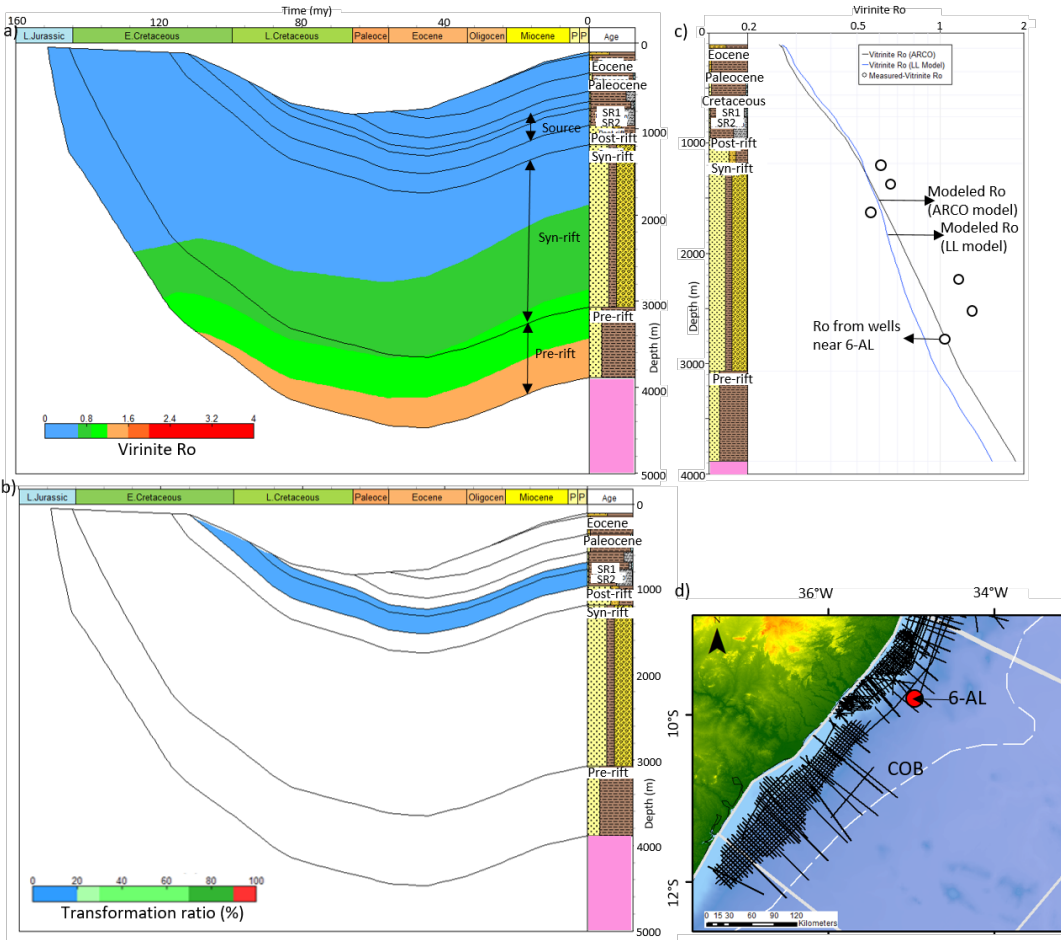
Figure 5.13 Burial plot and thermal history model for ANP well 1-BRSA-1104-SES. **a)** Burial history and predicted maturity for source rocks of the Albian-Cenomanian Riachuelo and the Cenomanian-Coniacian Cotinguiba Formations. **b)** Predicted transformation ratio predicted for the Riachuelo and Cotinguiba Formations. **c)** Modeled temperature-depth relationship calibrated using temperature data from the ANP well reports. **d)** Basemap showing the location of the well 1-BRSA-1104-SES shown as the red dot.

ANP well 1-ALS-6-AL is located in the northwestern Alagoas sub-basin and penetrated a 1.8-km-thick, syn-rift sedimentary succession on the platform and a 0.2-km-thick sedimentary sequence deposited during the post-rift and thermally-controlled phase of subsidence. The pre-

rift interval is predicted to be partially in the gas and oil window in the present-day, while the syn-rift interval lies mainly in the oil window (Figure 5.14a).

The basin model results as seen from the measured Ro values do not predict maturity for any of the late Cretaceous source rock intervals (Figure 5.14a). Both late Cretaceous source rocks are too shallowly buried to be significantly transformed and therefore are not predicted to be productive source rocks in this part of the study area (Figure 5.14b). The basin model is calibrated using vitrinite reflectance data from the ANP well report (Figure 5.14c). The uplifting event during Cenozoic is probably due to the late Cenozoic- Quaternary inversion event (Szatmari and Milani, 1999; Vasconcelos et al., 2019).

Figure 5.14 1-D burial and thermal basin model based on log from ANP well 1-ALS-6-AL (6-AL). **a)** Burial history and predicted maturity of the Albian-Cenomanian Riachuelo and Cenomanian-Coniacian Cotinguiba potential source horizons. **b)** Transformation ratio predicted by the basin model for the Riachuelo and Cotinguiba potential source horizons. **c)** Modeled vitrinite reflectance-depth relationship calibrated with temperature data from ANP well reports. **d)** Basemap showing the location of ANP well 1-ALS-6-AL (6-AL) as the red dot.



Regional maturity trends predicted by lithospheric thermal modeling integrating (3D)

Maps of modeled vitrinite reflectivity tied to the pseudo-well results were created for the Albian-Cenomanian Riachuelo and Continguiaba Formation with modeling of ‘high-’ and ‘low-’ temperature and resulting thermal maturity scenarios. Given the lack of control in the ultra-deepwater region, these two, end-member scenarios help define the range of thermal maturities that could exist under a reasonable range of thermal regimes and constrain the maturity risk across the offshore study area.

In the “high-case” scenario, the Riachuelo source rock is predicted to be mature for oil over the basin floor and slope areas in the southwestern Sergipe sub-basin (Figure 5.15a). The Riachuelo source is predicted to have reached the gas-condensate window in the northwestern Sergipe sub-basin and in the southwestern Alagoas Basin. In a “low-case” scenario, the Riachuelo source rock is predicted to be currently mature for oil in the central area of the deep-water basin (Figure 5.15b). In both end-member cases, the areas of highest thermal maturity area are predicted to exist in this same central part of the study area that is buried by a major submarine fan that is fed by a major, terrigenous fluvial drainage system.

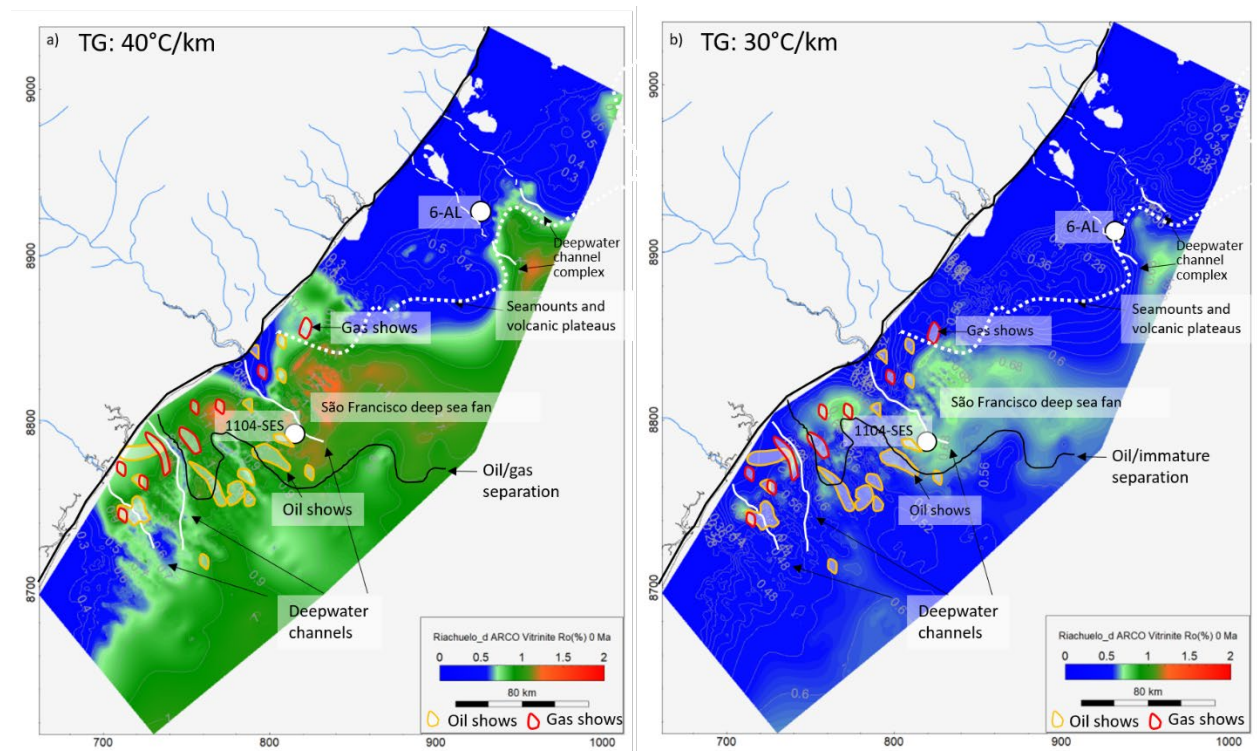


Figure 5.15 Modeled vitrinite reflectivity for the Riachuelo source interval. **a)** Map of modeled vitrinite reflectivity (%) for the Albian-Cenomanian Riachuelo source interval in the ‘high-case’ scenario. **b)** Map of modeled vitrinite reflectivity (%) for the Riachuelo source interval in the ‘low-case’ scenario. Mapped deepwater channels are shown in white lines. The locations of the two 1D models are in white circles. Oil shows from the Geopost website (Geopost, 2021) are shown in orange polygons. Gas shows from the GeoExpro website (Rodriguez et al., 2017) are shown in red polygons. Seamounts and volcanic plateaus are highlighted in white dotted polygons.

Figure 5.16 shows the transformation ratio of the Albian-Cenomanian Riachuelo source rock. In this “high-case” scenario, the source rock has been largely transformed across the southeastern study area. However, there is nearly no hydrocarbon transformation in the northeastern region due to the lack of source rock that is likely the result of magmatic activity during the late Cretaceous and Cenozoic (Figure 5.9c, 5.16a). In this “low-case” scenario, the source rock has entered the oil window but is not fully transformed with an average, predicted transformation ratio of 0.3% in the central study area (Figure 5.16b).

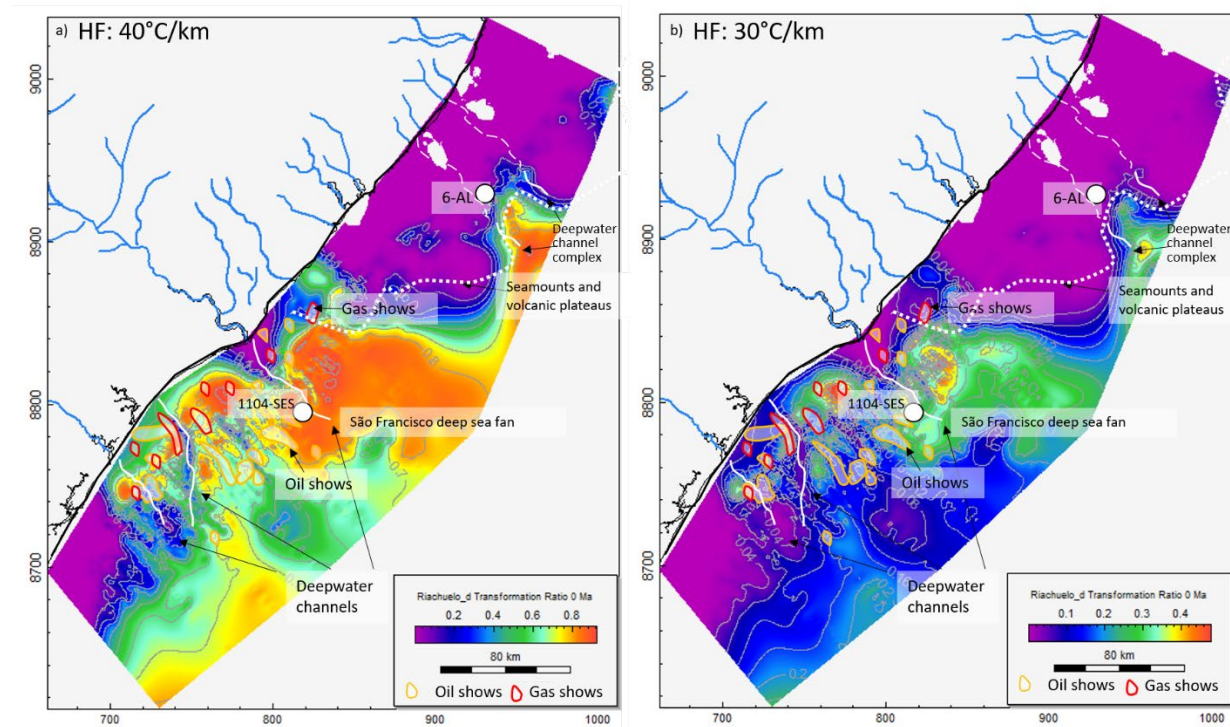
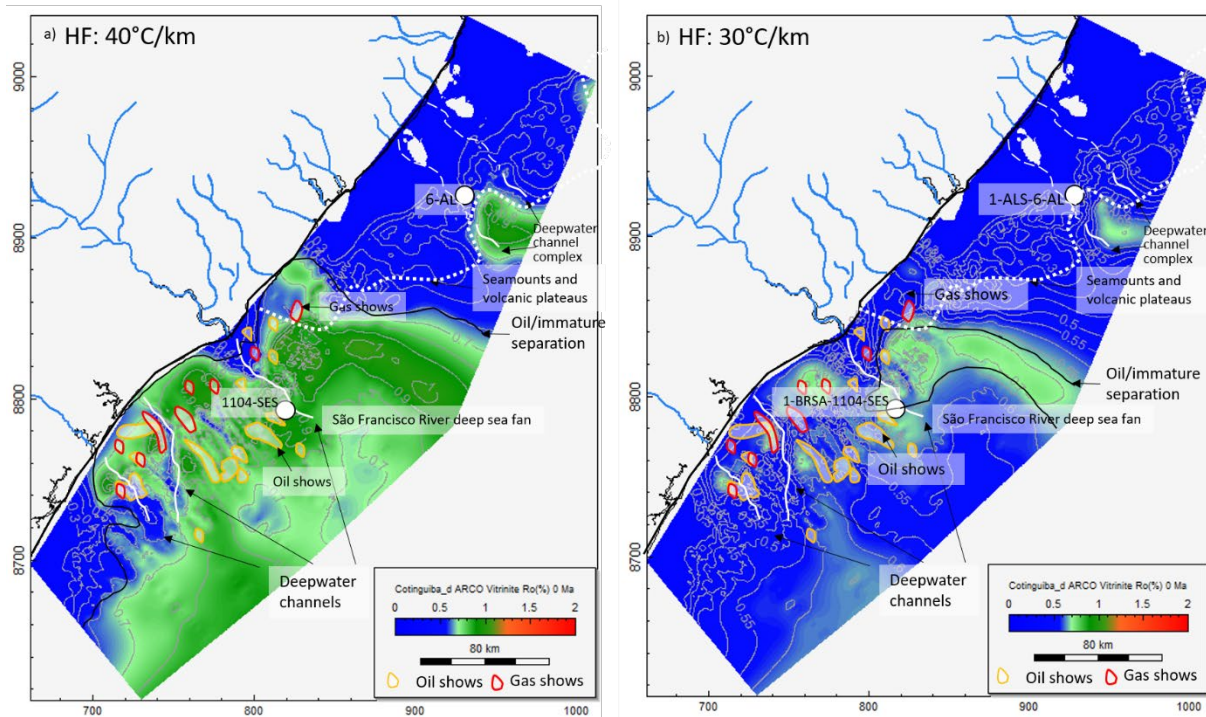


Figure 5.16 Modeled transformation ratio for the Riachuelo source interval. **a)** Map of modeled transformation ratio (%) for the Albian-Cenomanian Riachuelo source interval in the ‘high-case’ scenario. **b)** Map of modeled transformation ratio (%) for the Riachuelo source interval in the ‘low-case’ scenario. Mapped deepwater channels are shown in white lines. The locations of the two 1D models are in white circles. Oil shows from the Geopost website (Geopost, 2021) are shown in orange polygons. Gas shows from the GeoExpro website (Rodriguez et al., 2017) are shown in red polygons. Seamounts and volcanic plateaus are highlighted in white dotted polygons.

Figure 5.17 summarizes the current thermal maturity distribution for the Cenomanian-Coniacian Cotinguiba Formation. In this “high-case” scenario, the Cotinguiba source rock is currently predicted to be mature for oil over the basin floor, slope, and platform areas of the offshore Sergipe sub-basin - except in the southwestern corner (Figure 5.17a). In the Alagoas sub-basin, the source rock entered the oil window to the southwest while most of the northern region has remained immature due to the lack of source rock that is likely the result of magmatic activity during the late Cretaceous and Cenozoic (Figure 5.17a).

In the “low-case” scenario, the Cotinguiba source rock is today predicted to be mature for oil, but only in the deep basinal region in the southeastern Alagoas Basin (Figure 5.17b). Source rock transformation ratio distribution is summarized in Figure 5.18. Similar to the Riachuelo Formation for this “high-case” scenario, the source rock has been completely transformed in the southeastern study area and over a larger area as compared to the Riachuelo Formation (Figure 5.16).

Figure 5.17 Modeled vitrinite reflectivity for the Cotinguiba source interval. **a)** Map of modeled vitrinite reflectivity (%) for the Cenomanian-Coniacian Cotinguiba source interval in the ‘high-case’ scenario. **b)** Map of modeled vitrinite reflectivity (%) for the Cotinguiba source interval in the ‘low-case’ scenario. Mapped deepwater channels are shown in white lines. The locations of the two 1D models are in white circles. Oil shows from the Geopost website (Geopost, 2021) are shown in orange polygons and gas shows from the GeoExpro website (Rodriguez et al., 2017) are shown in red polygons. Mapped deepwater channels are shown in white lines and locations of the two 1D models are shown by the white circles. Late Cretaceous-Cenozoic seamounts and volcanic plateaus are indicated by the white, dashed lines and SDRs filling half-grabens are shown by white polygons.



Source rocks has been completely transformed only in the deep basinal region in the northeastern part of the study area (Figure 5.18a). In this “low-case” scenario, the source rock has entered the oil window but is not fully transformed with an average transformation ratio of 0.35% in the central part of the study area (Figure 5.18b). In both end-member scenarios, the location of the thermally mature region coincides with locations of oil shows reported from the Geopost website (Geopost, 2021) along with direct hydrocarbon indicators (DHIs) described below.

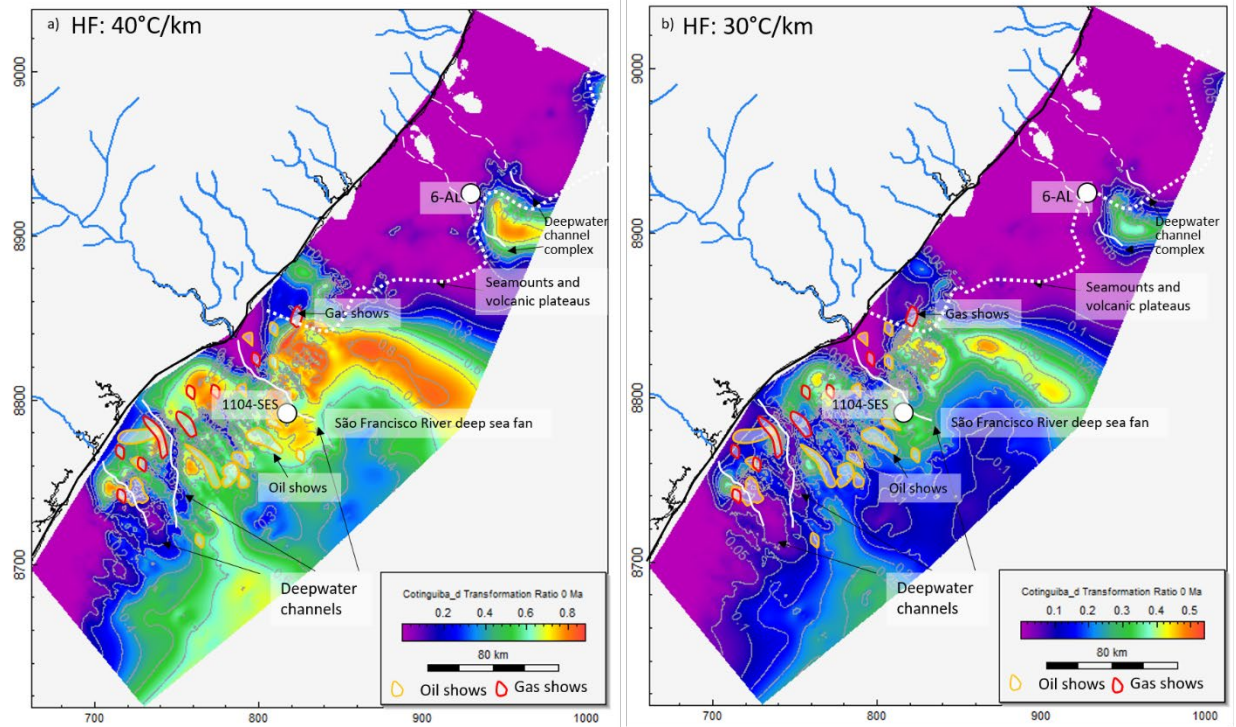


Figure 5.18 Modeled transformation ratio for the Cotinguiba source interval. **a)** Map of modeled transformation ratio (%) for the Cenomanian-Coniacian Cotinguiba source interval in the ‘high-case’ temperature scenario. **b)** Map of modeled transformation ratio (%) for the Cotinguiba source interval in the ‘low-case’ temperature scenario. Mapped deepwater channels are shown by white lines and the locations of the two 1D modeled wells are shown by white circles. Oil shows from the Geopost website (Geopost, 2021) are shown by orange polygons and gas shows from the GeoExpro website (Rodriguez et al., 2017) are shown by red polygons. Late Cretaceous-Cenozoic seamounts and volcanic plateaus are indicated by the white, dashed lines.

Discussion

Structural restoration illustrating main tectonic events affecting basin history

The amount of crustal extension was measured using structural restorations based on the geologic and structural interpretations from ION seismic profile A-A’ in the central Sergipe sub-basin (Figure 5.19a). For the restoration in Figure 5.19a, I progressively removed the sedimentary units using 2-D flexural backstripping and palinspastic reconstruction.

The average, modern water depth along seismic profile A-A' is over 4 km deep, with the shallowing basinward near the large seamount. Nine sedimentary units were interpreted from the seismic line that thin to the southeast and are separated by ten formation tops that include: seafloor, top Miocene, top Oligocene, top Eocene, top Paleocene, top Cretaceous, top Maestrichtian, the Turonian/Cenomanian unconformity, top Cenomanian, and the basement (Figure 5.19, 5.6).

The sedimentary units are slightly faulted on the southeastern edge of the seamount. Two large normal faults dip northwestward on the northwestern side of the profile and form two half-grabens filled with sedimentary rocks and SDRs. The normal faults do not extend above the top Cenomanian unconformity, which acts as a “breakup unconformity” that separates the syn-rift units from the post-rift units. This relationship indicates that rifting had ceased at least before the end of the Cenomanian and seafloor spreading had initiated (Matos et al., 2021).

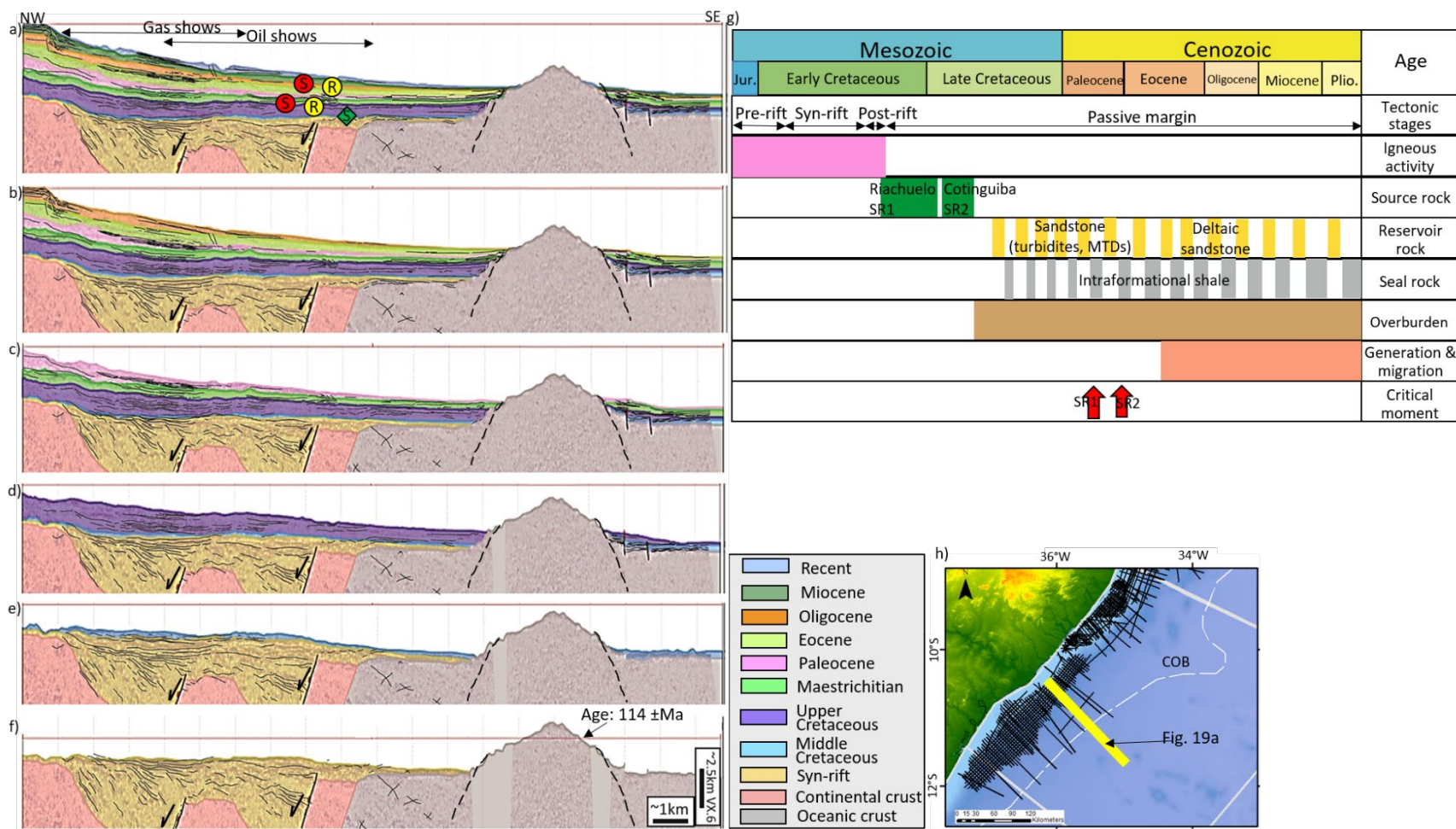
Figure 5.19b shows the result of backstripping and decompaction of the interval from the base Miocene to the seafloor. Figure 5.19c shows the result of the backstripping and decompaction of the Eocene-Oligocene interval, which contains the younger reservoirs of shelf-edge deltaic sandstone (Figure 5.19g).

Figure 5.19d shows structural restoration after backstripping and decompaction of the Paleocene and Maestrichtian interval, which contains the major reservoir units that include MTD (seismic facies 3, Figure 5.3) and sandy turbidite deepwater channel fills (seismic facies 6) (Figure 5.19g).

Figure 5.19e shows structural restoration after backstripping and decompaction of the Upper Cretaceous sedimentary strata, which contain some of the main reservoir units of the offshore basin (Cainelli, 1992) (Figure 5.19g). Slip along the two large normal faults was

restored, and 2 km (3%) of extension was calculated. Figure 5.19f shows the final structural restoration following removal of fault slip and backstripping and decompaction of Late Cretaceous strata which contains the two major source rock units (Figure 5.19g).

Figure 5.19 Structural restoration of seismic line A-A' (location of line shown in map of Figure 5.2). **a)** Uninterpreted seismic line. **b)** Interpretation after backstripping and de-compacting water and Miocene sediments. **c)** Interpretation after backstripping and de-compacting Oligocene and Eocene sediments. **d)** Interpretation after backstripping and de-compacting Paleocene and Maestrichtian sediments. **e)** Structural restoration after backstripping and de-compacting Upper Cretaceous sediments with slip along faults restored and the amount of extension calculated. **f)** Interpretation after backstripping and de-compacting Middle Cretaceous sediments. **g)** Critical moment diagram for the Sergipe-Alagoas Basin summarizes key elements of the petroleum systems including: Albian-Turonian source rocks; sandy turbidites, MTDs, and shelf-edge deltaic sandstone as reservoirs, and intercalated shale units as seals. Overburden was deposited from Coniacian to present. The critical moment for the main Albian-Cenomanian Riachuelo source rock (SR1) is Middle Eocene and Late Eocene for the Cenomanian-Coniacian Cotinguiba source rock (SR2). **h)** Basemap showing the locations of the seismic line are in the yellow polygon.



Main elements of the Sergipe-Alagoas petroleum system

The combination of seismic observations, stratigraphic interpretation, and basin modeling presented in this chapter describe a likely working petroleum system centered in the deep basinal area of the Sergipe sub-basin and southwestern Alagoas Basin (Figure 5.20). According to the model, the two Cretaceous source rocks, the Albian-Cenomanian Riachuelo Formation and the Cenomanian-Coniacian Cotinguiba Formations (Figure 5.19g) reached the oil window during the Eocene.

Reservoir intervals are inferred to be present in the Upper Cretaceous through Eocene and include MTDs (facies 3; Figure 10), and deepwater channels (facies 5,6, Figure 11), that are all fed by long run-out (100's of kilometers) turbidite systems originating from the sediments flux offshore through slumps, debris flows, and high- and low-density turbidity currents. Thicker sedimentary units are concentrated in the Sergipe sub-basin fed by the Sao Francisco shelf-edge delta system (Cainelli, 1992) (Figure 5.10).

The main seals are inferred as pelagic to hemipelagic shales of the same unit (seismic facies 1, Figure 5.19g), with the traps being mostly stratigraphic onlaps onto the passive margin slope. Hydrocarbon accumulation in this slope setting is limited mainly by the presence of the source rock and the geometry of the pinch-out or erosional absence of the sandstone reservoir. Basin modeling indicates that the onset of petroleum generation was reached with burial depth around 2000 m and with the peak of oil generation occurring during the Middle to Late Eocene (Figure 5.13, 5.19g).

Figure 5.20a summarizes the source rock “sweet spots”, or lower-risk play fairways within the study area based on the distribution of predicted, mature source rocks. This source rock “stoplight map” shows the locations of high, medium, and low risk areas of source rocks

shown in red, yellow, and green colors, respectively. Oil shows from the Geopost website (Geopost, 2021) are shown as orange polygons and gas shows from the GeoExpro website (Rodriguez et al., 2017) are shown red polygons. Hydrocarbon shows are concentrated in the southern Sergipe sub-basin, which correlates to the thickest source rock unit mapped from the 2D seismic grid and therefore have the lower risk factor. The contour line illustrates the predicted, optimal value of vitrinite reflectance for the Riachuelo source rock in the “high-case” scenario. The locations of oil shows from the Geopost website (Geopost, 2021) also coincides with the thermally-matured zone predicted by the proposed 3D basin model (Figure 5.15).

Figure 5.20b summarizes the reservoir rock ‘sweet spots’ within the study area. The reservoir rock “stoplight map” shows the locations of high, medium, and low source rock risk in red, yellow, and green colors, respectively. Gas shows are concentrated nearshore because the shelf-edge delta system development has created a localized area of thick overburden (Figure 5.20b). The hydrocarbon shows reported on the Geopost website (Geopost, 2021) correlate well with these thicker, shelf-edge, sandstone reservoir units. The southwestern ultra-deepwater region is considered as a wide, hydrocarbon play fairway because of the presence of thick source rock rocks and overlying reservoirs consisting of Cretaceous clastic MTDs (Figure 5.20).

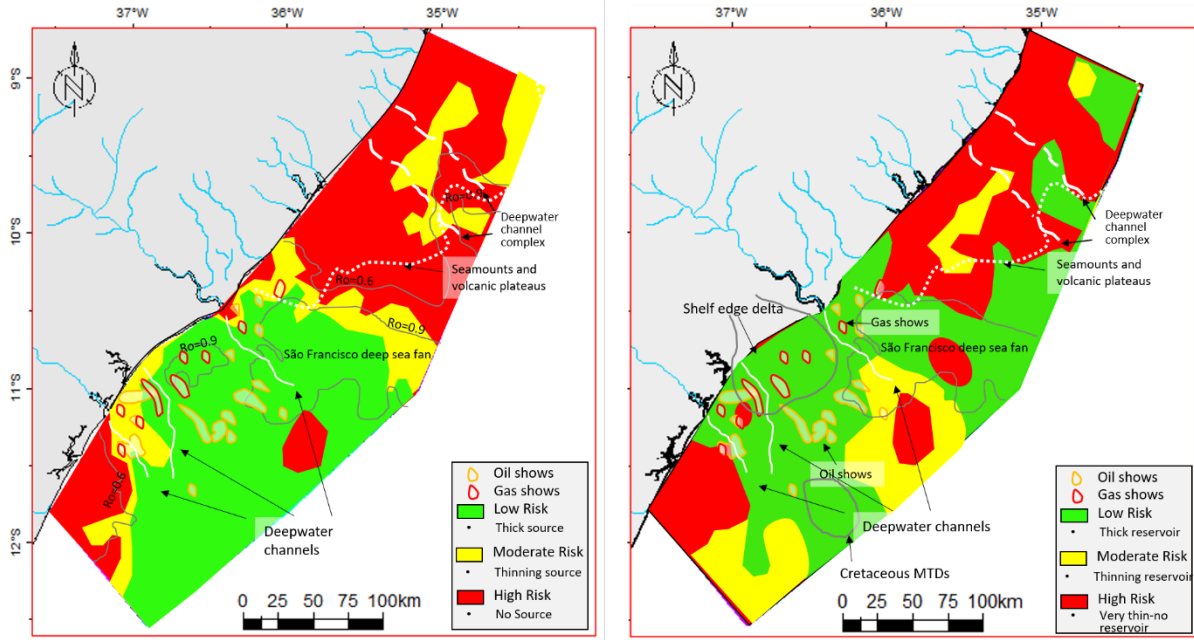


Figure 5.20 Source rock and reservoir rock “sweet spots”. **a)** Source rock stoplight map showing the locations of high risk hydrocarbon zones based on absent or thin source rocks (red polygons), medium risk source rock areas (yellow polygons), and low source source rocks areas (green areas). The contour line illustrates the predicted vitrinite reflectance value of the Albian-Cenomanian Riachuelo source rock in a ‘high-case’ temperature scenario. The locations of higher thermal maturity areas correlate with thicker source rock units and coincide with known oil shows and seeps as compiled from the Geopost website (Geopost, 2021). **b)** Reservoir rock stoplight map using the same color coding as for the source rocks in a). The locations of higher thermal maturity correlate with thick reservoir rock units and match known oil and gas shows locations as compiled from the Geopost and GeoExpro website indicated by the orange polygons for oil and red polygons for gas (Rodriguez et al., 2017; Geopost, 2021). Seamounts and volcanic plateaus are highlighted in white dotted polygons.

Direct hydrocarbon indicators (DHI) compared with basin model predictions

The results of basin modeling predict that an active petroleum system is present in both the Sergipe sub-basin and the southwestern Alagoas sub-basin (Figure 5.20). To support the predicted mature areas from basin models (Figures 5.15-5.18), examples of direct hydrocarbon indicators were compiled from the grid of 2D seismic lines.

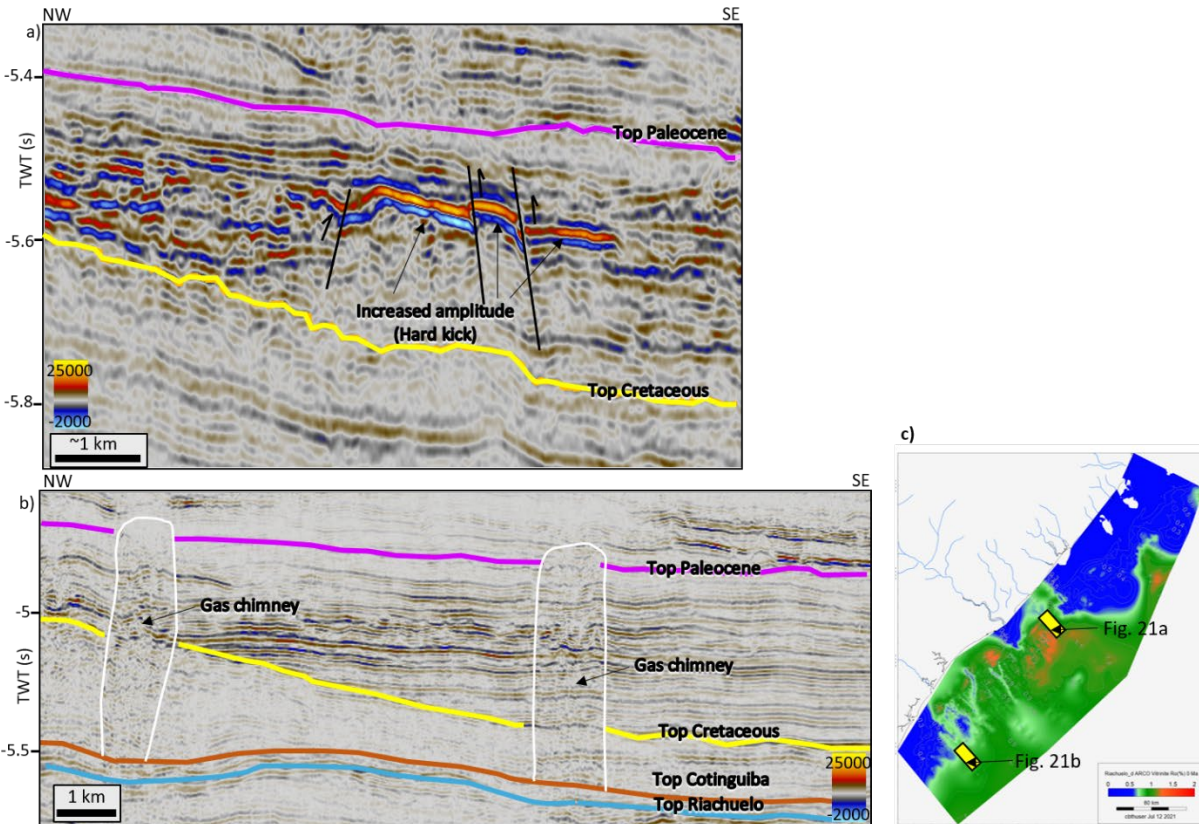
Figure 5.21a shows the Paleocene stratigraphic section in the southwestern Alagoas Basin with normal and thrust faults deforming a complex structural high. The thrust fault could be

related to the later Cenozoic-Quaternary reactivation proposed by previous studies (Szatmari and Milani, 1999; Vasconcelos et al., 2019). The seismic section shows bright reflectors with amplitude dim-outs adjacent to normal and thrust faults. The amplitude dim-out may represent a fluid contact although this single 2D line does show the size of the structural trap.

Gas chimneys provide another type of DHI observed from the grid of 2D seismic lines. A gas chimney results from a subsurface leakage of gas from a poorly-sealed hydrocarbon accumulation (Nourollah et al., 2010). For this reason, gas chimneys are expressed on seismic reflection data as areas of poor data quality or “wipe-outs”.

Figure 5.21b shows two examples of gas chimneys produced by the vertical migration of hydrocarbons from underlying horizons of known source rocks into the overlying Cretaceous and Paleocene clastic reservoirs. The locations of both DHIs shown in Figure 5.21a and b correlate with areas of high thermal maturity shown on the 3D basin model (Figure 5.16).

Figure 5.21 Examples of direct hydrocarbon indicators as compiled from seismic lines in the southwestern Alagoas sub-basin to support basin modeling predictions for mature, late Cretaceous source rocks. **a)** Bright reflectors showing amplitude dim-outs adjacent to normal and reverse faults deforming Paleocene strata. **b)** Example of gas chimneys indicating vertical migration of hydrocarbons from late Cretaceous source rocks into overlying late Cretaceous and Paleocene reservoirs. **c)** Modeled transformation ratio (%) for the Riachuelo source interval in the ‘high-case’ temperature scenario with the locations of DHIs shown on the seismic lines in a) and b). The locations of the two seismic lines are shown by the yellow polygons.



Conclusions

Interpretation of a regional 2D grid of seismic reflection data reveals the overall structure and stratigraphy of the Sergipe-Alagoas Basin in the northeastern Brazilian margin that is divided into four, distinctive megasequences bounded by regional unconformities: 1) the pre-rift crystalline Precambrian basement and Early Neocomian sedimentary rock sequence; 2) the syn-rift sequence of Neocomian-Middle Aptian age; 3) the post-rift sag basin of Middle to Late Aptian age, and 4) the passive margin sequence of Late Aptian to Recent age.

1D thermal modeling at two representative locations in the deepwater area indicates that the main Albian-Cenomanian Riachuelo (SR1) and Cenomanian-Coniacian Cotinguiba source rock (SR2) entered the oil window in the period from Middle to Late Eocene. Hydrocarbon

generation and expulsion continue into the present-day period of maximum burial and thermal maturity beneath a thick, passive margin, clastic sedimentary overburden.

Regional 3D modeling using estimates of lithospheric thickness and heat-flow properties for the study area predicts; 1) the Riachualo source interval will reach gas-condensate maturity in the distal basinal area and to be oil-mature over extensive areas of the slope and platform region; 2) the Riachualo source interval will reach the oil window over the basin floor, slope and platform areas throughout the Sergipe sub-basin - except in the southwestern corner of the study area.

My prediction for an regional extension of a potential working petroleum system in the across an extensive play fairway through the southwestern part of the study area of the Sergipe-Alagoas Basin is supported by: 1) observations of high-amplitude anomalies on 2D seismic lines from the slope and deepwater areas which indicates a fluid contacts possibly linked to a trapped, oil phase; 2) mapping of two laterally continuous late Cretaceous source rocks with known source rock potential: the Albian-Cenomanian Riachuelo (SR1) and Cenomanian-Coniacian Cotinguiba source rock (SR2); and 3) the presence of thick units of MTDs and deepwater channel complex system fed by the extensive onshore terrigenous drainage system that deposits sand-rich reservoir rocks directly above the two late Cretaceous source rock intervals.

I propose that onlapping, clastic stratigraphic traps are likely present in the distal reaches of the turbidite system within the Upper Cretaceous to the Eocene section and could provide a promising new drilling target for deepwater hydrocarbons in the offshore Sergipe-Alagoas Basin.

Bibliography

- Asmus, H.E. 1984. Geologia da Margem Continental Brasileira. *In* Schobbenhaus, C., Campos, D.A., Derze, G.R., Asmus, H.E., eds., *Geologia do Brasil, Texto Explicativo do Mapa Geológico do Brasil*. MME/DPNPM, Brasília, 443-472.
- Araújo, C.C.D., Moretti, P.A., Madrucci, V., da Silva, N.C., Toczeck, A. and Almeida, A.B., 2012. Pre-salt facies in the Carmópolis Area, northeast Brazil: stratigraphy and depositional model. AAPG International Conference and Exhibition, Milan, Italy, 50544, 193-249.
- Azambuja Filho, N.C. de, Cruz, F.E. da, Arienti, L.M and Hook, S., 1998. Guidebook to the rift-drift Sergipe-Alagoas Basin. *In* Azambuja Filho, N.C., ed., *Virtual field guide of Sergipe-Alagoas basin - CD, Brazil*. Rio-98 AAPG/ABGP International Conference and Exhibition, Rio de Janeiro, 1-69.
- Beglinger, S.E., van Wees, J.D., Cloetingh, S. and Doust, H., 2012. Tectonic subsidence history and source-rock maturation in the Campos Basin, Brazil. *Petroleum Geoscience*, 18(2), 153-172.
- Beglinger, S.E., Doust, H. and Cloetingh, S., 2012. Relating petroleum system and play development to basin evolution: Brazilian South Atlantic margin. *Petroleum Geoscience*, 18(3), 315-336.
- Bueno, G.V., 2004. Diacronismo de eventos no rifte Sul-Atlântico. *Boletim de Geociências da Petrobras*, Rio de Janeiro, 12(2), 203-229.
- Blaich, O.A., 2008. Northeastern Brazilian margin: Regional tectonic evolution based on integrated analysis of seismic reflection and potential field data and modelling. Unpublished M.S. thesis, University of Oslo, 105 p.

- Cainelli, C., 1992, Sequence stratigraphy, canyons, and gravity mass flow deposits in the Piaçabuçu Formation, Sergipe–Alagoas Basin, Brazil. Unpublished doctoral dissertation, the University of Texas, 263 p.
- Cainelli, C. and Mohriak, W.U., 1999. Some remarks on the evolution of sedimentary basins along the Eastern Brazilian continental margin. Episodes-Newsmagazine of the International Union of Geological Sciences, 22(3), 206-216.
- Caixeta, J.M., Ferreira, T.S., Machado Jr, D.L., Teixeira, J.L. and Romeiro, M.A., 2014. Albian rift systems in the northeastern Brazilian margin: an example of rifting in hyper-extended Continental crust. AAPG International Conference & Exhibition, Istanbul, Turkey, 7, 1-13.
- Castro, H.R., Figueiredo, F.T., Franco, L.S., Gomes, P.V., Soares, I.R., Andrade, L.L., Ramos, M.A. and Moraes, J.D., 2019. Facies distribution as a response to early rift tectonic activity in the Sergipe-Alagoas Basin, northeastern Brazil. Sedimentary Geology, 383, 216-237.
- Chang, H.K., Kowsmann, R.O., Figueiredo, A.M.F., Bender, A.A., 1992. Tectonics and stratigraphy of the East Brazil Rift System: An overview. Tectonophysics, 213, 97–138.
- Contreras, J., Zühlke, R., Bowman, S. and Bechstädt, T., 2010. Seismic stratigraphy and subsidence analysis of the southern Brazilian margin (Campos, Santos and Pelotas basins). Marine and Petroleum Geology, 27(9), 1952-1980.
- Corbett, P.W., 2015. Reservoir Characterization Challenges in Pre-Salt Brazilian Carbonates. AAPG Geoscience Technology Workshop, Carbonate Plays around the World – Analogs to Support Exploration and Development, New Orleans, Louisiana, 1-68.

- Cruz, L.R., 2008. Caracterização tectono-estratigráfica da seqüência transicional na sub-bacia de Sergipe. Unpublished doctoral dissertation, Federal University of Rio Grande Do Norte, 195 p.
- Dantas, M.V.S. and Holz, M., 2020. High-resolution sequence stratigraphy of a cretaceous mixed siliciclastic-carbonate platform succession of the Sergipe–Alagoas Basin, NE Brazil. *Facies*, 66(1), 1-17.
- Evans, R., 1978. Origin and significance of evaporites in basins around Atlantic margin. *AAPG Bulletin*, 62(2), 223-234.
- Fauth, G., Bruno, M.D.R., Villegas-Martín, J., Savian, J.F., Guerra, R.D.M., Krahl, G., Lima, F.H.D.O., Strohschoen Jr, O., Mello, R.G.D., Lopes, F.M. and Leandro, C.G., 2021. Drilling the Aptian–Albian of the Sergipe–Alagoas Basin, Brazil: paleobiogeographic and paleoceanographic studies in the South Atlantic. *Scientific Drilling*, 29, 1-17.
- Feijó, F. J., 1994, Bacias de Sergipe e Alagoas: Boletim de Geociências da Petrobrás. Rio de Janeiro, 8(1), 149–161.
- Ferreira, T.S., Caixeta, J.M. and Francisco, C., 2013. Tectonic evolution of the Jequitinhonha-Almada-Camamu rifted margin. XIV International Symposium on Tectonics Conference, 1, 1-4.
- Garcia, A.J.V., Garcia, G.G., Dantas, M.V.S., Figueiredo, S.A.S., Leite Santos, K.A., Carvalho, I.O., Ribeiro, D.D. and Rocha, L.L., 2015. Multiscale characterization of coquinas reservoirs in analogues outcrops, Sergipe Alagoas (Brazil) and Lusitanian (Portugal) basins. AAPG/SEG International Conference & Exhibition, Melbourne, Australia, 102-105.

- Garcia, A.J.V. and Rocha, L.M., 2012. Diagenetic Model Related to Unconformity Surfaces and Application in the Exploration of Deep Reservoirs in Sergipe-Alagoas Basin, Brazil. AAPG Annual Convention and Exhibition, Long Beach, California, 1-5.
- Geopost, 2021. <https://www.geopostenergy.com/>, accessed on Jan, 2021.
- Gómez, J., Schobbenhaus, C. and Montes, N., 2019. Geological Map of South America. Scale, 1:5000000.
- Guimaraes, P.D.T.M., 1988. Basin analysis and structural development of the Sergipe-Alagoas Basin, Brazil. Unpublished doctoral dissertation, the University of Texas at Austin, 265 p.
- Hamza, V.M., Vieira, F.P. and Silva, R.T., 2018. Anomalous heat flow belt along the continental margin of Brazil. *International Journal of Earth Sciences*, 107(1), 19-33.
- Katz, B.J. and Mello, M.R., 2000. Petroleum Systems of South Atlantic marginal basins-an overview. In M. R. Mello and B. J. Katz, eds., *Petroleum systems of South Atlantic margins*. AAPG Memoir, 73, 1–13.
- Kamal'deen, O.O. and Alves, T.M., 2014. Mass-transport deposits controlling fault propagation, reactivation and structural decoupling on continental margins (Espírito Santo Basin, SE Brazil). *Tectonophysics*, 628, 158-171.
- Kifumbi, C., Scherer, C.M.D.S., Jones, F.H. and Kuchle, J., 2017. High resolution stratigraphy of initial stages of rifting, Sergipe-Alagoas Basin, Brazil. *Brazilian Journal of Geology*, 47(4), 657-671.
- Koning, T., 2013. Fractured and weathered basement reservoirs: Best practices for exploration and production—Examples from USA, Venezuela, and Brazil. AAPG Annual Convention and Exhibition, Pittsburgh, Pennsylvania, 1-29.

- Koutsoukos, E.A., Mello, M.R., de Azambuja Filho, N.C., Hart, M.B. and Maxwell, J.R., 1991a. The upper Aptian–Albian succession of the Sergipe Basin, Brazil: an integrated paleoenvironmental assessment. *AAPG Bulletin*, 75(3), 479-498.
- Koutsoukos, E.A., Mello, M.R. and de Azambuja Filho, N.C., 1991b. Micropalaeontological and geochemical evidence of mid-Cretaceous dysoxic-anoxic palaeoenvironments in the Sergipe Basin, northeastern Brazil. In Tyson, R. V. and Pearson, T. H., eds, *Modern and Ancient Continental Shelf Anoxia*, London Geological Society Special Publication, 58(1), 427-447.
- Lana, M.D.C., 1990. Bacia de Sergipe-Alagoas: uma hipótese de evolução tectono-sedimentar. Origem e evolução de bacias sedimentares. *Petrobrás*, Rio de Janeiro, 311, 1-332.
- Leyden, R., Asmus, H., Zembruski, S., and Bryan, G., 1976. South Atlantic diapiric structures. *AAPG Bulletin*, 60(2), 196-212.
- Macellari, C., 2017. Exploration trends in South America. AAPG 2017 Annual Convention and Exhibition, Houston, Texas, 1-26.
- Matos, R.M.D., De, 2021. Magmatism and hotspot trails during and after continental breakup in the South Atlantic. *Marine and Petroleum Geology*, 129, 1-24.
- Matos, R.M.D., De, Krueger, A., Norton, I. and Casey, K., 2021. The fundamental role of the Borborema and Benin – Nigeria provinces of NE Brazil and NW Africa during the development of the South Atlantic Cretaceous Rift system. *Marine and Petroleum Geology*, 127, 104872-104902.
- Martinez, J.F., Cartwright, J., and Hall, B., 2005. 3D seismic interpretation of slump complexes: examples from the continental margin of Israel. *Basin Research*, 17(1), 83-108.

- Meister, E.M. and Aurich, N., 1972. Geologic outline and oil fields of Sergipe basin, Brazil. AAPG Bulletin, 56(6), 1034-1047.
- Mello, M.R., Koutsoukos, U. and Figueira, C.A., 1991. Brazilian and West African Oils: Generation, Migration, Accumulation and Correlation. 13th World Petroleum Congress, OnePetro, 3(1), 153-164.
- Mello, R. M., Koutsoukos, E.A., Mohriak, W.U. and Bacoccoli, G., 1994. Selected Petroleum Systems in Brazil. In Magoon, L., B., and Dow, W., G., eds, *The Petroleum System—From Source to Trap*. AAPG Memoir, 60, 499-512.
- Mello, R.M., 2016. A paleobathymetric model and evolution of the Brazilian marginal basins during the Late Maastrichtian to Eocene based on benthic foraminiferal biofacies. Unpublished doctoral dissertation, University of Massachusetts Amherst, 308 p.
- Milani, E.J., Davison, I., 1988. Basement control and transfer tectonics in the Reconcavo–Tucano–Jatoba Rift, Northeast Brazil. *Tectonophysics*, 154, 41–70.
- Mohriak, W.U., Rabelo, J.L., De Matos, R.D. and De Barros, M.C., 1995. Deep seismic reflection profiling of sedimentary basins offshore Brazil: Geological objectives and preliminary results in the Sergipe Basin. *Journal of Geodynamics*, 20(4), 515-539.
- Mohriak, W.U., M.R. Mello, M. Bassetto, I.S. Vieira, and E.A.M. Koutsoukos, 2000. Crustal Architecture, Sedimentation, and Petroleum Systems in the Sergipe-Alagoas Basin, Northeastern Brasil. In: M.R. Mello and B.J. Katz, eds., *Petroleum Systems of South Atlantic Margins*. AAPG Memoir, 73, 273-300.
- Mounguengui, M.M. and Guiraud, M., 2009. Neocomian to early Aptian syn-rift evolution of the normal to oblique-rifted North Gabon Margin (Interior and N'Komi Basins). *Marine and Petroleum Geology*, 26(6), 1000-1017.

- Mullin, P., Mann, R., Pilcher, R. and Gomes, P.O., 2004. Petroleum systems of the Sergipe-Alagoas basin, with comparison to proximal basins of Brazil and West Africa. American Association of Petroleum Geologists ICE abstract.
- Neto, ODAC, Lima, WS and Cruz, FG, 2007. Sergipe-Alagoas basin. PETROBRAS Geosciences Bulletin, 15 (2), 405-415.
- Ojeda, H., 1982. Structural framework, stratigraphy, and evolution of Brazilian marginal basins. AAPG Bulletin, 66(6), 732-749.
- Petersohn, E., Ferreira, M.A., Zalán, P.V., Haeser, B., Avila, R.M., Arnemann, C.M., Bastos, G., Santos, J.M., Freitas, V.A., Fernandez, R.O. and Morelato, R., 2015. A Renewed View on the Petroleum Potential of the Eastern Margin of Brazil. AAPG Annual Convention and Exhibition abstract, 1 p.
- Ponte, F.C., Fonseca, J.D.R. and Moralesa, R.G., 1977. Petroleum geology of eastern Brazilian continental margin. AAPG Bulletin, 61(9), 1470-1482.
- Ponte, F.C. and Asmus, H.E., 2004. The Brazilian marginal basins: current state of knowledge; As bacias marginais brasileiras: estagio atual de conhecimento. Boletim de Geociências da Petrobras, 1-12.
- Rodriguez, K., Saunders, M., Hodgson, N., and Geiger, L., 2017. Integration of key data has resulted in a better understanding of the petroleum system, allowing for the identification of multiple untested play types. GeoExpro, 14(3), <https://www.geoexpro.com/articles/2017/07/sergipe-basin-undrilled-potential-surpasses-giant-offshore-discoveries>, accessed on April, 2021.

- Riguetti, A.L., Dal'Bó, P.F., Borghi, L. and Mendes, M., 2020. Bioclastic accumulation in a lake rift basin: The Early Cretaceous coquinas of the Sergipe–Alagoas Basin, Brazil. *Journal of Sedimentary Research*, 90(2), 228-249.
- Schiefelbein, C.F., Urien, C.M., Dickson, W., Zumberge, J.E., 2020. Geochemical assessment of basins along the western South Atlantic margin. *International Conference and Exhibition, Buenos Aires, Argentina*, 1-38.
- Schrank, A.B., Altenhofen, S.D. and De Ros, L.F., 2017. Diagenetic Preservation and Modification of Porosity in Aptian Lithic Reservoirs from the Sergipe–Alagoas Basin, Northeast Brazil. *Journal of Sedimentary Research*, 87(11), 1156-1175.
- Silva Jr, R., de Moraes Rios-Netto, A., Silva, S.C., Valle, B., Borghi, L. and Abbots-Queiroz, F., 2020. Middle Cretaceous calcareous nannofossils from the cored well UFRJ-2-LRJ-01-SE, Sergipe-Alagoas Basin, Brazil: New biostratigraphy and paleobiogeographic inferences. *Cretaceous Research*, 106, 1-12.
- Souza, R.S.D., De Ros, L.F. and Morad, S., 1995. Dolomite diagenesis and porosity preservation in lithic reservoirs: Carmópolis Member, Sergipe-Alagoas Basin, northeastern Brazil. *AAPG Bulletin*, 79(5), 725-747.
- Souza-Lima, W. and Hamsi Jr., G. 2003. *Bacias Sedimentares Brasileiras: Bacias da Margem Continental*. *Fundação Paleontológica Phoenix*, 50, 1-4.
- Szatmari, P., Lima, C.M.D, Fontaneta, G., Melo Lima, N.D., Zambonato, E., Menezes, M.R., Bahniuk, J., Coelho, S.L., Figueiredo, M., Florencio, C.P. and Gontijo, R., 2021. Petrography, geochemistry and origin of South Atlantic evaporites: The Brazilian side. *Marine and Petroleum Geology*, 127, 1-31.

- Szatmari, P. and Milani, E.J., 1999. Microplate rotation in northeast Brazil during South Atlantic rifting: Analogies with the Sinai microplate. *Geology*, 27(12), 1115-1118.
- Trindade, L.A.F., 1992. Geochemical assessment of petroleum migration and mixing in the Potiguar and Sergipe-Alagoas basins, Brazil. Unpublished doctoral dissertation, Stanford University, 333 p.
- Turcotte, D.L. and Schubert, G., 2002. *Geodynamics*. Cambridge university press.
- Vasconcelos, D.L., Bezerra, F.H., Medeiros, W.E., de Castro, D.L., Clausen, O.R., Vital, H. and Oliveira, R.G., 2019. Basement fabric controls rift nucleation and postrift basin inversion in the continental margin of NE Brazil. *Tectonophysics*, 751, 23-40.
- Viana, A.R., 2001. Seismic expression of shallow-to deepwater MTDs along the southeastern Brazilian margin. *Marine Geophysical Researches*, 22(5), 509-521.